

National Centre for Nuclear Research
Department of Nuclear Techniques and Equipment
Radiation Detectors Division



DISSERTATION

**Optimization of Detectors for Time-of-Flight
Positron Emission Tomography**

Tomasz Szczęśniak

Świerk 2011

Narodowe Centrum Badań Jądrowych

Departament Aparatury i Technik Jądrowych
Zakład Fizyki Detektorów



ROZPRAWA DOKTORSKA

**Optymalizacja Detektorów dla Pozytonowej
Tomografii Emisyjnej z Czasem Przelotu**

Tomasz Szczęśniak

Rozprawa doktorska wykonana
w Narodowym Centrum Badań Jądrowych
w Zakładzie Fizyki Detektorów
pod kierunkiem
prof. dr hab. Marka Moszyńskiego

Świerk 2011

Rodzicom

Abstract

The aim of this thesis is to understand the time resolution limitations of scintillation detectors proposed for Time of Flight Positron Emission Tomography (TOF PET). This goal is achieved by an analysis of the fundamental properties of the scintillation detector, such as the photomultiplier's quantum efficiency and time jitter or the scintillator's light output and decay time constant.

The first part of the thesis presents the most important aspects of positron emission tomography (PET) as well as possible improvements due to incorporation of the time of flight (TOF) technique. Scintillation detectors are also described in detail, including their general properties and time resolution capabilities, along with a theoretical description of timing with photomultiplier (PMT) systems. In the second part, the experimental data obtained by the author from a wide set of scintillation detectors are presented. These results, mostly dealing with timing resolution, are discussed in terms of the properties and dependencies introduced in the first part of the thesis.

At the beginning of the experimental part, the limits of achievable time resolution with an LSO scintillator and fast, 2-inch diameter XP20D0 photomultiplier are presented. These data prove that the idea of a TOF PET system with detector modules based on the LSO crystal is highly realistic. Next, time resolution optimization of the LSO-based detector is shown and discussed with regard to the Hyman theory of timing. An analysis of the most important parameters affecting the time resolution of a detector consisting of a XP20D0 phototube and LSO scintillator is further extended to a wide set of photomultipliers, including not only fast, timing devices but also slow, general purpose tubes and multi-channel PMTs. A summary of all the gathered data allows for a conclusion about the general dependency of time resolution on the time jitter of the photomultiplier used. This linear dependency is shown for many types of photomultipliers in a plot of normalized time resolution (normalized to a photoelectron number and excess noise factor) as a function of the time jitter in the center of a photocathode. The plot is later extended to other types of photodetectors, such as silicon photomultipliers (SiPMs).

The thesis also deals with alternative concepts of PET block detector configuration. One of the studied ideas is a detector where one monolithic scintillator, read by multi-anode PMT, is used instead of many pixelated crystals. The time resolution of such a design is presented and compared with data obtained with the use of the classic XP20D0 PMT and small LSO samples.

Another tested improvement of the PET block detector is the application of LSO crystals co-doped with calcium. The timing characterization of such LSO samples with different co-doping percentages, ranging from 0 to 0.4 atomic % of Ca added to the starting raw material, is presented and discussed with respect to a high quality LSO sample without co-doping. The results show that calcium added to the LSO composition considerably improves its scintillating and timing properties.

Finally, the timing properties of a scintillation detector with a light readout by means of a silicon photomultiplier are presented and discussed. The results of the timing measurements

made with LSO and LFS scintillators and $3 \times 3 \text{ mm}^2$ SiPM are compared with the data obtained with the use of the PMTs, presented in the previous chapters.

Streszczenie

Celem rozprawy jest zrozumienie ograniczeń związanych z czasową zdolnością rozdzielczą detektorów scyntylacyjnych proponowanych dla Pozytonowej Tomografii Emisyjnej z Czasem Przelotu (TOF PET). Cel ten jest osiągnięty poprzez analizę takich podstawowych własności detektora scyntylacyjnego jak wydajność kwantowa i wewnętrzna czasowa zdolność rozdzielcza fotopowielacza, a także ilość i czas zaniku światła w scyntylatorze.

Pierwsza część rozprawy przedstawia najważniejsze aspekty pozytonowej tomografii emisyjnej (PET), a także możliwe usprawnienia dzięki wprowadzeniu techniki czasu przelotu (TOF). Szczegółowo opisane są tu także detektory scyntylacyjne, włączając w to ich ogólne właściwości, możliwości związane z czasową zdolnością rozdzielczą oraz opis teoretyczny układów czasowych używających fotopowielaczy (PMT). W części drugiej przedstawione są dane eksperymentalne otrzymane przez autora z szeroką gamą detektorów scyntylacyjnych. Wyniki te, głównie dotyczące czasowej zdolności rozdzielczej, są dyskutowane w odniesieniu do właściwości i zależności wprowadzonych w pierwszej części rozprawy.

Na początku części eksperymentalnej przedstawione są ograniczenia związane z możliwą do uzyskania czasową zdolnością rozdzielczą ze scyntylatorem LSO i szybkim, dwucalowym fotopowielaczem XP20D0. Te dane dowodzą, że pomysł systemu TOF PET, z zastosowaniem modułów detekcyjnych opartych o kryształy LSO jest wysoce realistyczny. Następnie, przedstawiona jest optymalizacja czasowej zdolności rozdzielczej detektora opartego o LSO, która dyskutowana jest w odniesieniu do teorii Hymana. Wcześniejsza analiza najbardziej istotnych parametrów mających wpływ na czasową zdolność rozdzielczą detektora składającego się z fotopowielacza XP20D0 i scyntylatora LSO jest rozszerzona na inne typy fotopowielaczy, wliczając w to nie tylko „szybkie” urządzenia przeznaczone do pomiarów czasowych, ale także „wolne” fotopowielacze ogólnego zastosowania, a także fotopowielacze wielokanałowe. Podsumowanie wszystkich zebranych wyników pozwala wyciągnąć wnioski dotyczące ogólnej zależności czasowej zdolności rozdzielczej od czasowych rozrzutów własnych użytego fotopowielacza. Ta liniowa zależność jest przedstawiona dla wielu typów fotopowielaczy na wykresie znormalizowanej czasowej zdolności rozdzielczej (znormalizowanej do liczby fotoelektronów oraz współczynnika fluktuacji wzmocnienia) w funkcji czasowych rozrzutów własnych w centralnej części fotokatody. W dalszej części jest ona rozszerzona na fotodetektory innego typu, takie jak fotopowielacze krzemowe (SiPM).

Rozprawa zajmuje się również alternatywnymi koncepcjami budowy detektora dla PET. Jednym z badanych pomysłów jest detektor gdzie zamiast wielu małych kryształów (pikseli) zastosowany jest jeden monolityczny scyntylator, odczytywany przez fotopowielacz wielokanałowy. W pracy przedstawiono czasową zdolność rozdzielczą takiej konstrukcji i porównano ją z danymi otrzymanymi z klasycznym fotopowielaczem XP20D0 i małymi próbkami LSO.

Innym testowanym usprawnieniem detektora PET jest zastosowanie kryształów LSO domieszkowanych wapniem. Charakterystyka czasowa tego rodzaju próbek LSO z różnym procentowym domieszkowaniem, wahającym się od 0 do 0.4%, w materiale startowym, jest

zaprezentowana i dyskutowana w odniesieniu do niedomieszkowanej próbki LSO wysokiej jakości. Wyniki pokazują, że wapń dodany do związku LSO znacząco poprawia jego własności scyntylacyjne i czasowe.

Na końcu przedstawione i przedyskutowane są własności czasowe detektora scyntylacyjnego z odczytem światła za pomocą fotopowielacza krzemowego. Wyniki pomiarów czasowej zdolności rozdzielczej wykonane ze scyntylatorami LSO i LFS, i fotodetekтором SiPM o powierzchni $3 \times 3 \text{ mm}^2$ są porównane z danymi otrzymanymi dla fotopowielaczy, przedstawionymi we wcześniejszych rozdziałach.

Contents

1. General introduction	1
1. Time-of-Flight positron emission tomography	1
2. Aim of the work	1
3. Thesis structure	3
2. Positron Emission Tomography	5
1. Operation principles	5
A. Radiation sources	5
B. Scanner geometry	6
2. Block detector design	6
A. Introduction	6
B. Early designs	7
C. Present designs	7
3. Spatial resolution	9
A. Annihilation process	9
B. Positron range	10
C. Non-collinearity	10
D. Spatial resolution of scintillation detectors	11
4. Factors affecting image contrast	12
A. Depth of interaction	12
B. Types of coincidences	13
5. Possible improvements of the PET image	14
A. Increased dose	14
B. Longer scanning time	14
C. More efficient scintillation detectors	14
D. Extended energy spectrum	14
E. Increased solid angle	15
F. Time-of-Flight	15
6. References	15
3. Time-of-Flight information in PET	17
1. Incorporation of TOF in PET	17
A. TOF principles	17
B. Required time resolution	18
2. Benefits of TOF in PET	19
A. Reduction of statistical noise	19
B. Reduced random event rate	21
C. Reduced axial blurring	22
D. Possibility of a simultaneous emission and transmission scan	23
3. References	23

4. Scintillating crystals in PET	25
1. General description of scintillators.....	25
A. Definition.....	25
B. Interaction of gamma rays with matter	25
C. Scintillation mechanism in activated inorganic crystals.....	26
2. Basic parameters of scintillators.....	28
A. Detection efficiency.....	28
B. Scintillation efficiency.....	28
C. Decay time.....	30
D. Energy resolution	30
E. Other properties	31
3. Scintillators used in PET	31
A. NaI:Tl.....	31
B. BGO.....	32
C. LSO.....	32
D. Other scintillators	33
4. References.....	34
5. Photomultipliers.....	37
1. Introduction	37
A. Operation principles	37
B. Timing properties	38
2. Photocathode	38
A. Sensitivity	38
B. Types and materials	39
3. Photoelectron collection efficiency	39
A. Input optics.....	39
B. Electron multiplier	40
4. Transit time spread.....	41
5. Anode.....	42
A. Anode construction and space charge effect.....	42
B. Screening grid at the anode	43
6. Excess noise factor	44
A. Origin of the excess noise factor	44
B. Experimental example.....	44
7. References.....	45
6. Theory of Time Resolution of Photomultiplier Systems	47
1. Characteristics of the output pulse	47
A. Introduction.....	47
B. Photocathode illumination function.....	47
C. Single photoelectron response (SER).....	48
D. Statistical fluctuations of the SER parameters.....	49
E. Output current pulse.....	50

2.	<i>Time resolution</i>	50
A.	<i>Machine times</i>	50
B.	<i>Examples of approximate analytical calculations and Monte Carlo results</i>	51
C.	<i>Hyman theory</i>	53
D.	<i>Comparison with experiments</i>	56
3.	<i>References</i>	60
7.	<i>Experimental methods</i>.....	61
1.	<i>Number of photoelectrons</i>	61
2.	<i>Timing measurements</i>	62
A.	<i>Time resolution</i>	62
B.	<i>Decay time constant</i>	63
C.	<i>Time jitter</i>	64
D.	<i>Electronics</i>	65
3.	<i>References</i>	65
8.	<i>Study of timing with LSO on XP20D0</i>.....	67
1.	<i>Introduction</i>	67
A.	<i>Motivation</i>	67
B.	<i>Aim of the study</i>	67
2.	<i>Prospects for Time-of-Flight PET with LSO scintillators</i>	68
A.	<i>Photomultipliers and scintillators</i>	68
B.	<i>Time resolution with 10x10x5 mm³ LSO</i>	68
C.	<i>Time resolution with 4x4x20 mm³ LSO</i>	70
D.	<i>Conclusion</i>	72
3.	<i>A Further Study of Timing with LSO on XP20D0</i>	72
A.	<i>Scintillators</i>	73
B.	<i>Photomultipliers</i>	74
C.	<i>Optimization of the time resolution</i>	75
D.	<i>Comparison to the Hyman theory of timing</i>	77
4.	<i>Time resolution of the two-PMTs system</i>	79
A.	<i>Time resolution</i>	79
B.	<i>Pulse arrival time effect</i>	81
C.	<i>Influence of the gain of the PMTs</i>	82
D.	<i>Anode pulse shape</i>	83
5.	<i>Conclusions</i>	84
6.	<i>References</i>	85
9.	<i>Fast photomultipliers for TOF PET</i>.....	87
1.	<i>Introduction</i>	87
A.	<i>Motivation</i>	87
B.	<i>Aim of the study</i>	87
2.	<i>Experimental details</i>	87
A.	<i>Experimental setup</i>	87
B.	<i>Tested photomultipliers</i>	88

3. Results	89
A. Number of photoelectrons dependence of timing	89
B. Time jitter dependence of timing	90
C. Influence of the initial rise time of the anode pulse	93
D. Decay time constant dependence of timing	95
4. Discussion	96
A. Factors influencing timing in an LSO based detector	96
B. An ideal timing photomultiplier	97
C. Ideal PMT versus the real world	97
D. Conclusions	98
5. References	98
10. A Time Resolution Study of a Continuous Crystal Detector for TOF PET	101
1. Introduction	101
A. Motivation	101
B. Aim of the study	101
2. Experimental details	102
A. Scintillators and photomultiplier	102
B. Experimental methods	103
C. Arrangement of the sum-signal	103
3. Results	104
A. Time jitter	104
B. Time resolution with 10x10x5 mm ³ LSO	105
C. Time resolution with 20x20x20 mm ³ LYSO	107
4. Discussion	110
A. Timing characteristic of the H8711-200MOD	110
B. Position decoding in a continuous crystal	111
C. Conclusions	111
5. References	112
11. Timing Resolution and Decay Time of LSO Crystals Co- doped with Calcium	113
1. Introduction	113
A. Motivation	113
B. Aim of the study	113
2. Detector details	113
A. Scintillators	113
B. Photomultiplier	114
C. Experimental methods	114
3. Results	114
A. Number of photoelectrons	114
B. Time resolution	116
C. Decay time constants	118
D. Energy resolution	120

4. Conclusions.....	121
5. References.....	121
12. Time Resolution of Scintillation Detectors Based on SiPMs in Comparison with Photomultipliers	123
1. Introduction	123
A. Motivation	123
B. Aim of the study.....	123
C. The fundamental properties of SiPMs in comparison to PMTs	124
2. Experimental details.....	124
A. Photodetectors and scintillators.....	124
B. MPPC preamplifier.....	125
3. Results	125
A. Time resolution.....	125
B. Light pulse shape.....	128
C. Photon detection efficiency	128
D. Excess noise factor	129
E. Time jitter and crosstalks	131
F. Comparison with photomultipliers	136
4. Conclusions.....	137
5. References.....	137
13. Summary	139
Acknowledgments	143

1. General introduction

1. Time-of-Flight positron emission tomography

Emission tomography is a kind of medical imaging which uses radioactive materials in order to reproduce the physiological properties of a human body. Computed tomography (CT), based on X-rays, shows the anatomical image of a patient. Emission tomography, in contrast to CT, allows to create a functional image of the internal organs. Therefore, CT shows how patients look like inside, whereas emission tomography exhibits how their organs work.

Positron Emission Tomography (PET) uses radiopharmaceuticals based on β^+ emitters. Such isotopes, due to the annihilation of an electron and the emitted positron, become a source of two 511 keV gamma quanta radiated collinearly in two opposite directions. Simultaneous detection of these two quanta, originating from the same decay event, allows to assign a line of response (LOR) which contains the position of the radiation source. Information gathered from thousands of such response lines makes it possible to reconstruct a radioisotope distribution inside a patient's body and, consequently, the localization of regions with increased metabolism.

Standard algorithms of image reconstruction assume that for a single event, the localization probability of a source position is equal for the whole line of response. However, significant improvement of the reconstructed image quality can be achieved due to the incorporation of additional information about Time-of-Flight (TOF) of annihilation quanta. Knowledge of the time difference between detection of the first and second photon allows to narrow down the source localization area. The length of the TOF line of response is determined by the time resolution of the used gamma-radiation detectors. Ultimately, the localization area can be reduced from the full diameter of a PET scanner (about 90 cm) to only 8 cm, assuming a detector time resolution of 500 ps. Images reconstructed in TOF PET systems are characterized by improved signal to noise ratio and, hence, better image contrast.

2. Aim of the work

Improvement of image quality in PET scanners due to TOF information needs proper optimization of the detectors used, especially as concerns their time resolution performance. At present, most of the scanners in PET tomographs are based on scintillation modules in the form of block detectors. This type of construction consists of a matrix of scintillators (typically 8x8 or 9x9) read by a few photomultipliers (four in most cases). In the present work a number of experiments with a wide set of scintillation detectors is discussed with respect to the requirements for a TOF PET block detector.

The aim of the thesis is to understand the limitations and optimization methods of time resolution of scintillation detectors proposed for TOF PET. Special attention is paid to studies of dependencies between the fundamental properties of photodetectors and

scintillators, such as quantum efficiency, transit time spread (time jitter), light output and the decay time constant of scintillators. The presented results of the time resolution experiments are analyzed and compared with theoretical predictions given by the Hyman theory of timing with photomultiplier systems.

The above studies were triggered by the EU 6th Framework Programme project entitled *Molecular Imaging for Biologically Optimised Cancer Therapy (BIOCARE)*, led by the Karolinska Institute in Stockholm, Sweden. In a part of the project new developments related to the optimization of TOF PET detectors were planned and realized, which confirms the importance of incorporating the TOF technique into modern PET systems.

Moreover, cooperation with Photonis (formerly Philips), one of the major producers of photomultipliers, made possible experiments with plenty of photodetectors, including new versions of existing constructions and prototypes that are commercially unavailable.

The LuSiO₅:Ce (LSO) scintillating crystal was used during most of the studies. This scintillator (or similar LYSO) is used in a majority of modern PET scanners and replaced Bi₄Ge₃O₁₂ (BGO), on which older constructions were based. In addition, due to close collaboration with Chuck Melcher (inventor of LSO) at the University of Tennessee, also measurements with new types of LSO crystals, co-doped with calcium, were possible and are reported in the thesis.

The thesis is based on the following papers:

- [1] T. Szczesniak, M. Moszynski, A. Nassalski, P. Lavoute, and A. G. Dehaine, "A further study of timing with LSO on XP20D0 for TOF PET," *IEEE Trans. Nucl. Sci.*, vol. 54, no. 5, pp. 1464–1473, Oct. 2007.
- [2] T. Szczesniak, M. Moszynski, L. Swiderski, A. Nassalski, A. Syntfeld-Kazuch, A. G. Dehaine, and M. Kapusta, "A comparative study of fast photomultipliers for timing experiments and TOF PET," *IEEE Trans. Nucl. Sci.*, vol. 56, no. 3, pp. 1017–1023, Jun. 2009.
- [3] T. Szczesniak, M. Moszynski, L. Swiderski, A. Nassalski, P. Lavoute, and M. Kapusta, "Fast photomultipliers for TOF PET," *IEEE Trans. Nucl. Sci.*, vol. 56, no. 1, pp. 173–181, Feb. 2009.
- [4] T. Szczesniak, M. Moszynski, A. Syntfeld-Kazuch, L. Swiderski, M. A. Spurrier-Koschan, and C. L. Melcher, "Timing resolution and decay time of LSO crystals co-doped with calcium," *IEEE Trans. Nucl. Sci.*, vol. 57, no. 3, pp. 1329–1334, Jun. 2010.
- [5] T. Szczesniak, M. Moszynski, L. Swiderski, A. Nassalski, A. Syntfeld-Kazuch, P. Ojala, and C. Bohm, "A time resolution study of a continuous crystal detector for TOF PET," *IEEE Trans. Nucl. Sci.*, vol. 57, no. 1, pp. 40–47, Feb. 2010.
- [6] T. Szczesniak, M. Moszynski, M. Grodzicka, D. Wolski, L. Swiderski, M. Szawlowski, and M. Kapusta, "Time resolution of scintillation detectors based on SiPM in comparison to photomultipliers," in *Nuclear Science Symposium Conference Record (NSS/MIC), 2010 IEEE*. IEEE, 2010, pp. 1728–1735.

Moreover some data reported in the other papers, with a significant contribution of the Author, were used in the thesis, as follow:

- [7] M. Moszynski, M. Kapusta, A. Nassalski, T. Szczesniak, D. Wolski, L. Eriksson, and C. Melcher, “New prospects for Time-of-Flight PET with LSO scintillators,” *IEEE Trans. Nucl. Sci.*, vol. 53, no. 5, pp. 2484–2488, Oct. 2006.
- [8] T. Szczesniak, M. Gierlik, M. Kapusta, M. Moszynski, D. Wolski, P. Lavoute, and E. Rossignol, “The 75 mm diameter Photonis XP43D2 photomultiplier with the screening grid at the anode for timing experiments,” *IEEE Trans. Nucl. Sci.*, vol. 53, no. 3, pp. 1540–1546, Jun. 2006.
- [9] M. Moszynski, M. Gierlik, M. Kapusta, A. Nassalski, T. Szczesniak, C. Fontaine, and P. Lavoute, “New Photonis XP20D0 photomultiplier for fast timing in nuclear medicine,” *Nucl. Instr. Meth. A*, vol. 567, no. 1, pp. 31–35, Nov. 2006.
- [10] M. Moszynski, T. Szczesniak, M. Kapusta, M. Szawlowski, J. Iwanowska, M. Gierlik, A. Syntfeld-Kazuch, L. Swiderski, C. Melcher, L. Eriksson *et al.*, “Characterization of scintillators by modern photomultipliers—a new source of errors,” *IEEE Trans. Nucl. Sci.*, vol. 57, no. 5, pp. 2886–2896, Oct. 2010.

3. Thesis structure

The thesis consists of two main parts. The first part presents the most important aspects of positron emission tomography and improvements due to the incorporation of the Time-of-Flight technique. Moreover, in this part the details of scintillation detectors are discussed, as are their time resolution capabilities along with a theoretical description of photomultiplier systems. The second part covers the experimental data obtained by the author with a wide set of scintillation detectors. The results are discussed in terms of the properties and dependencies that were introduced in the first part.

The first chapter is a general description of the thesis. The aim of the second chapter is to introduce the reader to the principles of positron emission tomography. Here, except for the physical principles, particular emphasis is put on a description of the PET block detector and the factors affecting the reconstructed image contrast. Incorporation of the Time-of-Flight technique into the PET reconstruction algorithms is one of the methods leading to image contrast improvement. Details of TOF information in PET, together with the benefits of such improvement, are presented in chapter 3. Chapters 2 and 3 are, in fact, the general motivation for the thesis. The presented capabilities of the PET system, as well as the numerous advantages of TOF PET scanners, should convince the reader that the topic presented in the thesis is of great importance to the medical community.

Components of the block detector are described in detail in chapters 4 and 5. Chapter 4 contains a general description of scintillators and their basic parameters, especially important in TOF PET. In the last section of this chapter, the scintillators most commonly used in PET, such as BGO and LSO, are presented together with their advantages and disadvantages. The information gathered in this chapter suggests that LSO is presently the only candidate for TOF PET and, hence, this type of scintillator was used in the studies presented by the author.

The most important elements of photomultipliers are presented in chapter 5. Here, the crucial properties of a photodetector, such as the number of photoelectrons, time jitter, excess noise factor and anode pulse, are introduced with respect to the construction details and various types of PMTs. In a following chapter a theoretical description of time resolution with photomultiplier systems is presented. In both chapters experimental examples of basic PMT properties and experimental verification of the timing theory are also shown.

Chapter 7 begins the second part of the thesis, in which the experimental set-ups and methods used in timing measurements are described. Subsequent chapters present the experimental studies carried out by the author. These chapters have a similar structure starting with motivation for a given measurement, followed by experimental details and results, and ending with a discussion and conclusions.

Chapter 8 presents the limits of achievable time resolution with an LSO scintillator and a fast photomultiplier XP20D0 with a diameter of 2 inches. The results presented in section 2 are basic reference data and the starting point for most of the later measurements. Moreover, these data have proven that the idea of TOF PET with an LSO crystal is highly realistic. Section 3 discusses the time resolution optimization of an LSO-based detector with regard to the Hyman theory of timing (presented in chapter 6). Section 4 shows the benefits of improved light collection efficiency with the common light readout of a double-PMT system.

The experimental data of the time resolution measurements, made with a wide range of photomultipliers, are presented in chapter 9. The set of tested PMTs includes not only fast timing devices but also slow, general-purpose tubes and multi-channel PMTs. An analysis of the gathered data showed a general dependency of time resolution on time jitter. The plot introduced in this chapter allows for a comparison of the timing capabilities of various radiation detectors based on a given type of scintillator and any kind of photomultiplier. Moreover, as is presented in chapter 12, this plot can be extended to the other types of photodetectors, such as silicon photomultipliers.

In chapter 10 the idea of a novel construction of a PET block detector is presented, where one continuous, monolithic crystal is used instead of many scintillating pixels. The reported measurements were triggered by the results obtained in section 3 of chapter 8, which showed time resolution improvement due to a light readout by means of two photomultipliers. In the case of this continuous crystal, the scintillation light is read by a 16-channel PMT.

Chapters 8 to 10 cover the time resolution measurements with various types of photomultipliers and detector configurations. The last two chapters are focused on a new type of LSO crystal – co-doped with calcium and a competitor of the classic photomultiplier – the silicon photomultiplier (SiPM).

The timing characterization of LSO samples with different co-doping percentages, ranging from 0 to 0.4 atomic % of Ca added to the starting raw material, is presented in chapter 11. The measurements compare the time resolution, light output and decay time constants of classic and new, co-doped LSO crystals. The results show that calcium added to the LSO composition considerably improves its scintillating properties and creates a new generation of LSO scintillators.

Finally, in chapter 12 the timing properties of a scintillation detector with a light readout by means of a silicon photomultiplier are discussed. Silicon photomultipliers are currently widely being studied by many research groups in the world in order to apply them in TOF-PET or TOF-PET-MRI systems. The presented results of timing measurements obtained with LSO and LFS scintillators and $3 \times 3 \text{ mm}^2$ devices are compared to the PMT properties presented in the previous chapters. The final discussion concerning the timing capabilities of SiPMs is made on the basis of the plot introduced in chapter 9 containing both PMT and SiPM data.

Chapter 13 contains the general conclusions and a summary of the thesis.

2. Positron Emission Tomography

1. Operation principles

A. Radiation sources

The aim of Positron Emission Tomography (PET) is to visualize the functional activity of live organisms. This task is carried out through the imaging of positron emitter distribution inside the human or animal body.

The positrons are emitted by β^+ decaying isotopes. This kind of beta decay is a process in which a proton is converted into a neutron, positron and electron neutrino:



The β^+ emitters are injected into the patient with the use of a radioactive drug that is labeled with a positron-emitting isotope. The drug localizes itself in different places inside the body according to its metabolic properties. The labeled drugs or radiopharmaceuticals are based on isotopes of the most common elements of organic materials, e.g. oxygen (^{15}O), carbon (^{11}C) or nitrogen (^{13}N). However, the isotope of fluorine (^{18}F), which is used as a substitute for hydrogen, e.g. in FluoroDeoxyGlucose (FDG), is the most widely used isotope in clinical applications. Besides the β^+ emitter, the PET drug must also be characterized by a short half-life in order to minimize the patient's exposure to radiation. The half-lives of radiopharmaceuticals vary from several minutes (^{15}O -2min, ^{13}N -10min, ^{11}C -20min) to several hours (^{18}F -110min). Examples of radionuclides used in PET in order to create images of various body processes are presented in Table I [1].

TABLE I
POSITRON EMITTERS USED IN PET IMAGING

Radiopharmaceutical	Biological process
^{18}F - FDG	Glucose metabolism
^{18}F - FMISO	Hypoxia
^{18}F - Estradiol	Receptor
^{18}F - Annexin	Apoptosis
^{18}F - Fluorothymidine (FLT)	Proliferation
^{11}C - Thymidine	
^{11}C - Verapamil	Multi-drug resistance
^{11}C - Acetate	Membrane biosynthesis
^{15}O - H_2O	Vascularity / Blood flow

B. Scanner geometry

Images in positron emission tomography are reconstructed on the basis of electronic signals due to a simultaneous detection of two 511 keV gamma quanta emitted after annihilation of a positron. These gamma rays are registered by a ring of detectors surrounding the patient. In an ideal case, the signal registered in one detector, in coincidence with the second signal registered in the opposite detector, originates from a single β^+ decay. Since annihilation quanta are emitted nearly collinearly, such a coincidence event allows to determine the line-of-response (LOR) that virtually connects the two triggered detectors. The line-of-response determines the area (the line with a length equal to the scanner's diameter) where the source is localized. A collection of LORs from a large number of events gathered during the PET scan makes it possible to reconstruct the radiopharmaceutical distribution inside the body and, next, to create a tomography image. A diagram of a typical PET scanner architecture and operation is presented in Fig. 1.

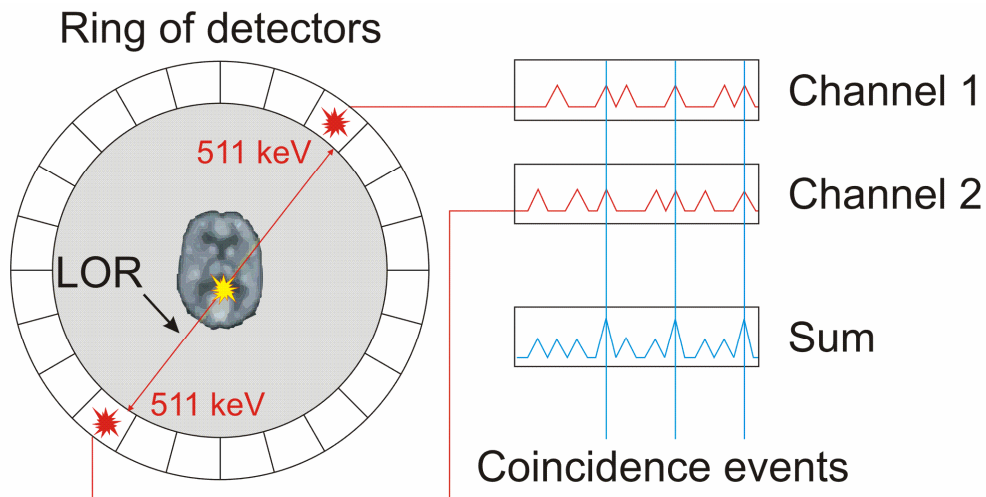


Fig. 1. Diagram of a PET scanner. A patient injected with a radiopharmaceutical is surrounded by a ring of detectors which transform the gamma energy, especially annihilation quanta of 511 keV, into electronic signals. The signals registered in coincidence originate from a single annihilation event and allow the creation of the line-of-response on which the source is localized.

2. Block detector design

A. Introduction

A single PET detector module, like most of the radiation detectors, consists of two main elements, a scintillator and a photodetector. First, radiation energy is converted into weak flashes of light in the scintillator, and then these scintillation photons are converted into electric signals in the photodetector. The detector design, i.e. the scintillator shape and chemical compound as well as photodetector type, is always optimized for a specific application. The most common scintillators in PET are NaI:Tl (used in the first systems), BGO, LSO or GSO. The number of photodetectors used in nuclear imaging is limited mainly to three devices: photomultipliers, avalanche photodiodes and silicon photomultipliers. Both scintillators and photodetectors are discussed in detail in the subsequent chapters.

B. Early designs



Fig. 2. First prototype of a PET detection system (A and B) based on 24 detectors consisting of single NaI:Tl scintillators coupled to single photomultipliers [2]. The images of a radioactive phantom acquired by the system are also presented (C).

The first prototype of a gamma camera, invented by Hal Anger in 1952, was based on a large pinhole collimator placed in front of the NaI:Tl scintillator, whose light was registered on a photographic plate. Later in 1956, Anger developed a similar camera but with a light readout made by means of a close-packed array of 7 photomultipliers [3]. In the newer design the position of the interaction point within the crystal was calculated by taking into account the light spread in the scintillator and the differences in the amount of light detected by several photomultipliers. This method of determining the gamma interaction position is called *Anger logic* and is still used in most of the presently available nuclear imaging devices, both in Single Photon Emission Computed Tomography (SPECT) and PET. The detection systems in most of the presently available SPECT scanners are based on two gamma camera modules. In this configuration also coincidence measurements with positron emitting isotopes are possible, however, application of the pinhole collimator dramatically reduces detection efficiency and the number of coincidences.

Early PET systems were based on detectors in which a single crystal was coupled to a single photomultiplier [4], [5], [6], [7]. The first prototype of a PET detection system, created by Phelps et al. in 1975, is presented in Fig. 2 [2]. It consists of 24 NaI:Tl based detectors in a hexagonal arrangement. In this design the lack of a collimator significantly improves detection efficiency, but spatial resolution is limited by the size of the scintillators. Improvement of the spatial resolution could be possible due to the application of smaller crystals coupled to smaller PMTs, but such a modification leads to higher costs and a large number of electronic channels. Moreover, the size of the detectors makes it difficult to build a multi-slice scanner.

C. Present designs

The presently used block detector design, where a matrix of small, discrete crystals is read by a few photomultipliers, was born in the 1980s [8], [9]. An example of a single block detector module from a clinical PET scanner [10] is presented in Fig. 3.

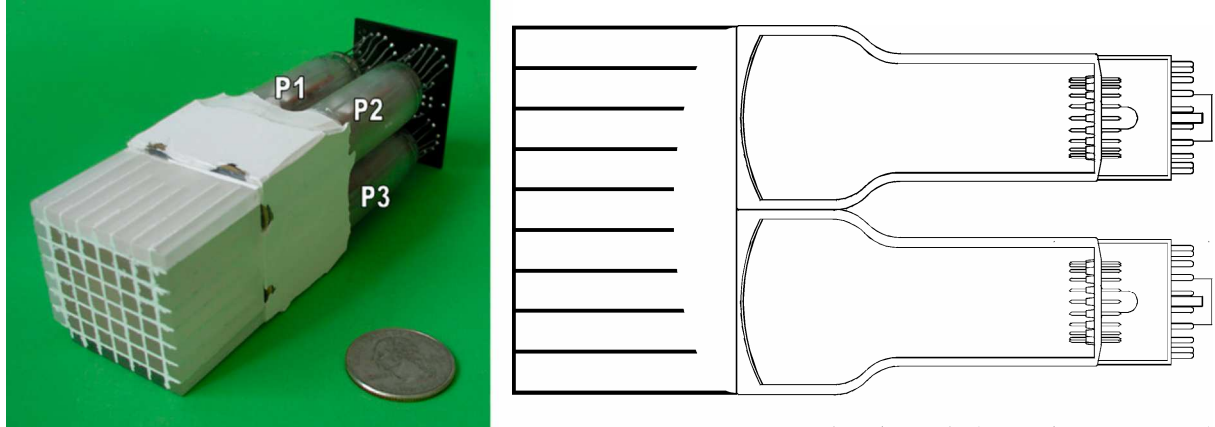


Fig. 3. Diagram (right) and example of a single block detector module from a clinical PET scanner (left). The scintillation block consists of a matrix of single pixels whose light is read by only 4 photomultipliers (P1 – P4). (Courtesy of University of Tübingen).

Retrieval of information about the position of the gamma interaction point in the scintillator block, or in other words, decoding the crystal in which the interaction took place, is carried out using Anger logic. In order to shape the light reaching the photomultipliers in a way that assures optimal pixel identification, the interface of the reflecting cover between the crystals is specially arranged (see Fig. 3). The single crystals in the block are not fully optically separated and the length of the reflector is shorter in the middle of the scintillator block. In consequence, the light related to the events absorbed in different pixels is differently distributed to the photomultipliers. The ratios of light detected by each of the photomultipliers allow identification of a single pixel in which the gamma energy was deposited. The pixel coordinates may be calculated by using the Anger weighting algorithm in the following way (P1 – P2 denote the signal amplitude of a given PMT):

$$X = \frac{P1 + P2 - P3 - P4}{P1 + P2 + P3 + P4}, \quad Y = \frac{P2 + P4 - P3 - P1}{P1 + P2 + P3 + P4} \quad (2)$$

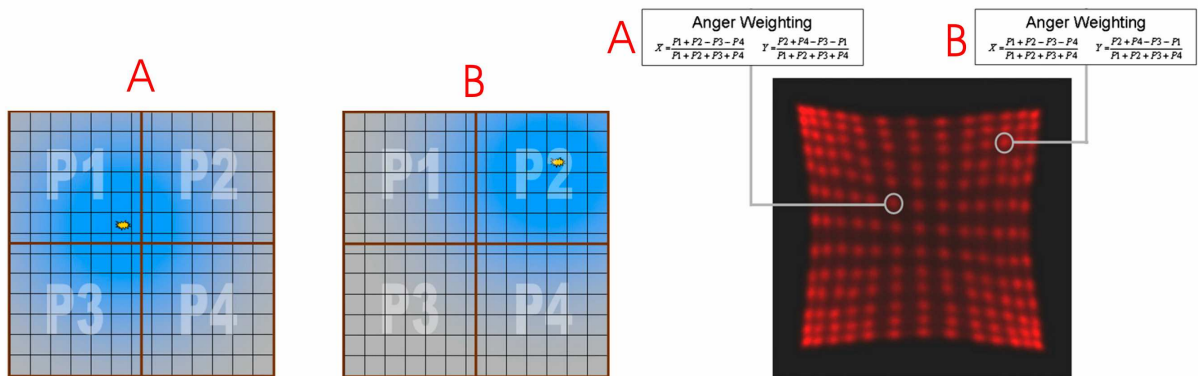


Fig. 4. Example of crystal decoding using the Anger weighting algorithm (Courtesy of University of Tübingen).

A graphical illustration of crystal identification by means of Anger logic together with an example of the 2D response profile of a block detector are presented in Fig. 4. The number of individual pixels in the block is defined by the light yield of the scintillator used. In the case

of BGO, 64 crystals can be decoded, while in the case of LSO, the detector may consist of 169 crystals.

In 1993 a modification of the block detector configuration was proposed by Wong et al. [11], [12], [13]. In their design, called *quadrant sharing*, a single photomultiplier services four crystal blocks instead of one. A diagram of the new, modified block detector is presented in Fig. 5, following [13].

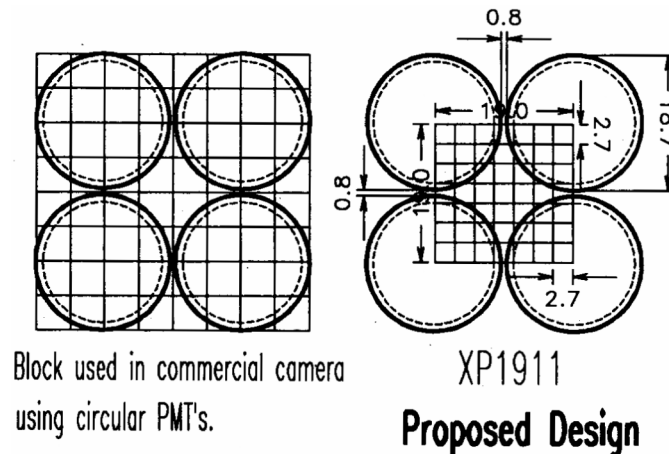


Fig. 5. Diagrams of a classic block detector module with circular PMTs (left) and a quadrant sharing design (right) proposed by Wong et al. (reprint from [13]).

The biggest advantage of such a configuration is the highly reduced number of necessary photomultipliers. In the case of the quadrant sharing configuration, the number of PMTs is equal to the number of scintillator blocks, so the photodetector costs can be reduced by a factor of 4. However, the fact that one photomultiplier is shared between 4 blocks causes a large increase of the system dead time. An event registered in a single scintillator block deadens the 8 adjacent blocks which share the same PMTs.

3. Spatial resolution

A. Annihilation process

The spatial resolution in PET is limited by the physics of β^+ radiation and the annihilation process. The total energy of β^+ decay is shared between a positron and neutrino. On average, one-third of that energy translates into a kinetic energy of the positron [14] (compare row one and two in Table II). After emission, the positron loses its kinetic energy mainly by Coulomb interactions with electrons in the surrounding tissue. Since the rest mass of a positron and electron is identical, each interaction between these two particles has a large influence on the positron path. In consequence, the positron changes its movement direction many times. After thermalization of the positron energy, its interaction with an electron (with the same spin) leads to the creation of a positronium – a hydrogen-like particle with an orbiting pair of an electron and positron. The positronium is unstable and decays (in water) after about 1.8 ns or 125 ps [14]. The pair of electron and anti-electron annihilates, emitting two nearly collinear and anti-parallel photons with energies equal to 511 keV. The electron and positron possessing opposite spins annihilate directly, without creating the positronium. Instantaneous

annihilation, prior to thermalization, is also possible, but such a process occurs at a level of 2% of all the events [15].

B. Positron range

The radial distribution of annihilation events is sharply peaked at the position of positron emission. However, the positron range, i.e. the distance between the positron emission site and positron annihilation point, determines the fundamental limitation of the PET spatial resolution. It is worth differentiating the term *range* from *path length*, since both are widely used but in an ambiguous manner. The *range* describes the penetration depth. The *path length* (sum of collision lengths), on the other hand, is defined as an integral of the reciprocal of the stopping power of the medium and describes the continuous slowing down approximation range [16]. Due to the Coulomb scattering of positrons, and hence their tortuous path in matter, the path length is always much larger than the range. The positron energy, half-life, theoretical path length and experimentally obtained range in water for the isotopes commonly used in PET are presented in Table II [16]. It is worth noticing that the path length of positrons is slightly longer as compared to the electrons. Due to their positive charge, the positrons are repelled from the nucleus where the electron density, and hence collision probability, is greatest, whereas the electrons are attracted [14]. Following the data in Table II, spatial resolution is limited to 1-2 millimeters, depending on the radiopharmaceutical. The shortest positron range, of about 1 mm at full width at half maximum (FWHM), is related to the lowest energy of anti-electrons emitted by ^{18}F .

TABLE II
ENERGY AND RANGE OF POSITRON-EMITTING ISOTOPES USED IN PET IMAGING

	^{18}F	^{11}C	^{13}N	^{15}O	^{68}Ga	^{82}Rb
Max energy [MeV]	0.633	0.959	1.197	1.738	1.898	3.148
Mean energy [MeV]	0.203	0.326	0.432	0.696	0.783	1.385
Half-life [min]	109.7	20.3	10.0	2.0	68.3	1.3
Theor. path length for electron in water [mm]	0.239	0.498	0.535	0.822	0.908	1.561
Exp. radial range in water, FWHM [mm]	0.102	0.111	0.142	0.149	0.168	0.169
Exp. radial range in water, FWTM [mm]	0.180	0.219	0.278	0.357	0.395	0.580

C. Non-collinearity

Another physical aspect connected with the annihilation process, which has a fundamental influence on the PET spatial resolution, is the lack of collinearity of photons emitted after annihilation. The positron or positronium possesses residual momentum prior to annihilation, and hence the direction of the annihilation quanta is given by the sum of vectors of 511 keV photon momentum and positronium residual momentum. The diagram of the worst-case scenario, where the annihilation photons are emitted perpendicular to the vector of the

positronium momentum, is presented in Fig. 6. The residual momentum of the positronium is equally divided between both annihilation quanta. Since $\sqrt{E_k m} \ll mc$, the deflection angle in one direction is equal to: $\sin \alpha \approx \alpha = \sqrt{E_k/mc^2}$, where E_k – residual kinetic energy of a positronium, m – mass of electron and positron, c – speed of light.

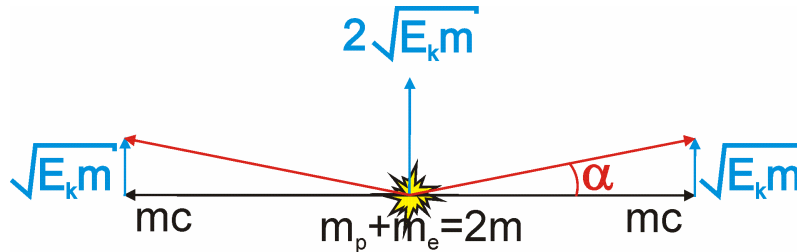


Fig. 6. Diagram of momentum vectors of positronium and annihilation quanta. The annihilation photons are emitted in the direction given by the vector sum of photon momentum and positronium residual momentum.

The kinetic energy of a positronium is less than 10 eV, which leads to 0.47 degree at FWHM of an angular uncertainty in an aqueous solution [14], [17], [18]. The influence of non-collinearity on the spatial resolution depends on the PET scanner diameters. Resolution loss for different detector ring sizes is presented in Table III [7]. The PET image is less affected by non-collinearity in the case of higher maximal energies of emitted positrons (above 3 MeV). That is when the positron range plays a major role [14].

TABLE III
SPATIAL RESOLUTION LOSS FOR VARIOUS DIAMETERS OF A PET DETECTOR RING

Ring diameter [cm]	60	80	100
Resolution loss [mm]	1.3	1.7	2.2

D. Spatial resolution of scintillation detectors

Another limitation of PET image quality is the intrinsic spatial resolution of the detectors used [19]. Their spatial resolution, as in any imaging system, can be described by the FWHM of the so-called point spread function (PSF) [7]. PSF can be illustrated as a blurred spot reflecting the point object. In the case of the PET imaging system, PSF represents its response to a collimated point source placed at a given range from the detector. The image of any object is a convolution of that object's real shape with the PSF of the detecting device or simply the intensity of the object weighted by the PSF [20] (see Fig. 7).

The resolution of the coincidence detectors is given by the FWHM of their PSF, which in this case is a convolution of the point spread functions of both detectors [21]. In the case of a block detector, which consists of many single scintillation crystals, all of the registered events are assumed to interact in the central part of the crystal. In consequence, the PSF becomes similar to a step function with a total width equal to the size of the crystal. Moreover, the PSF for the two detectors in coincidence is represented by a triangle with

a base width equal to the crystal size and, hence, the PSF FWHM is one-half of the crystal size [7]. The typical single crystal size in a PET scanner is equal to 4 mm, so spatial uncertainty due to detector intrinsic resolution is at a level of 2 mm.

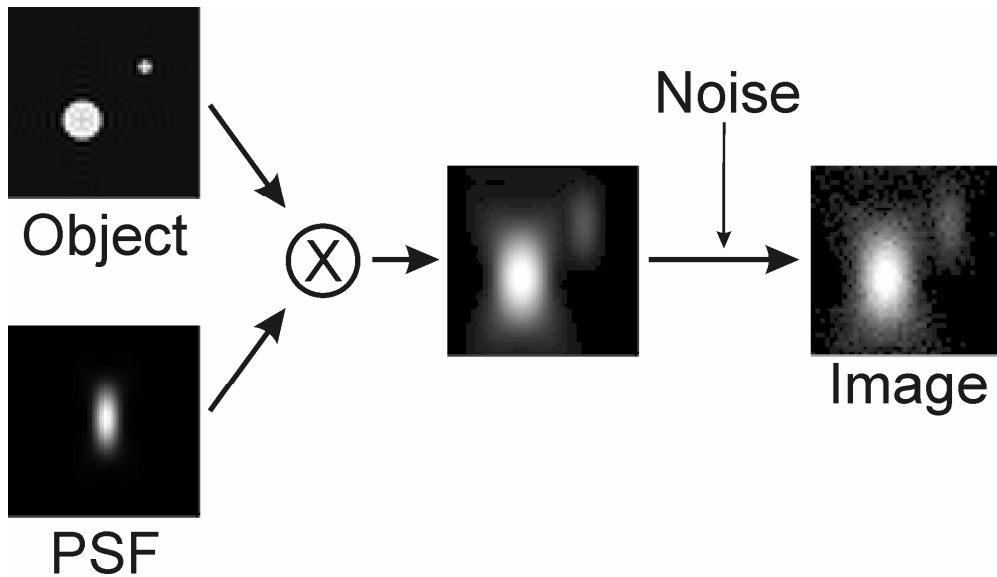


Fig. 7. Diagram of image formation as a convolution of a real object (light sources) with the point spread function of an imaging device. The photon noise that must be considered in the final image is also presented.

A summary of the three discussed mechanisms affecting PET spatial resolution is presented in Table IV [7]. The Table shows the best possible resolution of a PET system with a diameter of 80 cm, for a given positron emitter, limited by the combination of positron range, non-collinearity of annihilation quanta and the spatial resolution of a scintillation detector.

TABLE IV
SPATIAL RESOLUTION OF THE 80 CM PET DETECTOR RING RESULTING FROM POSITRON RANGE,
GAMMA NON-COLLINEARITY AND CRYSTAL SIZE

Detector pair resolution [mm]	^{11}C [mm]	^{68}Ga [mm]	^{82}Rb [mm]
0	2.3	3.1	3.3
2	3.2	4.1	7.4
6	6.6	7.4	9.2

4. Factors affecting image contrast

A. Depth of interaction

The efficiency of gamma-ray detection is one of the most important parameters in nuclear imaging. The radiation detector has to be optimized in this respect, particularly its scintillation material and size of the crystals. Typically, a single crystal in a block detector used in PET is a few centimeters high (2 cm in most cases), which assures more than 80% of absorption of the 511 keV annihilation gammas (in LSO/LYSO or BGO) [22]. However, gamma radiation

travels some unknown distance inside the crystal and also between the neighboring crystals before full absorption. As a result, if a 511 keV photon enters the crystal at a certain angle, the point of interaction will be different from the point of entry. Without information about the depth of interaction (DOI), the line of response is created on the basis of the position at the front of the crystal where the full absorption took place. As is presented in Fig. 8, such LOR is incorrect because it refers to the wrong crystal. This effect is known as a *parallax error* and leads to image blurring, which increases as the source position moves radially away from the center of the scanner [7].

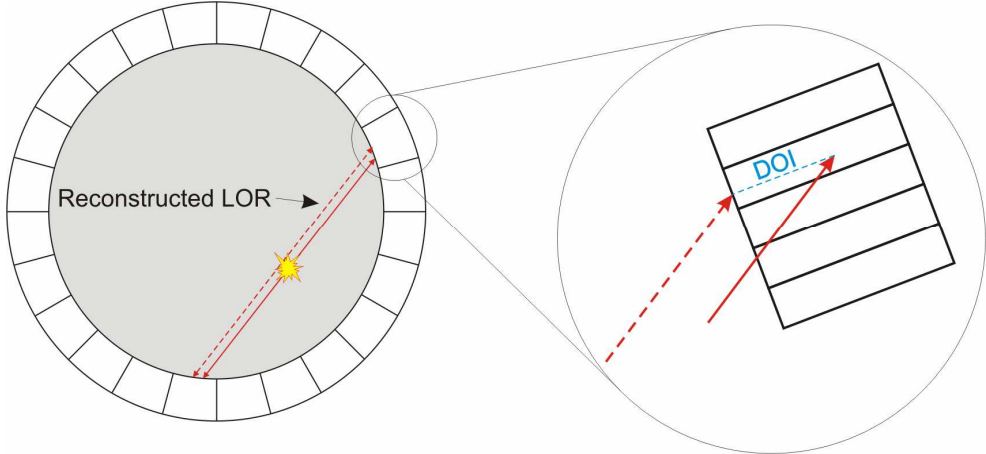


Fig. 8. Diagram of a parallax error in PET. LOR is assigned incorrectly because a gamma ray has penetrated more than one crystal before full absorption. With depth of interaction information, the interaction point would be defined precisely inside the crystal instead of at its front.

B. Types of coincidences

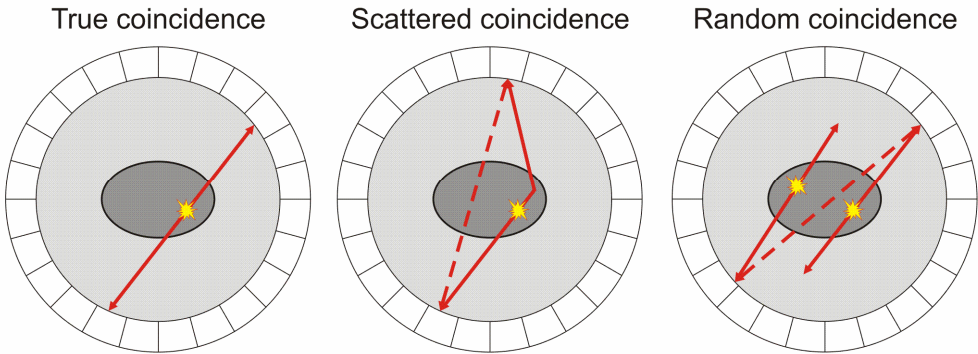


Fig. 9. Three kinds of coincidences accepted in the PET scanner.

In PET not all of the registered events correspond to true coincidences of two annihilation quanta. In fact, about one half of the events is caused by scattered photons or random coincidences. Since the patient’s body mainly consists of water, the probability of a Compton scattering of 511 keV photons is high, and hence one or both annihilation photons may change their movement direction before reaching the detector ring. Random coincidences occur when two photons originating from two different decays are registered simultaneously

in a device time window. As a result, a LOR reconstructed on the basis of scattered or random events is false. The three types of coincidences that are accepted in PET are presented in Fig. 9. True and scattered events are prompt events since both come from one decay, and the emitted gammas are detected almost simultaneously. The rates of prompt events depend linearly on the radiopharmaceutical activity, whereas random events increase as the square of activity. Random coincidences become dominant at high activity levels [7].

The aim of PET imaging is the measurement and reconstruction of true coincidences while minimizing the influence of scattered and random events. An increased number of the true events allows for improvement of the signal to noise ratio and image contrast.

5. Possible improvements of the PET image

A. Increased dose

A few options are possible in order to improve PET image quality. The first approach is to increase radiopharmaceutical activity. However, such an increase would result in much higher radiation exposure of the patients and is rather impossible. Moreover, many medical centers are already using the maximum dose rates accepted by their institutions (about 10-20 mCi for ^{18}F -FDG) [7].

B. Longer scanning time

Another simple method could be extending the scanning time, but this could have a negative influence on the patient's psychological condition. In most cases a PET examination is also combined with computed tomography (CT) and the requirement of a stable patient position during both scans together with long scanning time is hard to realize. An unstable body position is another factor that deteriorates image resolution. The solution of extended scanning time is also not optimal because it decreases the total number of PET patients, what is directly related to higher costs of a single scan.

C. More efficient scintillation detectors

From a physical point of view, an improvement of the PET image could be achieved by applying more efficient scintillators inside the detector ring. The systems currently being used are mainly based on BGO or LSO/LYSO crystals which are characterized by high density, above 7.1 g/cm^3 , and hence high stopping power of the 511 keV quanta. In the case of BGO, which possesses a higher than the LSO atomic number ($_{83}\text{Bi}$, $_{32}\text{Ge}$ compared to $_{71}\text{Lu}$, $_{14}\text{Si}$), detection efficiency at a level of 90% can be achieved with 30 mm high crystals [22]. The LSO-based detector can have similar efficiency with 40 mm high scintillators. More efficient systems, especially those close to 100%, are still unavailable. The biggest advantage of the new scintillators, such as LSO, is their high light output (about 4 times larger than BGO) and fast decay time (40 ns compared to 300 ns in BGO). The properties of the LSO allow for improvement of the block detector's energy resolution or the incorporation of the Time-of-Flight in PET.

D. Extended energy spectrum

One of the ideas for increasing tomography sensitivity was extending the accepted energy range below the 511 keV photopeak. This type of image acquisition was first tested with

a 2-head gamma camera based on NaI scintillators [23], because their efficiency is lower in comparison with the BGO or LSO detectors. Two energy windows were set, the first one at the photopeak and the second one at the Compton spectrum. The inclusion of lower energy events improved sensitivity by a factor of two, however, the influence of the Compton scattered photons was so large that it made this method clinically useless.

E. Increased solid angle

The most useful and technically available improvement is the increase of the solid angle covered by the detector ring. This approach leads to the removal of all axial collimation (3D imaging), reduction of the ring diameters and extension of the axial dimensions of the detectors. The sensitivity of a typical whole body scanner to true coincidences can be increased by a factor of 5 due to the removal of the axial collimation. Unfortunately, such an improvement is followed by 3 to 4 times larger acceptance of the scattered events. Moreover, the singles rates from outside of the field of view (FOV) are also increased [7].

F. Time-of-Flight

All of the methods described above allow sensitivity improvement but at the cost of other important parameters of the PET scanner or the PET examination. The application of the Time-of-Flight technique does not introduce any additional, unwanted effects. TOF is just additional information added to the system. Knowledge of the time difference between the detection of two photons registered in coincidence gives great benefits in image reconstruction, which are reflected in reduced noise and improved image contrast. The details of TOF PET are described in the next chapter.

6. References

- [1] R. Miyaoka, "Fundamentals of medical imaging," in *2009 IEEE NSS-MIC Short Course: Medical Imaging Fundamentals*, 2009.
- [2] M. Phelps, E. Hoffman, N. Mullani, and M. Ter-Pogossian, "Application of annihilation coincidence detection to transaxial reconstruction tomography," *J. Nucl. Med.*, vol. 16, no. 3, p. 210, 1975.
- [3] E. Tapscott, "Nuclear medicine pioneer, Hal O. Anger, 1920-2005." *J. Nucl. Med. Technol.*, vol. 33, no. 4, p. 250, 2005.
- [4] M. Phelps, E. Hoffman, S. Huang, and D. Kuhl, "ECAT: a new computerized tomographic imaging system for positron-emitting radiopharmaceuticals," *J. Nucl. Med.*, vol. 19, no. 6, p. 635, 1978.
- [5] M. Ter-Pogossian, N. Mullani, J. Hood, C. Higgins, and D. Ficke, "Design considerations for a positron emission transverse tomograph (PETT V) for imaging of the brain," *J. Comput. Assist. Tomogr.*, vol. 2, no. 5, p. 539, 1978.
- [6] R. Brooks, V. Sank, G. Chiro, W. Friauf, and S. Leighton, "Design of a high resolution positron emission tomograph: the Neuro-PET," *J. Comput. Assist. Tomogr.*, vol. 4, no. 1, p. 5, 1980.
- [7] M. Wernick and J. Aarsvold, *Emission tomography: the fundamentals of PET and SPECT*. Academic Press, 2004.
- [8] G. Muehllehner and J. Karp, "Positron emission tomography imaging – technical considerations," *Seminars in Nuclear Medicine*, vol. 16, no. 1, pp. 35–50, 1986.

- [9] M. Casey and R. Nutt, "A multicrystal two dimensional BGO detector system for positron emission tomography," *IEEE Trans. Nucl. Sci.*, vol. 33, no. 1, pp. 460–463, 1986.
- [10] B. Pichler, H. Wehrl, and M. Judenhofer, "Latest advances in molecular imaging instrumentation," *J. Nucl. Med.*, vol. 49, no. Suppl_2, p. 5S, 2008.
- [11] W. Wong, "A positron camera detector design with cross-coupled scintillators and quadrant sharing photomultipliers," *IEEE Trans. Nucl. Sci.*, vol. 40, no. 4, pp. 962–966, 1993.
- [12] W. Wong, J. Uribe, K. Hicks, and M. Zambelli, "A 2-dimensional detector decoding study on BGO arrays with quadrant sharing photomultipliers," *IEEE Trans. Nucl. Sci.*, vol. 41, no. 4, pp. 1453–1457, 1994.
- [13] W. Wong, J. Uribe, K. Hicks, and G. Hu, "An analog decoding BGO block detector using circular photomultipliers," *IEEE Trans. Nucl. Sci.*, vol. 42, no. 4, pp. 1095–1101, 1995.
- [14] M. Harpen, "Positronium: Review of symmetry, conserved quantities and decay for the radiological physicist," *Med. Phys.*, vol. 31, p. 57, 2004.
- [15] W. Heitler, *The quantum theory of radiation*. Dover Publications, 1984.
- [16] Z. Cho, J. Chan, L. Ericksson, M. Singh, S. Graham, N. MacDonald, and Y. Yano, "Positron ranges obtained from biomedically important positron-emitting radionuclides," *J. Nucl. Med.*, vol. 16, no. 12, p. 1174, 1975.
- [17] O. Mogensen, *Positron annihilation in chemistry*. Springer, 1995.
- [18] S. DeBenedetti, C. Cowan, W. Konneker, and H. Primakoff, "On the angular distribution of two-photon annihilation radiation," *Phys. Rev.*, vol. 77, no. 2, pp. 205–212, 1950.
- [19] E. Hoffman, S. Huang, D. Plummer, and M. Phelps, "Quantitation in positron emission computed tomography: 6. Effect of nonuniform resolution," *J. Comput. Assist. Tomogr.*, vol. 6, no. 5, p. 987, 1982.
- [20] Scientific Volume Imaging. Huygens deconvolution. [Online]. Available: <http://www.svi.nl/HuygensDeconvolution>
- [21] G. Muehllehner, M. P. Buchin, and J. H. Dudek, "Performance parameters of a positron imaging camera," *IEEE Trans. Nucl. Sci.*, vol. 23, no. 1, pp. 528–537, 1976.
- [22] Saint-Gobain Crystals. Efficiency calculations for selected scintillators. [Online]. Available: http://www.detectors.saint-gobain.com/uploadedFiles/SGdetectors/Documents/Technical_Information_Notes/Efficiency-Calculations.pdf
- [23] P. Nellesmann, H. Hines, W. Braymer, G. Muehllehner, and M. Geagan, "Performance characteristics of a dual head SPECT scanner with PET capability," in *Proc. IEEE Nuclear Science Symp. and Medical Imaging Conf. Record*, vol. 3, 1995, pp. 1751–1755.

3. Time-of-Flight information in PET

1. Incorporation of TOF in PET

A. TOF principles

In standard PET systems the reconstruction of the positron annihilation regions is made on the basis of a set of lines of response on which a gamma source is localized. The sum of data from many coincidence events, and hence many LORs, allows the reconstruction.

However, one can think of a different method that would utilize timing information instead of geometrical information delivered by the lines of response. Finding the annihilation point should be possible using information about the Time-of-Flight (TOF) of 511 keV quanta from the point of origin to the detector. Measurement of the time difference between detection of the first and second coincident gamma gives information about the distance from the LOR's middle point to the true source position.

The principle of application of TOF information in order to localize a positron annihilation site is presented in Fig. 1. Let us mark the radius of the PET scanner ring as d and the distance from the scanner central point to any other point as x . Now, the time of flight of the first annihilation gamma t_1 , absorbed in PMT 1, is equal to: $t_1 = (d + x)/c$, where c is the speed of light. The second gamma will be registered in PMT 2 after time: $t_2 = (d - x)/c$. The time difference between detection of both quanta is equal to: $\Delta t = |t_1 - t_2| = 2x/c$ and hence the source position can be found by using the simple formula: $x = \Delta t \cdot c/2$.

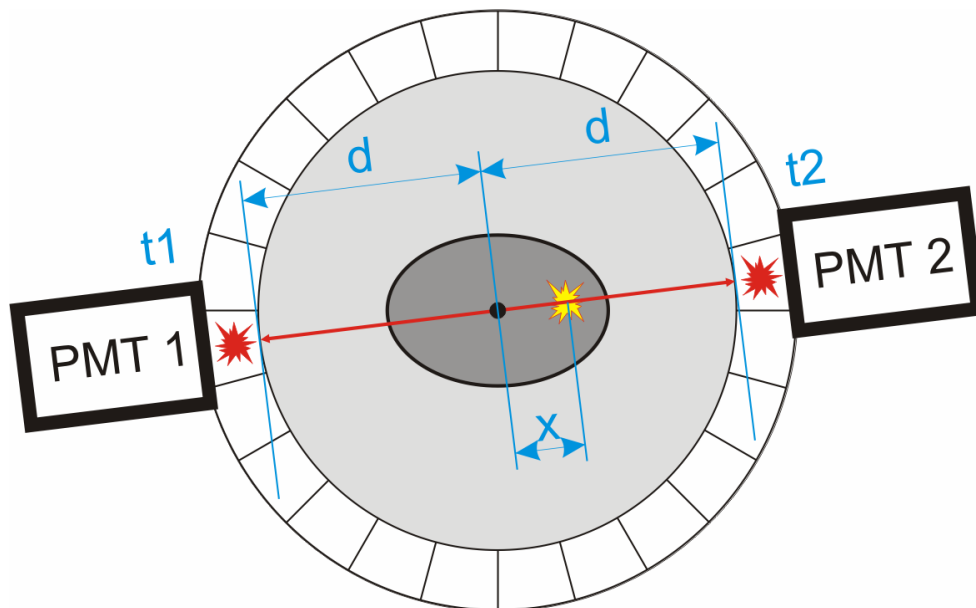


Fig. 1. Calculation of a positron position on the basis of TOF information.

So, if it is possible to calculate the position of a positron annihilation region using the Time-of-Flight information, why are all of the commercial systems using the standard procedure? The answer to this question is too poor time resolution of the currently available scintillation detectors.

B. Required time resolution

Following the information presented in chapter 2, the spatial resolution of a PET scanner is mainly limited by the positron range, photon non-collinearity and detector design, especially the size of the crystals. Currently, commercially available PET scanners have a spatial resolution at a level of 5 mm (Philips Gemini: 4.7 mm). Light travels such a distance in about 17 ps, which corresponds to the requirement of about 33 ps time resolution in the detection of the time difference between two 511 keV annihilation quanta. Unfortunately, none of the current detector configurations is able to achieve time resolution at the level of picoseconds or even a tenth of picoseconds. The best results obtained in laboratory conditions for detectors applicable to PET are close to 200 ps, however, a time resolution of only 500 ps is achievable in actually developed scanners.

With regard to the time resolution of a PET detector module, the scintillating crystal is the most crucial element. The rise time of light generated in scintillators is affected by the light collection process inside the crystal volume. This parameter should be as short as possible in order to assure good time resolution, however, in PET it is limited by the shape of the pixel-like crystals used. Another important factor connected with the scintillator is its light output, which means the number of photons generated per energy unit. Since photons are timing information carriers, more photons, especially emitted in a short time range (fast decay time), means more timing data and less spread of their arrival times at the photodetector and, in consequence, better time resolution.

With the exception of basic scintillator properties, such as rise time, light output and decay time, the crystal size also affects time resolution. Inside the crystal the photons are emitted in all directions so that they have different path lengths and arrival times at the photodetector (see red paths in Fig. 2). Such an additional spread can be minimized by setting a very low threshold in the discriminators and triggering the electronics by the first photons that did not undergo reflections. The speed of light is lower in the detector medium by a factor which is the refractive index of a material, e.g. if we assume a 2-cm high LSO crystal, whose refractive index is 1.8, then the time difference between the detection of photons emitted at the front of the pixel and close to the photodetector is equal to about 120 ps (compare incident gammas indicated in blue in Fig. 2). Moreover, without the depth of interaction information, the point of gamma absorption is not known inside the crystal volume, and hence the crystal height becomes the limit of spatial resolution even when the time resolution is at the level of picoseconds.

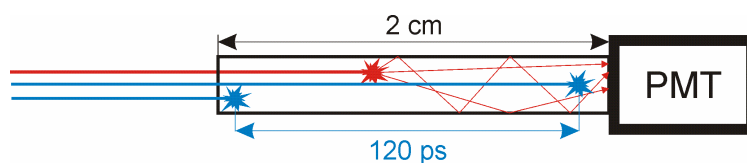


Fig. 2. Scintillation photon paths (red) and possible gamma absorption point (blue) in a pixel-like crystal.

The second element of a detection module is the photodetector (a photomultiplier in most cases). Optimization of this device is also of great importance for a final timing performance. The time resolution capabilities of a photodetector are described mainly by 3 factors: number of photoelectrons, transit time jitter and excess noise factor (ENF) [1]. In the case of photomultipliers, the number of photoelectrons is a function of photocathode quantum efficiency and photoelectron collection efficiency on the first dynode. Time jitter is the intrinsic time resolution of a photodetector for one photoelectron, and in photomultipliers it is associated with the different path lengths and initial velocities of electrons traveling from the photocathode to the first dynode [2]. The excess noise factor of PMTs is the result of gain spread in electron multiplication processes.

Scintillators and photodetectors are discussed in more detail in chapters 4 and 5.

2. Benefits of TOF in PET

A. Reduction of statistical noise

Although the 500 ps of time resolution corresponds to only about 7.5 cm of spatial resolution, TOF information is still very useful in image reconstruction.

Without the Time-of-Flight, a single line of response does not carry any further information about the source position along this line. In consequence, during image reconstruction, the probability of gamma source localization is homogeneous on the whole length of the LOR, what is schematically marked as the red area in Fig. 3. Incorporation of the Time-of-Flight information improves the localization of the annihilation point along the line of response. The time resolution of 500 ps changes the probability distribution from flat at the whole LOR to Gaussian around the source position and with an FWHM of $\Delta x = \Delta t \cdot c/2$, which corresponds to about 7.5 cm (the blue area in Fig. 3).

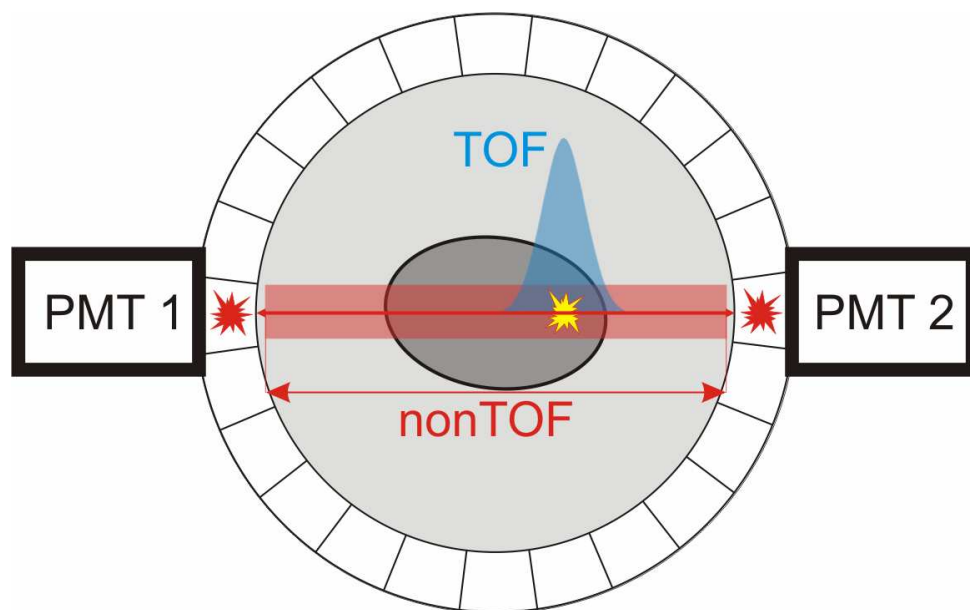


Fig. 3. Comparison of the probability distributions of annihilation point position included in conventional (red area) and TOF (blue Gaussian shape) systems.

Time resolution of 500 ps is insufficient enough to fully replace the conventional algorithms with a pure TOF reconstruction, but it is enough to significantly reduce the statistical noise in a reconstructed image since the region of interest is restricted to a much smaller area. Without the TOF information, a single coincidence event contributes to all the image pixels along its LOR. The mean noise contribution to the other image pixels is removed by filters applied in the reconstruction algorithm (filtered backprojection). However, the filters do not remove the statistical fluctuations which increase the noise in all of the image pixels. With the TOF information, a single event adds noise only to the image pixels close to the annihilation point and within the range given by the system time resolution. Moreover, the contribution to each of the surrounding pixels is weighted by the Gaussian distribution.

The TOF-improved localization provides a huge performance increase in contrast of the reconstructed PET images [3], [4]. The noise variance reduction factor f depends on the size of the emission source D and the system time resolution Δt , and is given by [5], [6]:

$$f = \frac{D}{\Delta x} = \frac{2D}{c\Delta t} \quad (1)$$

As can be seen above, noise reduction appears when the line segment Δx is shorter than the size of the emission source D . In the case of a whole-body PET scanner, a patient's size with a diameter of about 35 cm can be assumed, so the 500 ps of time resolution leads to almost a 5x reduction in the noise variance. Moreover, improvement in the image contrast starts ($f > 1$) even with much poorer time resolution, but below 2 ns. For smaller organs, such as the brain (D of about 20 cm), the time resolution requirements are higher and noise reduction appears below 1 ns.

PET: Impaired Image Quality in Larger Patients

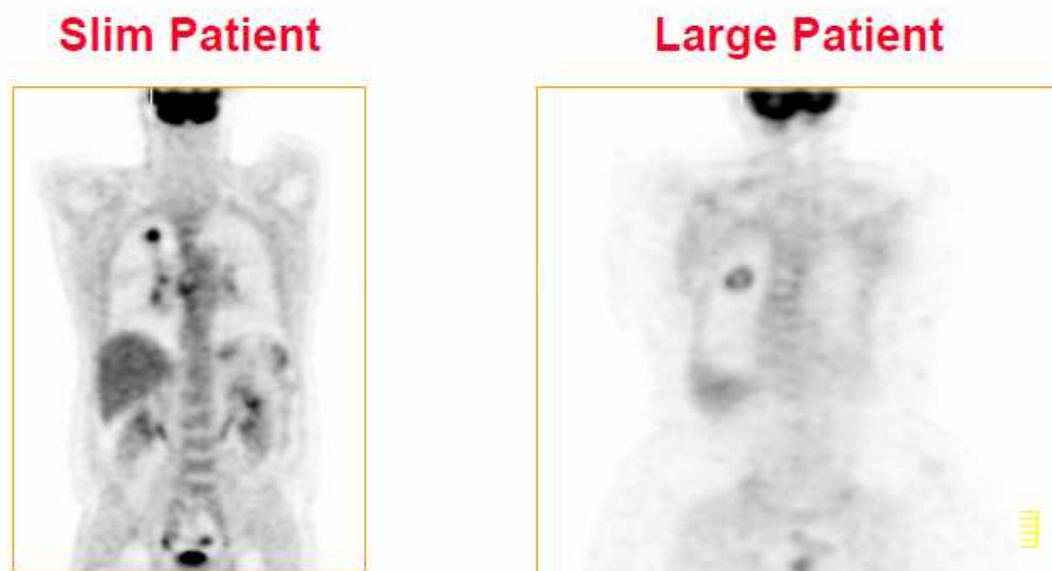


Fig. 4. Comparison of image contrast in non-TOF system for 60 kg and 120 kg patients.

The fact that the noise variance reduction is proportional to the diameter of the studied

object is of great benefit to the heaviest patients, for whom the PET image contrast is largely affected by scattered and random events. A comparison of images acquired without TOF during the same scan time with slim and large patients is presented in Fig. 4. For the large patients, the TOF information works as a higher number of counts that improves statistics and increases efficiency. In a standard PET system a patient weighing 120 kg must be scanned about 2.3 times longer than a 60 kg patient to obtain the same image quality.

It is worth adding that the TOF technique also allows for a reduction of the noise originating from random [7], [8] and scattered [9] coincidences, what further improves the reconstructed image quality.

B. Reduced random event rate

Incorporation of the Time-of-Flight in PET requires improved time resolution of the detector ring. Such a scanner upgrade allows the reduction of the random events rate R , which for a single LOR is given by:

$$R = 2R_1R_2\Delta T \quad (2)$$

where R_1 and R_2 are the single detector event rates and ΔT is the hardware coincidence timing window. The total number of random events is the sum over all the LORs and is proportional to the coincidence timing window ΔT . The hardware coincidence window in conventional PET is equal to 12 ns, and the mean contribution from random events can be subtracted during the reconstruction process, but the statistical fluctuations remain. The influence of the random events rate on the final, reconstructed image is often determined by the Noise Equivalent Count Rate (NECR) [10]:

$$NECR = \frac{T^2}{T + S + 2R} \quad (3)$$

where T , S and R are the count rates of true, scattered and random events, respectively.

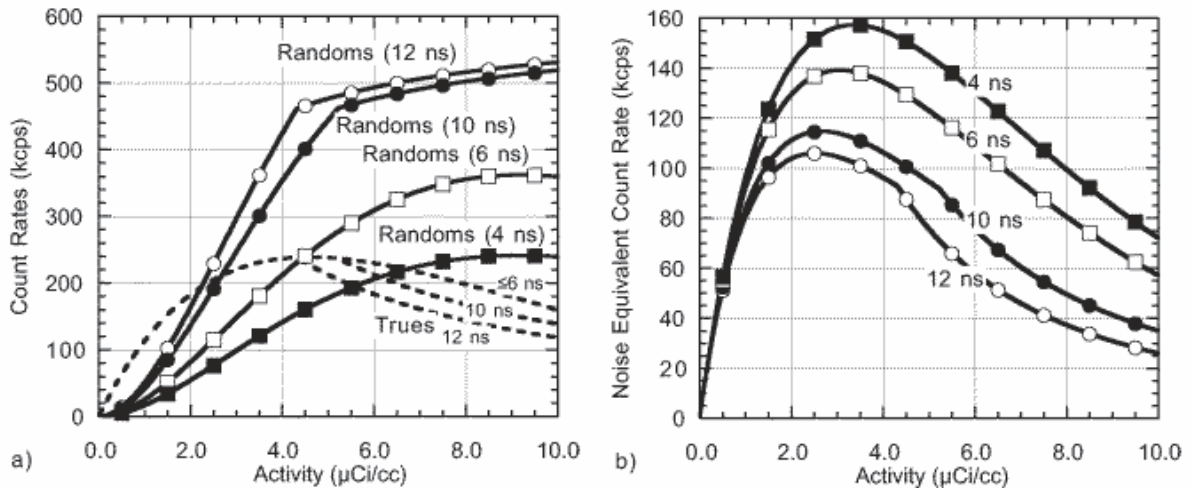


Fig. 5. Predicted randoms and trues rates (left) and NECR (right) versus activity concentration and coincidence window width. The object imaged was a uniform cylinder with a diameter of 20 cm and the camera simulated had a detector ring with a diameter of 82 cm and 15 cm axial extent.

The dependency of the number of random and true events on the coincidence window width

together with the NECR values are shown in Fig. 5 [6]. The presented measurements were performed with a 20-cm long phantom with a diameter of 20 cm and imaged in a 2-D mode. The plot in Fig. 5a shows that simple narrowing of the timing window leads to lower random events counting rates. The level of improvement in the case of randoms depends linearly on the window width (for low source activity). The rapidly changed slope of randoms for 12 ns and 10 ns observed at high activity levels is the effect of increased electronics dead time. In order to assure high efficiency, the coincidence window is in most cases set at a level of two FWHM of the time resolution of the detection system. This means that the data presented in Fig. 5 correspond to 6, 5, 3 and 2 ns time resolution. The reduced hardware timing window also decreases the maximal counting rates that have to be computed by the electronics. This effect is reflected in the point where the slope is changed for randoms. This point is shifted towards a higher activity level (compare randoms for 12 ns and 10 ns). Moreover, the narrower window also influences the shape of the true rates dependency indicated as dashed lines in Fig. 5. In the case of windows set at 12 ns and 10 ns, the rate of the true events drops at certain activity levels due to the increased dead time in the electronics, and hence the limited detection efficiency. When the window is set below 6 ns, both the true and random dependencies are smooth.

The benefits of narrowing the hardware coincidence timing window and reduced random events rates can be perfectly seen in Fig. 5b, where the NECR values versus the source activity are presented for various window widths. The technical limit for the hardware timing window is equal to about 4 ns since this is the time of flight of the gamma rays through the whole PET detector ring. The difference between the conventional 12 ns timing window and 4 ns shows an almost 50% improvement in the NECR.

C. *Reduced axial blurring*

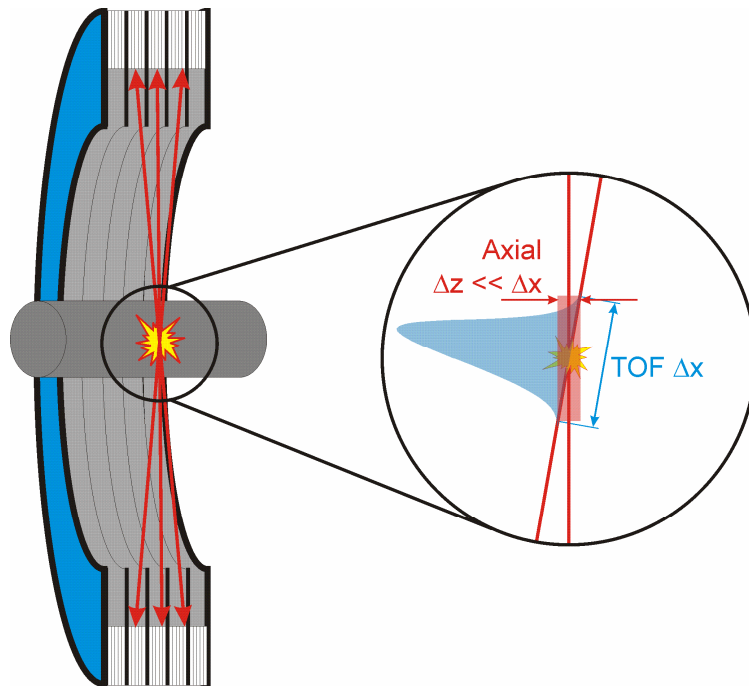


Fig. 6. Diagram of axial spatial resolution improvement due to the incorporation of TOF information in PET.

The Time-of-Flight information in PET has a significant influence not only on the reconstructed image contrast, but also on the spatial resolution along the axis perpendicular to the detector ring. The TOF spatial uncertainty Δx along a line of response is equal to a few centimeters, but the projection of Δx on the scanner axis provides precise information about the axial slice in which the registered event took place (see Fig. 6). Such axial information added to the reconstruction algorithms, both 2D and 3D, considerably decreases axial blurring (especially near the edge of the field of view) [11], [12]. The level of improvement is proportional to the ratio between the TOF distance uncertainty and the diameter of the emission source [6].

D. Possibility of a simultaneous emission and transmission scan

As all kinds of radiation, gamma rays attenuate while traveling through a medium. The attenuation length of 511 keV photons in water or tissue is equal to 10 cm. This means that e.g. during a brain scan (about 20 cm in diameter) more than 80% of the events is lost. Such intensity loss must be taken into account during image reconstruction of any tomography data (CT, SPECT, PET).

The probability P_1 that the first annihilation photon will reach a detector is given by: $P_1 = e^{-\mu d_1}$ where μ is the attenuation coefficient and d_1 is the distance that a gamma ray travels through the medium (patient's body). Similarly, for the second photon: $P_2 = e^{-\mu d_2}$. The coincidence event detection probability P is a product of individual photon detection probabilities: $P = e^{-\mu(d_1+d_2)}$. The sum of d_1 and d_2 is the total path inside the medium that the photons had to travel before registration of a single coincidence event took place. This means that probability P is independent of the source position along the LOR. Moreover, the attenuation correction of an internal source is the same as an external source. Thus, the attenuation correction in PET can be made on the basis of the transmission data from the external rod or point source which is rotating around the patient. Most of the dedicated ring scanners use a coincidence-based attenuation scan [13].

The transmission scan can take 10–15 minutes [14]. Incorporation of TOF in PET opens up the possibility of simultaneous measurement of the transmission and emission data. Such a technique is possible even without the TOF, but the amount of scattered events makes the emission data useless. TOF information eliminates this scatter contamination, and allows the simultaneous collection of emission and transmission data and, thus, reduced total scanning time [6]. Since the distance between the patient and the external source is equal to about 15 cm, a time resolution at a level of 1 ns or less is required in order to distinguish the transmission and emission events [15].

3. References

- [1] M. Moszynski and B. Bengtson, "Status of timing with plastic scintillation detectors," *Nucl. Instr. Meth.*, vol. 158, pp. 1–31, 1979.
- [2] E. Gatti and V. Svelto, "Review of theories and experiments of resolving time with scintillation counters," *Nucl. Instr. Meth.*, vol. 43, no. 1, pp. 248–268, 1966.

- [3] D. L. Snyder, L. J. Thomas, and M. M. Ter-Pogossian, "A mathematical model for positron-emission tomography systems having time-of-flight measurements," *IEEE Trans. Nucl. Sci.*, vol. 28, no. 3, pp. 3575–3583, 1981.
- [4] T. Tomitani, "Image reconstruction and noise evaluation in photon time-of-flight assisted positron emission tomography," *IEEE Trans. Nucl. Sci.*, vol. 28, no. 6, pp. 4581–4589, 1981.
- [5] R. Miyaoka, "Fundamentals of medical imaging," in *2009 IEEE NSS-MIC Short Course: Medical Imaging Fundamentals*, 2009.
- [6] W. W. Moses, "Time of flight in pet revisited," *IEEE Trans. Nucl. Sci.*, vol. 50, no. 5, pp. 1325–1330, 2003.
- [7] T. Holmes, D. Snyder, and D. Ficke, "The effect of accidental coincidences in time-of-flight positron emission tomography," *IEEE Trans. Med. Imag.*, vol. 3, no. 2, pp. 68–79, 1984.
- [8] T. J. Holmes, D. C. Ficke, and D. L. Snyder, "Modeling of accidental coincidences in both conventional and time-of-flight positron-emission tomography," *IEEE Trans. Nucl. Sci.*, vol. 31, no. 1, pp. 627–631, 1984.
- [9] B. Bendriem, F. Soussaline, R. Campagnolo, B. Verrey, P. Wajnberg, and A. Syrota, "A technique for the correction of scattered radiation in a PET system using time-of-flight information," *J. Comput. Assist. Tomogr.*, vol. 10, no. 2, p. 287, 1986.
- [10] S. C. Strother, M. E. Casey, and E. J. Hoffman, "Measuring pet scanner sensitivity: relating countrates to image signal-to-noise ratios using noise equivalents counts," *IEEE Trans. Nucl. Sci.*, vol. 37, no. 2, pp. 783–788, 1990.
- [11] M. Defrise, P. E. Kinahan, D. W. Townsend, C. Michel, M. Sibomana, and D. F. Newport, "Exact and approximate rebinning algorithms for 3-D PET data," *IEEE Trans. Med. Imag.*, vol. 16, no. 2, pp. 145–158, 1997.
- [12] M. Daube-Witherspoon and G. Muehllehner, "Treatment of axial data in three-dimensional PET," *J. Nucl. Med.*, vol. 28, no. 11, p. 1717, 1987.
- [13] M. Daube-Witherspoon, R. E. Carson, and M. V. Green, "Post-injection transmission attenuation measurements for PET," *IEEE Trans. Nucl. Sci.*, vol. 35, no. 1, pp. 757–761, 1988.
- [14] M. Wernick and J. Aarsvold, *Emission tomography: the fundamentals of PET and SPECT*. Academic Press, 2004.
- [15] M. Yamamoto, D. C. Ficke, and M. M. Ter-Pogossian, "Effect of the software coincidence timing window in time-of-flight assisted positron emission tomography," *IEEE Trans. Nucl. Sci.*, vol. 30, no. 1, pp. 711–714, 1983.

4. Scintillating crystals in PET

1. General description of scintillators

A. Definition

A scintillator is a medium which converts ionizing radiation into weak flashes of light – scintillations. The number of photons emitted after the interaction of an ionizing particle is proportional to its energy deposited in the scintillator. This is the most important feature of scintillators which allows the reconstruction of an energy spectrum of the detected particles. Depending on the scintillator material, the scintillation light is emitted in the visible or ultraviolet region with a characteristic decay time ranging from a few nanoseconds to a few microseconds. Scintillators can be made from hundreds of organic or inorganic chemical compounds [1] having the form of gas, a liquid or solid. Light, organic materials (liquids and plastics) are mostly used for detection of charge particles, such as alpha particles, electrons and beta rays. Inorganic scintillators possess higher density and a higher effective atomic number, and are used in the detection of X-rays and gamma radiation due to much better detection efficiency. Such inorganic crystals are used in PET, where the detection of 511 keV gamma rays is required.

B. Interaction of gamma rays with matter

The interaction of gamma rays in matter is described mainly by four processes: the photoelectric effect, Compton scattering, pair production and Rayleigh scattering. The latter two phenomena are unimportant from the point of view of PET scintillation materials. Rayleigh elastic scattering of photons does not produce free, high-energy, ionized electrons. Pair production happens only where the gamma energy is higher than 1022 keV.

In the photoelectric effect, a photon or gamma ray is absorbed by the atom and the initial photon energy (E_γ) is transferred to the release of the bounded electron and further to its kinetic energy. Thus, the energy of such a free photoelectron E_{phe} is reduced by the binding energy E_b :

$$E_{phe} = E_\gamma - E_b \quad (1)$$

Only the bound electrons undergo the photoelectric effect, and the probability of such interaction is the highest for the most tightly bound electrons, i.e. located at the K shell of the atom. Photoelectric absorption is predominant for low-energy gamma rays and X-rays. Moreover, the probability of this kind of interaction is enhanced in materials with a high atomic number (Z). It is hard to express the probability of the photoelectric effect using a simple formula valid for all materials with different Z and all ranges of energies of incident photons. In general, this probability is described by the atomic cross-section τ_p and is proportional to the Z and inversely proportional to the gamma energy E_γ in the following way [2]:

$$\tau_p = const \cdot \frac{Z^n}{E_\gamma^m} \quad (2)$$

In the above equation, the n index varies between 4 and 4.6 for the gamma-ray energy region from 100 keV to 3 MeV, whereas the m exponent is equal to 1 at energies above 600 keV, 2 at energies above 150 keV and 3 for lower energy values [2].

As a result of a Compton scattering, an incident photon transfers a part of its energy to the kinetic energy of an unbounded electron (recoil electron). After interaction, the incident photon is deflected through an angle θ with respect to its original direction. Since the energy transfer to the electron can cover any part of the initial photon energy, all scattering angles are possible. The energy of the deflected photon is expressed by the well-known Compton formula and the recoil electron energy is given by:

$$E_{phe} = E_\gamma - \frac{E_\gamma}{1 + \frac{E_\gamma}{mc^2}(1 - \cos\theta)} \quad (3)$$

where mc^2 is the rest-mass of the electron (511 keV). The probability of a Compton scattering per atom of the absorber depends on the number of electrons available as scattering angles and, therefore, increases linearly with Z [3]. The Compton scattering is a predominant effect for gamma-ray energies typical of radioisotope sources.

A comparison of the probabilities of three kinds of interactions depending on the gamma energy and the absorber atomic number Z is presented in Fig. 1. The two solid lines represent equal probabilities of the Compton effect, and the photoelectric effect (left curve), or the Compton effect and the pair production phenomena (right curve).

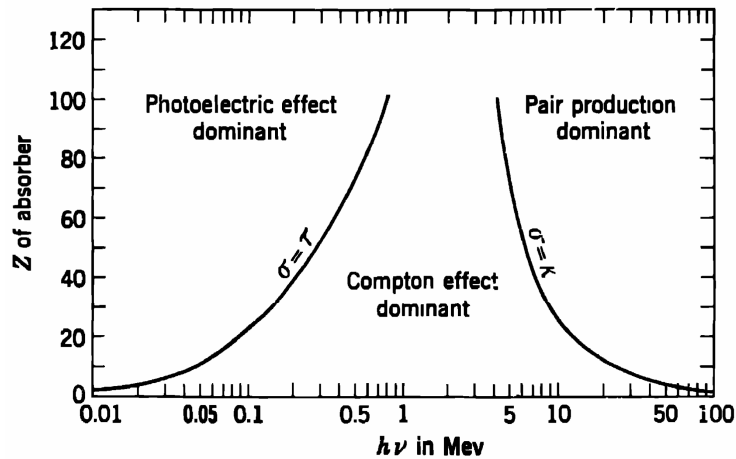


Fig. 1. Relative importance of the three major types of gamma-ray interaction. The solid lines show the values of Z and gamma energies for which the two neighboring effects are equal. Reprint from [2].

C. Scintillation mechanism in activated inorganic crystals

Gamma rays or X-rays become “visible” to a scintillator due to ionization phenomena. The high energy of incident photons is transferred to the kinetic energy of unbounded, fast electrons. The electrons are “information carriers” inside the detector. These particles lose

their energy through excitation of the bounded electrons of the medium and next, as a result of de-excitation, the scintillation photons are emitted in processes of fluorescence or phosphorescence. Fluorescence is the prompt emission of a visible light and, hence, is the most desirable channel of scintillation material de-excitation. Phosphorescence, or delayed fluorescence, are both characterized by much longer emission times and are the cause of unwanted effects, such as long decay components and afterglow.

The absorption of energy in a scintillating crystal elevates an electron from the valence band (leaving a hole there) to the conduction band. Such an excited electron may return to the valence band emitting a photon. However, the energy of a typical band gap is larger than the energy of visible light. Thus, activators need to be introduced into the crystal lattice, which cause a modification of the energy band structure. Such changed energy bands are shown in Fig. 2. In consequence, an activator energy states appear in the forbidden gap of a pure crystal, thus creating an additional channel for electrons to de-excite back to the valence band. The transitions between the activator states release energy in a visible photon emission range and are the basis of a scintillation process. Such de-excitation sites are called *luminescence centers* or *recombination centers*, and their energy structure in the host crystalline lattice determines the emission spectrum of the scintillator.

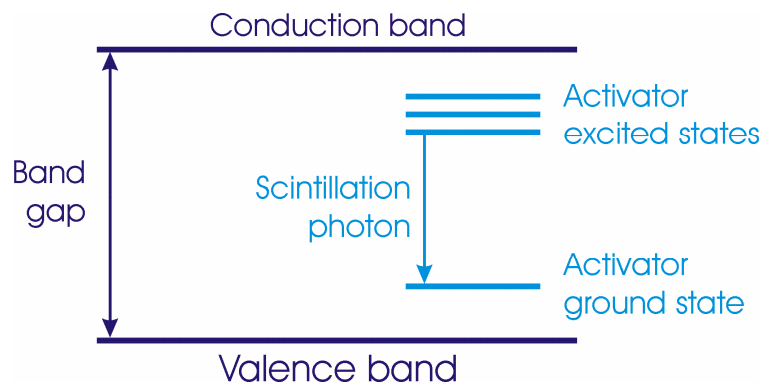


Fig. 2. Diagram of the energy bands in an activated scintillation crystal.

The excited medium, after the energy deposition of a gamma ray, consists of many electrons in the conduction band and corresponding holes in the valence band. The holes may drift to the activator site and ionize it. Such an ionized activator can accept an electron from the conduction band, thus creating excited activator states. The typical half-lives of such states are of the order of 50–500 ns [3]. Activator de-excitation is followed by the emission of a visible photon. The time characteristic of the scintillation light is determined by the configuration and decay times of the activator excited states.

Activator de-excitation through fast emission of visible photons is preferable. However, the transition between the excited state and ground state may be forbidden. In this case, in order to de-excite, the electron needs to be transferred to the upper energy state (by thermal excitation), where the transition to the ground state is allowed. As a result of this process a slow, phosphorescent light appears which is the source of long decay time components and afterglow.

The excited medium of a scintillator may also de-excite in radiationless transitions,

generally defined as quenching. These kinds of processes cause light loss during conversion of particle energy into scintillation light.

2. Basic parameters of scintillators

A. Detection efficiency

The detection efficiency of a scintillator is described by its stopping power of gamma rays (or any other kind of radiation) together with the ability to convert the stopped quanta into visible light. Intrinsic detection efficiency, which is independent of the counting geometry, is defined as a ratio between the number of pulses recorded and the number of gamma quanta incident on the detector. The gamma quanta can be recorded only after any kind of interaction within the scintillator. Such interaction removes the photon from the beam (in the photoelectric effect or during pair production) or scatters it (in the Compton effect), which leads to the attenuation of the primary gamma-ray beam. Attenuation of gamma rays in any medium is given by the well-known exponential function:

$$\frac{I}{I_0} = e^{-\mu t} \quad (4)$$

where I_0 and I are the gamma-ray intensities before entry into the detector and at position t inside the detector, respectively. The parameter μ is the linear attenuation coefficient which reflects the probability per unit length that a gamma-ray photon will interact with the medium. This probability is the sum of probabilities of each possible interaction phenomena, i.e. the photoelectric effect (τ), Compton effect (σ) and pair production (κ):

$$\mu = \tau + \sigma + \kappa \quad (5)$$

Pair production is not important in PET applications. The linear attenuation coefficient in the case of the photoelectric effect is given by [2]:

$$\tau = \tau_p \cdot N = \tau_p \cdot \frac{\rho}{A} \Rightarrow \tau \propto \rho \cdot Z^n \quad (6)$$

where N is the number of atoms per cubic centimeter, A is the atomic mass and ρ is the scintillator density. Similarly, for the Compton effect:

$$\sigma \propto N \cdot Z \Rightarrow \sigma \propto \rho \cdot Z \quad (7)$$

Taking into account the above dependencies, detection efficiency is limited by the density and effective atomic number of the scintillation material.

The reciprocal of the linear attenuation coefficient describes the mean free path of gamma rays in a given medium, which is defined as the average distance traveled in the absorber before the first interaction takes place.

A dense and heavy scintillator in a PET detector has two main advantages. First of all, it generally improves PET system detection efficiency. The second advantage is the possibility of applying scintillating crystals with a reduced length, which leads to a reduction of the parallax error and image blurring.

B. Scintillation efficiency

Scintillation efficiency, or scintillator light output (LO), describes how effectively gamma-ray energy (or the energy of any other nuclear radiation) is converted into visible light.

Scintillation efficiency is a product of the efficiencies of the three phenomena [4]: conversion (β), transfer (S) and luminescence (Q). The number of photons emitted per 1 MeV of gamma radiation can be expressed as:

$$LO \propto \frac{1}{E_g} \beta \cdot S \cdot Q \quad (8)$$

where E_g is the band gap energy of the host crystal. The conversion efficiency β describes the process of creation of the initial number of electron-hole pairs after gamma-ray interaction. The transfer efficiency S reflects the probability that the activator excited state will be filled by the electron from the valence band of the host crystal. The Q parameter is the activator luminescence efficiency which describes the chance of visible photon emission during de-excitation. Following [5], luminescence quantum efficiency Q can be expressed as:

$$Q = \frac{P_r}{P_r + P_{nr}} \quad (9)$$

where P_r and P_{nr} are the probabilities of a radiative or non-radiative de-excitation, respectively.

For many activators Q is close to 1, and β can also be close to 1 in wide bandgap insulators, hence the transfer efficiency becomes the main parameter affecting the light output of modern scintillators [6]. The energy loss during the transfer stage is caused by the trapping of electrons or holes and also by their non-radiative recombination. An example of the measured S and Q efficiencies for a few scintillators is presented in Table I [7].

TABLE I
CALCULATED E-H PAIRS AND MEASURED LIGHT OUTPUT FOR DIFFERENT SCINTILLATORS

Scintillator	Calculated e-h / MeV	Observed ph / MeV	Efficiency $S \cdot Q$
CsI:Tl	69 444	65 000	0.936
NaI:Tl	75 330	38 000	0.504
BGO	88 889	8 500	0.096
LSO:Ce	69 444	27 300	0.393

The electrons can be called the scintillator input or starting information, whereas the number of emitted photons is the output information, which later becomes input for the photodetector. The light output is the most important parameter of any scintillating material because the number of emitted photons has a direct influence on the two crucial properties of a radiation detector. These properties are energy resolution and time resolution. Both are proportional to the inverse square root of the number of photons emitted by the scintillator.

The improved energy resolution of the PET detector allows to reduce the noise in the image due to a narrower energy window and better discrimination of true from scattered events. The improved time resolution (at the level of 4 ns) leads to a narrower hardware coincidence timing window and, hence, to a better image contrast due to improved discrimination of random events. A time resolution below 500 ps allows for the incorporation of TOF

information in PET.

C. Decay time

The decay time of a scintillation light pulse is directly related to the life-time of the excited states that were created in the crystal after nuclear radiation absorption. De-excitation of such states can take place in two ways, i.e. as a radiative transition followed by a photon emission or as a non-radiative transition (quenching). The probability of de-excitation is the sum of probabilities of both kinds of transitions. Since the life-time of the excited state is inversely proportional to the probability of de-excitation of that state, the decay time τ of a luminescence induced in a scintillator can be expressed as:

$$\tau \propto \frac{1}{P_r + P_{nr}} \quad (10)$$

where P_r and P_{nr} are the probabilities of a radiative or non-radiative de-excitation, respectively. A comparison of the above equation with the one describing luminescence quantum efficiency shows that the increased probability of a non-radiative transition makes the scintillator faster, but also less bright due to the reduced light output. Following [8], the decay time is proportional to the transition wavelength, which is reflected in the speed of the scintillators, whose light is emitted in the ultra-violet range.

The dependence in time t of the intensity J of the light emitted by the scintillator with a single luminescent center is given by a single exponential function:

$$J(t) = J_0 \exp\left(-\frac{t}{\tau}\right) \quad (11)$$

where J_0 is the initial intensity at $t=0$. However, many scintillators possess two or more decay components, and then the light intensity is described by the sum of the exponential functions:

$$J(t) = \sum_i \frac{N_i}{\tau_i} \exp\left(-\frac{t}{\tau_i}\right) \quad (12)$$

where N_i is the number of photons emitted in the component i characterized by the decay time τ_i .

The decay time of a scintillation light pulse is a key factor that defines the coincidence time resolution and dead time of the PET detector system. The time resolution is determined by the fastest component of the light pulse, whereas the dead time results from slow components.

As was mentioned in section B, improved time resolution leads to better discrimination of random events and allows the incorporation of TOF information in PET.

D. Energy resolution

The energy resolution $\Delta E/E$ of the full energy peak, measured with a scintillator coupled to a photomultiplier (PMT) or avalanche photodiode (APD), can be written as [9], [10] :

$$(\Delta E/E)^2 = (\delta_{sc})^2 + (\delta_{st})^2 + (\delta_p)^2 + (\delta_n)^2 \quad (13)$$

where δ_{sc} is the intrinsic resolution of the crystal, δ_{st} is the statistical contribution of a photodetector, δ_p is the transfer resolution and δ_n is the dark noise contribution.

The last two parameters depend on the photodetector used and the full detector design, and

will not be discussed here. The second parameter (statistical contribution) is, in general, inversely proportional to the square root of the number of emitted photons or scintillation efficiency described in section B.

The first component is the intrinsic energy resolution of the crystal and constitutes a fundamental limitation of the energy resolution. Intrinsic resolution is mainly associated with the non-proportional response of the scintillator [9], [10] to numerous secondary gamma and X-ray quanta, as well as secondary electrons (delta rays) produced in the stopping process of gamma radiation in the crystal. The latter process seems to be dominant in the degradation of energy resolution. Some of the crystals, e.g. LSO, seem to show particularly poor energy resolution exceeding that expected from the non-proportionality, which can be correlated with their thermoluminescence integrated intensity and afterglow [11]. A similar correlation of intrinsic energy resolution and afterglow was observed for LGSO [12]. The experimentally determined intrinsic resolution is also affected by inhomogeneities in the scintillator, causing local variations in the light output and non-uniform reflectivity of the reflecting cover of the crystal.

As in the case of high scintillation efficiency, improved intrinsic energy resolution, and hence improved overall energy resolution of the PET detector, allows to reduce the noise in the image due to a narrower energy window and better discrimination of true from scattered events.

E. Other properties

- Non-hygroscopic – crystals should not deteriorate due to water absorption from the atmosphere
- Low self-absorption – crystals should be highly transparent for the emitted scintillation photons
- Index of refraction close to the index of refraction of the material of the photodetector input window (about 1.5)
- Low price and simple production technology
- Scintillation light emitted in the range of 380–500 nm – well fitted to the photodetector quantum efficiency curve
- High resistance to radiation damage

3. Scintillators used in PET

A. NaI:Tl

Thallium doped Sodium Iodide (NaI:Tl) was first demonstrated in 1948 by R. Hofstadter [13] and since then has been the most popular scintillator in all areas of application where radiation detection is needed. Sodium Iodide was also originally used by Hal Anger in his first gamma camera intended for use in the first nuclear imaging device. This device was based on the single photon computed tomography (SPECT) principle. Presently, SPECT scanners are still dominated by NaI:Tl detectors.

Sodium Iodide possesses a high light output of about 40 000 photons per MeV and good energy resolution at a level of 8% at FWHM for 511 keV. The decay time constant of 230 ns assures time resolution for 511 keV slightly below 1 ns [14]. Despite the fact that these

parameters are better as compared to BGO or LSO (except for time resolution), the application of NaI:Tl in PET is limited mainly due to its low density and low effective atomic number. Moreover, this kind of crystal is hygroscopic and needs to be hermetically packed in order to protect the scintillator from humidity. From the commercial point of view, the main advantage of Sodium Iodide is its low price due to the well-developed technology of the crystal growth process.

Presently, PET systems are dominated by BGO or LSO crystals, however, scanners based on Sodium Iodide were built in the past. One of them was C-PET [15], where 6 curved NaI:Tl scintillators were used in a 90 cm ring with a 25.6 axial field of view. In this construction, detection efficiency was partially improved due to a large field of view and scanning without septa.

B. BGO

Bismuth Germanate $\text{Bi}_4\text{Ge}_3\text{O}_{12}$ (BGO) is an undoped scintillator characterized by high density (7.1 g/cm^3) and a very high, effective atomic number due to the content of bismuth ($Z=83$). BGO is a non-hygroscopic, relatively hard material that possesses the highest detection efficiency of gamma rays. Photofraction, i.e. the probability that a gamma ray will be fully absorbed in the crystal, is much higher in BGO than in other scintillators that can be used as PET detectors. Photofraction in LSO is lower by 25%, whereas in NaI:Tl it is less than half of the BGO. A PET detector made of 3 cm high crystals assures a detection efficiency of 511 keV quanta at the level of 90%. Such short crystals have a direct influence on scanner performance by reducing the parallax error and image blurring.

The scintillation light in BGO is emitted due to optical transitions in Bi^{3+} ions. This crystal does not contain an activator, however, the absorption and emission spectra are well separated, which assures minimal self-absorption.

The disadvantage of BGO is its low light output of only about 9000 photons per MeV. Moreover, the wavelength of emitted light is shifted toward green and is equal to 480 nm, which further decreases the number of photons registered by the photodetectors, whose quantum efficiencies are lower for longer wavelengths. The low light output affects energy resolution, which for 511 keV is equal to about 18% at FWHM (for pixel crystals), which is about three times worse than in NaI:Tl. The rise time of the BGO light pulse is slow (about 3 ns) and the light is emitted with a main decay time constant of 300 ns. Such timing, characteristic of the light pulse together with the low number of emitted photons, leads to a time resolution at a level of 2 ns for 511 keV [14].

Despite the disadvantages, high detection efficiency and a well-developed production process have made the BGO one of the most popular scintillator in PET (without TOF) applications.

C. LSO

Cerium-doped lutetium oxyorthosilicate, $\text{Lu}_2\text{SiO}_5:\text{Ce}$ (LSO), is one of the most promising inorganic scintillators for application in Time-of-Flight PET systems. The crystal was discovered by C.L. Melcher and J.S. Schweitzer, and their first paper about LSO appeared in 1992 [16]. This scintillator is characterized by a high effective atomic number $Z_{\text{eff}} = 66$, which assures a high detection efficiency of 511 keV annihilation quanta. Because the

detectors in PET scanners work in coincidence pairs and two annihilation quanta have to be registered simultaneously, the detection efficiency for a single event is proportional to Z_{eff}^2 . Hence, the detection sensitivity for coincident 511 keV photons in the case of LSO is 1.5 times smaller as compared to BGO. However, the biggest advantages of LSO, such as a high light output of 30 000 photons/MeV, better than BGO energy resolution and fast decay time of 40 ns, make it the main competitor of BGO, and practically the only solution for TOF PET. Moreover, LSO is a dense, non-hygroscopic and mechanically durable material with a wavelength of emitted light equal to 420 nm, which is perfectly fitted to the typical characteristics of popular photodetectors (photomultipliers, avalanche photodiodes, silicon photomultipliers). Besides the TOF potential, the timing characteristics of the LSO light pulse allow narrowing of the hardware coincidence timing window, and hence reduction of the random events rate, especially in 3D PET. This feature was used in the Reveal PET system developed by CTI (presently Siemens), where the timing window was set at a level of 6 ns.

The biggest disadvantage of the LSO scintillator is its internal radioactivity. This lutetium-based crystal contains the naturally occurring (2.6%) isotope ^{176}Lu , which beta decays to ^{176}Hf and emits a cascade of three gamma rays: 307, 202 and 88 keV. The total rate of this internal activity (both gamma and beta) is equal to 39 cps/g. In consequence, in PET systems based on LSO, the count rate in a single detector module highly increases, which may affect the signal to noise ratio, especially in low dose examinations. The second disadvantage of the LSO scintillator is its sensitivity to visible light, which induces the long-term phosphorescence background in the crystal.

The LSO compound was originally invented by C.L. Melcher [17] and patented in 1990. However, since then a few similar crystals with exactly the same properties have been developed, such as $\text{Lu}_{1.8}\text{Y}_{0.2}\text{SiO}_5:\text{Ce}$ (LYSO) made by Saint-Gobain Crystals or Lutetium Fine Silicate (LFS) made by Zecotek Photonics [18].

Presently, most of the commercially available PET scanners are based on LSO (Siemens Biograph TruePoint PET-CT Systems) or LYSO (Philips Gemini PET/CT Systems) detector modules.

D. Other scintillators

The first TOF PET systems, built about 25 years ago [19], [20], [21], were based on CsF and BaF_2 scintillators. Nevertheless, due to the low stopping power of these crystals for 511 keV annihilation quanta, their performance was not as good as the classic PET scanner with BGO. Recent years have brought four fast scintillators with a high light output: LSO, $\text{Gd}_2\text{SiO}_5:\text{Ce}$ (GSO), $\text{YAlO}_3:\text{Ce}$ (YAP) [22], and $\text{LuAlO}_3:\text{Ce}$ (LuAP) [23]. LSO is presently one of the two major scintillators (besides BGO) in commercial PET systems. YAP can be used in small animal PETs [24] or Compton cameras, whereas GSO crystals were applied in one of the Philips Allegro PET systems [25].

Scintillating crystals that meet the conditions of the PET detector modules are presented in Table II.

TABLE II
PROPERTIES OF THE SCINTILLATORS POSSIBLE TO USE IN PET

Scintillator	Light output [ph/MeV]	Decay constant [ns]	Emission wavelength [nm]	Density [g/cm ³]	Effective atomic number	Index of refraction	Hygroscopic
NaI:Tl	38 000	230	410	3.7	51	1.85	yes
CsI:Tl	66 000	900	550	4.5	52	1.80	slightly
BGO	8 000	300	480	7.1	75	2.15	no
LSO/LYSO	30 000	40	420	7.4	66	1.82	no
BaF ₂ fast/slow	2000/10000	0.6/620	220/310	4.9	53	1.51	slightly
LaBr ₃	75 000	16	380	5.1	45	1.9	yes
GSO	8 000	60	440	6.7	59	1.85	no
LGSO	23 000	40	420	7.5	63	1.82	no
LuAP	12 000	18	365	8.3	64.9	1.94	no
YAP	17 000	30	350	5.5	33.5	1.95	no

4. References

- [1] S. Derenzo, M. Boswell, M. Weber, and B. K. Scintillation properties. Lawrence Berkeley National Laboratory. [Online]. Available: <http://scintillator.lbl.gov/>
- [2] R. Evans and A. Noyau, *The atomic nucleus*. McGraw-Hill, 1955, vol. 787.
- [3] G. Knoll, *Radiation Detection and Measurement, 3rd edition*. John Wiley and Sons, New York, 2000.
- [4] A. Lempicki, A. Wojtowicz, and E. Berman, "Fundamental limits of scintillator performance," *Nucl. Instr. Meth. A*, vol. 333, no. 2-3, pp. 304–311, 1993.
- [5] J. Birks *et al.*, *The theory and practice of scintillation counting*. MacMillan, 1964.
- [6] C. Kuntner and P. Lecoq, "Evaluation of new inorganic scintillators for application in a prototype small animal PET scanner," Ph.D. dissertation, Vienna, Tech. U., 2003.
- [7] A. Lempicki and J. Glodo, "Ce-doped scintillators: LSO and LuAP," *Nucl. Instr. Meth. A*, vol. 416, no. 2-3, pp. 333–344, 1998.
- [8] P. Rodnyi, *Physical processes in inorganic scintillators*. CRC, 1997.
- [9] P. Dorenbos, J. T. M. de Haas, and C. W. E. van Eijk, "Non-proportionality in the scintillation response and the energy resolution obtainable with scintillation crystals," *IEEE Trans. Nucl. Sci.*, vol. 42, no. 6, pp. 2190–2202, 1995.
- [10] M. Moszynski, J. Zalipska, M. Balcerzyk, M. Kapusta, W. Mengesha, and J. Valentine, "Intrinsic energy resolution of NaI(Tl)," *Nucl. Instr. Meth. A*, vol. 484, no. 1-3, pp. 259–269, 2002.
- [11] M. Kapusta, P. Szupryczynski, C. L. Melcher, M. Moszynski, M. Balcerzyk, A. A. Carey, W. Czarnacki, M. A. Spurrier, and A. Syntfeld, "Non-proportionality and

- thermoluminescence of LSO:Ce,” *IEEE Trans. Nucl. Sci.*, vol. 52, no. 4, pp. 1098–1104, 2005.
- [12] M. Moszynski, A. Nassalski, W. Czarnacki, A. Syntfeld-Kazuch, D. Wolski, T. Batsch, T. Usui, S. Shimizu, N. Shimura, K. Kurashige, K. Kurata, and H. Ishibashi, “Energy resolution of LGSO scintillators,” *IEEE Trans. Nucl. Sci.*, vol. 54, no. 3, pp. 725–731, 2007.
- [13] R. Hofstadter, “Alkali halide scintillation counters,” *Phys. Rev.*, vol. 74, no. 1, p. 100, 1948.
- [14] M. Moszynski, C. Gresset, J. Vacher, and R. Odru, “Timing properties of BGO scintillator,” *Nucl. Instr. Meth.*, vol. 188, no. 2, pp. 403–409, 1981.
- [15] L. Adam, J. Karp, M. Daube-Witherspoon, and R. Smith, “Performance of a whole-body PET scanner using curve-plate NaI(Tl) detectors,” *J. Nucl. Med.*, vol. 42, no. 12, p. 1821, 2001.
- [16] C. L. Melcher and J. S. Schweitzer, “Cerium-doped lutetium oxyorthosilicate: a fast, efficient new scintillator,” *IEEE Trans. Nucl. Sci.*, vol. 39, no. 4, pp. 502–505, 1992.
- [17] C. Melcher, “Lutetium orthosilicate single crystal scintillator detector,” US Patent 4,958,080, Sep. 18, 1990.
- [18] M. Grodzicka, M. Moszynski, T. Szczesniak, A. Syntfeld-Kazuch *et al.*, “Characterization of LFS-3 scintillator in comparison with LSO,” *Nucl. Instr. Meth. A*, vol. 652, no. 1, pp. 226–230, Oct. 2011.
- [19] R. Allemand, C. Gresset, and J. Vacher, “Potential advantages of a cesium fluoride scintillator for a time-of-flight positron camera,” *J. Nucl. Med.*, vol. 21, no. 2, p. 153, 1980.
- [20] M. Laval, R. Allemand, R. Campagnolo, P. Garderet, R. Gariod, P. Guinet, M. Moszynski, E. Tournier, and J. Vacher, “Contribution of the time of flight information to the positron tomographic imaging,” in *Proc. of Third World Congress of Nucl. Med. and Biol.* Pergamon Press, Paris, 1982, p. 2315.
- [21] N. Mullani, D. Ficke, R. Hartz, J. Markham, and G. Wong, “System design of fast PET scanners utilizing time-of-flight,” *IEEE Trans. Nucl. Sci.*, vol. 28, no. 1, pp. 104–108, 1981.
- [22] V. Baryshevsky, M. Korzhik, V. Moroz, V. Pavlenko, A. Fyodorov, S. Smirnova, O. Egorycheva, and V. Kachanov, “YAlO₃: Ce-fast-acting scintillators for detection of ionizing radiation,” *Nucl. Instr. Meth. B*, vol. 58, pp. 291–293, 1991.
- [23] A. Lempicki, M. H. Randles, D. Wisniewski, M. Balcerzyk, C. Brecher, and A. J. Wojtowicz, “LuAlO₃:Ce and other aluminate scintillators,” *IEEE Trans. Nucl. Sci.*, vol. 42, no. 4, pp. 280–284, 1995.
- [24] A. Del Guerra, G. Di Domenico, M. Scandola, and G. Zavattini, “YAP-PET: first results of a small animal positron emission tomograph based on YAP:Ce finger crystals,” *IEEE Trans. Nucl. Sci.*, vol. 45, no. 6, pp. 3105–3108, 1998.
- [25] G. Muehlrhner, J. Karp, and S. Surti, “Design considerations for PET scanners,” *Q. J. Nucl. Med.*, vol. 46, no. 1, pp. 16–23, 2002, the quarterly journal of nuclear medicine: official publication of the Italian Association of Nuclear Medicine (AIMN) and the International Association of Radiopharmacology (IAR).

5. Photomultipliers

1. Introduction

A. Operation principles

A photomultiplier is a device that converts and amplifies weak light signals into a measurable electric current. The first commercially available photomultipliers (PMTs) appeared about 75 years ago. Presently, they belong to the most widely used photodetectors applied in high energy physics, homeland security devices or nuclear medicine. All of the commercially available PET systems possess detector modules based on photomultipliers. The most important PMT advantages are: high gain, low noise, good quantum efficiency, ultra fast response, excellent timing performance, single photon detection capability and finally, a wide range of sensing areas (from centimeters to a few inches).

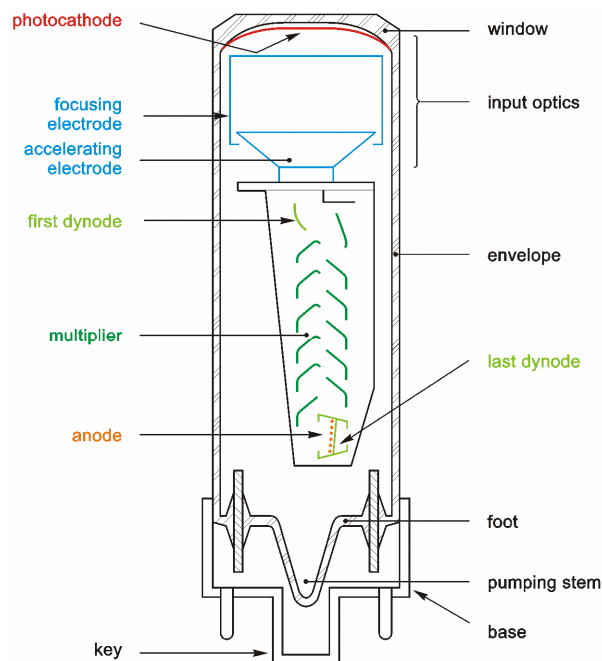


Fig. 1. Diagram of a photomultiplier, based on the Philips 56AVP, following [1].

A photomultiplier's operation principle uses two phenomena: the photoelectric effect and the secondary emission of electrons. A diagram of a typical photomultiplier is presented in Fig. 1. The photons striking the photocathode (red) are converted into electrons due to the photoelectric effect. Next, these electrons (called photoelectrons) are accelerated and focused on the first dynode (light green) by the electric field of the focusing electrode and accelerating electrode (blue). Each time the photoelectron strikes the dynode, this dynode emits several secondary electrons which are further accelerated to the next dynode by the interdynode potential. In this way, the dynode structure (green) can amplify one photoelectron at the first

dynode to 10^3 – 10^8 photoelectrons, leaving the last dynode (light green). Finally, the photoelectrons emitted at the last dynode, moving towards the anode grid (orange), induce the current and provide an output signal. The output signal is proportional to the number of primary photoelectrons emitted at the photocathode, which in turn are proportional to the number of detected photons.

B. Timing properties

The time resolution capabilities of modern, fast photomultipliers are associated mainly with [2]:

- the number of photoelectrons released from the photocathode (which is a function of the photocathode sensitivity) and the photoelectron collection efficiency on the first dynode,
- the transit time jitter of electrons traveling from the photocathode to the first dynode,
- spread in the gain of the electron multiplier, which affects the pulse height and time distributions of the output pulses – excess noise factor.

2. Photocathode

A. Sensitivity

The most important parameter describing the photocathode is its quantum efficiency (QE) ρ , defined as a ratio (expressed in %) of the number of emitted photoelectrons n_k to the number of photons striking the photocathode n_p :

$$\rho = \frac{n_k}{n_p} \quad (1)$$

Since the exact number of incident photons is difficult to measure, the QE is frequently described by *cathode radiant sensitivity*, $S_{k\lambda}$ (expressed in mA/W), i.e. the ratio between the current produced at photocathode I_k to the incident light power Φ_e . Cathode sensitivity is not uniform and depends on the incident light wavelength, so the radiant sensitivity is defined for a specific wavelength λ , customarily for 400 nm ($S_{k,400nm}$):

$$S_k = \frac{I_k [A]}{\Phi_e [W]}, \quad S_{k,\lambda} = \lim_{d\lambda \rightarrow \infty} \frac{dI_k}{d\Phi_e} \quad (2)$$

The same quantity S_k , but with the incident light power Φ_v , expressed in photometric units [lm], is called *cathode luminous sensitivity*, which in contrast to the radiant sensitivity is defined for a wide spectrum, typical for a given application. In the case of photometry and scintillation, the application of a tungsten-filament lamp with a color temperature of 2856 K is used as a reference light source. The two types of luminous sensitivity are the most commonly used in the data sheets:

- White sensitivity – reflects the photocathode’s response to white light, i.e. the whole spectrum of the reference lamp. The phototubes with spectral characteristics extended to longer wavelengths are characterized by higher white sensitivity.
- Blue sensitivity – reflects the response to the blue part of the light from the reference light source. The reduced spectral range is obtained by using Corning C.S. No. 5-58 filter ground and polished to half stock thickness. Blue sensitivity, also called corning blue (CB), is often expressed in $\mu\text{A/lmF}$, where F stands for filtered.

In the case of bi-alkali photocathodes, the ratio of blue to white sensitivity is close to 0.15.

The relation between radiant sensitivity and luminous blue sensitivity is given by:

$$\frac{S_k(\text{blue})}{S_{k,400nm}} \approx 0.125 \times 10^{-3} [W/lm] \quad (3)$$

The quantum efficiency can be calculated using the cathode radiant sensitivity in the following way:

$$\rho[\%] = 124 \frac{S_{k,\lambda} [mA/W]}{\lambda [nm]} \quad (4)$$

B. Types and materials

The QE of a given photocathode depends on the composition and thickness of the photosensitive material. The most common materials used in the production of photocathodes are [1] silver-oxygen-cesium (AgOCs), antimony-cesium (SbCs), and the bi and tri-alkali compounds SbKCs, SbRbCs, and $SbNa_2KCs$. These compounds define the *spectral sensitivity characteristics*, i.e. the dependence of the QE on the wavelength of incident light. An example of such characteristics for various types of photocathodes is presented in Fig. 2a. The long wavelength limit is caused by the photoemission threshold of the material, whereas sensitivity at the short wavelength is limited by the glass material of the photomultiplier input window. Increased thickness of the bi and tri-alkali photocathodes allows an extension of the sensitivity curves toward longer wavelengths, however, at the expense of blue sensitivity. Transmission as a function of the wavelength for different types of glass is presented in Fig. 2b.

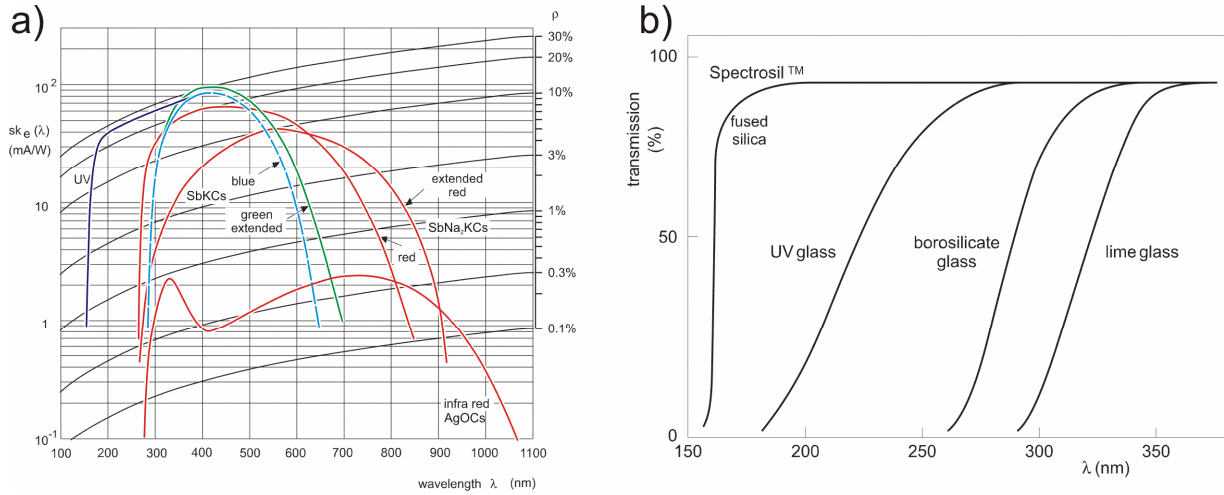


Fig. 2. Spectral sensitivity characteristics for various types of photocathodes (a) and the transmission properties of different types of glass (b).

3. Photoelectron collection efficiency

A. Input optics

Photoelectron collection efficiency is defined [1] as the ratio between the number of electrons reaching the useful area of the first dynode and the total number of electrons emitted by the cathode. Depending on the input optics, i.e. the number and type of focusing and

accelerating electrodes, the photomultipliers can be divided into 3 groups:

- Fast tubes – intended for timing applications in which the input optics is optimized for as fast as possible and almost simultaneous collection of all the photoelectrons emitted at the photocathode on the first dynode. Such optimization leads to a very short rise time of the anode pulse, but the collection efficiency of electrons emitted at the external parts of the photocathode is poor, thus causing a slight decrease in the photoelectron number in respect to QE.
- Slow tubes – intended for spectroscopic measurements and optimized for maximal collection efficiency of all photoelectrons, even those emitted at the external parts of the photocathode at the cost of the output pulse rise time. The input optics in this type of photomultipliers is very simplified and often does not contain any focusing or accelerating electrodes. Moreover, in the slow tubes the first dynode is much larger as compared to the fast PMTs.
- Standard tubes – which are general-purpose photomultipliers with a design that is a compromise (timing-favored or collection-efficiency-favored) between fast and spectroscopic PMTs. Such tubes have simpler input optics and a larger first dynode than the fast tubes.

B. Electron multiplier

The dynode structure presented in Fig. 1 and Fig. 3a, called *linear focusing*, consists of linearly arranged dynodes facing each other in a way that ensures progressive focusing of the electron paths between successive stages. In this construction the transit time of electrons between the dynodes is minimized, thus leading to a fast response and improved timing properties of the phototube. The first dynode in the linear focusing configuration differs from the rest of the multiplier: it possesses higher gain, is slightly larger and its position is optimized for the collection of photoelectrons at the second dynode.

Examples of other electron multiplier designs are presented in Fig. 3.

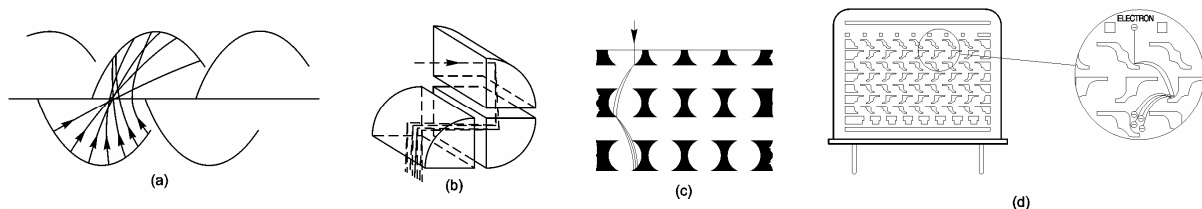


Fig. 3. Dynode configurations of electron multipliers: (a) linear focused, (b) box-and-grid, (c) foil (Photonis), (d) metal channel (Hamamatsu).

In photomultipliers where the electron collection efficiency and excellent uniformity are crucial, the box-and-grid type of multiplier is used (Fig. 3b). This type of structure consists of large, quarter cylindrical dynodes which assure a large collection area at the first dynode and between the stages. The consequence of dynode size and shape is a low electric field at the internal surface of the boxes, which leads to poor timing characteristics.

The configurations of foil or metal channel dynodes (Fig. 3c and 3d) are used in position sensitive multi-channel photomultipliers. In this type of PMT the dynode structure, in addition to signal amplification, must also keep position information about the photoelectron emission point at the photocathode through all the stages. This feature is achieved by special types of

dynodes in the form of parallel thin metal foils with specially designed holes. The single hole has a diameter of the order of tens of millimeters, and the shape of the holes differs slightly between manufacturers. An electron focused on one such hole (sub-channel) propagates only within its vertical axis, which assures a low level of crosstalks. Since the foil or metal channel dynodes are thin, this type of electron multiplier allows for a very compact construction of multi-channel photomultipliers. The small space between the dynodes leads to a fast response, but also makes the tube more fragile to nonlinearity. The biggest disadvantage of this type of multiplier is poor electron collection efficiency on the first dynode. This is due to the large dead space of the dynodes in areas where there is no perforation and where electrons cannot be multiplied.

4. Transit time spread

The design of the area between the photocathode and the first dynode is crucial for the timing characteristics of the photomultiplier. The photomultiplier response time to a delta light pulse differs between single events. The different flying paths of photoelectrons are the source of variations of their transit times between the photocathode and the first dynode. An example of the electron paths and equipotential lines of the electric field in a fast photomultiplier is presented in Fig. 4a. A schematic representation of the transit time spread, often called *time jitter*, is presented in Fig. 4b. Time jitter is defined by the FWHM of the probability density function of anode pulse arrival times. This value is proportional to the reversed square root of the number of emitted photoelectrons, however, in most cases it is measured for single photoelectron pulses induced by single photons distributed over the whole surface of the photocathode. Time jitter represents the intrinsic time resolution of a photodetector. An increase in the gain of the first dynode up to 15 in modern photomultipliers considerably reduced the contribution of the time jitter originating in the dynode structure.

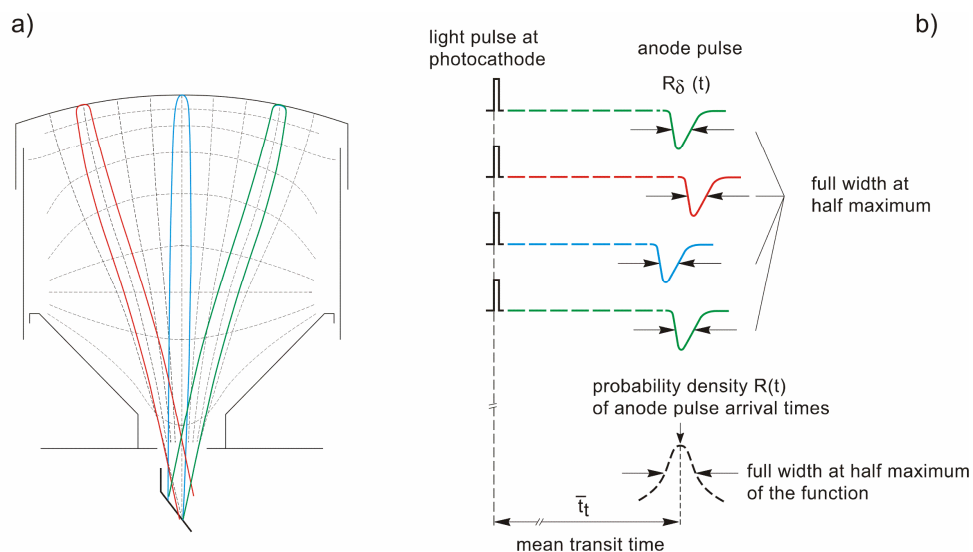


Fig. 4. Photoelectron trajectories and equipotential lines of the electric field in a fast photomultiplier (a). Diagram of an anode pulse transit time spread (b).

The transit time spread has two components:

- Chromatic component – resulting from a spread of the initial velocities and emission angles of the photoelectrons. The chromatic contribution also affects the photoelectrons originating from the same point at the photocathode that are not affected by the geometric component.
- Geometric component – resulting from different lengths of the primary paths of electrons emitted from different points on the photocathode. In this case, the largest contribution to the time jitter is caused by photoelectrons emitted behind the first dynode (red in Fig. 4a).

Both components depend on the strength of the electric field, so an increase in the field causes the time jitter improvement. Minimizing the electron path length differences also decreases the transit time spread. In fast photomultipliers this is done by the application of additional focusing electrodes. Another method is the use of a concave photocathode.

5. Anode

A. Anode construction and space charge effect

As is illustrated in Fig. 1, the configuration of the anode and the last dynode differs from the rest of the multiplier structure. In most of the general purpose photomultipliers, the anode is a grid placed inside the last dynode. Such a configuration assures the best possible collection efficiency of the secondary electrons emitted by the last dynode. Moreover, the small distance between the two electrodes assures a high electric field in this area, which minimizes the space charge effect (see below) and allows a linear response of the phototube. Because the last dynode partially surrounds the anode grid, it also forms a kind of electrostatic screen.

The space charge effect appears in the dynode structure at high currents, when the cloud of secondary electrons in the inter-dynode region cannot be sufficiently collected by the next dynode. The total electric charge of such a cloud affects the electron trajectories, thus causing collection loss or even a return of some electrons to the dynode from which they were emitted. In consequence, the output signal at the anode is no longer proportional to the number of primary photons and the photomultiplier becomes nonlinear. The space charge limited current density J_s can be expressed by the Child-Langmuir formula valid for a diode with plane-parallel electrodes:

$$J_s = 2.2 \cdot 10^{-6} \frac{V^{3/2}}{d^2} \quad (5)$$

where V is the inter-electrode voltage and d is the inter-electrode distance in centimeters. Formula (5) shows that the low distance between the last dynode and the anode grid together with a high electric field increase the space charge current limit.

In the case of the discussed anode construction, the electrons emitted from the penultimate dynode pass through the anode grid on their way to the last dynode. Hence, in most of the photomultipliers, the linearity is limited by the electric field between the anode and the penultimate dynode, which is 3 to 5 times lower as compared to the last-dynode – anode area.

In the case of multichannel photomultipliers with foil or metal channel dynodes, the anodes are simply the metal electrodes, and these types of PMTs are more sensitive to the space charge effect.

One of the methods of improving the linearity range is the use of a progressive instead of equal voltage distribution in the last stages of the voltage divider.

B. Screening grid at the anode

The study presented in [3] and [4] strongly suggests that time resolution deterioration in fast photomultipliers is also associated with the design, as described above, of the grid-anode placed inside the last dynode. Despite all of the mentioned advantages, this configuration has one major drawback – the anode signal consists of two components:

- the main one due to the collection of electrons from the last dynode,
- a smaller, parasitic one induced in the anode by the electrons traveling from the penultimate dynode to the last one

This parasitic component is earlier in time in relation to the main anode pulse, and can cause a triggering of the fast discriminator. In other words, the initial rise time of the anode pulse is slightly slowed down due to the addition of a small parasitic pre-pulse to the main anode pulse. Thus, the discriminator threshold in the case of the triggering point set at the main anode pulse is far too high as compared to the one resulting from the statistical properties of the scintillation detectors requiring a low fraction of the anode pulse height for the best time resolution [5]. If the threshold is set lower, at the level of the parasitic component, the time resolution is affected by the deteriorated rise time of the output pulse.

In the past, i.e. in the XP1021 PMT, a special grid was placed in front of the anode to improve the initial slow rise of the anode pulse [6], in other words, to minimize the parasitic component. This PMT was known for its very good timing capabilities [5]. A diagram of the geometry of the last stages in a linear focused photomultiplier, together with the position of the screening grid, is presented in Fig. 5.

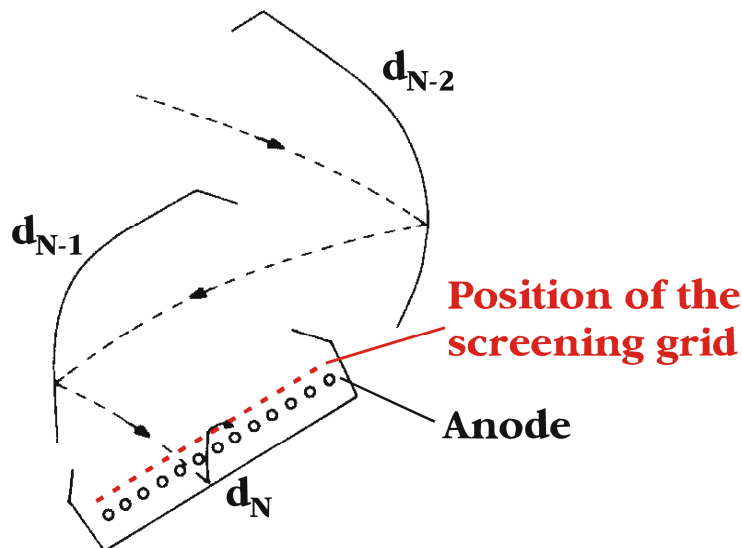


Fig. 5. Geometry of the last dynodes and the anode in a typical linear focused photomultiplier together with the position of the screening grid.

It was verified in [7], [8] and [9] that the screening grid at the anode can be a solution that makes possible the suppression of the parasitic component. Due to the screening grid, the time resolution measured with various scintillators can be improved by a factor of 1.15–1.2,

compared to a standard photomultiplier without the screening grid. This improvement is independent of the decay time constants of the scintillation light pulses and the time jitter of the scintillation detector.

The study of 2-inch PMTs, equipped with the screening grid [7], has allowed a successful launch of a new type of commercially available fast photomultiplier XP20D0, which is superior in timing [8]. The time resolution improvement, due to the application of the screening grid, was also confirmed during studies of large 3-inch PMTs XP43D2 performed by the author [10].

6. Excess noise factor

A. Origin of the excess noise factor

Signal amplification in a photomultiplier is possible due to the secondary emission process in the dynode structure. Due to the statistical nature of this process, the amplitude of the photomultiplier output pulse fluctuates. Such a gain spread during electron multiplication is a source of the *excess noise*, which affects both the pulse height resolution and timing resolution. The excess noise factor can be calculated on the basis of a single photoelectron spectrum since its pulse height resolution reflects the gain variations of the dynode structure.

B. Experimental example

An example of single photoelectron spectra recorded with two types of Photonis (1-inch XP1020, 1.5-inch XP3060) and Hamamatsu (1-inch R9800, 1.5-inch R9420) fast photomultipliers is presented in Fig. 6 [11]. When comparing the peak height resolution (PHR) of the Photonis and Hamamatsu PMTs, it is easy to notice the significant advantage of both Photonis tubes with superb resolutions of 55%. Also, a separation of the peak from noise is excellent for the XP1020 and XP3060. In the case of Hamamatsu, the PHR is much worse and equal to 95%. The R9800 spectrum is symmetrical, such as in the case of both Photonis tubes. The spectrum for the R9420 PMT is asymmetrical because its right slope is raised due to the contribution of the two photoelectron events.

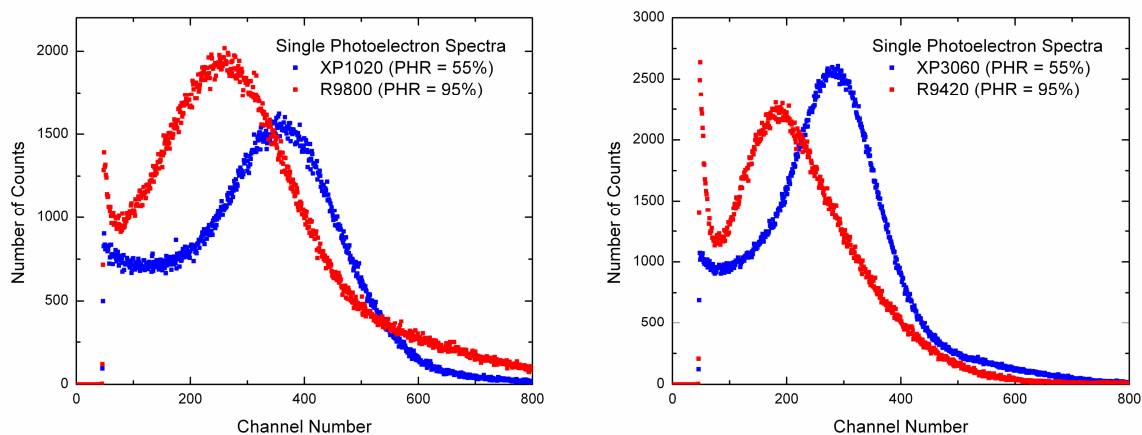


Fig. 6. Single photoelectron spectra recorded for 1-inch PMTs, XP1020 and R9800 (left), and 1.5-inch PMTs, XP3060 and R9420 (right).

The excess noise factor (ENF) is related to the single photoelectron peak resolution expressed in $\sigma(R_e)$ in the following way:

$$ENF = 1 + R_\sigma^2 \quad (6)$$

The value for both Photonis tubes is equal to 1.05, while for the Hamamatsu photomultipliers $ENF = 1.20$.

As well as the gain variations, the excess noise factor in the photomultipliers is mostly affected by the multiplication coefficient of the first dynode, whose gain is a few times higher than for the rest of the dynodes.

7. References

- [1] S. Flyckt and C. Marmonier, *Photomultiplier Tubes: Principles and Applications*. Photonis, Brive, France, 2002.
- [2] M. Moszynski and B. Bengtson, "Status of timing with plastic scintillation detectors," *Nucl. Instr. Meth.*, vol. 158, pp. 1–31, 1979.
- [3] B. Bengtson and M. Moszynski, "Timing improved by the use of dynode signals studied with different scintillators and photomultipliers," *Nucl. Instr. Meth.*, vol. 204, no. 1, pp. 129–140, 1982.
- [4] J. De Vries and F. Kelling, "Fast timing with photomultiplier dynode pulses," *Nucl. Instr. Meth. A*, vol. 262, no. 2-3, pp. 385–393, 1987.
- [5] B. Bengtson and M. Moszynski, "Timing properties of scintillation counters," *Nucl. Instr. Meth.*, vol. 81, no. 1, pp. 109–120, 1970.
- [6] G. Pietri, "Progress in photomultiplier tubes for scintillation counting and nuclear physics," *IRE Trans. Nucl. Sci.*, vol. 9, no. 3, pp. 62–72, 1962.
- [7] M. Moszynski, M. Kapusta, D. Wolski, M. Balcerzyk, S. Flyckt, P. Lavoute, C. Marmonier, and H. Mach, "New fast photomultipliers with a screening grid at the anode," *IEEE Trans. Nucl. Sci.*, vol. 51, no. 4, pp. 1701–1706, 2004.
- [8] M. Moszynski, M. Gierlik, M. Kapusta, A. Nassalski, T. Szczesniak, C. Fontaine, and P. Lavoute, "New Photonis XP20D0 photomultiplier for fast timing in nuclear medicine," *Nucl. Instr. Meth. A*, vol. 567, no. 1, pp. 31–35, 2006.
- [9] M. Moszynski, "Prospects for new fast photomultipliers," *Nucl. Instr. Meth. A*, vol. 337, no. 1, pp. 154–164, 1993.
- [10] T. Szczesniak, M. Gierlik, M. Kapusta, M. Moszynski, D. Wolski, P. Lavoute, and E. Rossignol, "The 75 mm diameter Photonis XP43D2 photomultiplier with the screening grid at the anode for timing experiments," *IEEE Trans. Nucl. Sci.*, vol. 53, no. 3, pp. 1540–1546, Jun. 2006.
- [11] T. Szczesniak, M. Moszynski, L. Swiderski, A. Nassalski, A. Syntfeld-Kazuch, A. G. Dehaine, and M. Kapusta, "A comparative study of fast photomultipliers for timing experiments and TOF PET," *IEEE Trans. Nucl. Sci.*, vol. 56, no. 3, pp. 1017–1023, Jun. 2009.

6. Theory of Time Resolution of Photomultiplier Systems

1. Characteristics of the output pulse

A. Introduction

The accuracy of determining the time of nuclear particle interaction inside a scintillation detector depends on its output signal and triggering method of the electronics. From the point of view of time resolution measurements, the detection process of any kind of radiation by a scintillation detector is determined by:

- Transfer of the particle energy into a scintillator through excitation of its optical states.
- Light emission due to de-excitation of the excited states with characteristic decay time defined by the life time of these states.
- Light collection from the scintillator volume to a photomultiplier's photocathode.
- Emission of photoelectrons from the photocathode.
- Collection of the photoelectrons on the first dynode.
- Multiplication of the photoelectrons in the dynode structure of the photomultiplier.
- Generation of a current pulse at the output of the photomultiplier.
- Triggering method of the electronic instrumentation by the PMT output pulse.

The theory of time resolution of scintillation counters covers the statistical analysis of the detector output pulses. The two main theories were introduced by Gatti and Svelto [1], [2], [3], and Hyman [4], [5]. Both have a similar logical structure, however, they assume slightly different analytical functions of the probability distributions that describe individual processes occurring in the scintillation counter after the detection of a nuclear particle. The functions presented by Hyman [5] will be discussed here since his data are known to be more consistent with the experimental results [6], [7], [8].

B. Photocathode illumination function

The processes listed above, from one to three, determine the time distribution of the photons striking the photocathode and can be summarized in a photocathode illumination function $I(t)$ normalized to the mean number of photoelectrons emitted in one scintillation event. The function in its simplest form can be written as a single exponential decay $I(t) = I_0 \exp(-t/\tau)$ reflecting an ideal detector with the scintillator's mean life time τ , and processes one and three negligible. Such a function was used by Hyman in the first steps of his analysis [4], however, the drawbacks of this form were also listed.

Both the scintillator's excitation by radiation and further energy transfer to luminescent centers have statistical time properties that decide about the rise time of the scintillation light pulse and should also be included in $I(t)$. Hyman, after an analysis of the data covering the light pulse shape studies presented by Koehlin and Raviart [9], defined the $I(t)$ function as [5]:

$$I(t) = \left(\frac{\gamma\tau}{\gamma-1} \right) \left(\exp\left(-\frac{t}{\tau}\right) - \exp\left(-\frac{t\gamma}{\tau}\right) \right) \text{ and } \gamma = \frac{\tau}{\tau_1} \quad (1)$$

where τ is the decay time constant and τ_1 is the rise time constant of a scintillation light. Equation (1) is valid for a scintillation light pulse produced in three steps. First, a particle deposits energy in the crystal, causing excitation of state A in a short period of time as compared to the subsequent processes. Next, de-excitation of state A, with characteristic time τ_1 , populates state B (the luminescent centers). Finally, the scintillation light is emitted after de-excitation of state B with the characteristic decay time τ .

The statistical fluctuations of such a defined average function are described by Poisson statistics and hence a variance equal to $I(t)dt$ can be attributed to the $I(t)dt$ photoelectrons emitted in the time period dt .

C. *Single photoelectron response (SER)*

The properties of a photodetector (a photomultiplier in this case) can be described by a single photoelectron response (SER) function which is characterized by three parameters: the number of electrons (A) at the photomultiplier's output (amplitude), time (h) between emission of a photoelectron from the photocathode and the centroid of a consequent current output pulse, and standard deviation (σ) of this pulse width, relative to its centroid.

The average value of A , assuming the same secondary emission gains (g) of each dynode, is equal to:

$$A = g^{n-1} \quad (2)$$

where $n-1$ is the number of dynodes (all n electrodes excluding the anode).

The mean value of time h is a sum of the mean flight times between successive dynodes (assuming independent probability density functions of successive flights):

$$h = h_0 + h_1 + h_2 + \dots + h_{n-1} \quad (3)$$

where each index denotes the flight leaving the considered dynode and 0 denotes the flight time between the cathode and the first dynode. Here, the continuous induction of electrons in flight from the last dynode to the anode is neglected and simply only the arrival time at the anode is considered.

The average value of a pulse width variance σ^2 can also be expressed as a sum of consecutive variances associated with the probability density functions of the flight times between dynode i and $i+1$:

$$\sigma^2 = \sigma_1^2 + \sigma_2^2 + \dots + \sigma_{n-1}^2 \quad (4)$$

In the above formula, the variance related to the photoelectron traveling from the photocathode to the first dynode is excluded since this single photoelectron contributes only to the statistical shift of the whole SER, but not to its width. If all σ_i are equal and denoted by σ_{dd} , formula (4) can be written as:

$$\sigma^2 = (n-1)\sigma_{dd}^2 \quad (5)$$

In general, the average shape of the single photoelectron response $f_\sigma(t)$ will be given by the convolution of probability density functions of all $n-1$ cascaded flights between dynode i and $i+1$:

$$f_\sigma(t) = f_1(t) * f_2(t) * \dots * f_{n-1}(t) \quad (6)$$

An analysis of the single photoelectron pulse shapes recorded with the 56AVP photomultiplier allowed Hyman to find a reasonable description of the single photoelectron response in the form of the clipped Gaussian function [4]:

$$f_{\sigma}(t) = \frac{1.1125}{(2\pi)^{1/2} \sigma} \left\{ \frac{35}{32} \exp\left[-\frac{(t - 2.2166\sigma)^2}{2\sigma^2}\right] - \frac{3}{32} \right\} \text{ and } \int_{-\infty}^{+\infty} f_{\sigma}(t) dt = 1 \quad (7)$$

valid for: $0 \leq t \leq 4.4332\sigma$, $f_{\sigma}(t) = 0$ for $t < 0$ and $t > 4.4332\sigma$. Formula (7) is the response at the anode to light striking the photocathode in the form of a δ function.

D. Statistical fluctuations of the SER parameters

The single photoelectron response is affected by statistical fluctuations of amplitude (gain), time and width, so the corresponding variances of A , h and σ have to be taken into account in the analysis.

The fluctuations of a photomultiplier amplification are mainly caused by the gain spread of the first dynode. The amplitude variance ε_A^2 for a photomultiplier with a sufficiently high number of equal dynodes can be written as [3]:

$$\varepsilon_A^2 = [g/(g-1)] \cdot \varepsilon_g^2 \quad (8)$$

where g is the secondary emission factor and ε_g is the relative variance of the number of secondary electrons in a single secondary emission process. Assuming that this process can be described by Poisson statistics, ε_g^2 should be equal to $1/g$. Formula (8) can be obtained by using the theory of the branching process [10] and the detailed calculations are presented in [3]. Similar results were shown by Hyman [4], however, he introduced the coefficient r describing the gain fluctuations at n stages with an equal mean gain g at each stage:

$$r = (1 + \varepsilon_A^2)^{1/2} = [1 + (g^n - 1)/g^n (g - 1)]^{1/2} \quad (9)$$

Note that for $\varepsilon_g^2 = 1/g$ in (8) and high n in (9), $g^n - 1 \cong g^n$, and ε_A^2 in (8) and (9) are equal.

The statistical fluctuations of time h are related to the flight time differences of electrons inside the photomultiplier. The photoelectrons traveling between the photocathode and the first dynode have the main contribution to these fluctuations due to different initial velocities and the point of emission at the photocathode. The width of such transit times distribution (σ') is called *time jitter* or *transit time spread*. Following the calculations presented in [3], the variance of the time jitter can be written as:

$$\sigma'^2 = \sigma_{ph}^2 + \frac{\sigma_{dd}^2}{g-1} \frac{g}{g-1} \quad (10)$$

where σ'_{ph} denotes the variance of the flight times of photoelectrons from the photocathode to the first dynode and the second part of this equation describes the flight time of photoelectrons through the dynode structure. The probability density function proposed by Hyman [4] in the case of the electrons transit time $f_{\sigma}(t)$ is Gaussian and identical as formula (7), but with the width equal to σ' .

Gatti and Svelto [3] showed that the variance of width σ of the single photoelectron response can be expressed as:

$$\text{var } \sigma = \frac{\sigma_{dd}^2}{2(n-1)} \frac{1}{g-1} \quad (11)$$

A comparison of formulas (10) and (11) shows that the variance of σ is much smaller than the variance related to the transit time spread and hence can be neglected.

E. Output current pulse

In the further discussion a photomultiplier response will be considered only with respect to a single photoelectron impinging the first dynode (photoelectron emission at the photocathode will be omitted) [3]. In this approach a PMT is an ideally deterministic object whose transfer function is a single photoelectron response. All the fluctuations of the electron flight times σ^2 (even the second term in (10)), as well as spread in gain ε_A^2 will be attributed to the cathode-first dynode area. Following the above assumptions, the electron multiplier can be treated as a conventional, noiseless electrical network having $\delta(t)$ response equal to the single photoelectron response.

All of the statistical properties of a photomultiplier are comprised into an *equivalent illumination function* which is a convolution of the photocathode's illumination function $I(t)$ (e.g. given by (1)) and the probability distribution function of the electrons transit time $f_\sigma(t)$:

$$I^*(t) = I(t) * f_\sigma(t) \quad (12)$$

The current pulse at a photomultiplier's output $i(t)$ is described by a convolution of the equivalent illumination function (12) and the single photoelectron response (7):

$$i(t) = I^*(t) * f_\sigma(t) \quad (13)$$

If all the mean values and statistical fluctuations of the parameters describing the equivalent illumination function and single photoelectron response are known, the above general formula allows to calculate the shape of the output current pulse $i(t)$ together with its characteristic times.

2. Time resolution

A. Machine times

The next step of the theoretical analysis considers the triggering methods of the electronics by the PMT output signal defined by (13). These methods lead to different characteristic times, called *machine times*, to which the instrumentation is sensitive. Machine time is the time difference between the beginning of the detector output pulse and the triggering time of the electronics.

Three of several types of detector response related to different methods of triggering the electronics are:

- Straight response – the trigger time signal is generated when the current pulse from a PMT $i(t)$ exceeds a given threshold h measured as a fraction of the maximum amplitude of the average of many current pulses.
- Integral response – the trigger time signal is generated when an integrated current pulse from a PMT exceeds a given level of C/R measured as a fraction of a total charge of the average anode pulse.
- Centroid response – the trigger time signal is generated at the centroid position of the pulse due to a pre-selected amount of charge collected at the anode, and the triggering fraction is measured with reference to the total charge of the mean anode pulse.

In the case of all the machine times, the limited time resolution of a scintillation detector is

caused by statistical fluctuations of the shape and amplitude of the photomultiplier output pulses. Examples of typical anode current pulses calculated for 10 to 100 photoelectrons, using Monte Carlo methods, are presented in Fig. 1, following [4].

Calculation of variances of the above-defined machine times leads to values that constitute the theoretical limits of the time resolution for a given system. Numerical data can be obtained by approximate analytical calculations or using Monte Carlo methods.

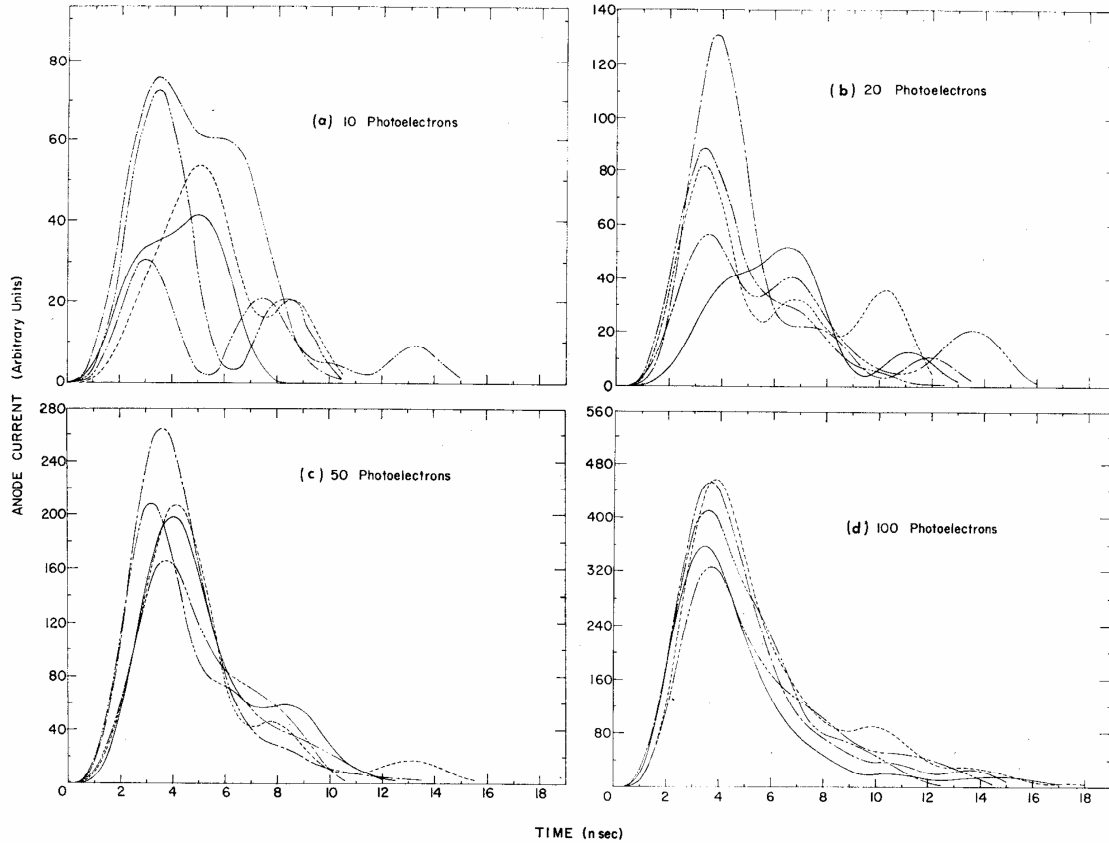


Fig. 1. Typical waveforms of the anode current pulse, calculated using Monte Carlo methods. Reprint from [4].

B. Examples of approximate analytical calculations and Monte Carlo results

First, a simplified example of a detection system will be considered with the SER described by a Dirac delta function $\delta(t)$. Such a system reflects a detector consisting of a scintillator with a decay time that is much longer than the time jitter of the photomultiplier used. In this case, a detector current output pulse is affected only by the characteristic times of the scintillation light (photocathode illumination function).

Following Post and Schiff [11], and assuming a total number of R photoelectrons and an exponential equivalent illumination function with the decay time τ which is:

$$I^*(t) = (R/\tau)\exp(-t/\tau) \quad (14)$$

the variance of the arrival times of the C^{th} electron (describing the trigger level) can be expressed as:

$$\varepsilon^2 = (\tau^2/R^2)C \left\{ 1 + \frac{2}{3}(C+1) + \dots \right\} \quad (15)$$

Calculations for a scintillation light pulse described by the characteristic decay time τ_1 and rise time τ_2 were performed by El-Wahab and Kane [12]. Their equivalent illumination function was defined as:

$$I^*(t) = \left\{ \frac{R}{(\tau_1 - \tau_2)} \right\} \left\{ \exp\left(-t/\tau_1\right) - \exp\left(-t/\tau_2\right) \right\} \quad (16)$$

An example of the calculated probability density functions of arrival times of the C^{th} electron (normalized collected charge) for a total number of $R = 100$ photoelectrons and different values of the τ_1/τ_2 ratio are presented in Fig. 2. The FWHM of these distributions, which determines the time resolution in the function of C , is presented in Fig. 3.

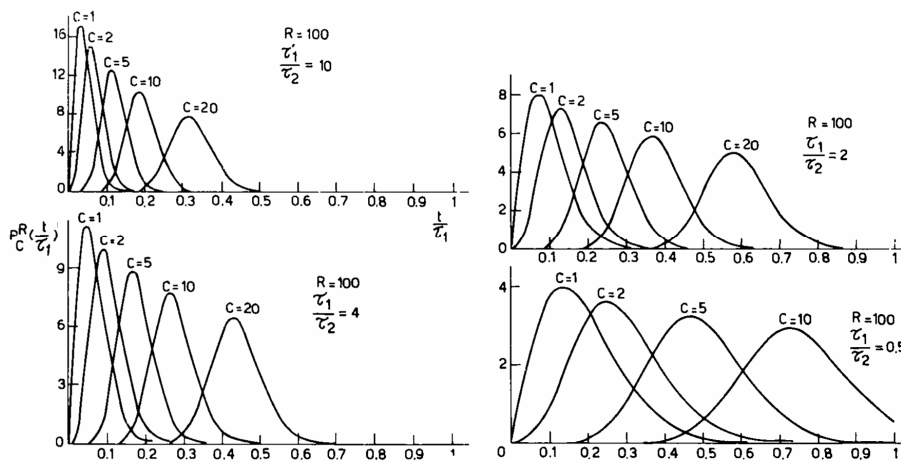


Fig. 2. Probability density functions for a trigger set at the C^{th} electron, a total of $R=100$ photoelectrons and different ratio between rise time and decay time of a scintillation pulse. Reprint from [3].

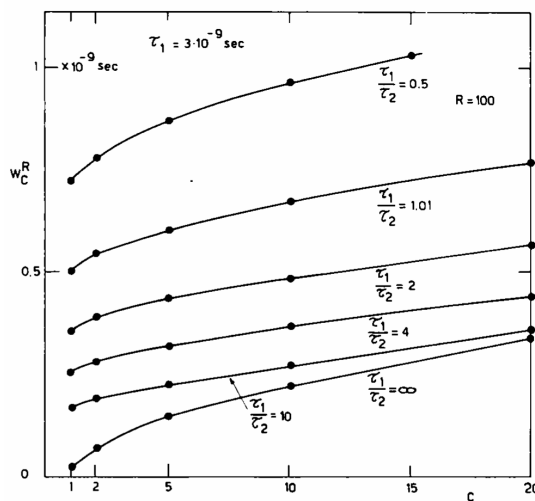


Fig. 3. The FWHM in the function of the trigger set at the C^{th} electron of the PDF calculated by El-Wahab and Kane. Reprint from [3].

The transit time spread of electrons traveling from the photocathode to the first dynode was

incorporated into the Monte Carlo calculations made by Gatti and Svelto [2]. They proposed the probability density function that describes the time jitter in an exponential form. The presented plots of variances in the function of C (normalized output charge in the number of electrons) showed that the minimum value of the time resolution can be obtained for $C \rightarrow 0$. Moreover, the influence of the photomultiplier parameters on time resolution, even in the case of slow decaying scintillators, was also shown. The data obtained in [2] for the different values of the SER width λ , time jitter ε_{ph} and gain variations ε_A are presented in Fig. 4. Curve 1 represents an ideal photodetector with statistical contribution only due to photoelectron emission statistics. Curve 2 includes a finite width of the SER, whereas curve 3 is valid for the SER width equal to 0 but finite time jitter. Curve 4 reflects a real detector.

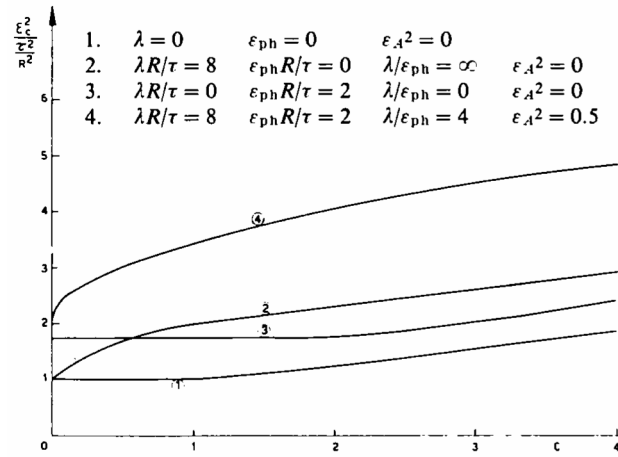


Fig. 4. Centroid time variances calculated using Monte Carlo methods for different statistical parameters of a photomultiplier. Reprint from [3].

C. Hyman theory

The theoretical model proposed by Hyman [5] assumes a finite rise time of the scintillation light pulse and the photocathode illumination function given by equation (1). The effect of different ratios γ between the rise time and decay time on the output current pulse is presented in Fig. 5. In the theory, the transit time of photoelectrons between the photocathode and the first dynode as well as a single photoelectron response are described by similar clipped Gaussian functions (7). The only difference is the value of the distribution widths, denoted as σ' and σ , and with variances described by (10) and (11) in the case of the time jitter and SER, respectively. In the analysis it is also assumed that the system is linear and superposition is valid.

Following Hyman [5], a standard deviation of the time resolution $\langle \delta t \rangle$ in the case of the integral response (without the time jitter) can be written as:

$$\frac{\langle \delta t \rangle N^{1/2}}{r} = \frac{\left\{ \int_0^{t'} I^*(\tau) d\tau \left[\int_0^{t'-\tau} du f_\sigma(u) \theta(4.4332\sigma - u) \right]^2 \right\}^{1/2}}{i(t)} \quad (17)$$

where $\theta(4.4332\sigma - u) = 1$ for positive arguments and $\theta(4.4332\sigma - u) = 0$ for negative

arguments, $i(t)$ is a current pulse at the anode, t' is the trigger time of the electronics that is a function of C/R , N is the number of photoelectrons, r reflects the photomultiplier gain variations and is given by (9). Similar results, although in the form of more complex integrals, were presented by Hyman [4] for the straight, integral and centroid response. In each mode the form with and without the time jitter was discussed.

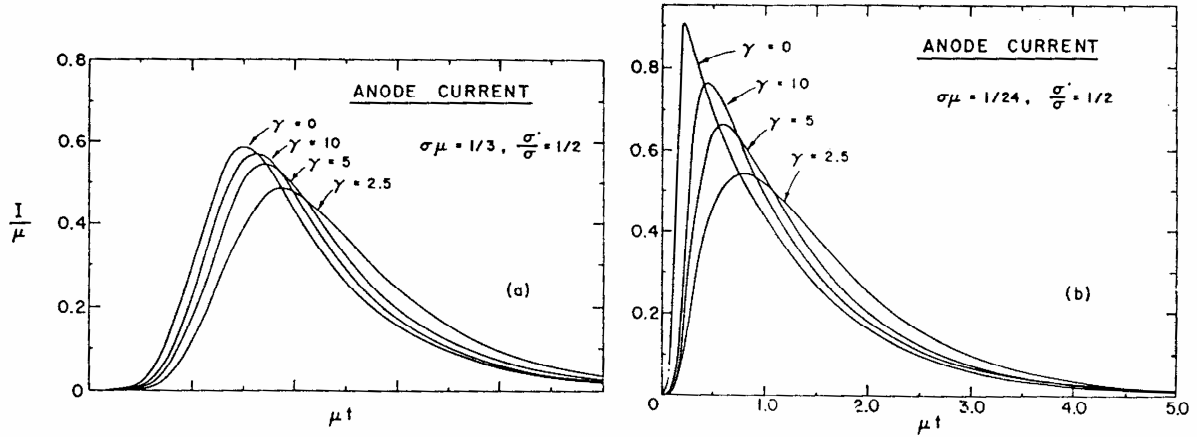


Fig. 5. Calculated anode current with γ as a parameter. Reprint from [5].

Hyman performed analytical calculations for various values reflecting the different parameters of a scintillator and photomultiplier. The results were presented in the form of curves, where the standard deviation of the time resolution is normalized in the following way:

$$\frac{\langle \delta t \rangle N^{1/2}}{\tau \cdot r} = H\left(\frac{C}{R}, \frac{\sigma}{\tau}, \frac{\sigma'}{\sigma}, \gamma\right) \quad (18)$$

and where function H depends on the following parameters: triggering fraction C/R , ratio between the width of SER and scintillation decay time σ/τ , ratio between the time jitter and the SER width σ'/σ , and ratio between the rise time and decay time of the scintillation light pulse γ .

Examples of the calculated and normalized curves in the case of an integral response are presented in the following figures. In Fig. 6 the data for $\gamma \rightarrow \infty$ and the different values of σ/τ and σ'/σ are presented as a function of a fraction of the anode pulse. A similar plot, but for γ equal to 2.5, is shown in Fig. 7. The Hyman curves allow to find an optimal triggering point for a given detection system or an influence of the change of system parameters, such as scintillator decay time or photomultiplier time jitter.

An analysis of the C/R curves shows that their shape and optimum position depend on the σ'/σ ratio. A comparison of the plots presented in Fig. 6 and 7 leads to the conclusion that the introduction of an exponential rise time of the scintillation light deteriorates the time resolution, but does not affect the shape of the Hyman curves. The width of the single photoelectron response has no effect on the time resolution, however, it changes the shape of the C/R curves and shifts the optimum toward higher trigger levels.

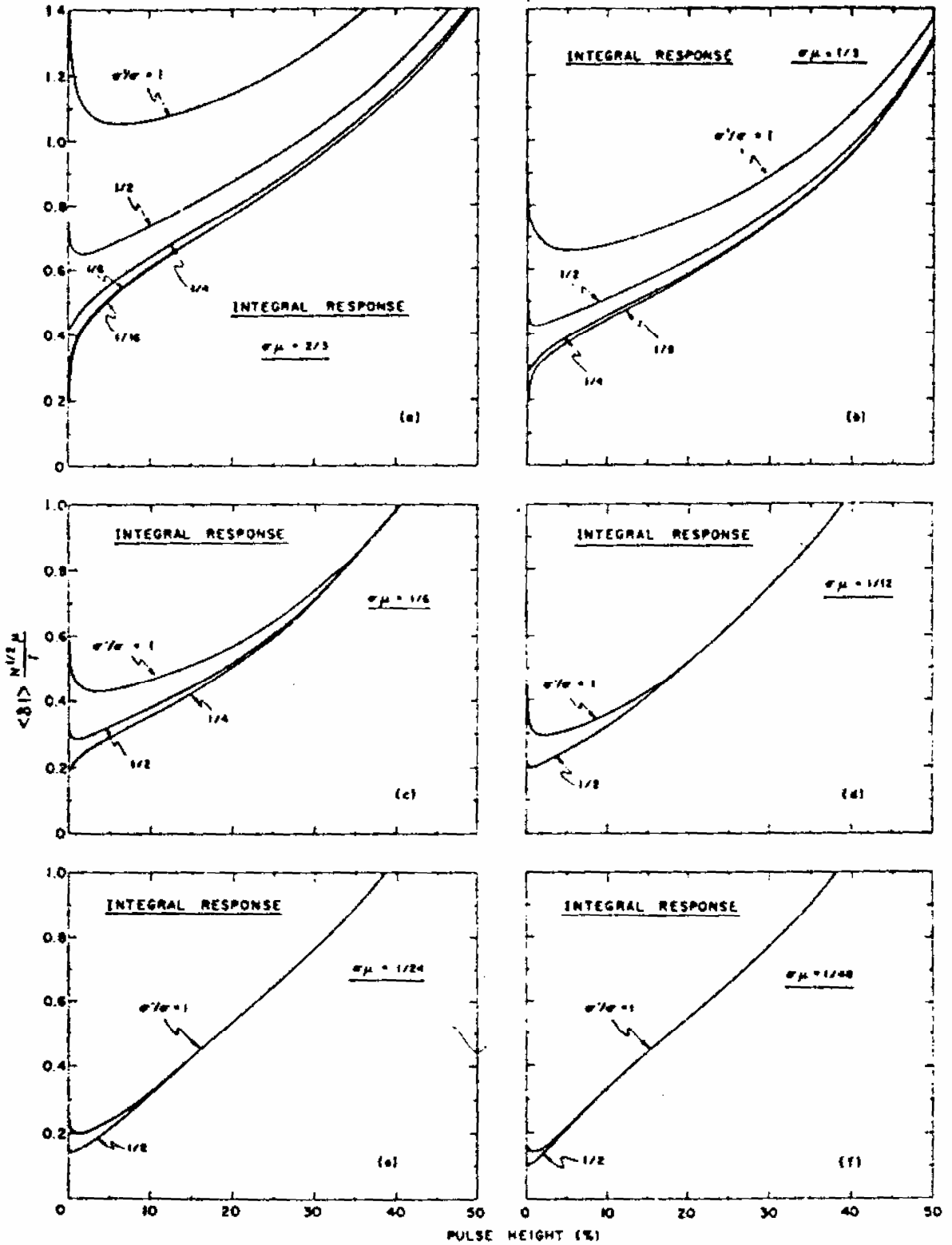


Fig. 6. Width of the triggering time distribution for an integral response and $\gamma \rightarrow \infty$ as a function of a fraction of the pulse used. Reprint from [5].

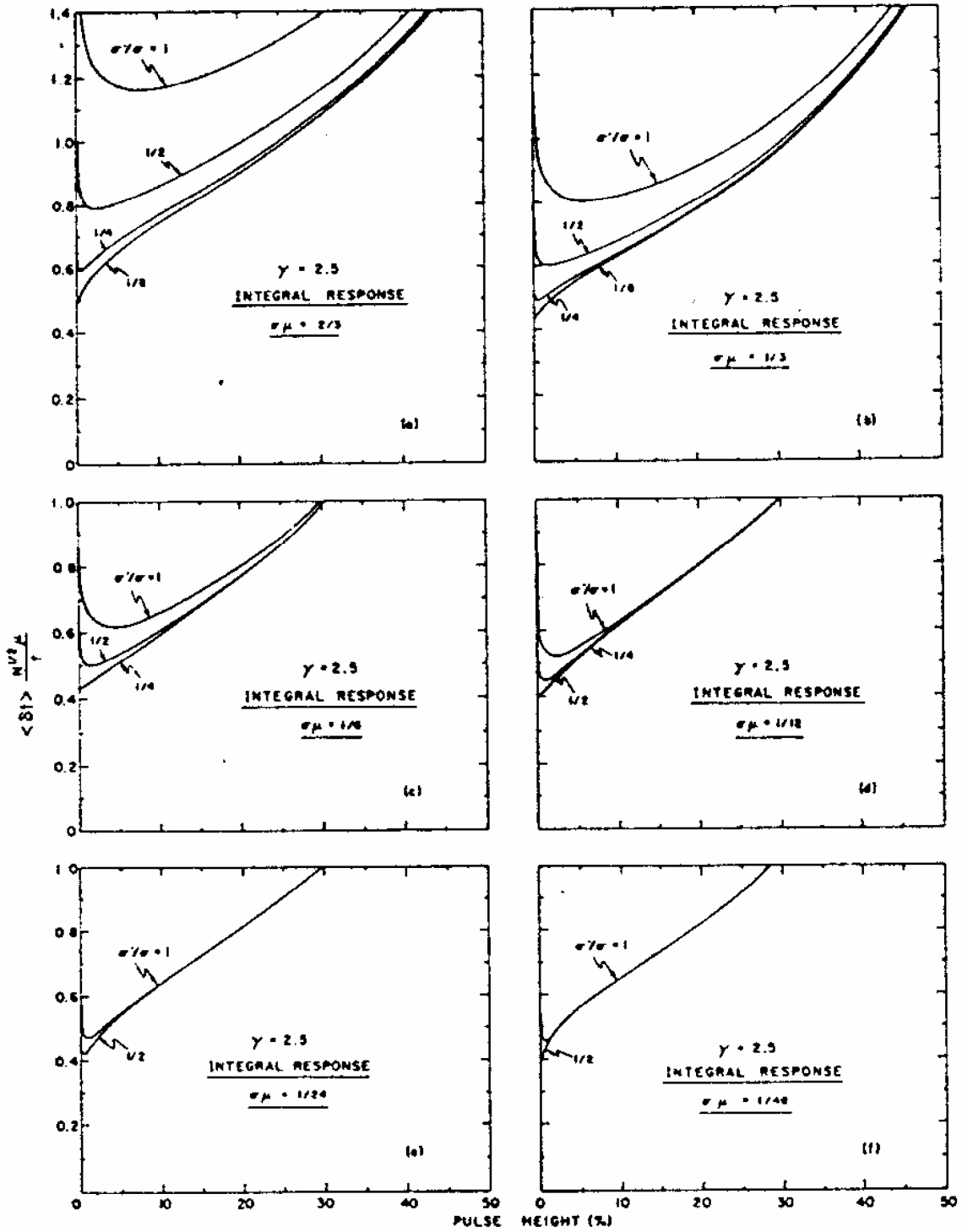


Fig. 7. Width of the triggering time distribution for an integral response and $\gamma = 2.5$ as a function of a fraction of the pulse used. Reprint from [5].

D. Comparison with experiments

The Hyman theory predictions, in comparison with experimental data, are not completely reliable since the theory does not account for all the physical and geometrical characteristics of the scintillator. Gatti and Svelto [3] have pointed out the main discrepancies between the

theoretical and experimental values of the time resolution as a function of the triggering fraction C/R :

- The minima in the theory are obtained for lower C/R than observed experimentally.
- Separate curves are observed experimentally for different energy, while with the normalized unit used one single curve is expected.
- The experimental values are better than the theoretical ones by about a factor of 2, referring to a curve for 100 keV.

A modification of the Hyman theory that assures agreement with the experimental data was introduced by Bengtson and Moszyński [13]. The authors compared the time resolution properties of the NE111 and Naton136 scintillators (similar decay times) of different heights to extract the influence of light collection in the crystal and the faster rise time of the NE111. Fig. 8 shows the C/R curves obtained for the tested scintillators.

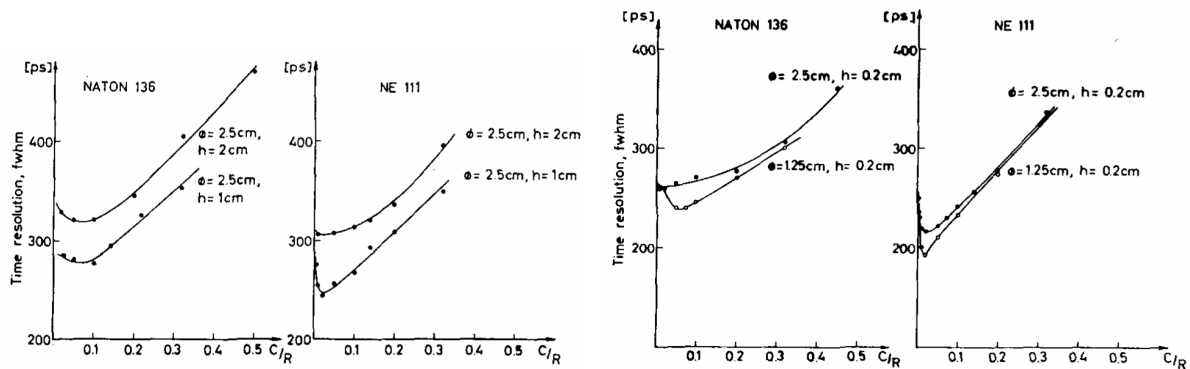


Fig. 8. Influence of scintillator height (left) and utilized photocathode area (right) on C/R curves. Reprint from [13].

The influence of the scintillator height is presented on the left. For a 1-cm and 2-cm Naton136, the shape of the curves is similar and the time resolution is improved with a smaller crystal. In the case of the NE111, not only is the time resolution improved, but also the shape of the C/R curve is changed, moving the optimal threshold from about 7% for the 2-cm crystal to 2% for the 1-cm scintillator. Moreover, the time resolution obtained with the NE111 is better compared to the Naton136, despite the fact that the light yield from the NE111 is 40% smaller.

The curves on the right in Fig. 8 present the influence of the utilized photocathode area on the optimal C/R threshold. In these measurements thin scintillators with diameters of 1.25 cm and 2.5 cm were used. A further change of the C/R curves' shape is seen. The curve for the thin Naton136 with a diameter of 2.5 cm is very similar to that for the NE111 with a height of 2 cm.

As was mentioned in the previous section, in the Hyman theory the shape of the C/R curves, and in particular the optimal threshold value, strongly depend on the σ'/σ ratio. Moreover, an exponential rise of the light pulse from the scintillator impairs the time resolution, but it has a very weak influence on the optimal value of C/R and the shape of the curves.

From the plots presented in Fig. 8 it is visible that the shape of the C/R curves depends on the timing properties of the scintillators. The shape of the experimental curves changes in the same way as the shape of the theoretical ones for the different values of σ'/σ [5]. It is

interesting to note that the optimal fraction value moves from 7% for Naton136 to 2% for NE111. A similar change has been found between the 56AVP and XP1020 photomultipliers [14] characterized by different time jitter.

These facts suggest that the scintillator contributes to σ' , and for further analysis this parameter in the Hyman theory should be redefined in the following way:

$$\sigma'^2 \equiv \sigma'_{tot}{}^2 = \sigma'_{SC}{}^2 + \sigma'_{PM}{}^2 \quad (19)$$

where σ'_{SC} is the standard deviation of a Gaussian function describing the time spread of the scintillator and σ'_{PM} is the standard deviation of a Gaussian function describing the time spread of a photomultiplier.

In consequence, a new description of the photocathode illumination function is introduced in the form of the following convolution:

$$I(t) = f_{SC}(t) * e^{-t/\tau} \quad (20)$$

where $f_{SC}(t)$ is the clipped Gaussian function describing the generation and collection of light in the scintillator. A similar description of the light pulse has been suggested before by Bertolini et al. [6]. A quantitative comparison of the experimental C/R curves and the two families of theoretical curves ($\sigma/\tau = 2/3$ and $\sigma/\tau = 1/3$) is shown in Fig. 9. All of the curves are normalized according to eq. (18). The shape of the experimental curves measured for the different scintillators follows the shape of the theoretical curves calculated for different parameters of photomultipliers, which confirms the need of the above redefinition of the σ' parameter.

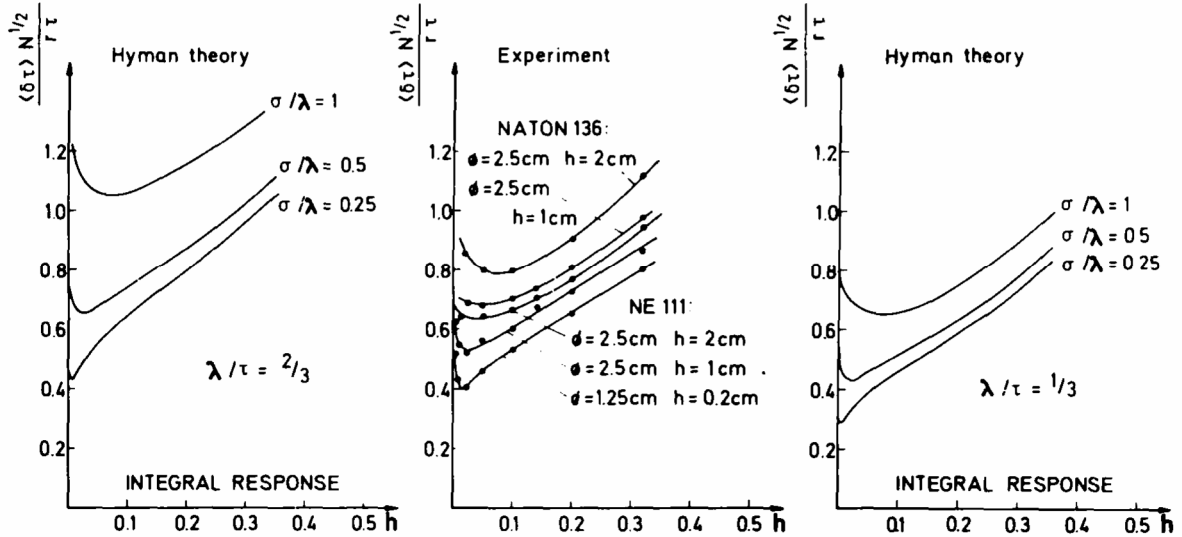


Fig. 9. Comparison of the theoretical curves of Hyman [5] with the time resolution dependency on the pulse height fraction measured with the Naton136 and NE111 scintillators of different dimensions coupled to the XP1021 photomultiplier. Reprint from [13].

The dependency of the time resolution versus energy is contained in the average number of photoelectrons emitted from the photocathode (N). This number is distributed around the average value with a spread which is reflected in the pulse height resolution δE , which is proportional to \sqrt{E} . During investigations of the dependency of time resolution on the absorbed energy, it is important to set the width of the energy window ΔE proportional to \sqrt{E} .

The time resolution studies according to the above considerations were carried out in [13], [8] using NE111 scintillators and XP1021 photomultipliers. The results of the experiments are shown in Fig. 10. For the correct choice of window settings, the time resolution is proportional to $1/\sqrt{E}$ and gives excellent agreement with the theoretical predictions given by Gatti and Svelto [1], [2], [3] and Hyman [4], [5]. For comparison, the results for a window ΔE proportional to E are also shown and which have been used by many authors [15], [14]. It is worth underlining that the time resolution versus energy is independent of the energy window when constant fraction timing is used in the experiment.

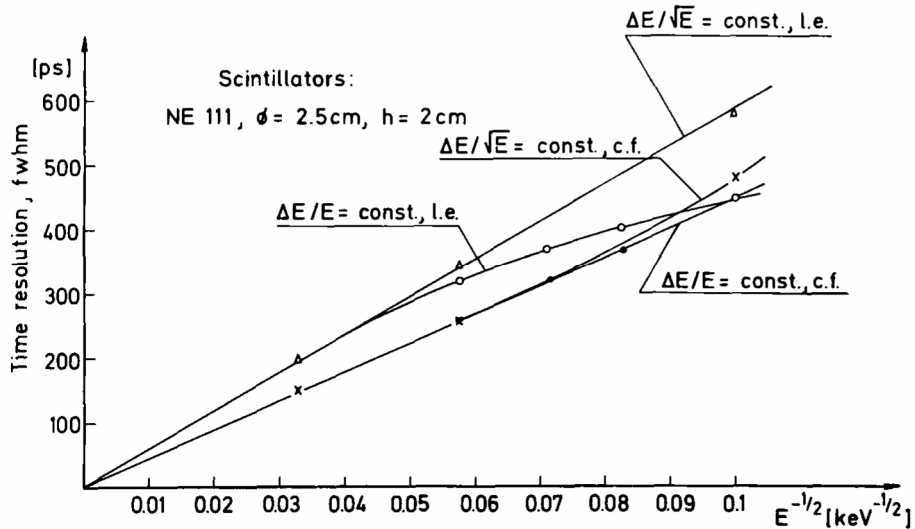


Fig. 10. Time resolution versus energy for two types of pulse height selection for leading edge and constant fraction timing. Reprint from [13].

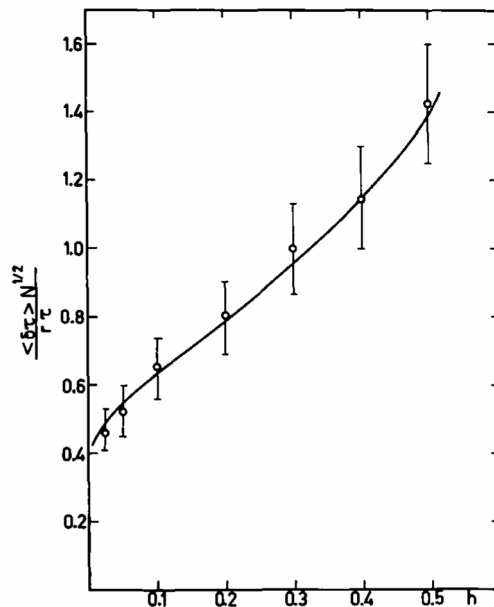


Fig. 11. The best fit (obtained for $\sigma'_{tot} = 0.3$ and $\sigma = 1.2$) of the calculated dependency of the time resolution on the pulse height fraction to the distribution of the experimental points averaged over the measurements at different energies between 50 and 200 keV. Reprint from [8].

A study [8] of the time resolution as a function of the pulse height fraction performed for a 2-mm thick NE111 scintillator coupled to a XP1021 photomultiplier showed a quantitative agreement with the predictions of the modified Hyman theory. Fig. 11 presents the fit of calculated dependency and measurement points of time resolution versus the pulse height fraction. The experimental points were averaged for energies between 50 and 200 keV.

3. References

- [1] E. Gatti and V. Svelto, "Theory of time resolution in scintillation counters," *Nucl. Instr. Meth.*, vol. 4, no. 4, pp. 189–201, 1959.
- [2] E. Gatti and V. Svelto, "Revised theory of time resolution in scintillation counters," *Nucl. Instr. Meth.*, vol. 30, no. 2, pp. 213–223, 1964.
- [3] E. Gatti and V. Svelto, "Review of theories and experiments of resolving time with scintillation counters," *Nucl. Instr. Meth.*, vol. 43, no. 1, pp. 248–268, 1966.
- [4] L. Hyman, R. Schwarcz, and R. Schluter, "Study of high speed photomultiplier systems," *Rev. Sci. Instr.*, vol. 35, no. 3, pp. 393–406, 1964.
- [5] L. Hyman, "Time resolution of photomultiplier systems," *Rev. Sci. Instr.*, vol. 36, no. 2, pp. 193–196, 1965.
- [6] G. Bertolini, V. Mandl, A. Rota, and M. Cocchi, "Time resolution measurements with XP1020 photomultipliers," *Nucl. Instr. Meth.*, vol. 42, no. 1, pp. 109–117, 1966.
- [7] W. McDonald and D. Gedcke, "Time resolution studies on large photomultipliers," *Nucl. Instr. Meth.*, vol. 55, pp. 1–14, 1967.
- [8] J. Bialkowski, Z. Moroz, and M. Moszynski, "Further study of timing properties of scintillation counters," *Nucl. Instr. Meth.*, vol. 117, no. 1, pp. 221–226, 1974.
- [9] Y. Koechlin and A. Raviart, "Analyse par échantillonnage sur photons individuels des liquides fluorescents dans le domaine de la sub-nanoseconde," *Nucl. Instr. Meth.*, vol. 29, no. 1, pp. 45–53, 1964.
- [10] W. Feller, *Probability theory and its application*. John Wiley, New York, 1957.
- [11] R. F. Post and L. I. Schiff, "Statistical limitations on the resolving time of a scintillation counter," *Phys. Rev.*, vol. 80, no. 6, p. 1113, Dec 1950.
- [12] M. El-Wahab and J. Kane, "An analytic treatment for scintillation counter time resolution functions," *Nucl. Instr. Meth.*, vol. 15, no. 1, pp. 15–22, 1962.
- [13] B. Bengtson and M. Moszynski, "Timing properties of scintillation counters," *Nucl. Instr. Meth.*, vol. 81, no. 1, pp. 109–120, 1970.
- [14] G. Present, A. Schwarzschild, I. Spirn, and N. Wotherspoon, "Fast delayed coincidence technique: The XP1020 photomultiplier and limits of resolving times due to scintillator characteristics," *Nucl. Instr. Meth.*, vol. 31, no. 1, pp. 71–76, 1964.
- [15] A. Schwarzschild, "A survey of the latest developments in delayed coincidence measurements," *Nucl. Instr. Meth.*, vol. 21, pp. 1–16, 1963.

7. Experimental methods

1. Number of photoelectrons

The number of photoelectrons per energy unit (N_{phe}) can be determined using the Bertolaccini et al. method [1], [2]. This method is based on a comparison of the two spectra registered in a multi-channel analyzer (MCA).

The first spectrum is a single photoelectron spectrum recorded with a photomultiplier whose photocathode is completely covered from external light sources. In such a configuration the spectrum is a result of only dark counts due to the thermal emission of mostly single photoelectrons from the photocathode. The centroid or peak position (PP_{phe}) of the single photoelectron spectrum defines its mean amplitude at the photomultiplier output.

The second spectrum is obtained with a scintillator coupled to the photomultiplier and represents the energy spectrum of gamma rays from the radioactive source containing a characteristic peak or point (like full energy peak or the Compton edge), whose energy is well known. The characteristic peak position reflecting the chosen energy (PP_E) should be higher than a few hundred keV due to the non-proportional response of scintillators in low-energy ranges. In most cases the photoelectron number is calculated on the basis of the 662 keV full energy peak from the ^{137}Cs gamma source. When energies below 100 keV are used (e.g. due to non-linearity of the photodetector), the final result has to be corrected for the scintillator non-proportionality curve. Examples of a single photoelectron spectrum together with the energy spectrum for ^{137}Cs are presented in Fig. 1.

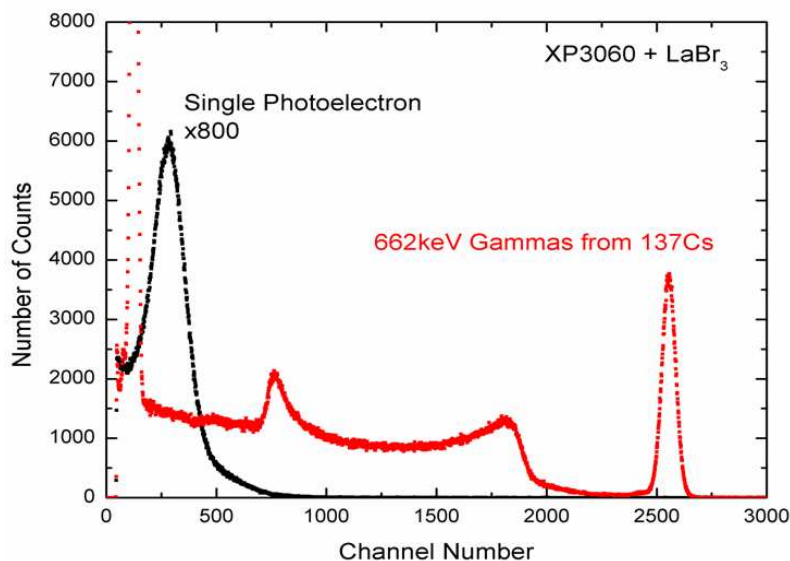


Fig. 1. Examples of spectra (recorder with Photonis XP3060 photomultiplier and LaBr₃ scintillator) used for calculation of the number of photoelectrons.

In the case of measurements of the decay time, instead of the reference scintillation detector a very fast photomultiplier R5320 from Hamamatsu, characterized by a time jitter of 140 ps, was used as a single photon detector. The energy windows were set at the single photoelectron peak in Hamamatsu R5320 and at the 662 keV full energy peak in Photonis XP20D0 coupled with the tested crystal.

The tested crystals were wrapped with Teflon, but only on the sides, leaving one surface opened to the Hamamatsu PMT. Such a configuration assures the detection of single photons from the scintillator, induced by a ^{137}Cs gamma source.

C. Time jitter

The experimental setup used during the time jitter measurements was also a modified version of the slow-fast arrangement and is presented in Fig. 4. This time, the time response of the photomultiplier for single photons generated by the LED light source was measured.

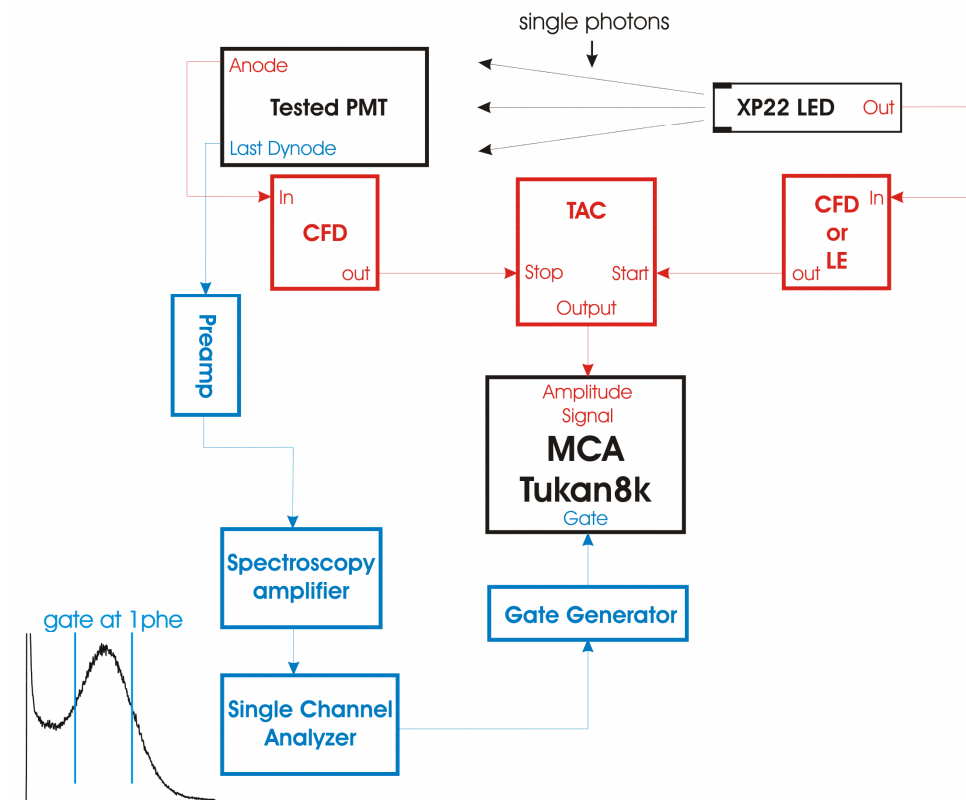


Fig. 4. Slow-fast arrangement for the time jitter measurements using an XP22 light emitting diode.

The time jitter of all the tested photomultipliers was measured using a light pulser based on an XP22 light emitting diode (LED) driven by an avalanche transistor. The FWHM of its light pulse was determined in the past by a microchannel-plate photomultiplier to be equal to 130 ps [5]. The effective wavelengths of light seen by the PMT with the bi-alkali photocathode were centered at 560 nm. The energy window in the PMT track was set at the single photoelectron peak and instead of a reference detector the pulse from the XP22 LED was used to trigger the “start” discriminator.

The time spectra of the single photoelectrons were measured in two modes, when the LED pulser illuminated a full photocathode and a spot 8 mm in diameter in the center of the photocathode. In the second case the entire surface of the PMT input window, except the hole that was 8 mm in diameter in the center, was covered to avoid light.

D. Electronics

The timing measurements were carried out using the fast Leading Edge Discriminator Polon 1520 and the Constant Fraction Discriminator Ortec 935. Time spectra were measured with an Ortec 566 Time-to-Amplitude Converter and recorded by the PC-based multi-channel analyzer Tukan8k [6]. The time calibration of the Time-to-Amplitude Converter was done using a precise Time Calibrator Ortec 462 based on a quartz clock.

3. References

- [1] M. Bertolaccini, S. Cova, and C. Bussolatti, "A technique for absolute measurement of the effective photoelectron per keV yield in scintillation counters," in *Proc. Nuclear Electronics Symp., Société Française des Electroniciens et des Radioelectriciens*, 1968.
- [2] M. Moszynski, M. Kapusta, M. Mayhugh, D. Wolski, and S. Flyckt, "Absolute light output of scintillators," *IEEE Trans. Nucl. Sci.*, vol. 44, no. 3, pp. 1052–1061, 1997.
- [3] L. Bollinger and G. Thomas, "Measurement of the time dependence of scintillation intensity by a delayed-coincidence method," *Rev. Sci. Instr.*, vol. 32, no. 9, pp. 1044–1050, 1961.
- [4] M. Moszynski and B. Bengtson, "Light pulse shapes from plastic scintillators," *Nucl. Instr. Meth.*, vol. 142, no. 3, pp. 417–434, 1977.
- [5] M. Moszynski, J. Vacher, and R. Odru, "Application of the HR 400 microchannel plate photomultiplier to study the light pulse shape from fast and slow scintillators by means of the single photon method," *Nucl. Instr. Meth.*, vol. 204, no. 1, pp. 141–147, 1982.
- [6] Z. Guzik, S. Borsuk, K. Traczyk, and M. Plominski, "TUKAN - an 8K pulse height analyzer and multi-channel scaler with a PCI or a USB interface," *IEEE Trans. Nucl. Sci.*, vol. 53, no. 1, pp. 231–235, 2006.

8. Study of timing with LSO on XP20D0

1. Introduction

A. Motivation

The first Time-of-Flight PET scanners, based on CsF and BaF₂ scintillators, were built about 25 years ago [1], [2], [3]. Nevertheless, due to low stopping power of these crystals for 511 keV annihilation quanta, their performance was not as good as a classic PET scanner with BGO crystals. It is obvious that a good scintillator for TOF-PET should be characterized not only by a fast decay constant but must also be sufficiently dense to ensure high stopping power. Scintillators such as LaBr₃ and LSO are presently one of the strongest candidates for the TOF PET detectors. However, significantly lower stopping power of LaBr₃ compared to LSO suggest study of the fast timing with the latter one as more practical solution. This is particularly supported by the recent studies of performance of the Photonis XP20D0 photomultiplier, carried out with LSO and LaBr₃ crystals, which showed a comparable time resolution measured with both crystals [4]. As it will be shown in the next section (following [5]), very good time resolution recorded with a 4x4x20 mm³ LSO crystal coupled to the XP20D0 PMT confirms that an LSO crystal (7.4 g/cm³) is the best candidate for the future TOF-PET [5], [6].

A further improvement of the time resolution, due to the common light readout by a cluster of photomultipliers in a block detector, was proposed by Kuhn et al [7]. They measured time resolution of 313 ps for two block detectors based on 4x4x30 mm³ LaBr₃ crystals [8] and time resolution of 295 ps using a sum of the signals from the cluster of 7 PMTs [7]. These results triggered further studies (presented in the second part of this chapter) of the time resolution with the LSO crystals; in particular, with a light readout by means of several photomultipliers.

B. Aim of the study

In the first part of this chapter, a comparison of timing with Hamamatsu R5320 and Photonis XP20D0 PMTs is shown in relation to the classic fast timing photomultiplier XP2020, following the data presented in [5].

In order to improve the performance of positron emission tomography scanners, precise optimization of the detectors used is required, in particular, their timing capabilities. Such optimization of the time resolution with an LSO crystal coupled to the XP20D0 PMT using a leading-edge fast discriminator (LE) and a constant fraction discriminator (CFD) is presented in the second section. The results of the leading-edge time resolution are compared with the predictions of the Hyman theory of timing (presented in chapter 6) .

In the third part, the tests of the time resolution with the system realizing the light readout by two PMTs is presented. During the reported measurements a finger-like 4x4x20 mm³ LSO crystal was placed in the center of each PMT and in the middle of the system, between the PMTs and, in each case, the light was collected via a light guide to both PMTs.

2. Prospects for Time-of-Flight PET with LSO scintillators

A. Photomultipliers and scintillators

In Table I the properties of the photomultipliers studied in [5] are collected. The XP20Y0/DA is the prototype of the XP20D0, studied in [9]. In comparison to the classic XP2020, in XP20D0 the number of dynodes was reduced to 8, to avoid an influence of the space charge effect on the time resolution [10] and the screening grid was applied at the anode. Moreover the XP20D0 PMTs possess very high sensitivity of the photocathode. The blue sensitivity of $13.7 \mu\text{A}/\text{lmF}$ of the PMT No. 2026 corresponds to a quantum efficiency of about 34% at 400 nm. The R5320 photomultiplier was tested in its original assembly H6610DY, delivered by Hamamatsu. Time jitter, listed in Table I, was measured for all the PMTs using a light pulser based on an XP22 light emitting diode [11]. A very low time jitter of 140 ± 7 ps at FWHM for the R5320, comparable to that reported in [6], is more than three times better than that of XP20D0.

TABLE I
THE MAIN PARAMETERS OF THE TESTED PHOTOMULTIPLIERS

Type	XP2020 No. 25377	XP20Y0/DA No. 021	XP20D0 No. 2025	XP20D0 No. 2026	R5320 No. BA0091
Diameter	51 mm				25 mm
Photocathode	Bialkali				
Window	borosilicate glass				Quartz
Blue sensitivity [$\mu\text{A}/\text{lm F}$]	10.4	12.2	13.2	13.7	8.9
White sensitivity [$\mu\text{A}/\text{lm}$]	70.5	110.2	150	150	81.3
Time jitter [ps]	500±25	660±30	610±30	520±25	140±7
Screening grid	No	Yes	Yes	Yes	No
No of dynodes	12	8	8	8	10

All the measurements were done with two LSO crystals. First one, with the dimension of $10 \times 10 \times 5 \text{ mm}^3$, was used in the comparative study of photomultipliers. The second, finger-like crystal, with the size of $4 \times 4 \times 20 \text{ mm}^3$, was used in the feasibility study of a TOF PET detector. The mechanically polished LSO crystals were wrapped with several layers of white Teflon tape.

B. Time resolution with $10 \times 10 \times 5 \text{ mm}^3$ LSO

In all the studies the slow-fast arrangement was used with the Ortec 935 Constant Fraction Discriminator adjusted separately for the best timing for each combination of the scintillator and photomultiplier.

First, comparison of timing with Hamamatsu R5320, and Photonis XP2020 and XP20D0 PMTs was performed using a $10 \times 10 \times 5 \text{ mm}^3$ LSO crystal. This selected crystal allowed

determining of the limits of the time resolution achievable with LSO when scintillation light is not affected by the light transport and attenuation inside the crystal. In Table II, the measured numbers of photoelectrons with different PMTs are collected.

TABLE II
PHOTOELECTRON NUMBERS MEASURED WITH LSO CRYSTAL COUPLED
TO THE TESTED PMTs

PMT	Blue sensitivity [$\mu\text{A}/\text{lm F}$]	Phe Number [phe/MeV]	Phe number/ blue sensitivity [phe/MeV / $\mu\text{A}/\text{lm F}$]
XP2020			
No. 25377	10.4	6300 \pm 200	606 \pm 20
XP20D0			
No. 021	12.2	6900 \pm 200	565 \pm 20
No. 2025	13.2	7700 \pm 200	583 \pm 20
No. 2026	13.7	8100 \pm 200	591 \pm 20
R5320			
No.BA0091	8.9	5400 \pm 200	607 \pm 20

It is worth noting the superior numbers of photoelectrons measured with the XP20D0 PMTs due to enhanced blue sensitivity of the photocathodes. In the case of PMT No. 2026, the photoelectron number is up to 50% larger than that of XP2020 and R5320 equipped with the standard bialkali photocathodes. The last column presents the normalized photoelectron number to the blue sensitivity. It shows that the number of photoelectrons follows well the blue sensitivity of the tested PMTs.

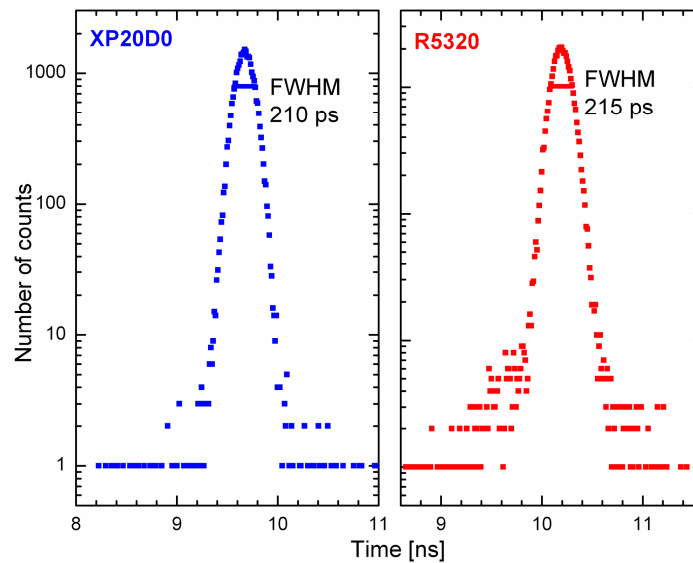


Fig. 1. Time spectra obtained with $10 \times 10 \times 5 \text{ mm}^3$ LSO crystal coupled to Photonis XP20D0 and Hamamatsu R5320 PMTs, as measured for the 511 keV full energy peak in relation to the small BaF_2 crystal.

Fig. 1 presents comparison of time spectra measured with the Photonis XP20D0, No 2026 and the Hamamatsu R5320. An excellent and comparable time resolution was recorded with both PMTs, close to 200 ps. The results of the measurements with all the tested PMTs and the analysis of the time resolution with respect to the number of photoelectrons measured at 511 keV are collected in Table III.

TABLE III
TIME RESOLUTION MEASURED WITH LSO CRYSTAL COUPLED
TO THE TESTED PMTs

PMT	Time resolution, δt [ps]		Phe number ^{b)} [phe]	$\frac{\delta t \sqrt{N}}{[\text{ps} \sqrt{\text{phe}}]} \times 10^3$
	Measured	Tested detector ^{a)}		
XP2020				
No. 25377	257±5	222±6	3200±100	12.6±0.4
XP20D0				
No. 021	225±4	185±5	3500±100	10.9±0.4
No. 2025	214±4	172±5	3930±100	10.8±0.4
No. 2026	210±4	166±5	4140±100	10.6±0.4
R5320				
No.BA0091	215±5	173±5	2760±100	9.1±0.4

a) corrected for the contribution of the BaF₂ reference detector of 128 ps.

b) photoelectron number for 511 keV

The measured time resolution, presented in the second column, is corrected for the contribution of the reference BaF₂ detector (128 ps) and shown in the third column. In the fourth column the number of photoelectrons corresponding to the 511 keV peak is listed. The last column shows the time resolution of the tested detectors normalized to the number of photoelectrons.

The measured time resolution with the XP20D0 PMTs is comparable to that of R5320 and significantly better than that recorded with the XP2020. It reflects advantages of XP20D0 associated with the screening grid at the anode and high quantum efficiency. In the case of R5320, the excellent time resolution is due to a very low time jitter.

The time resolution normalized to the number of photoelectrons, is better for XP20D0 than for XP2020 reflecting an improvement due to the screening grid at the anode. An improvement of 1.17 is observed, comparable to that reported in [9]. The time resolution normalized to the number of photoelectrons is superior in the case of the R5320 PMT. It is a consequence of a very low time jitter of this tube. However, the improvement by a factor of 1.18 over XP20D0 and even a factor of 1.36 over XP2020 seems to be rather low compared to more than three times lower time jitter.

C. Time resolution with 4x4x20 mm³ LSO

In the second part of the experiments, the 4x4x20 mm³ LSO crystal was tested coupled to the XP20D0, no. 2026. First, it was coupled in the center of the PMT. In this case the number of photoelectrons was reduced by about 25%, to 5900 ± 200 phe/MeV, because of the reduced light collection in the long and narrow crystal. The measured time resolution of 234 ± 5 ps

corresponds to the time resolution of 196 ± 5 ps for the single LSO detector, which follows well the reduced number of photoelectrons.

In order to better approximate a real performance of the future block detector, a further study was carried out with an 11 mm thick and 52 mm in diameter Lucite disc light diffuser coupled optically to the PMT (see Fig. 2). The edge of the disc was covered with black tape to avoid light reflections and to approximate the block detector geometry where light spreads out to the neighboring PMTs.

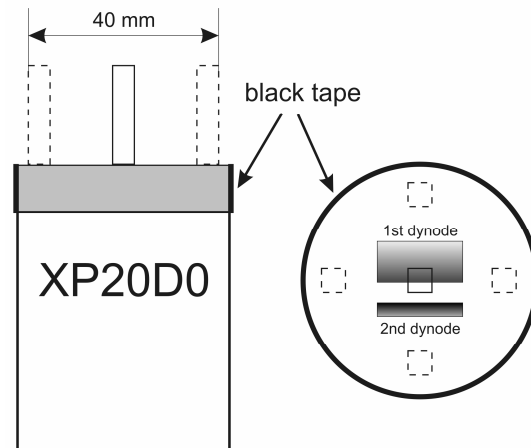


Fig. 2. Position of the light diffuser at the photocathode of the XP20D0 PMT and positions of the LSO crystals tested in the experiment.

The measurements were carried out with the LSO crystal coupled in the center, and then at the edges of the PMT, parallel and perpendicular to the dynode plane (see Fig. 2). The photoelectron number measured for the LSO crystal coupled in the center was reduced further to 4400 ± 150 phe/MeV. It showed that about 25% of the light was spread out, potentially to the neighboring PMTs.

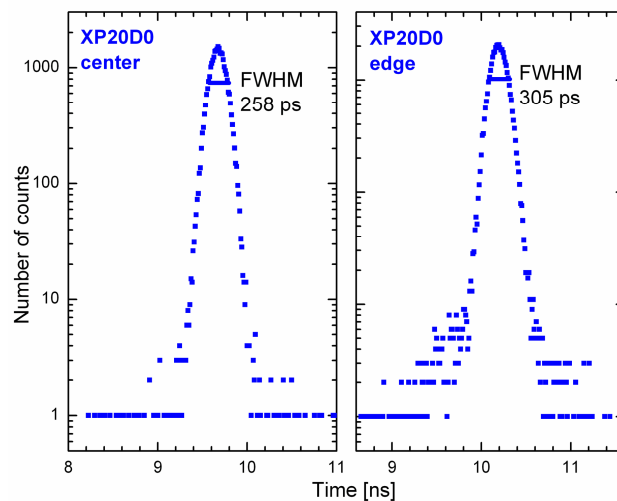


Fig.3. Time spectra measured with $4 \times 4 \times 20$ mm³ LSO coupled in the center and at the edge of the light diffuser.

The time resolution measured with the crystal located in the center of the PMT was equal to 258 ± 6 ps. The time resolution at the edges of the PMT, was deteriorated to 305 ± 7 ps, in average. Timing spectra measured at both crystal positions are presented in Fig. 3. The time resolution of the single LSO detector was equal to 234 ± 5 ps and 277 ± 6 ps, respectively. Again, in both positions of the LSO crystal, the time resolution followed the number of photoelectrons. The results of the measurements at all the positions of the LSO crystal and the analysis of the time resolution with respect to the number of photoelectrons measured at 511 keV are collected in Table IV.

TABLE IV
TIME RESOLUTION MEASURED AT DIFFERENT POSITIONS ON THE PHOTOCATHODE

Position of LSO	Time resolution, δt [ps]		Phe number ^{b)} [phe]	$\frac{\delta t \sqrt{N}}{[\text{ps} \sqrt{\text{phe}}]} \times 10^3$
	Measured	Tested detector ^{a)}		
No light diffuser,				
Center	234±5	196±5	3015±100	10.8±0.4
With light diffuser:				
Center	258±6	224±6	2250±70	10.6±0.4
PIN 17-18	300±6	272±6	1610±60	10.9±0.4
PIN 7-8	314±6	287±6	1410±50	10.8±0.4
PIN 13-14	305±6	277±6	1530±50	10.8±0.4
PIN 3-4	300±6	271±6	1620±60	10.9±0.4

a) corrected for the contribution of the BaF₂ reference detector of 128 ps.

b) photoelectron number for 511 keV

The same values of the normalized time resolution shown in the fifth column of the Table III and IV confirm that the time resolution is not affected by a possible local deterioration of the PMT time jitter and follows the number of photoelectrons. It is observed also for “the worst” position on the photocathode, behind the first dynode, being the most critical part of the photocathode with the lowest photoelectron collection efficiency in the linear-focused PMTs. Moreover, the results show that in the very well polished finger-like crystal, the main component of the light transport is due to the total internal reflection, weakly increasing the total time jitter of the detector [12], [13].

D. Conclusion

The performed measurements strongly suggests that the time-of-flight PET, based on LSO crystals, is a realistic proposition for further studies and development. This conclusion is based on the excellent time resolution measured with the finger-like 4x4x20 mm³ LSO crystal coupled to XP20D0 PMTs and a possible further improvement due to the light readout by the cluster of PMTs in the block detector, according to Kuhn et al [8].

3. A Further Study of Timing with LSO on XP20D0

The aim of this part was to solve the problem of optimization of the time resolution with

LSO crystal coupled to the XP20D0 PMT. Such optimization was made using a leading-edge fast discriminator (LE) and a constant fraction discriminator (CFD) and the results of the leading-edge timing were compared with the Hyman theory of timing [14].

A. Scintillators

The timing measurements were done with two LSO crystals. The first one, with dimensions of $10 \times 10 \times 5 \text{ mm}^3$, coupled to a single XP20D0, was used for the optimization of timing with CFD and LE. The second, finger-like crystal, $4 \times 4 \times 20 \text{ mm}^3$ in size, was used for measurements of timing with two PMTs coupled to a common light guide. The mechanically polished LSO crystals were wrapped with several layers of white Teflon tape.

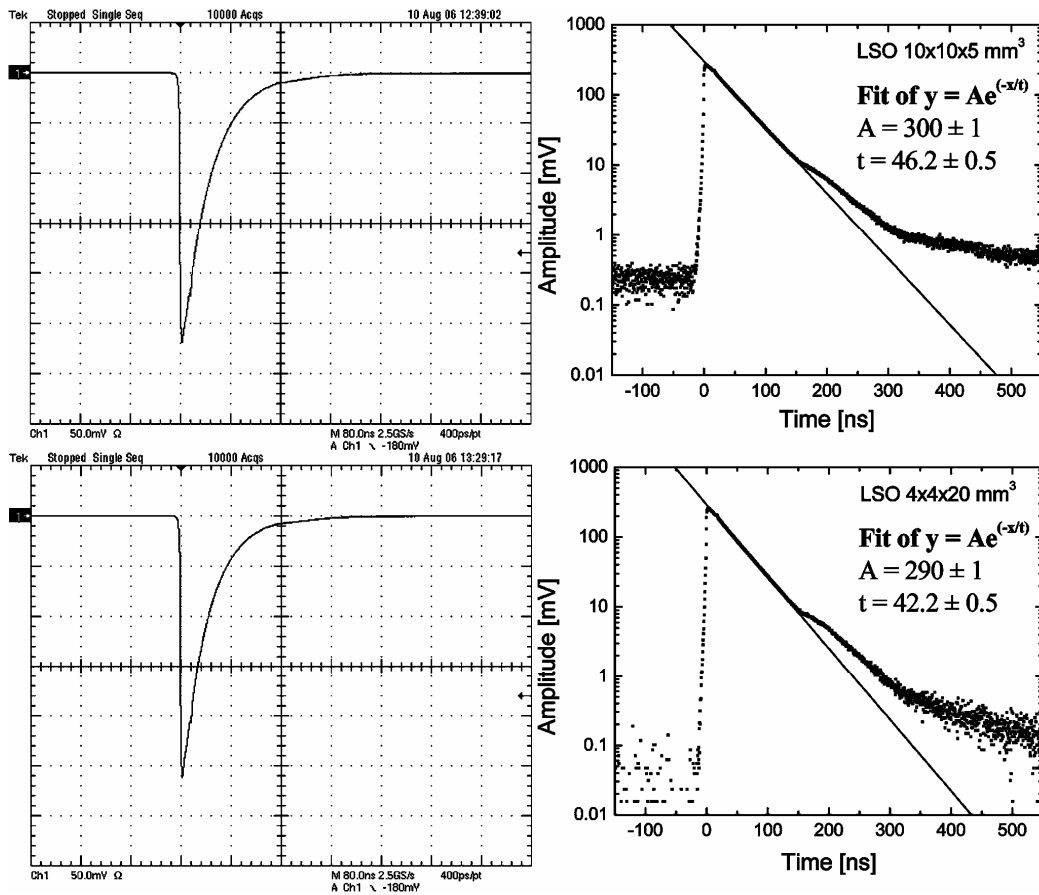


Fig. 4. Screen captures of the average anode pulses for LSO $10 \times 10 \times 5 \text{ mm}^3$ (top one) and LSO $4 \times 4 \times 20 \text{ mm}^3$ (bottom one). The result of fitting of a single exponential decay for each crystal is also presented. The “step” which occurred in both right side spectra is caused by the afterpulses in the PMT.

In order to define the light pulse shape properties of the crystals, both scintillators were coupled to the Hamamatsu R5320 PMT, which is characterized by a very fast time response of about 800 ps at FWHM (Full Width at Half Maximum) and 700 ps rise time of the single photoelectron anode pulse [5], [15]. The scintillators were irradiated by a ^{22}Na gamma source and an average anode signal of 10 000 acquisitions was recorded by a Tektronix Digital Oscilloscope type TDS5034B. Events taken into account have been chosen by a triggering level set to about 2/3 of the anode pulse. Screen captures of the pulses and the results of fitting of a single exponential decay are presented in Fig. 4. The main properties of the crystals are

presented in Table V. The observed difference of the decay time between the two crystals is characteristic for LSO. The excitation and emission process in the LSO crystals leads to a variation in the decay time between 36 ns and 48 ns [16] [17].

TABLE V
THE MAIN PARAMETERS OF THE SCINTILLATORS USED

Scintillator	Size [mm ³]	Manufacturer	λ_{pk} [nm]	Measured decay time [ns]
LSO:Ce	10x10x5	CTI	420	46.2 ± 0.5
	4x4x20			42.2 ± 0.5

B. Photomultipliers

The studies were carried out on two XP20D0 tubes representing the commercial Photonis production [18], [4]. In Table VI, the main characteristics of the PMTs are presented. Note that this type of a PMT is optimized for timing measurements due to the application of a screening grid at the anode [9] and high blue sensitivity of the photocathode. Also, the number of dynodes was reduced to 8, which minimizes the influence of the space charge effect on time resolution [10]. The number of photoelectrons per energy unit (phe/MeV) was measured using Bertolaccini method [19] and ¹³⁷Cs gamma source.

TABLE VI
THE MAIN PARAMETERS OF THE PHOTOMULTIPLIERS USED

Type	XP20D0	
	SN2083	SN2087
Photocathode	Bi-alkali	
Window	Borosilicate glass	
Blue sensitivity [$\mu\text{A}/\text{lmF}$] ^{a)}	12.65	12.75
No of dynodes	8	
Screening grid	Yes	
Gain/Voltage [V]	2.4×10 ⁵ /978	2.4×10 ⁵ /1008
Phe/MeV for LSO 10x10x5 mm ³	6600 ± 200	7000 ± 200
Phe/MeV for LSO 4x4x20 mm ³	5200 ± 200	5000 ± 200

a) where F stands for filtered for blue sensitivity.

The time jitter of both tested photomultipliers was measured using a light pulser based on an XP22 light emitting diode (LED) (see chapter 7) [11]. Fig. 5 presents the time spectra of the single photoelectrons measured when the LED pulser illuminated the full photocathode and a spot of 8 mm in diameter in the central part of the photocathode. The results of the measurements, including FWHM and FWTM (Full Width at Tenth Maximum) are collected in Table VII.

Comparable time jitter was obtained for the central part and the whole photocathode, what

confirms an excellent uniformity of the photoelectron collection from the external regions of the photocathode. The observed small shoulders at the late slopes in the case of the time spectra for the whole photocathode reflect a contribution of photoelectrons from the region “behind” the first dynode. These photoelectrons are always the poorer focalized ones.

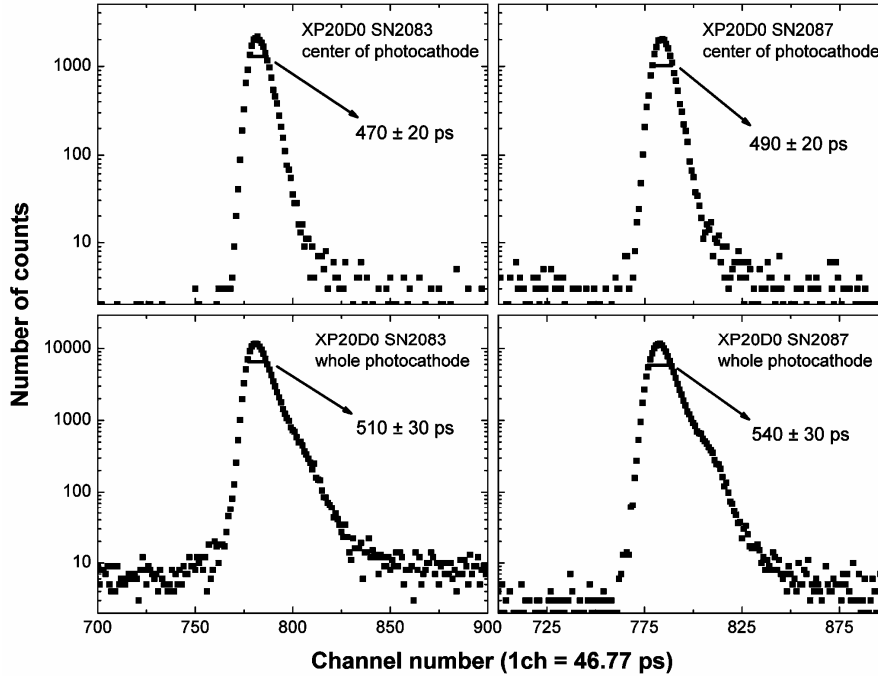


Fig. 5. Time spectra of the single photoelectrons measured for the XP20D0 SN2083 and SN2087. The light pulse from the LED pulser with FWHM of 130 ps illuminated the whole photocathode and its central part.

TABLE VII
THE TIME JITTER OF THE PHOTOMULTIPLIERS USED

PMT	Center of the photocathode		Whole photocathode	
	FWHM [ps]	FWTM [ps]	FWHM [ps]	FWTM [ps]
XP20D0				
SN2083	470 ± 20	920 ± 50	510 ± 30	1090 ± 50
SN2087	490 ± 20	950 ± 50	540 ± 30	1170 ± 60

C. Optimization of the time resolution

The optimization of the electronics for the best time resolution was a starting point for all later measurements of the time resolution with a sum of the signals from two PMTs. All the measurements of this part were performed with a single $10 \times 10 \times 5 \text{ mm}^3$ LSO crystal coupled to the single XP20D0 PMT, SN2026 with blue sensitivity equal to $13.7 \mu\text{A/lmF}$. The size of the selected scintillator allowed the determination of the limit of achievable time resolution not affected by light transport and attenuation in the crystal.

The first measurements of timing were made using a constant fraction discriminator with

various settings of a threshold and shaping delay. The results of these tests are presented in Fig. 6. Based on the behavior of the time resolution with the shaping delay, the constant fraction discriminator was replaced by a fast leading-edge discriminator. The results of the time resolution measurements with different thresholds set on LE are presented in Fig. 7. Analysis of the plots shows that, for the LSO crystal, the lowest possible threshold set on the LE leads to the best timing results, which are even better than that measured with the CFD.

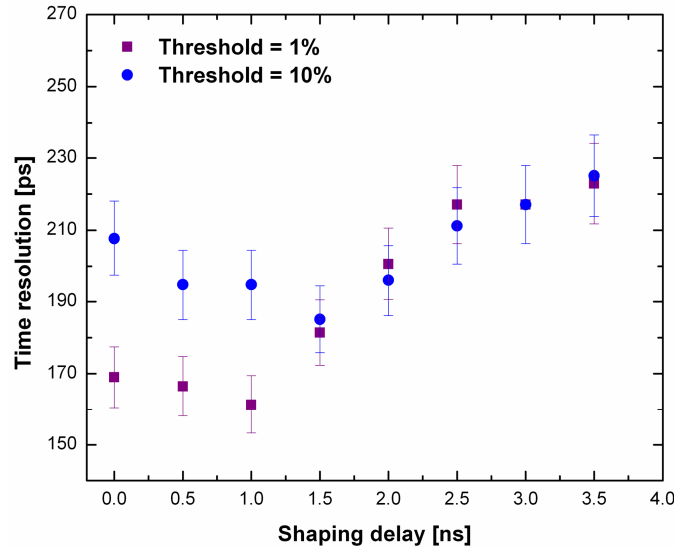


Fig. 6. Time resolution dependence due to a shaping delay of a constant fraction discriminator. Values on the plots are corrected for the contribution of the BaF₂ reference detector.

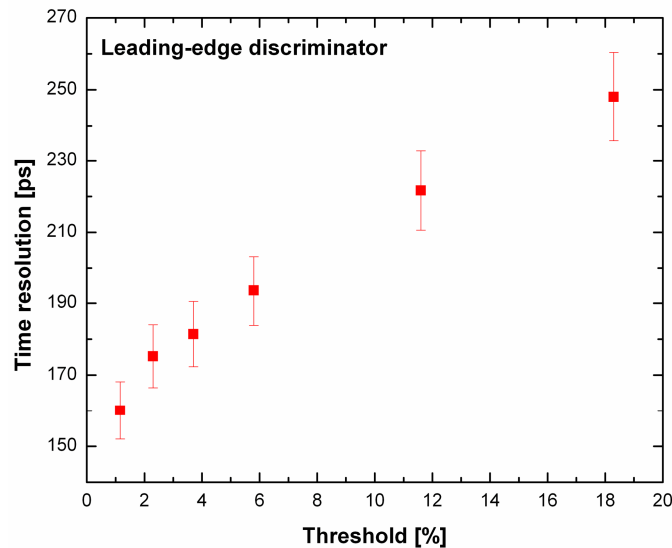


Fig. 7. Time resolution dependence due to threshold set on a fast leading-edge discriminator. Values on the plots are corrected for the contribution of the BaF₂ reference detector.

After establishing the best conditions for the timing measurements, both LSO crystals were tested with XP20D0, SN2083 (PMT 1) and SN2087 (PMT 2). The results of the time resolution measured with both PMTs are collected in Table VIII. The time resolution at FWHM, presented in the second column, corresponds to the mean value of at least four

independent measurements. The corrected values for the contribution of the reference BaF₂ detector are collected in the third column. In the fourth column, the photoelectron numbers corresponding to the energy window are listed. Since, the time resolution is in general inversely proportional to the square root of the number of photoelectrons it is hard to compare results obtained with different detectors characterized by different quantum efficiencies of the PMTs and different parameters of the scintillators. Normalization of the measured time resolution by multiplying it by the square root of the number of photoelectrons for a given energy leads to the value independent on the detector differences. Such normalized values are presented in the last column of Table VIII.

TABLE VIII
THE TIME RESOLUTION MEASURED WITH LSO CRYSTALS COUPLED DIRECTLY TO THE PMT

PMT	Time resolution at FWHM, Δt [ps]		Phe number for 511 keV [phe]	$\frac{\Delta t \sqrt{N}}{[\text{ps} \sqrt{\text{phe}}]} \times 10^3$
	Measured	Corrected ^{a)}		
LSO 10x10x5 mm ³				
PMT 1	215 ± 6	172 ± 9	3200 ± 100	9.7 ± 0.5
PMT 2	212 ± 6	170 ± 9	3600 ± 100	10.2 ± 0.5
LSO 4x4x20 mm ³				
PMT 1	242 ± 7	206 ± 9	2600 ± 100	10.5 ± 0.5
PMT 2	240 ± 7	204 ± 9	2500 ± 100	10.2 ± 0.5

a) corrected for the contribution of the BaF₂ reference detector of 128±4 ps

D. Comparison to the Hyman theory of timing

The measured time resolution using the LE discriminator is compared below with the prediction of the Hyman theory of timing [14]. The details of the theory were presented in chapter 6. Briefly, Hyman has presented a prediction of the time resolution for a given system as a series of plots for different values of parameters, characterizing the scintillation detector. These parameters are the number of photoelectrons (N), the decay constant of the light pulse (τ), the gain dispersion of the electron multiplier (r), the time jitter of the PMT and its response for the single photoelectron, represented by their standard deviations, σ' and σ , respectively. The standard deviation of the time distribution (δt) is normalized in the theory in the following way [14]:

$$\frac{\delta t \cdot \sqrt{N}}{\tau \cdot r} = H(h) \quad (1)$$

where h is the triggering fraction of the anode pulse.

Fig. 8 presents the normalized time resolution versus pulse height fraction used to trigger the fast discriminator, calculated by Hyman [14] for the set of parameters fitted well to those of the LSO crystal coupled to the XP20D0 PMT. The plots were calculated for $\sigma/\tau = 1/48$ which corresponds well to $\sigma \approx 1$ ns for the single photoelectron response of the XP20D0 and

$\tau = 48$ ns, which is close to the decay time constant of LSO. According to [14], the plotted curve for $\sigma'/\sigma = 1/2$ is practically not improved further for the lower time jitter of the XP20D0.

The whole curve in Fig. 8 cannot be compared to that presented in Fig. 7, since the calculations were done by Hyman for a so-called integral response, corresponding to the triggering of the fast discriminator by the integrated anode pulse. In contrast, the experiment was done for a so-called straight response, when the current pulse of the PMT triggered the discriminator. However, according to Hyman [14] the best time resolution is independent of the type of response. Thus, one can use the best time resolution predicted by the curve in Fig. 8 for a direct comparison to the experimental tests.

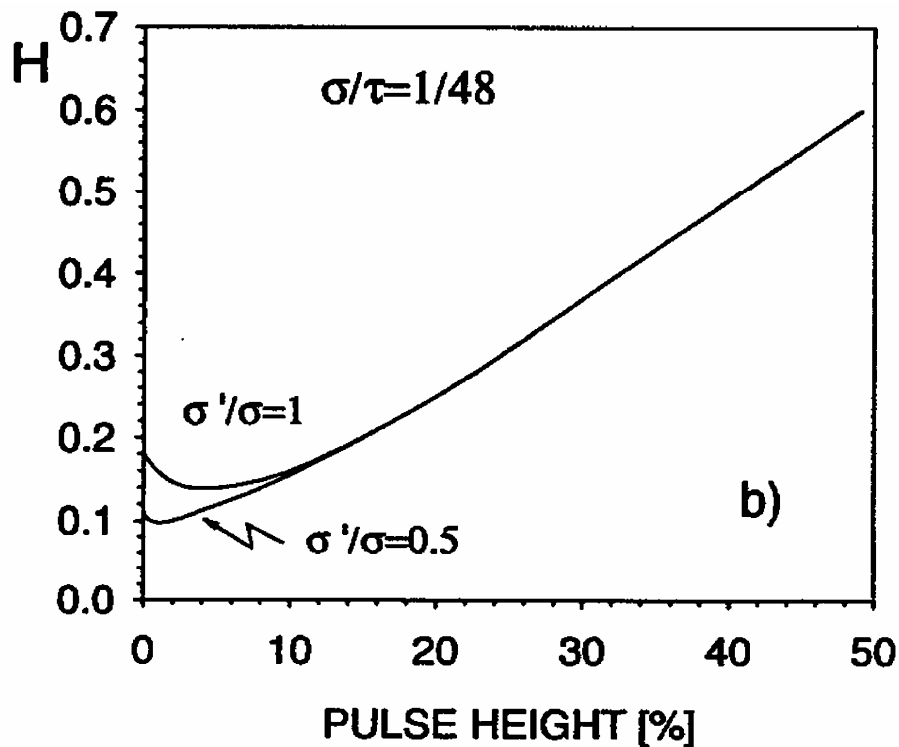


Fig. 8. The normalized time resolution, according to eq. (1), versus the triggering fraction of the PMT anode pulse, following [14].

Table IX summarizes results of the calculation of the H parameter based on the experimental data. In column 2, the decay time constants of the tested crystals, according to Table V, are given. Columns 3 and 4 follow the data of Table VIII, with the time resolution in column 4 expressed by the standard deviation. The last column presents the H parameter, which can be compared to the best one plotted in Fig 8, following the Hyman predictions. An r value of 1.05 was used, which is typical for the XP2020 family of the PMTs.

Excellent agreement is seen between the experiment and the Hyman theory predictions. Moreover, it reflects the fact that, for LSO, the time resolution is weakly affected by the time jitter of the PMT and it is mainly controlled by the decay time constant of the light pulse and the number of photoelectrons.

TABLE IX
CALCULATION OF THE BEST H PARAMETER BASED ON THE EXPERIMENTS

PMT	Measured decay time, τ [ns]	Phe number for 511 keV, N [phe]	Time resolution of the tested detector, δt [ps]	H ^{a)}
LSO 10x10x5 mm ³				
PMT 1	46.2 ± 0.1	3200 ± 100	73 ± 4	0.085 ± 0.005
PMT 2		3600 ± 100	72 ± 4	0.089 ± 0.005
LSO 4x4x20 mm ³				
PMT1	42.2 ± 0.1	2600 ± 100	88 ± 4	0.101 ± 0.005
PMT2		2500 ± 100	87 ± 4	0.098 ± 0.005

a) the $r = 1.05$ was used, typical for the XP2020 family of PMTs.

4. Time resolution of the two-PMTs system

A. Time resolution

In this section, the tests of timing with the system realizing the light readout by two PMTs are presented. The experimental arrangement of the system is shown in Fig. 9. The measurements were made with a finger-like 4x4x20 mm³ LSO crystal placed in the center of each PMT and in the middle of the system, between the PMTs. In each case the scintillation light was collected via 1 cm thick light guide to the both PMTs. All elements of the system were coupled using silicon grease.

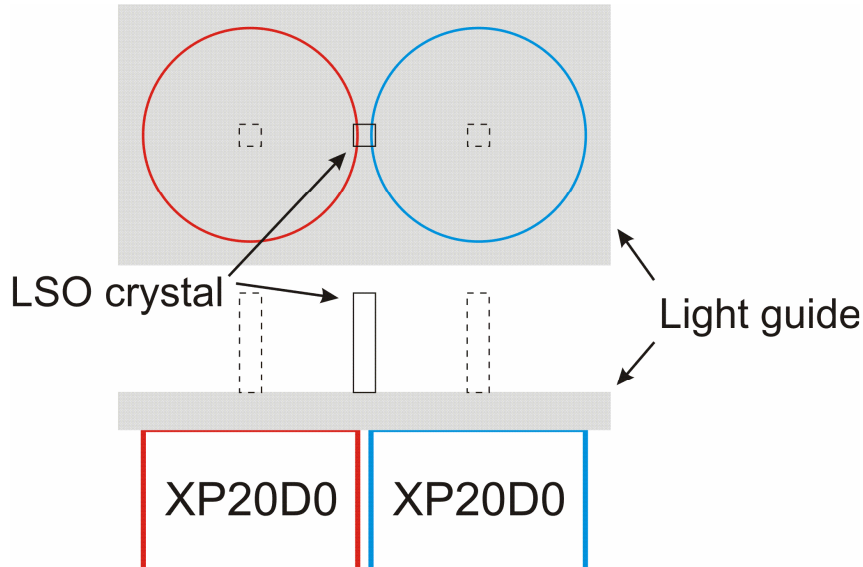


Fig. 9. Positions of the LSO crystal and experimental arrangement of the light guide and PMTs.

For all the three positions of the crystal, the time resolution was measured in two modes. In the first mode, the anode signal was gathered separately giving individual time spectra of each PMT. In the second mode, the output signal was a sum of signals from both PMTs. In order to

achieve a sum-signal, two cables with anode signals from each PMT were simply connected into one cable. To avoid reflections in the signal, short cables of about 10 cm were used for anode signals before connecting them into one cable. The impedance of the PMT base was equal to 1 M Ω .

Fig. 10 shows sample spectra for all the acquisition modes for the LSO placed in the middle of the two PMTs, whereas the results of the time resolution measurements for all the crystal positions are collected in Table X.

In the case of positioning of the crystal in the middle of each PMT, the time resolution is completely independent of the additional signal from the second PMT. This is not surprising because the amount of light collected by the second tube is fully negligible in comparison to the light collected by the primary PMT.

A large improvement in timing for the sum of signals has been achieved in the case when the scintillator was placed in the middle of the light guide, between the PMTs. This is a consequence of improved light collection by the two PMTs, which gives 1000 photoelectrons for 511 keV in comparison to only about 500 photoelectrons measured with PMT 1 and PMT 2 separately. It leads to an improvement of the time resolution from about 490 ps to 350 ps. The time resolution normalized to the number of photoelectrons gives almost identical values and that is another proof that the obtained timing results are mainly affected by the number of photoelectrons collected by the PMTs.

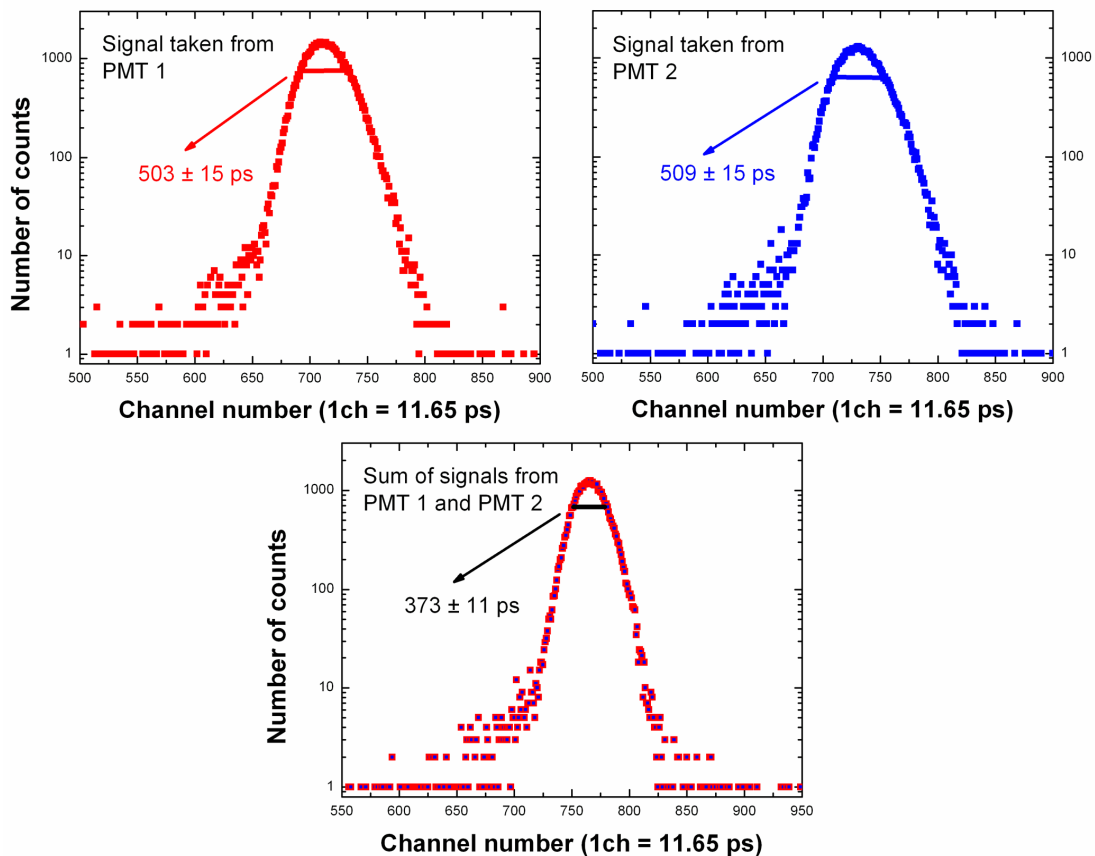


Fig. 10. Time spectra for LSO placed in the center of the light guide, between PMTs. Values on the plots are uncorrected for the contribution of the reference detector.

TABLE X
THE TIME RESOLUTION FOR THREE POSITIONS OF THE LSO CRYSTAL

Signal taken from	Time resolution at FWHM, δt [ps]		Phe number for 511 keV [phe]	$\delta t\sqrt{N}$ [ps $\sqrt{\text{phe}}$] $\times 10^3$
	Measured	Corrected ^{a)}		
LSO crystal in the center of the PMT 1				
PMT 1	271 ± 8	239 ± 9	1600 ± 100	9.5 ± 0.5
PMT 1 + PMT 2	276 ± 8	245 ± 10	1600 ± 100	9.8 ± 0.5
LSO crystal in the center of the PMT 2				
PMT 2	269 ± 8	237 ± 9	1700 ± 100	9.8 ± 0.5
PMT 1 + PMT 2	269 ± 8	237 ± 9	1700 ± 100	9.8 ± 0.5
LSO crystal between PMT 1 and PMT 2				
PMT 1	503 ± 15	486 ± 16	500 ± 50	10.9 ± 0.6
PMT 2	509 ± 15	493 ± 16	500 ± 50	11.0 ± 0.7
PMT 1 + PMT 2	373 ± 11	350 ± 12	1000 ± 70	11.1 ± 0.5

a) corrected for the contribution of the BaF₂ reference detector of 128 ± 4 ps

During the measurements, different settings of the experimental system were checked to minimize the influence of the differences between the properties of each PMT, such as gain or time jitter. The details are presented below.

B. Pulse arrival time effect

During the preliminary measurements, it seemed to be clear that an identical gain of both PMTs should give the best results when the output pulses are summed. To ensure this condition, single photoelectron spectra of both PMTs were compared and the voltage of the PMT with the higher gain was lowered.

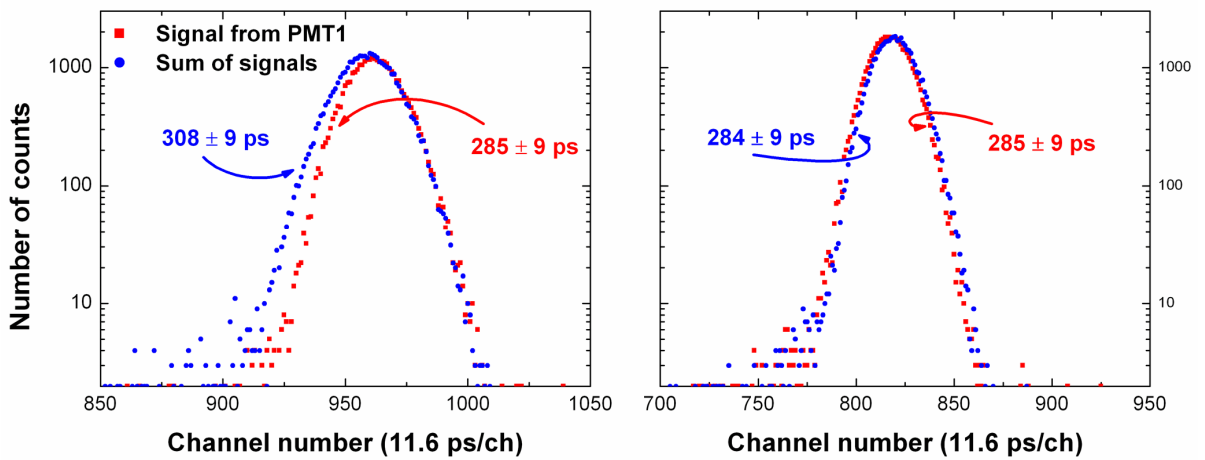


Fig. 11. Time spectra for LSO placed in the center of the PMT 1 for different (left) and identical (right) voltages.

Unfortunately, for the timing measurements, in the case of the sum of signals from two PMTs and for an LSO crystal placed in the center of the PMT with the lower voltage, a large deterioration on the fast side of the timing spectrum occurred (see Fig. 11 - left). Similar change of the time resolution did not appear when the LSO scintillator was placed in the center of the second PMT, with the higher voltage. This effect is associated with the different voltages on both PMTs. Such a situation leads to different transit times of the electrons inside the tubes and, in consequence, to different times of an output anode pulse appearing. In the case of an LSO crystal placed on the slower PMT, a sum of the slow main signal and the faster signal from the second PMT, gives a sum-pulse with a slower rise time. This slower rise time deteriorates the time resolution and produces broadening of the time spectrum. For the crystal placed on the faster PMT, the time resolution deterioration is not observed because the slower signal is “inside” the fast, main signal. It has to be noticed that, in both cases, the amplitude of the main signal is much higher than the second one. The prepulse effect disappears when both PMTs have identical voltages (see Fig. 11 - right).

C. Influence of the gain of the PMTs

In order to determine the influence of the gain difference of the PMTs on the timing resolution of the tested system, additional measurements have been done for identical gains and a 30% difference in gains.

TABLE XI
THE TIME RESOLUTION FOR DIFFERENT GAINS OF THE PMTs

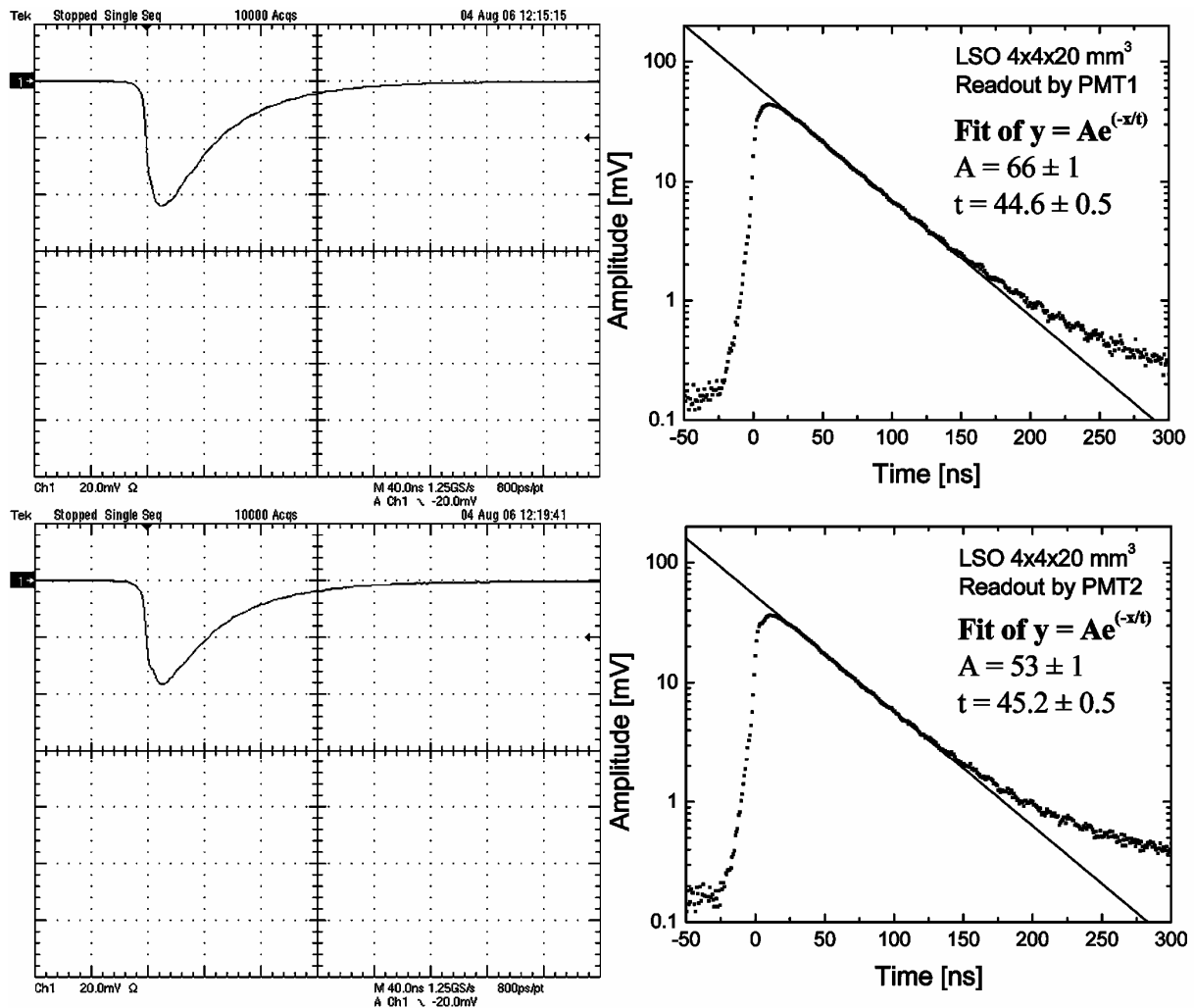
Signal taken from	Time resolution at FWHM, δt [ps]		Phe number for 511 keV [phe]	$\delta t\sqrt{N}$ [ps $\sqrt{\text{phe}}$] $\times 10^3$
	Measured	Corrected ^{a)}		
LSO crystal in the center of the PMT 1				
PMT 1	268 \pm 8	235 \pm 9	1700 \pm 100	9.7 \pm 0.5
PMT 1 + PMT 2	266 \pm 8	234 \pm 9	1700 \pm 100	9.6 \pm 0.5
LSO crystal between PMT 1 and PMT 2 for identical gains				
PMT 1	494 \pm 15	477 \pm 16	500 \pm 50	10.7 \pm 0.6
PMT 2	501 \pm 15	484 \pm 16	500 \pm 50	10.8 \pm 0.6
PMT 1 + PMT 2	370 \pm 11	348 \pm 12	1000 \pm 70	11.0 \pm 0.5
LSO crystal between PMT 1 and PMT 2 for 30% difference in gains				
PMT 1	492 \pm 15	475 \pm 15	500 \pm 50	10.6 \pm 0.6
PMT 2	489 \pm 15	471 \pm 15	550 \pm 50	11.1 \pm 0.6
PMT 1 + PMT 2	369 \pm 11	347 \pm 12	1050 \pm 70	11.2 \pm 0.5

a) corrected for the contribution of the BaF₂ reference detector of 128 \pm 4 ps

To adjust the gain, the single photoelectron spectra of both tubes were compared. The appropriate gain was set by changing a voltage divider ratio on the potentiometer of the screening grid [9]. Results of the timing measurements made in different conditions are collected in Table XI. Note that changing of the voltage parameters for the screening grid did not influence the time resolution of the system. The values in Table XI for an LSO crystal placed in the center of the PMT 1 are in perfect agreement with Table X. Comparison of the timing results gathered in Table XI leads to the main conclusion that the time resolution of the system is, in the limit of 30%, independent of the gain of its elements. This result has a serious practical impact: selection of the tubes for a block detector does not require precise matching of their gains in order to achieve optimal time resolution.

D. Anode pulse shape

In order to determine the pulse shape of the double-PMT system, the scintillator was placed in the middle of the light guide, between the PMTs, and it was irradiated by a ^{22}Na gamma source. Next, an average anode signal of 10 000 acquisitions was recorded by a Tektronix Digital Oscilloscope type TDS5034B for a single and double PMT readouts. The screen captures of the registered pulses as well as the results of fitting of a single exponential decay are presented in Fig. 12.



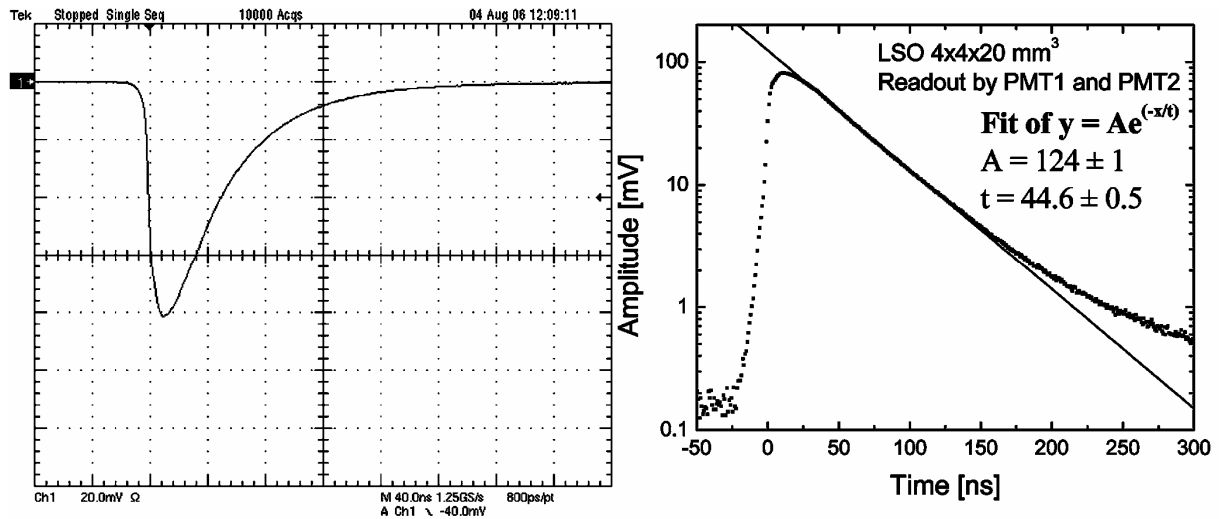


Fig. 12. Screen captures of the average anode pulses for LSO 4x4x20 mm³ and signals taken from PMT 1, PMT 2 and both. A result of the fitting of a single exponential decay for each case is also presented.

According to the results of the fitting, it is easy to observe that the reported adding of the two anode signals does not destroy the decay time constant of the output pulse. The amplitude of the final signal is simply a sum of the amplitudes of the input signals. The two above facts show that the sum-signal is only a result of the improved light collection due to the light readout by means of two PMTs.

5. Conclusions

The data presented in the first part of this chapter strongly suggests that the time-of-flight PET, based on LSO crystals, is a realistic proposition that should be further studied. This conclusion is based on the excellent time resolution measured with 10x10x5 mm³ and 4x4x20 mm³ LSO crystals coupled to XP20D0 PMTs. A further improvement can be achieved with the development of PMTs that combine the performance of the XP20D0 and R5320, it means the lowest possible time jitter, high quantum efficiency and are equipped with the screening grid at the anode.

In the second part of this chapter, considerable differences in the time resolution for various settings and types of discriminators were shown. This strongly confirms that a proper optimization of the experimental system is a key factor for the timing measurements. Very good agreement of the experimental data with the Hyman theory shows the most important parameters that have to be considered during optimization of the timing setup electronics.

It was also shown, that in the case of LSO, the time resolution is weakly affected by the time jitter of the PMT and is mainly controlled by the decay time constant of the light pulse and the number of photoelectrons. The influence of each parameter is, of course, dependent on the detector used. In the case of LSO, the lowest possible threshold set on the LE discriminator leads to the best time resolution. However, for example in the case of timing with plastic scintillators characterized by a much faster light pulses, CFD would be a better choice [12].

In the third part of the presented experiments, very good time resolution of 350 ± 12 ps with

a single $4 \times 4 \times 20 \text{ mm}^3$ LSO and the system realizing light readout by two PMTs was reported. It is worth to underline that in the tested experimental arrangement the light collection performance was not fully optimized due to geometrical limitations. First of all, only two PMTs were used in the experiment but, even in this configuration, an improvement of the light collection by a factor of 2 was possible. Using more PMTs, for example adding two more above and two more below of our system, should considerably increase the amount of the collected light and, in consequence, the time resolution. Such a cluster of 6 PMTs is consistent with the current PET designs. Moreover, the scintillator was placed in the middle of the system, between PMTs and, in fact, in the region outside of the area of the input windows of the PMTs (see Fig. 9). This configuration also leads to loss of a considerable amount of light from the crystal. Nevertheless the results show that using a sum of signals from several PMTs improves timing and should allow for the achievement of good homogeneity of the time resolution over a whole surface of the detectors.

During the measurements, two additional important observations have been made. The transit time of the electrons inside the tube is crucial and, for the sum of anode signals, the same values of the voltage are needed to ensure good timing properties of the system. Moreover, different gains of the photomultipliers (in the range of 30%) have no influence on the final performance of the multi-PMT system. Finally, summing of the anode signals does not change the output sum-pulse decay time constant.

6. References

- [1] R. Allemand, C. Gresset, and J. Vacher, "Potential advantages of a cesium fluoride scintillator for a time-of-flight positron camera," *J. Nucl. Med.*, vol. 21, no. 2, p. 153, 1980.
- [2] M. Laval, R. Allemand, R. Campagnolo, P. Garderet, R. Gariod, P. Guinet, M. Moszynski, E. Tournier, and J. Vacher, "Contribution of the time of flight information to the positron tomographic imaging," in *Proc. of Third World Congress of Nucl. Med. and Biol.* Pergamon Press, Paris, 1982, p. 2315.
- [3] N. Mullani, D. Ficke, R. Hartz, J. Markham, and G. Wong, "System design of fast PET scanners utilizing time-of-flight," *IEEE Trans. Nucl. Sci.*, vol. 28, no. 1, pp. 104–108, 1981.
- [4] M. Moszynski, M. Gierlik, M. Kapusta, A. Nassalski, T. Szczesniak, C. Fontaine, and P. Lavoute, "New Photonis XP20D0 photomultiplier for fast timing in nuclear medicine," *Nucl. Instr. Meth. A*, vol. 567, no. 1, pp. 31–35, 2006.
- [5] M. Moszynski, M. Kapusta, A. Nassalski, T. Szczesniak, D. Wolski, L. Eriksson, and C. Melcher, "New prospects for time-of-flight PET with LSO scintillators," *IEEE Trans. Nucl. Sci.*, vol. 53, no. 5, pp. 2484–2488, 2006.
- [6] W. Moses and S. Derenzo, "Prospects for time-of-flight PET using LSO scintillator," *IEEE Trans. Nucl. Sci.*, vol. 46, no. 3, pp. 474–478, 1999.
- [7] A. Kuhn, S. Surti, J. Karp, G. Muehllehner, F. Newcomer, and R. VanBerg, "Performance assessment of pixelated LaBr₃ detector modules for time-of-flight PET," *IEEE Trans. Nucl. Sci.*, vol. 53, no. 3, pp. 1090–1095, 2006.
- [8] A. Kuhn, S. Surti, J. Karp, P. Raby, K. Shah, A. Perkins, and G. Muehllehner, "Design of a lanthanum bromide detector for time-of-flight PET," *IEEE Trans. Nucl. Sci.*, vol. 51, no. 5, pp. 2550–2557, 2004.

- [9] M. Moszynski, M. Kapusta, D. Wolski, M. Balcerzyk, S. Flyckt, P. Lavoute, C. Marmonier, and H. Mach, “New fast photomultipliers with a screening grid at the anode,” *IEEE Trans. Nucl. Sci.*, vol. 51, no. 4, pp. 1701–1706, 2004.
- [10] M. Moszynski, “Prospects for new fast photomultipliers,” *Nucl. Instr. Meth. A*, vol. 337, no. 1, pp. 154–164, 1993.
- [11] M. Moszynski, J. Vacher, and R. Odru, “Application of the HR 400 microchannel plate photomultiplier to study the light pulse shape from fast and slow scintillators by means of the single photon method,” *Nucl. Instr. Meth.*, vol. 204, no. 1, pp. 141–147, 1982.
- [12] B. Bengtson and M. Moszynski, “Timing properties of scintillation counters,” *Nucl. Instr. Meth.*, vol. 81, no. 1, pp. 109–120, 1970.
- [13] M. Moszynski, “Study of light collection process from cylindrical scintillators,” *Nucl. Instr. Meth.*, vol. 134, no. 1, pp. 77–85, 1976.
- [14] L. Hyman, “Time resolution of photomultiplier systems,” *Rev. Sci. Instr.*, vol. 36, no. 2, pp. 193–196, 1965.
- [15] Hamamatsu, *Hamamatsu R5320 Data Sheet*, 1996.
- [16] C. Melcher, M. Schmand, M. Eriksson, L. Eriksson, M. Casey, R. Nutt, J. Lefaucheur, and B. Chai, “Scintillation properties of LSO:Ce boules,” *IEEE Trans. Nucl. Sci.*, vol. 47, no. 3, pp. 965–968, 2000.
- [17] C. Melcher, M. Spurrier, L. Eriksson, M. Eriksson, M. Schmand, G. Givens, R. Terry, T. Homant, and R. Nutt, “Advances in the scintillation performance of LSO:Ce single crystals,” *IEEE Trans. Nucl. Sci.*, vol. 50, no. 4, pp. 762–766, 2003.
- [18] Photonis, *Photonis, Photomultiplier tubes catalogue*, 2005.
- [19] M. Bertolaccini, S. Cova, and C. Bussolatti, “A technique for absolute measurement of the effective photoelectron per keV yield in scintillation counters,” in *Proc. Nuclear Electronics Symp., Société Francaise des Electroniciens et des Radioelectriciens*, 1968.

9. Fast photomultipliers for TOF PET

1. Introduction

A. Motivation

The data presented in chapter 8 (following [1]) showed very good time resolution obtained with the $10 \times 10 \times 5 \text{ mm}^3$ LSO crystal coupled to Photonis XP20D0 and Hamamatsu R5320 photomultipliers. The results were almost identical for both detectors and close to 170 ps. Fig. 8.1 in section 8.2 presents the measured time spectra and Table 8.I contains data of sensitivity and transit time jitter of the PMTs. The XP20D0 possesses a high quantum efficiency (QE) and the measured photoelectron number is 40% higher than that of the R5320. On the other hand the R5320 has the time jitter of $140 \pm 7 \text{ ps}$ at FWHM, three times better than that of the XP20D0.

The above example shows that the final result of timing performance is a composition of the two major parameters of a PMT: its time jitter and quantum efficiency. In the case of XP20D0 the photocathode with very high quantum efficiency and application of the screening grid at the anode [2] resulted in the superior time resolution, even though the PMT had moderate time jitter. In the case of R5320 the photocathode sensitivity was low but due to the excellent time jitter the timing performance was equal to that of the XP20D0.

B. Aim of the study

The above observations triggered a further study of the most important properties of photomultipliers and their influence on timing and energy resolution, with a goal of optimizing the TOF PET systems. Thanks to a close cooperation with one of the largest producers of photomultipliers (Photonis in Brive, France), during last few years, a large amount of experimental data was collected from timing measurements using various types of PMTs. The aim of the presented studies is to show dependencies and general conclusions that were derived from these multiple experiments. This should help to develop an ultimate, PMT based detector for TOF-PET systems.

2. Experimental details

A. Experimental setup

The studies were done mainly with the $10 \times 10 \times 5 \text{ mm}^3$ LSO crystal coupled to the tested PMTs. The mechanically polished LSO crystals were wrapped with several layers of white Teflon tape. In order to characterize the dependency of the time resolution on the number of photoelectrons the data given in chapter 8 for the $4 \times 4 \times 20 \text{ mm}^3$ LSO pixel crystal were also used.

In the reference detector, a truncated cone, 20 mm and 25 mm in diameter and 15 mm high BaF_2 crystal coupled to the XP20Y0Q/DA PMT was used. Its time resolution of $128 \pm 4 \text{ ps}$ for the 511 keV full energy peak, selected in the side channel, was reported in [2].

Together with the time resolution measurements, the number of photoelectrons produced by the LSO crystal in the PMTs (using Bertolaccini method and ^{137}Cs gamma-source) and their time jitter (using XP22 LED) were measured in the course of this work. The details can be found in chapter 7. The time jitter was measured in two modes, when the LED pulser illuminated a full photocathode and a spot of 8 mm in diameter in the center of the photocathode. In the second case whole surface of the PMT input window, except the hole 8 mm in diameter in the center, was covered to avoid light.

B. Tested photomultipliers

The studies were carried out on a wide set of the photomultipliers, mostly representing the Photonis production [3]. All the tubes, except the 4-channel (Quad) XP1485 based on the metal foil dynodes, had bi-alkali photocathodes and linear focused dynode structure. In Table I, the main characteristics of all the PMTs are presented. Note, that this table contains PMTs of various types, with different constructions, diameters and designed for different applications. In general, the set can be divided into three groups: the first one of fast PMTs, optimized for timing measurements, the second one representing the semi-fast PMTs of a general use and the third group of the fast XP20D0 and Quad PMTs. The two latter tubes are characterized by a modified construction of the last dynode-anode region due to the screening grid in XP20D0 [1] and a simple anode construction in form of a plate instead of a grid in XP1485. The detailed description of the differences between the tubes of various kinds can be found in chapter 5. For all the photomultipliers a tapered voltage divider was used to assure good linearity of the anode pulse.

TABLE I
THE MAIN PARAMETERS OF THE STUDIED PHOTOMULTIPLIERS

PMT	Size [mm]	Blue sensitivity [$\mu\text{A}/\text{lmF}$] ^{a)}	Window	No of dynodes	Type of dynodes	Grid	Description	Phe number for LSO $10\times 10\times 5 \text{ mm}^3$ [phe/MeV]	Measured time jitter [ps]
XP2882 SN029	19	11.3	low K borosilicate	8	LF ^{b)}	No	Semi-fast	6000 ± 200	1560 ± 80
XP31X1	25	11.3	borosilicate	8	LF	No	Semi-fast	6000 ± 200	750 ± 40
XP31X2	25	9.8	borosilicate	8	LF	No	Fast	5100 ± 200	630 ± 30
XP3060 SN193	39	11.2	borosilicate	7	LF	No	Fast	6400 ± 200	620 ± 30
XP3060 SN018	39	11.5	borosilicate	7	LF	No	Fast	5300 ± 200	670 ± 30
XP1020 SN1021	25	11.3	borosilicate	8	LF	No	Fast	4900 ± 100	550 ± 30
XP20G0 SN162	39	12.7	borosilicate	10	LF	No	Fast	5600 ± 200	1300 ± 70
XP2020 SN25377	51	10.4	borosilicate	12	LF	No	Fast	6300 ± 200	500 ± 25
XP20D0 SN2026	51	13.7	borosilicate	8	LF	Yes	Fast	8100 ± 200	520 ± 25
XP20D0 SN2083	51	12.65	borosilicate	8	LF	Yes	Fast	6600 ± 200	510 ± 30
XP20D0 SN2087	51	12.75	borosilicate	8	LF	Yes	Fast	7000 ± 200	540 ± 30
XP1485 SN1789	38	13.5	borosilicate	8	Metal Foil	No	4-channel, Fast	6400 ± 200	1300 ± 70
R5320 BA0091	25	8.9	quartz	10	LF	No	Fast	5400 ± 200	140 ± 7

a) where F stands for filtered for blue sensitivity

b) Linear Focused

3. Results

A. Number of photoelectrons dependence of timing

In order to analyze the time resolution dependence on the number of photoelectrons gathered in the PMT, the results of the timing measurements with a given type of a PMT were studied. Three units of XP20D0 PMTs were used. Their blue sensitivities were equal to 13.7, 13.1 and 12.8 $\mu\text{A/lmF}$ which corresponds to QE of about 34%, 32.5% and 31.7% respectively.

It is important to say that these measurements are in general independent of the time jitter because PMT units of the same type, with the same input optics were used. Moreover, small differences of the time jitter existing between any given unit are further minimized by using LSO crystals that are small compared to the 2-inch diameter photocathode. In the case of the tested PMTs the same normalized time resolution was reported in chapter 8.

The data from experiments made with two LSO crystals were used in the analysis. The crystals are characterized by different light attenuation due to different dimensions of $10\times 10\times 5\text{ mm}^3$ and $4\times 4\times 20\text{ mm}^3$. These scintillators coupled to the XP20D0 SN2026 PMT yielded photoelectron numbers of 8100 phe/MeV and 5900 phe/MeV respectively, which means a 30% difference in light output of both crystals. To compare different numbers of photoelectrons, also the data from chapter 8 with the finger-like LSO crystal placed on the light diffuser in various positions in relation to the center of the photocathode had been taken into account. In such conditions the number of photoelectrons is determined not only by the QE of the PMT and light output of the scintillators used, but is also influenced by the light loss and poorer photoelectron collection efficiency resulting from the different positions of the crystal.

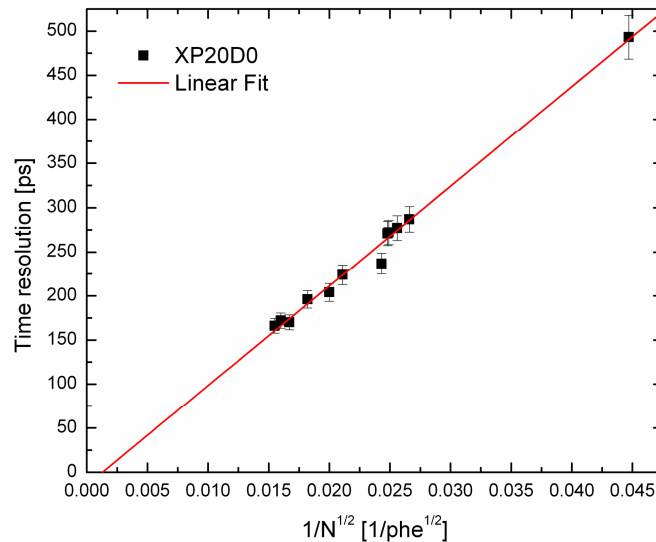


Fig. 1. The measured time resolution versus the number of photoelectrons collected in the PMT. Data points represent measurements made with three units of XP20D0 PMTs and two LSO samples: $10\times 10\times 5\text{ mm}^3$ and finger-like $4\times 4\times 20\text{ mm}^3$ placed in various positions in relation to the center of the photocathode, following chapter 8.

Fig. 1 presents measured time resolution (for the LSO detectors only) versus number of

photoelectrons collected in the PMT. The observed linear dependence of timing on the inverse square root of the number of photoelectrons confirms the importance of high photocathode quantum efficiency in timing measurements. Furthermore, the high number of photoelectrons improves not only the timing, but also the energy resolution particularly in the finger-like crystals used in PET detectors.

It is worthy to add that there are also some minor disadvantages of the PMTs with very high QE. Highly efficient photocathode can lead to the considerable increase of dark noise and may disturb linearity and gain stability of the tube. The improved QE of the photocathodes is also related to broadening of spectral sensitivity characteristic towards longer wavelengths, which affects the time jitter component originating from a variation of initial velocities of photoelectrons. All these changes in the PMT parameters have to be taken into account during the final detector construction.

B. Time jitter dependence of timing

Fig. 2 presents the time resolution, measured with the $10 \times 10 \times 5 \text{ mm}^3$ LSO crystal coupled to the number of the tested PMTs, plotted versus time jitter. The time jitter measured in the central part of the photocathode, corresponding to the 8 mm in diameter region is used in the plot. This region of the photocathode is comparable (regarding the photoelectron collection) to the size of the LSO exit window of $10 \times 10 \text{ mm}^2$. Time resolution, in turn, represents the time resolution of the single tested detector; it means that the measured value was corrected for the contribution of the BaF_2 reference detector (128 ps).

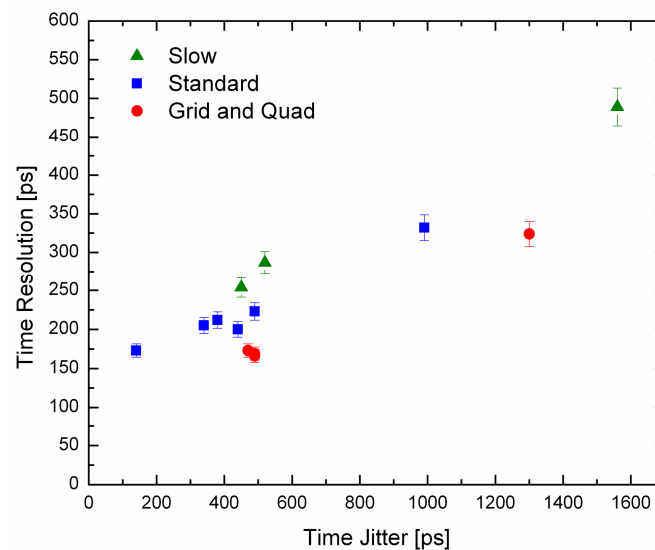


Fig. 2. Time resolution versus time jitter for the tested PMTs. Measurements were done for the $10 \times 10 \times 5 \text{ mm}^3$ LSO crystal. Presented values were corrected for the contribution of the reference detector.

Fig. 2 shows the general trend of deterioration of the time resolution with the increased time jitter of different PMTs. The square points (called “standard”) represent measurements done with classic, fast PMTs, such as XP2020, optimized for timing measurements. The triangle points (called “slow”) refer to the semi-fast PMTs, which provide a compromise between decent collection efficiency and average timing properties, what is reflected in a slower rise time of the anode pulse. Finally, the circle points represent fast PMTs with different way of

anode construction (XP20D0 and XP1485 Quad).

Large spread of the experimental points is seen exceeding their experimental errors. Such spread is a result of dependency between the time resolution and the number of photoelectrons produced at the photocathode. Note, that the best time resolution is shown for the XP20D0 PMTs, despite their moderate time jitter.

Because the time resolution is in general inversely proportional to the square root of the number of photoelectrons (see section A), it is hard to compare results obtained with different detectors characterized by different quantum efficiencies and equipped with different scintillators. Multiplying the time resolution by the square root of the number of photoelectrons for a given energy gives a normalized value independent of the detector differences.

In Fig. 3 the measured time resolution normalized to the number of photoelectrons and the parameter r versus the time jitter is presented. The parameter r (values between 1.05 and 1.2), reflects the gain dispersion of the electron multiplier (see chapter 6 for details). The gain dispersion was taken into account, since in the studied PMTs, a significant variation of the width of the single photoelectron peak was observed, down to 45% ($r = 1.05$) for XP3060, SN018.

The normalized time resolution (ΔT_n) was calculated in the following way:

$$\Delta T_n = \Delta t \cdot \sqrt{N} / r \cdot 10^3 \quad (1)$$

where Δt is the measured time resolution, N is the number of photoelectrons for 511 keV and the gain dispersion r is proportional to the energy resolution of the single photoelectron peak.

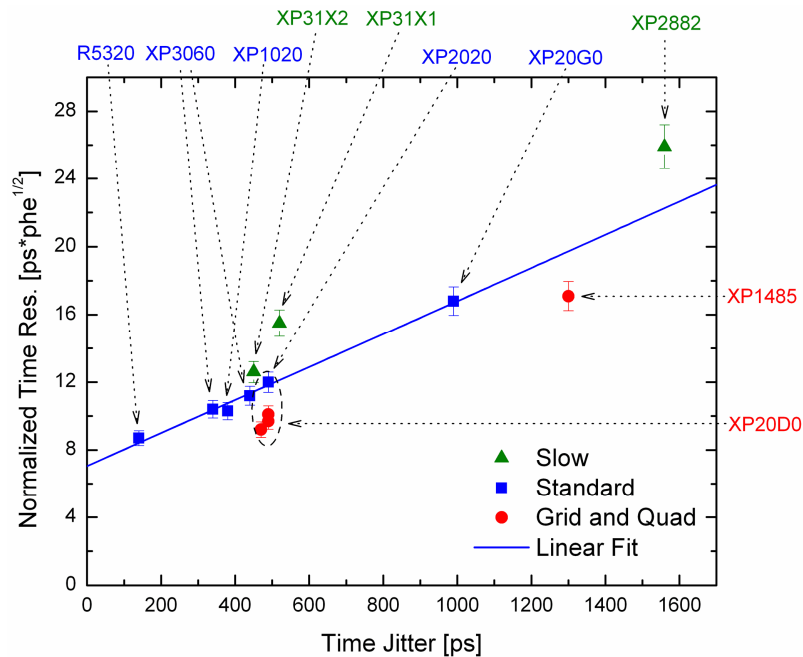


Fig. 3. Normalized time resolution versus time jitter for the tested PMTs. Measurements were done for the LSO crystal, as presented in Fig. 2.

The plot displays the linear growth of the time resolution versus the time jitter, especially well visible in the case of the classic fast PMTs (blue squares). It is worth noting the value of around 7×10^3 ps $\sqrt{\text{phe}}$ reflecting the ideal PMT, with the time jitter equal to zero. In such

a case the time resolution is limited only by a slow decay of the LSO light pulse. The time resolution measured with LSO and other slow decaying scintillators depends stronger on statistics of the photoelectrons produced in the decay process of the light pulse, while the time jitter of the PMT much weaker influences the measured time resolution. This effect was predicted by the Hyman theory of timing [4], [5] and it was known in the past for NaI(Tl) crystal [6], whose time resolution was often discussed in terms of the Post and Schiff theory [7].

In the case of fast scintillators such as plastics where the time jitter of a PMT is of great importance [8], [9], [10] a similar linear dependence should be observed but with a much steeper slope. Conversely, for the slow crystals like NaI(Tl) where timing is mainly controlled by the number of photoelectrons, the time jitter influence is minimized resulting in a flat dependence.

The triangular points in Fig. 3 represent the results obtained with the semi-fast PMTs characterized by a slow rise time of the anode pulse. Also in this case a linear dependence could be assumed but shifted up in respect to the classic, fast PMTs line. A similar situation applies to the circular points, which represent PMTs with a different anode construction.

All the results presented in Fig. 2 and Fig. 3, are collected in Table II.

TABLE II
TIMING PROPERTIES OF THE STUDIED PHOTOMULTIPLIERS

PMT	Phe number for 511 keV [phe]	Time resolution at FWHM ^{a)} , Δt [ps]	$\Delta t\sqrt{N}/r$ [ps $\sqrt{\text{phe}}$] $\times 10^3$	Time jitter in center [ps]
XP2882 SN029	3100 ± 100	489 ± 24	25.9 ± 1.3	1560 ± 80
XP31X1	3100 ± 100	287 ± 14	15.5 ± 0.8	520 ± 30
XP31X2	2600 ± 100	254 ± 13	12.6 ± 0.6	450 ± 20
XP3060 SN193	3300 ± 100	200 ± 10	11.2 ± 0.6	440 ± 20
XP3060 SN018	2700 ± 100	205 ± 10	10.4 ± 0.5	340 ± 20
XP1020 SN1021	2500 ± 100	212 ± 11	10.3 ± 0.5	380 ± 20
XP20G0 SN162	2900 ± 100	332 ± 17	16.8 ± 0.8	990 ± 50
XP2020 SN25377	3200 ± 100	223 ± 11	12.0 ± 0.6	490 ± 20
XP20D0 SN2026	4100 ± 100	166 ± 8	10.1 ± 0.5	490 ± 20
XP20D0 SN2083	3200 ± 100	173 ± 9	9.2 ± 0.5	470 ± 20
XP20D0 SN2087	3600 ± 100	169 ± 8	9.7 ± 0.5	490 ± 20
XP1485 SN1789	3300 ± 100	324 ± 16	17.1 ± 0.9	1300 ± 70
R5320 BA0091	2800 ± 100	173 ± 9	8.7 ± 0.4	140 ± 7

C. Influence of the initial rise time of the anode pulse

In all the measurements, presented in Figs 1, 2 and 3, the optimization of the electronics for the best time resolution was made. Analysis of the data collected with the XP20D0 PMTs shows that, for the LSO crystal, the lowest possible threshold set on a leading edge discriminator leads to the best timing results, even better than that measured with a constant fraction discriminator (see chapter 8). These experimental results are in perfect agreement with predictions of the Hyman theory of timing [4]. However, the PMT design has a big influence on the rise time of the anode pulse, so for certain types of tubes it is not possible to reach the sufficiently low fraction level and achieve good time resolution. The three families of PMTs presented in Fig. 3 can be considered as the three classes of the anode pulse shape quality, according to the dynode structure and electron focusing structure. The anode pulse shape quality means not only the rise time of the anode pulse but also the steepness of its initial part which is crucial for optimization of the LSO detector towards the best time resolution.

In Fig. 4 the dependency between centroid of the time spectra and fraction level set on the discriminator is presented. Change of the threshold level leads to the shift of the fraction time accordingly to the pulse shape, and in consequence, to the shift of the time spectrum centroid. Thus, this dependence reflects the rise time of the anode pulse. Note, the large difference between XP2882 and XP3060, which is one of the source of the large time resolution difference presented in Fig. 3.

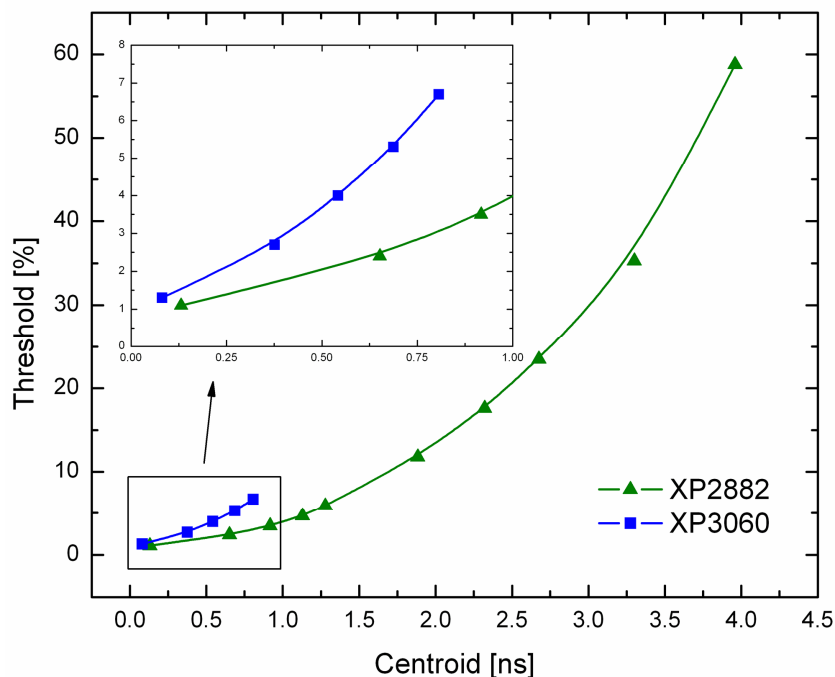


Fig. 4. The dependency between the centroid of the time spectra and the threshold set on a leading edge discriminator. Measurements were done for the $10 \times 10 \times 5$ mm³ LSO crystal.

Fig. 5 presents the dependence of the time resolution on the fraction level in the case of the XP2882, XP3060 and XP20D0 PMTs. Note a minimum on the XP2882 plot, corresponding to the best timing, obtained with the fraction level of about 10%. As it can be seen, for the first

class of photomultipliers, characterized by the slow rise time of the anode pulse (triangle points in Fig. 3) the very low threshold set on a discriminator deteriorates the time resolution. For the standard, fast PMTs, represented by the square points in Fig. 3, no improvement of the time resolution with the threshold level, for the fraction below 10% is observed. Only in the case of photomultipliers optimized for timing measurements, such as XP20D0, the time resolution can be improved by setting the lowest threshold level on a discriminator. The behavior of the circular points representing XP20D0 PMTs is consistent with the Hyman theory and plots presented in chapter 6.

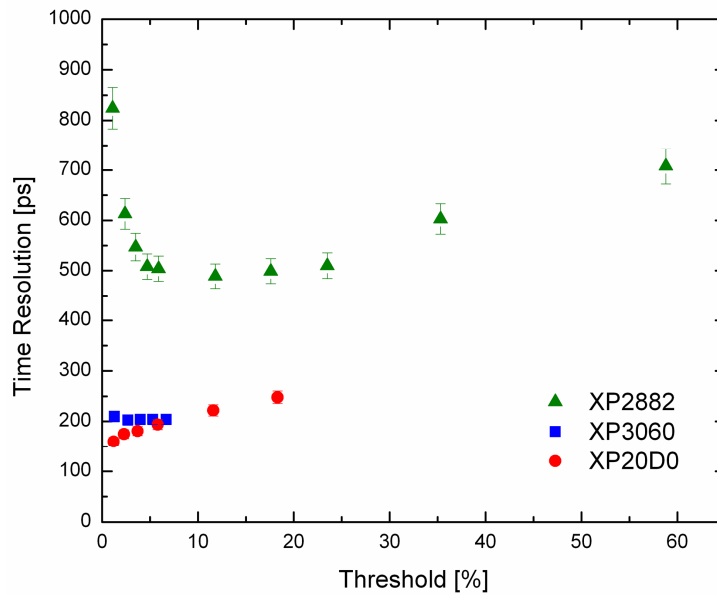


Fig. 5. Time resolution dependence on the LE threshold for the three PMTs representing different designs. Measurements were done for the 10x10x5 mm³ LSO crystal. Presented values were corrected for the contribution of the reference detector.

Above observations confirmed that the geometry of the last stages in the electron multiplier could improve timing properties of a given photomultiplier. This fact can be clearly seen for the two XP31X1 and XP31X2 PMTs. The new construction of XP31X2 allows improving the normalized time resolution from $15.5 \times 10^3 \text{ ps}\sqrt{\text{phe}}$ to about $12.6 \times 10^3 \text{ ps}\sqrt{\text{phe}}$, with the change of threshold level from about 10% to 6%, see Table II.

The group of points marked with dashed ellipse in Fig. 3 represent the same XP2020 family of photomultipliers. The only difference between the XP2020 and XP20D0 tubes, that improves timing is the screening grid at the anode introduced in the latter one (filled circles). This kind of the PMT optimization was described in details in chapter 5 and tested in [1], [2], [11]. The screening grid leads to suppressing of the parasitic component induced at the anode by the electrons traveling from the penultimate dynode to the last dynode, and in consequence to an improvement of the initial rise time of the anode pulse. A similar situation applies to the XP1485 Quad PMT, but here the screening grid is not needed because of the simplified anode construction. In the case of XP20D0 the anode is a grid inside the last dynode and in the case of XP1485 the anode is a metal plate followed by the foil dynodes structure.

D. Decay time constant dependence of timing

It is also interesting to look on behavior of the detector time resolution for different kinds of scintillators. All the measurements discussed in this part were made with the same type of the XP2020 photomultipliers and a large set of various crystals characterized by different properties, especially the decay time constant. The decay time constants, results of the timing measurements and the photoelectron numbers obtained with the tested scintillators are collected in Table III. The "time jitter" entry at the bottom of the Table represents the ideal scintillator with the decay time constant equal to 0. The plot of the normalized time resolution versus the square root of the decay time constant is presented in Fig. 6. The numbers collected in Table III and plotted in Fig. 6 are based on several experiments carried at the Soltan Institute in Swierk for the last 15 years, following [12], [2], [13], [11], [14], [15], [16], [17]. Although different XP2020 PMTs were used in the measurements, the adjustments of timing and experimental techniques were the same. Nevertheless, the presented plot represents only the general trend, which may help to understand better an influence of the decay time of scintillators on the time resolution.

TABLE III
TIMING PROPERTIES OF THE STUDIED SCINTILLATORS COUPLED TO THE XP2020
PHOTOMULTIPLIER

Crystal	Nphe/MeV [phe/MeV]	Norm.Time.Res. [ps $\sqrt{\text{phe}}$] $\times 10^3$	Decay Const. [ns]	Sqrt of Decay	Refs
NE111	1400 \pm 30	2.48 \pm 0.12	1.40 \pm 0.10	1.18	[19]
NaI(Tl)	4500 \pm 100	34.99 \pm 0.59	250.0 \pm 12.5	15.81	[19]
LuAP	2900 \pm 200	9.0 \pm 0.5	17.4 \pm 0.3	4.17	[20]
YAP	4300 \pm 100	10.8 \pm 0.5	26.70 \pm 0.12	5.17	[21]
LSO-1	6300 \pm 200	12.6 \pm 0.4	46.2 \pm 0.5	6.80	[1], [11]
LSO-2	5950 \pm 290	12.9 \pm 0.5	44.8 \pm 1.6	6.69	[22]
LYSO	5150 \pm 250	13.8 \pm 0.5	48.5 \pm 1.7	6.96	[22]
MLS	5340 \pm 270	12.5 \pm 0.5	47.8 \pm 1.7	6.91	[22]
LGSO	3130 \pm 160	15.5 \pm 0.6	78.6 \pm 2.8	8.87	[22]
CsF	510 \pm 30	4.0 \pm 0.2	2.80 \pm 0.14	1.67	[23]
NE213	1200 \pm 30	8.64 \pm 0.14	3.2 \pm 0.2	1.79	[19]
LaBr3	11940 \pm 590	11.3 \pm 0.4	18.4 \pm 0.6	4.29	[22]
LaCl3	7800 \pm 400	13.7 \pm 0.3	25.0 \pm 1.3	5.00	[2]
Time jitter	1phe	0.5	0	0	

In general, the linear dependence can be easily observed leading to the best time resolution for the fastest crystals. However, a group of blue squares above the general, linear trend reflects timing experiments done with the scintillators characterized by the finite rise time of their light pulses (NE213, LaBr₃ and LaCl₃). This kind of the time resolution deterioration is

very well known for ternary plastics [10] or liquid scintillators and it was reported recently for the LaBr₃ and LaCl₃ crystals [18].

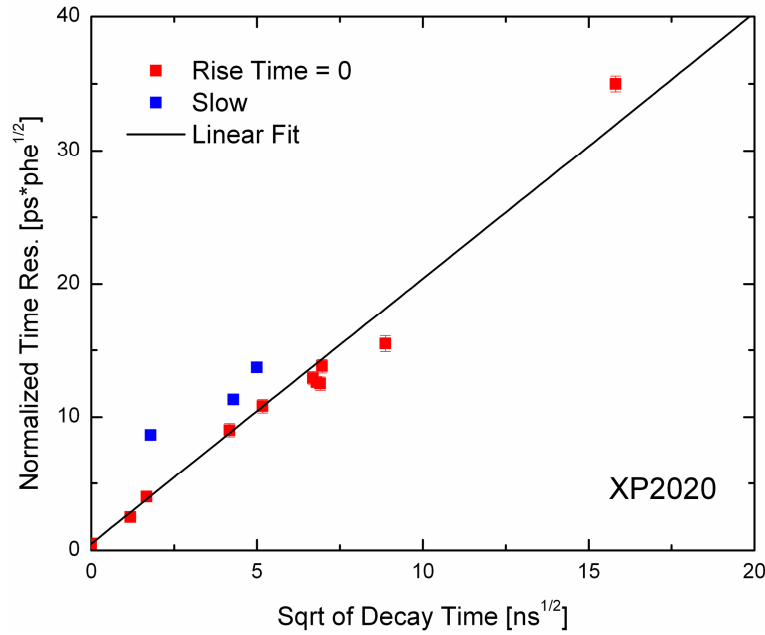


Fig. 6. Normalized time resolution versus square root of the decay time constant measured with various scintillators coupled to the XP2020 PMT.

4. Discussion

A. Factors influencing timing in an LSO based detector

Time resolution dependence on the number of photoelectrons and that on the time jitter can be easily seen in Figs 1 and 2, respectively. The most pronounced difference in the time jitter can be observed between XP20D0 SN2026 (490 ps) and Hamamatsu R5320 (with a superb value of 140 ps). However, a higher photoelectron number in the case of XP20D0 (supported also by the screening grid effect) leads to the same time resolution of about 170 ps despite the worse time jitter. Here a 3.5 times poorer time jitter is partly compensated by high QE of the photocathode giving 4100 photoelectrons, about 1.5 times more than 2800 measured for R5320. Worth noting is also an improvement of the normalized time resolution for the XP3060 PMTs from 11.2×10^3 ps $\sqrt{\text{phe}}$ (SN193) to 10.4×10^3 ps $\sqrt{\text{phe}}$ (SN018) correlated with the reduced time jitter from 440 ps to 340 ps, respectively. Difference in the time jitter between these two tubes reflects the evolution in the development process at Photonis addressed to an amelioration of the photoelectron collection in SN193 tube. However, 23% reduction of the time jitter gives only about 7% better normalized time resolution. Moreover, the measured time resolution in the case of both detectors was comparable (see Table II) due to a larger number of photoelectrons in the XP3060, SN193.

These above examples show that in the case of LSO the time resolution dependence on the number of photoelectrons is stronger than the one connected with the time jitter. Moreover, the impact of the anode pulse improvement seems to be also more significant than the time jitter. It is confirmed by a much better normalized time resolution measured with the

XP31X2, in comparison to the XP31X1, obtained due to modification of the last stages in its dynode structure. The improvement, by a factor of 1.2, is seen in Table II. A better time jitter of the XP31X2 seems to be less important in the light of the tests with the XP3060. The improved initial rise of the anode pulse in the XP20D0 due to application of the screening grid is equivalent to the reduction of the time jitter by a factor of two (see Fig. 3).

B. An ideal timing photomultiplier

Taking into account all the analysis and measurements presented in this chapter the ideal possible PMT can be discussed. First, let us point out the key factors influencing the time resolution together with the photomultipliers realizing these requirements in the best way. The time jitter of 140 ps gives Hamamatsu R5320 the leading position regarding the transit time spread. On the other hand the number of 4100 photoelectrons for 511 keV measured with the XP20D0 SN2026 and LSO crystal reflects much better QE of the Photonis tubes. As it was mentioned throughout this chapter the final timing of both detectors was equal to about 170 ps. The easiest thing that can be considered is “mixing” of both photomultipliers in order to achieve a PMT with very low time jitter and very high QE. If we take the normalized time resolution of $8.7 \times 10^3 \text{ ps}\sqrt{\text{phe}}$ corresponding to the R5320 (see Table II) and divide it by the square root of the 4100 photoelectrons measured for the XP20D0 SN2026 the final time resolution will be equal to about 135 ps.

It was the simplest approach. In the second step, also a possible fraction level relevant to the anode construction can be taken into account. As it is presented in Fig. 3, the R5320 and XP20D0 belong to different groups of the anode pulse quality proposed in the previous section. Assuming a linear dependence of the normalized time resolution on the time jitter for each group, a value of the time jitter equal to 140 ps leads to the normalized time resolution as low as $6.5 \times 10^3 \text{ ps}\sqrt{\text{phe}}$ in the case of the best group containing the XP20D0 tubes. Then, the photoelectron number recorded with the XP20D0 SN2026 gives the time resolution at the level of 100 ps. This value looks very promising, but is it realistic?

C. Ideal PMT versus the real world

First of all, the above estimations were carried out for the measurements made with the $10 \times 10 \times 5 \text{ mm}^3$ LSO crystal, whereas in PET block detectors finger-like scintillators are used. As it was presented in chapter 8, the light output of the typical $4 \times 4 \times 20 \text{ mm}^3$ crystal is about 30% lower in comparison to the mentioned $10 \times 10 \times 5 \text{ mm}^3$ sample. However, the fact that the highest QE of the Photonis photocathodes, could reach values of 40% [19], allows assume that the considered numbers of photoelectrons for $10 \times 10 \times 5 \text{ mm}^3$ LSO crystal are possible also in the case of the finger-like scintillators, which light is read by the most efficient photocathodes.

The second problem is that the photoelectron collection is not homogenous over the surface of the photocathode. Moreover, the light collected from the real block detector is also not homogenous and in most cases is spread between four PMTs in order to enable the Anger logic. In the experiments presented in chapter 8.2.C the difference in photoelectron numbers measured for a finger-like crystal placed in the center and at the edge of the 2 inch PMT reached up to 50%. It means that idealized, time resolution of 100 ps in the photocathode center will be deteriorated to 140 ps at its edge. This effect can be partly compensated in the

block detector by summing up the signals from several PMTs, as proposed by Kuhn et al [20] and tested in chapter 8.4.

Now, let us consider the LSO block detector read by the four XP1020 PMTs, the 1 inch version of the well known XP2020. Its normalized time resolution of $10.3 \times 10^3 \text{ ps}\sqrt{\text{phe}}$ is close to that measured with the XP20D0 due to a better time jitter of 380 ps. The same XP1020 PMT, equipped with the screening grid at the anode, should give improvement of the time resolution by a factor of 1.2, similarly to the data presented here for 2 inch XP2020 [2] or for 3 inch XP4312 in [21]. Thus, a value of $8.6 \times 10^3 \text{ ps}\sqrt{\text{phe}}$, which reflects the time resolution equal to about 170 ps seems to be realistic. Further, assuming the photoelectron number similar to the one recorded with XP20D0 SN2026, an improvement of timing up to 135 ps can be achieved. Finally, assumption of the time jitter level similar to the Hamamatsu R5320, leads to the time resolution of 100 ps. Again, this value appears to be a limit for the top class PMTs represented by the construction of the XP20D0 in Fig. 3.

The last statement presented in the previous paragraph is very promising, however one has to remember that an improvement of the time jitter is not an easy task. Very high quantum efficiency of the photocathode is connected with broadening of its spectral sensitivity characteristic towards longer wavelengths. It affects the time jitter component originating from a variation of initial velocities of photoelectrons. Thus, it is very hard to get both, very high quantum efficiency and very low time jitter. However, in the light of the presented study, in the case of an LSO, the high quantum efficiency is more important than the superb time jitter.

D. Conclusions

The time resolution of about 100 ps at FWHM for an LSO based detector, which corresponds to about 2 cm of spatial resolution for two PET detectors, seems to be realistic and appears to be a present limit for the top class PMTs.

The anode pulse shape quality is, besides time jitter and number of photoelectrons, the third important parameter determining the final timing properties of the detector.

In the case of LSO the dependence on the number of photoelectrons is stronger than the one connected with the time jitter.

Success of the TOF PET demands further development of PMTs that combine the performance of the XP20D0 and R5320 phototubes. The goal is the development of a fast PMT with the lowest possible time jitter, high quantum efficiency and improved anode pulse shape quality due to application of the screening grid at the anode.

Overall detector performance would also benefit from further improvements in an LSO crystal such as faster decay time and higher light output. Characterization of a new improved LSO, co-doped with Ca, which exhibits the decay time down to 30 ns and 30% higher light output [22] is presented in chapter 11.

5. References

- [1] M. Moszynski, M. Gierlik, M. Kapusta, A. Nassalski, T. Szczesniak, C. Fontaine, and P. Lavoute, "New Photonis XP20D0 photomultiplier for fast timing in nuclear medicine," *Nucl. Instr. Meth. A*, vol. 567, no. 1, pp. 31–35, 2006.

- [2] M. Moszynski, M. Kapusta, D. Wolski, M. Balcerzyk, S. Flyckt, P. Lavoute, C. Marmonier, and H. Mach, "New fast photomultipliers with a screening grid at the anode," *IEEE Trans. Nucl. Sci.*, vol. 51, no. 4, pp. 1701–1706, 2004.
- [3] Photonis, *Photonis, Photomultiplier tubes catalogue*, 2005.
- [4] L. Hyman, "Time resolution of photomultiplier systems," *Rev. Sci. Instr.*, vol. 36, no. 2, pp. 193–196, 1965.
- [5] M. Moszynski, T. Ludziejewski, D. Wolski, W. Klamra, and V. Avdeychikov, "Timing properties of GSO, LSO and other Ce doped scintillators," *Nucl. Instr. Meth. A*, vol. 372, no. 1-2, pp. 51–58, 1996.
- [6] F. Lynch, "Improved timing with NaI(Tl)," *IEEE Trans. Nucl. Sci.*, vol. 13, no. 3, pp. 140–147, 1966.
- [7] R. F. Post and L. I. Schiff, "Statistical limitations on the resolving time of a scintillation counter," *Phys. Rev.*, vol. 80, no. 6, p. 1113, Dec 1950.
- [8] M. Moszynski and B. Bengtson, "Status of timing with plastic scintillation detectors," *Nucl. Instr. Meth.*, vol. 158, pp. 1–31, 1979.
- [9] E. Gatti and V. Svelto, "Review of theories and experiments of resolving time with scintillation counters," *Nucl. Instr. Meth.*, vol. 43, no. 1, pp. 248–268, 1966.
- [10] B. Bengtson and M. Moszynski, "Timing properties of scintillation counters," *Nucl. Instr. Meth.*, vol. 81, no. 1, pp. 109–120, 1970.
- [11] M. Moszynski, "Prospects for new fast photomultipliers," *Nucl. Instr. Meth. A*, vol. 337, no. 1, pp. 154–164, 1993.
- [12] M. Moszynski, M. Kapusta, A. Nassalski, T. Szczesniak, D. Wolski, L. Eriksson, and C. Melcher, "New prospects for time-of-flight PET with LSO scintillators," *IEEE Trans. Nucl. Sci.*, vol. 53, no. 5, pp. 2484–2488, 2006.
- [13] T. Szczesniak, M. Moszynski, A. Nassalski, P. Lavoute, and A. G. Dehaine, "A further study of timing with LSO on XP20D0 for TOF PET," *IEEE Trans. Nucl. Sci.*, vol. 54, no. 5, pp. 1464–1473, Oct. 2007.
- [14] M. Moszynski, D. Wolski, T. Ludziejewski, M. Kapusta, A. Lempicki, C. Brecher, D. Winiewski, and A. Wojtowicz, "Properties of the new LuAP:Ce scintillator," *Nucl. Instr. Meth. A*, vol. 385, no. 1, pp. 123–131, 1997.
- [15] M. Moszynski, M. Kapusta, D. Wolski, W. Klamra, and B. Cederwall, "Properties of the YAP:Ce scintillator," *Nucl. Instr. Meth. A*, vol. 404, no. 1, pp. 157–165, 1998.
- [16] A. Nassalski, M. Kapusta, T. Batsch, D. Wolski, D. Mockel, W. Enghardt, and M. Moszynski, "Comparative study of scintillators for PET/CT detectors," *IEEE Trans. Nucl. Sci.*, vol. 54, no. 1, pp. 3–10, 2007.
- [17] M. Moszynski, C. Gresset, J. Vacher, and R. Odru, "Properties of CsF, a fast inorganic scintillator in energy and time spectroscopy," *Nucl. Instr. Meth.*, vol. 179, no. 2, pp. 271–276, 1981.
- [18] J. Glodo, W. Moses, W. Higgins, E. van Loef, P. Wong, S. Derenzo, M. Weber, and K. Shah, "Effects of Ce concentration on scintillation properties of LaBr₃:Ce," *IEEE Trans. Nucl. Sci.*, vol. 52, no. 5, pp. 1805–1808, 2005.
- [19] M. Kapusta, P. Lavoute, F. Lherbet, E. Rossignol, C. Moussant, and F. Fouche, "Breakthrough in quantum efficiency of bi-alkali photocathodes PMTs," in *Nuclear Science Symposium Conference Record, 2007. NSS'07. IEEE*, vol. 1. IEEE, 2007, pp. 73–77.
- [20] A. Kuhn, S. Surti, J. Karp, G. Muehllehner, F. Newcomer, and R. VanBerg, "Performance assessment of pixelated LaBr₃ detector modules for time-of-flight PET," *IEEE Trans. Nucl. Sci.*, vol. 53, no. 3, pp. 1090–1095, 2006.
- [21] T. Szczesniak, M. Gierlik, M. Kapusta, M. Moszynski, D. Wolski, P. Lavoute, and E. Rossignol, "The 75 mm diameter Photonis XP43D2 photomultiplier with the

- screening grid at the anode for timing experiments,” *IEEE Trans. Nucl. Sci.*, vol. 53, no. 3, pp. 1540–1546, Jun. 2006.
- [22] M. Spurrier, P. Szupryczynski, A. Carey, and C. Melcher, “Brightest and faster LSO,” in *IEEE 9th International Conference on Inorganic Scintillators and Their Applications (SCINT)*, 2007.

10. A Time Resolution Study of a Continuous Crystal Detector for TOF PET

1. Introduction

A. Motivation

Presently, most of the detectors used in positron emission tomography is based on a large number of pixelated scintillating crystals read by a much smaller number of photomultipliers. Commercially available TOF PET systems with pixelated block detectors are characterized by a coincidence time resolution around 600 ps [1]. In chapter 8 very good time resolution was presented with $10 \times 10 \times 5 \text{ mm}^3$ and $4 \times 4 \times 20 \text{ mm}^3$ LSO crystals coupled to the Photonis XP20D0 photomultiplier showing that LSO or LYSO scintillators (7.4 g/cm^3) are good candidates for a future TOF-PET [2]. A further improvement of the time resolution was achieved by using the common light readout from the cluster of PMTs in the block detector, as proposed by Kuhn et al [3] and tested in chapter 8.4. The better light collection from the $4 \times 4 \times 20 \text{ mm}^3$ LSO scintillator due to light readout by two PMTs led to an improvement of the time resolution from about 490 ps to 350 ps (see Fig. 10 in chapter 8). The difference by a factor of 1.4 was observed as expected from statistics.

Recently, a number of studies were devoted to the possible application of the continuous crystals in PET instead of the block detectors, with special methods of determination of the point of gamma rays interaction. Ojala et al [4] presented a study and comparison of different sensor configurations for accurate determination of the gamma interaction point in a monolithic scintillation crystal. This triggered an idea to replace a common pixelated block detector used in present TOF PET scanners by a continuous crystal. A comparative study of a number of different photomultipliers in fast timing, presented in chapter 9, showed the importance of the number of photoelectrons collected in a photomultiplier for the optimal time resolution. Use of one, monolithic scintillator, instead of many small pixels should considerably increase the number of photons collected at the photocathode of a PMT. Because the time resolution is inversely proportional to the square root of the number of photoelectrons, the timing performance of such a detector should be significantly improved. Of course, such a change involves introducing a multichannel photodetector to assure determination of the gamma interaction point inside the crystal.

B. Aim of the study

The aim of the studies presented in this chapter is to measure and optimize the timing properties of a detector consisting of a 16-channel photomultiplier H8711-200MOD from Hamamatsu and a $20 \times 20 \times 20 \text{ mm}^3$ LYSO crystal from Saint-Gobain. It is worth underline, that a PMT with very high quantum efficiency of 43% was selected for these experiments.

2. Experimental details

A. Scintillators and photomultiplier

Presented studies were carried out with three scintillating crystals. The 10x10x5 mm³ LSO crystal was used for general timing characterization of the tested photomultiplier. Then the monolithic 20x20x20 mm³ LYSO crystal was tested as a candidate for a future continuous TOF PET detector. Finally, measurements with the 4x4x20 mm³ LSO scintillator were performed for comparison with the results obtained for the monolithic 20x20x20 mm³ LYSO.

In each case the mechanically polished LSO/LYSO crystals were wrapped with several layers of white Teflon tape.

TABLE I
THE MAIN PROPERTIES OF THE HAMAMATSU H8711-200MOD PHOTOMULTIPLIER

		Type	Serial No.
		H8711-200MOD	ZB0730
White Sens. [uA/lm]	Blue Sens. [uA/lm]	QE [%] at 350nm	Uniformity Max/Min
117	15.5	43	1.5
Photocathode	Window	Structure	Stages
Bialkali	Borosilicate Glass	Metal Channel Dynodes	12

For the presented experiments the Hamamatsu 16-channel, multianode photomultiplier H8711-200MOD has been chosen. The main properties of this PMT are presented in Table I and the dimensional outline of its input window is shown in Fig. 1. This metal channel photomultiplier is characterized by very high quantum efficiency of 43%. Its single channel size of about 4 mm is comparable to typical finger-like crystals commonly used in PET.

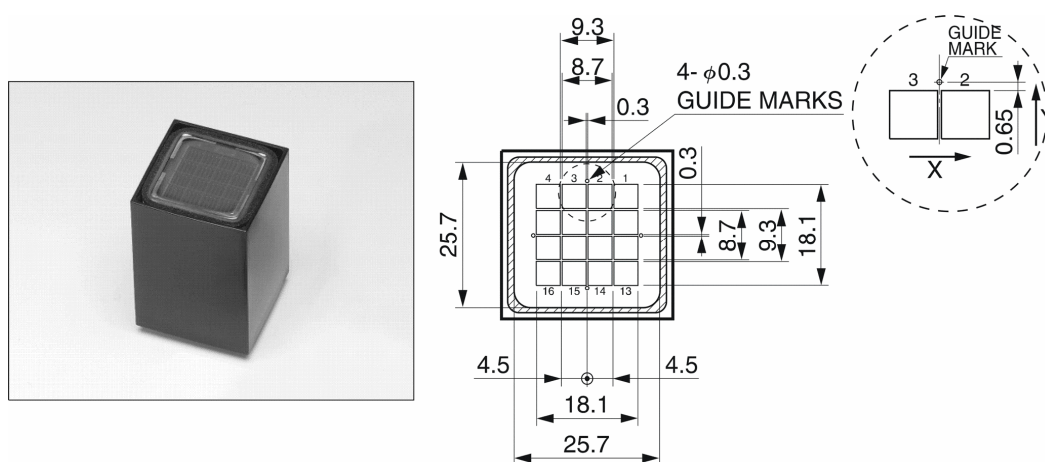


Fig. 1. The dimensional outline of the Hamamatsu H8711-200MOD input window.

The linear voltage divider with the ratios of: 2-2-2-1-1...1-1-1, integrated into the PMT assembly, was made by Hamamatsu.

B. Experimental methods

The number of photoelectrons per energy unit (phe/MeV) was measured for all the crystals using the Bertolaccini et al method. The time jitter of the tested photomultipliers was measured using a light pulser based on an XP22 light emitting diode. In all the timing measurements, a slow-fast arrangement was used for a precise selection of the required energy window set at the 511 keV full energy peak from a ^{22}Na gamma-source.

C. Arrangement of the sum-signal

In the previous experiment, described in chapter 8.4 the PMT anode signals were summed simply by connecting two short cables from the anode outputs into one cable. However, such a simple method is not useful for a PET detector, since the anode signals are needed for determination of the gamma interaction position. Moreover, the summing of the 16 anode signals into one cable destroys the rise time of the output pulse, leading to significant deterioration of the time resolution. Since the metal channel photomultipliers like H8711 possess a common dynode structure, the signal from the last dynode can be used instead of the sum of the anodes.

In the experimental set-up the sum of the anode signals was used only for energy gate generation. Each signal was plugged into a spectroscopy amplifier (2x Stelzer MA8000) and the output signals were sent to the summing module. The module had sixteen $500\ \Omega$ inputs and one output with $10\ \text{k}\Omega$ connected parallel. The output signal was then sent to a single channel analyzer.

Due to the fast decay time of the anode pulse the spectroscopy amplifier was working properly even without the preamplifier. Examples of the signal after the amplifier and the sum of 16 anode signals are presented in Fig. 2.

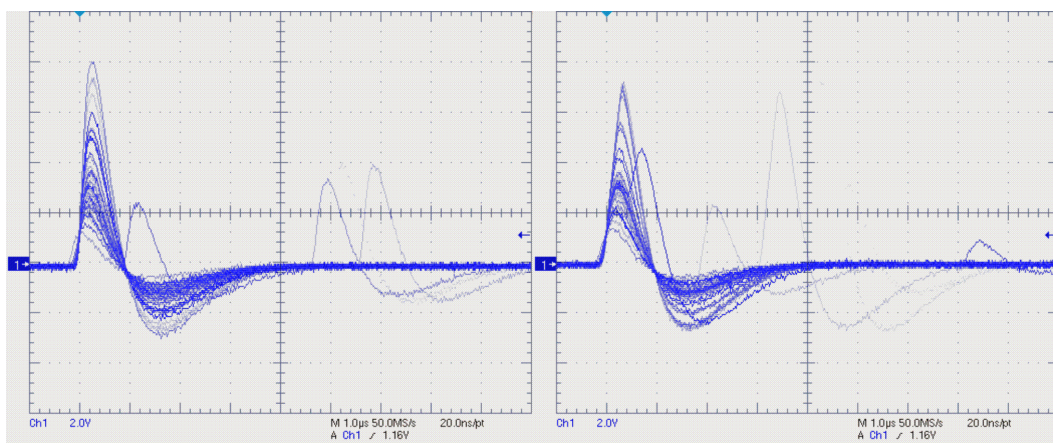


Fig. 2. Screen shots from a digital scope showing the output signal after the spectroscopy amplifier (left) and the sum of 16 anode signals (right). The time scale is 20ns/div.

3. Results

A. Time jitter

In the first part of the study a general characterization of the timing capabilities of the Hamamatsu H8711-200MOD photomultiplier was made.

The time jitter spectra recorded with the tested PMT are presented in Fig. 3. During the experiments the XP22 LED illuminated the whole photocathode. The signal from the area of interest on the photocathode was read in three different modes. First, the gate was generated using a sum of all 16 anode signals. In the next step only 4 central pixels were used and finally, the time jitter for only one pixel was tested.

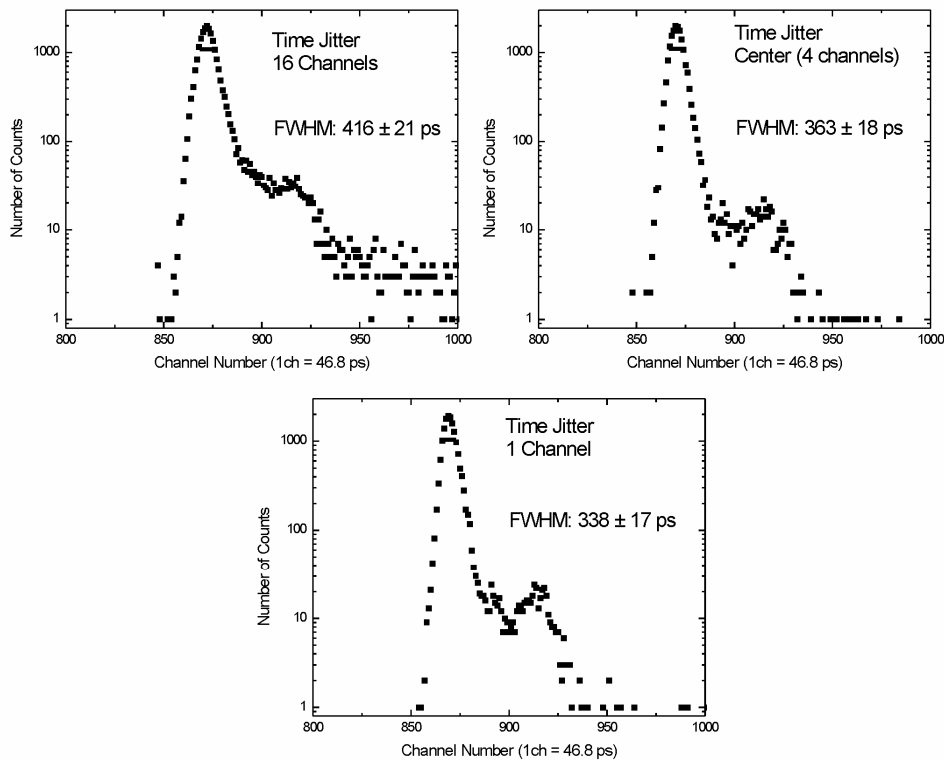


Fig. 3. Transit time jitter spectra measured with XP22 LED illuminating a whole area of the photocathode. First, the gate was set using all the channels of the PMT (top-left), next the gate was changed to allow events only from the central channels (top-right) and finally the time jitter for one channel was measured (bottom).

The results obtained for the tested Hamamatsu metal channel PMT are similar to the properties of commonly used fast photomultipliers with linear focusing dynode structure like Hamamatsu R9800, XP1020, XP3060 or XP20D0 [5], [6] (see chapter 9). However, when the output signal involves more anode signals, considerable deterioration of the time jitter is observed. The multi-anode time jitter spectra are broadened due to the transit time differences between the individual channels.

The second peak, with around one hundred times smaller amplitude, is visible at the right shoulder of all the spectra in Fig. 3. This is a common effect seen in time jitter spectra, induced by the photoelectrons not multiplied in the dynode structure but inelastically scattered back on the first dynode towards the photocathode.

B. Time resolution with $10 \times 10 \times 5 \text{ mm}^3$ LSO

This section is the second part of the general characterization of timing capabilities of the Hamamatsu H8711-200MOD photomultiplier. The presented results are compared with the timing data collected in [7], [5], [6] and mostly presented in chapters 8 and 9. The size of the selected scintillator allowed the determination of the limits of achievable time resolution when not affected by light transport and attenuation in the big, monolithic crystal.

Since in PET applications the PMT anode signals are often used for identification of where the gamma interaction took place, the signal from the last dynode was used for the time resolution measurements. As it was mentioned in section 2.C, the dynode structure of H8711 photomultiplier is common for all the channels and hence the last dynode signal can be used instead of summing of the anode signals.

Fig. 4 presents the time spectrum measured with the $10 \times 10 \times 5 \text{ mm}^3$ LSO crystal in coincidence with the BaF_2 reference detector. In this case the gate was derived from the 4 central pixels.

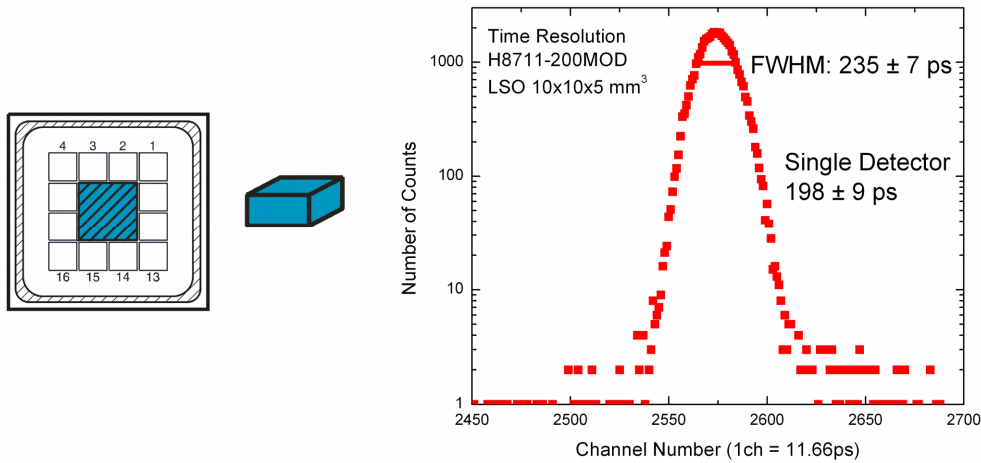


Fig. 4. The time spectrum measured with the $10 \times 10 \times 5 \text{ mm}^3$ LSO crystal placed in the center of the Hamamatsu H8711-200MOD 16-channel photomultiplier.

The more detailed results of the time resolution measurements together with a number of photoelectrons are presented in Table II. In the Table, the data collected with various fast timing photomultipliers with linear focusing dynode structure is also presented. The time resolution (at FWHM) for a single detector, after subtracting the contribution of the reference BaF_2 detector, is presented in the third column. The numbers of photoelectrons per MeV and for 511 keV are shown in the fourth and fifth column, respectively. In the last column the time resolution normalized to the number of photoelectrons and excess noise factor is shown.

The timing capabilities of the Hamamatsu H8711 phototube are similar to other candidates for a future TOF PET. However, the Hamamatsu tube suffers due to poor electron collection efficiency, which is reflected in the small number of photoelectrons. Photoelectron collection efficiency in multichannel photomultipliers is limited to about 60 – 70% due to geometrical open area of the metal channel dynodes. This type of electrodes possesses large dead area on the top, flat part of the dynodes (see chapter 5.3). The excellent timing value of 198 ps, was possible due to a very high QE of 43%.

TABLE II
TIME RESOLUTION MEASURED WITH THE 10x10x5 LSO COUPLED TO VARIOUS FAST
PHOTOMULTIPLIERS

PMT	Time resolution at FWHM, Δt [ps]		Nphe/MeV [phe/MeV]	Nphe for 511keV, N [phe]	$\Delta t/\sqrt{N}/\sqrt{ENF}$ [ps \sqrt{phe}] $\times 10^3$
	Measured	Corrected ^{a)}			
H8711	235 \pm 7	198 \pm 9	5900 \pm 200	3000 \pm 100	10.1 \pm 0.5
R9800 ^{b)}	237 \pm 7	199 \pm 9	6300 \pm 200	3200 \pm 100	10.3 \pm 0.5
XP1020 ^{b)}	247 \pm 7	211 \pm 9	4900 \pm 100	2500 \pm 100	10.3 \pm 0.5
XP3060 ^{c)}	238 \pm 7	200 \pm 9	6400 \pm 200	3300 \pm 100	11.2 \pm 0.5
XP20D0 ^{d)}	210 \pm 6	166 \pm 9	8100 \pm 200	4100 \pm 100	10.4 \pm 0.5

a) corrected for the contribution of the BaF₂ reference detector of 128 \pm 4 ps

b) data taken from [15]

c) data taken from [9]

d) data taken from [2]

The final result of the time resolution equal to 198 ps is an outcome of an optimization of the settings in the experimental set-up, especially the LE discriminator threshold. The dependency of timing on the fraction of a signal triggering the LE discriminator for the H8711 photomultiplier compared to that of linear focused PMTs is presented in Fig. 5. The plot was discussed in more details in chapter 9. For the H8711 phototube an optimum is seen around the 5% fraction, similar to the classic fast photomultipliers.

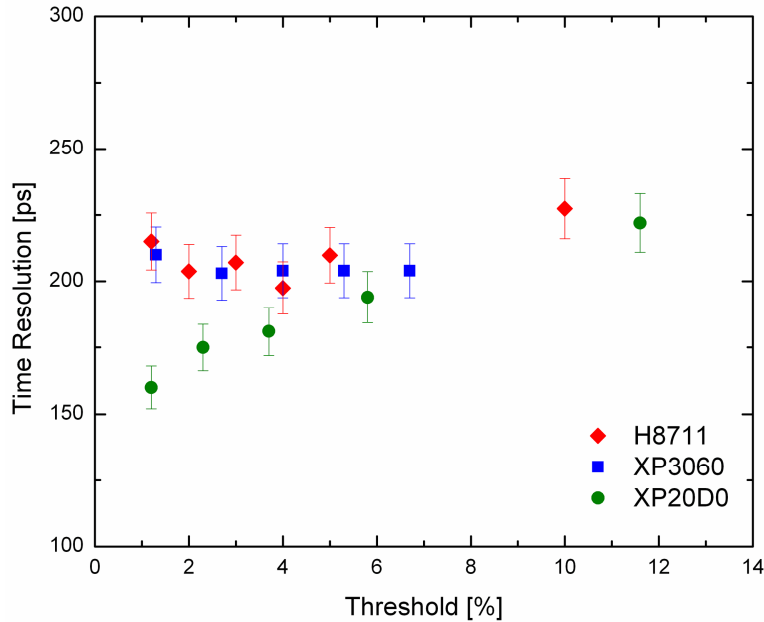


Fig. 5. The time resolution dependence on the LE threshold for the H8711-200MOD PMT and for two fast photomultipliers with linear focusing dynode structure. The measurements were done with the 10x10x5 mm³ LSO crystal. Presented values have been corrected for the contribution of the reference detector.

In chapter 9 the plot of the time jitter versus the normalized time resolution for the 10x10x5 mm³ LSO crystal was presented for various types of fast photomultipliers. Such plot is presented in Fig. 6 together with the data for the Hamamatsu H8711-20MOD tested in

this study (diamond point). The square points in Fig. 6 represent measurements done with classic fast PMTs. The relation is linear and proportional to the time jitter. The circle points at the bottom represent fast PMTs with a different anode construction, in particular with a screening grid at the anode (XP20D0) [8] and with a design characteristic for metal channel photomultipliers. In this case a linear dependence could also be assumed but shifted down in relation to the classic PMTs line.

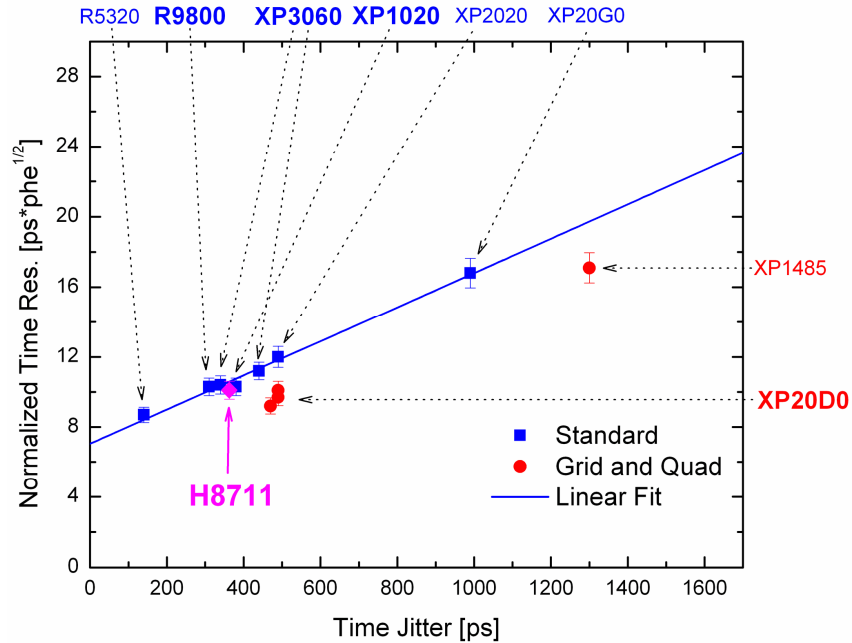


Fig. 6. The dependence of the normalized time resolution versus the time jitter for the tested H8711-200MOD phototube and other fast PMTs. The measurements were made with a $10 \times 10 \times 5 \text{ mm}^3$ LSO crystal.

The results obtained for the tested Hamamatsu phototube are in very good agreement with the data collected for various kinds of linear focused fast photomultipliers. However, the last dynode and the anode construction of this metal channel PMT should allow further improvement of the time resolution due to a lower fraction level. Such improvement is observed in the case of XP20D0, equipped with the screening grid at the anode [8] or for 4-channel PMT XP1485. The anode pulse of the metal channel PMT should not be affected by the prepulse resulting from electrons travelling between the penultimate dynode and the last dynode as it does in linear focused PMTs. However, high number of 16 channels may introduce additional effects that do not made the low fraction level advantageous.

C. Time resolution with $20 \times 20 \times 20 \text{ mm}^3$ LYSO

In the next part of the study the detector was tested with the continuous $20 \times 20 \times 20 \text{ mm}^3$ LYSO crystal. As in the case of measurements with the LSO crystal, all the timing information was gathered using the dynode pulse.

Fig. 7 presents the time spectrum measured with the $20 \times 20 \times 20 \text{ mm}^3$ LYSO crystal in coincidence with the BaF_2 reference detector. In this case the energy gate was formed using all the channels of the Hamamatsu PMT. Again, the final result of the time resolution of 272 ps is an effect of the optimized threshold setting of the LE discriminator. The plot of the

time resolution versus the fraction triggering the electronics is presented in Fig. 8.

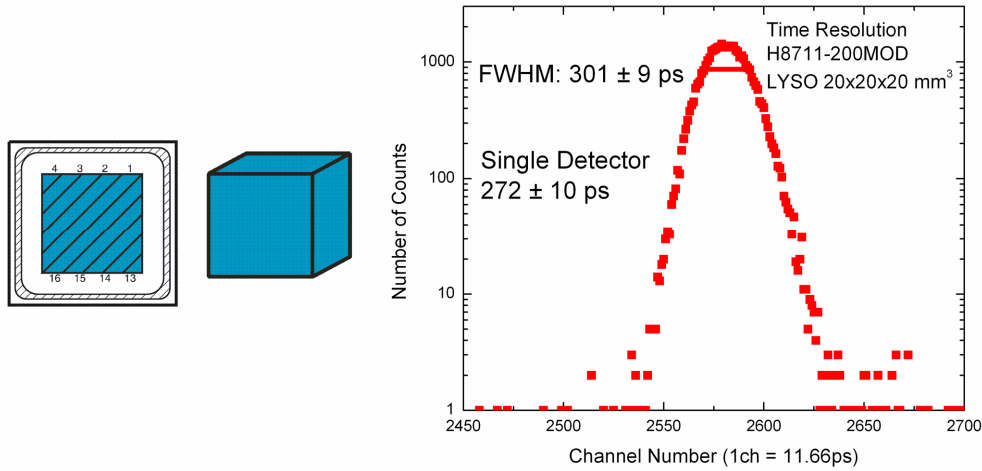


Fig. 7. The time spectrum measured with the $20 \times 20 \times 20 \text{ mm}^3$ LYSO crystal coupled to the Hamamatsu H8711-200MOD 16-channel photomultiplier.

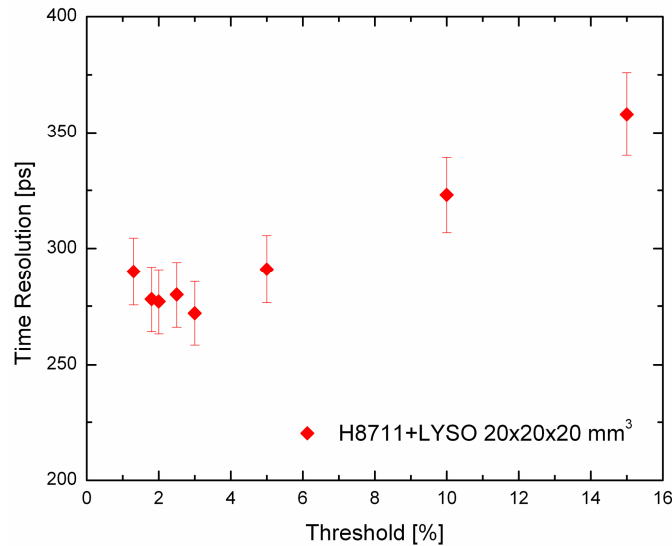


Fig. 8. The time resolution dependence on a LE threshold for the detector consisting of the H8711-200MOD photomultiplier and the $20 \times 20 \times 20 \text{ mm}^3$ LYSO crystal. The values were corrected for the contribution from the reference detector.

The time resolution measured with the large LYSO crystal is more than 35% worse than that of the small $10 \times 10 \times 5 \text{ mm}^3$ LSO. This is due to the smaller number of photoelectrons, only 4000 phe/MeV, compared to 5900 phe/MeV obtained with the LSO crystal. The observed light yield degradation is caused by geometrical effects of light transport in the larger crystal and also by different qualities of the tested crystals. The LSO was specially selected for timing measurements and possesses high light output whereas the LYSO is a standard crystal. The second effect, which deteriorates the time resolution in the monolithic scintillator, is a contribution from the time spread of the light collection inside the larger LYSO crystal. Nevertheless, the value of about 275 ps measured for a single continuous LYSO detector (after correction for the reference BaF_2 detector) suggests that the proposed

TOF PET system with the monolithic crystal could establish a new approach for this kind of tomography scanners.

The time resolution of the tested detector along with the number of photoelectrons is shown in Table III. The data recorded with the same 20x20x20 mm³ LYSO crystal but with the XP20D0 (QE=35%) photomultiplier was also added for comparison. The big difference in the numbers of photoelectrons between both tubes can be easily seen, despite the higher quantum efficiency of the Hamamatsu tube (QE=43%).

TABLE III
TIME RESOLUTION MEASURED WITH THE LYSO 20x20x20 COUPLED TO THE H8711 AND XP20D0 PHOTOMULTIPLIERS

Position	Time resolution at FWHM, Δt [ps]		Nphe/MeV [phe/MeV]	Nphe for 511keV, N [phe]	$\Delta t/\sqrt{N}/\sqrt{ENF}$ [ps \sqrt{phe}] x10 ³
	Measured	Corrected ^{a)}			
H8711	301 ± 9	272 ± 10	4000 ± 100	2100 ± 100	11.6 ± 0.5
XP20D0	260 ± 8	226 ± 9	6000 ± 200	3000 ± 100	12.1 ± 0.5

a) corrected for the contribution of the BaF₂ reference detector of 128 ± 4 ps

In Table IV a comparison is made between the continuous crystal detector and a single 4x4x20 mm³ LSO pixel placed in various positions on standard fast photomultipliers. In the case of the 16-channel Hamamatsu H8711 the energy gate was set using a single anode signal corresponding to the chosen pixel. In the case of the linear focused PMTs the time resolution was measured in five positions over a photocathode. Drawings of the crystal positions and pixels used in the tests with H8711 PMT are shown in Fig. 9.

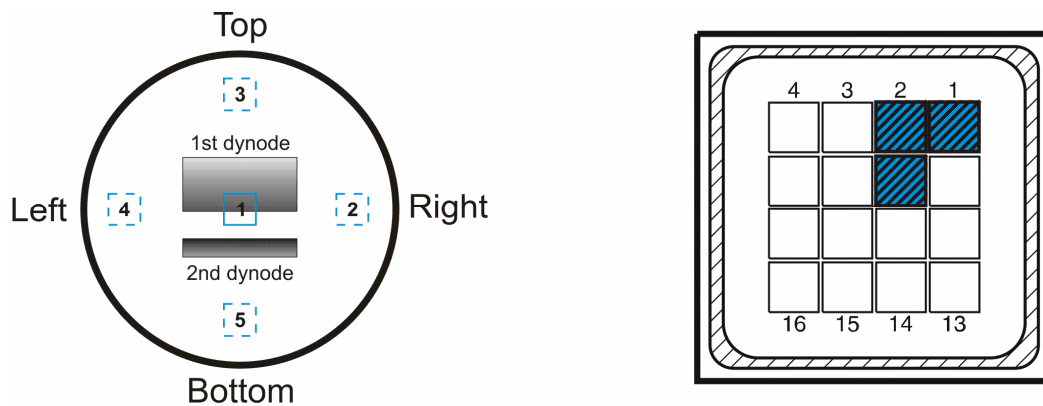


Fig. 9. Drawings of positions of the 4x4x20 mm³ LSO crystal on the photocathode in linear focused PMTs and pixels used in the H8711-200MOD photomultiplier.

In the case of the H8711 photomultiplier the time resolution is identical at all the three measured positions. The number of photoelectrons in each pixel is also the same. The situation is different in the case of the linear focused PMTs. The values in the middle of the standard fast photomultipliers are better in comparison to the values obtained with single pixels in the tested 16-channel Hamamatsu, however the results obtained on the remaining four positions are much worse. The time resolution measured for the three channels in the continuous crystal detector shows that the homogeneity of the time resolution over the whole

area of the detector is its major advantage.

TABLE IV
TIME RESOLUTION MEASURED WITH THE LYSO 20x20x20 COUPLED TO THE H8711 AND LSO 4x4x20 PLACED IN DIFFERENT POSITIONS ON LINEAR FOCUSED PMTs

Position	Time resolution at FWHM, Δt [ps]		Nphe/MeV [phe/MeV]	Nphe for 511keV, N [phe]	$\Delta t/\sqrt{N}/\text{ENF}$ [ps/ $\sqrt{\text{phe}}] \times 10^3$
	Measured	Corrected ^{a)}			
H8711 A1	297 ± 9	268 ± 10	4000 ± 100	2100 ± 100	11.5 ± 0.5
H8711 A2	299 ± 9	270 ± 10	4000 ± 100	2100 ± 100	11.5 ± 0.5
H8711 A6	298 ± 9	269 ± 10	4000 ± 100	2100 ± 100	11.5 ± 0.5
R9800 C.	246 ± 7	210 ± 9	6100 ± 200	3100 ± 100	10.9 ± 0.5
XP1020 C.	267 ± 8	234 ± 9	4700 ± 100	2400 ± 100	11.1 ± 0.5
Left	307 ± 15	279 ± 17	3800 ± 100	2000 ± 100	12.1 ± 0.8
Right	310 ± 15	282 ± 17	3900 ± 100	2000 ± 100	12.2 ± 0.8
Top	331 ± 17	305 ± 18	2900 ± 100	1500 ± 50	11.4 ± 0.7
Bottom	297 ± 15	268 ± 17	4000 ± 100	2100 ± 100	11.9 ± 0.8
XP3060 C.	272 ± 8	240 ± 9	6300 ± 200	3200 ± 100	13.2 ± 0.6
Left	350 ± 11	326 ± 11	3800 ± 100	2000 ± 100	14.2 ± 0.6
Right	322 ± 10	295 ± 11	4300 ± 100	2200 ± 100	13.5 ± 0.6
Top	328 ± 10	302 ± 11	3600 ± 100	1800 ± 100	12.5 ± 0.6
Bottom	335 ± 10	310 ± 11	4400 ± 100	2200 ± 100	14.1 ± 0.6
XP20D0 C.	234 ± 7	196 ± 9	5900 ± 200	3000 ± 100	10.5 ± 0.5

a) corrected for the contribution of the BaF₂ reference detector of 128 ± 4 ps

4. Discussion

A. Timing characteristic of the H8711-200MOD

In this chapter, all the experiments, discussion and analysis were made in order to understand the time resolution limitations of the continuous crystal detector.

The 16-channel photomultiplier H8711-200MOD used during the study showed poor photoelectron collection efficiency and in consequence a low number of photoelectrons. As it was showed in Chapter 9 in the case of LSO/LYSO crystals, the photoelectron number is a key factor influencing the final timing capabilities of a scintillation detector. This rule was also reflected in the present study. Even with very high quantum efficiency (43%) of the tested Hamamatsu PMT the time resolution obtained with the 20x20x20 mm³ LYSO was worst in comparison to the data obtained with the linear focused PMT with lower photocathode sensitivity (see Table III). The biggest advantage of the continuous crystal detector is its homogeneity of the time resolution over the whole area of the photocathode (see Table IV).

In the present study the time resolution was measured also with a single 4x4x20 mm³ LSO crystal placed on one of the channels in the H8711 photomultiplier. The result is presented in Table V. The obtained time resolution is equal to 255 ps for a single detector, whereas the photoelectron number is equal to 3900 phe/MeV. These values indicate that instead of a continuous crystal, a pixelated block detector coupled to a position sensitive photodetector could be an alternative solution for the future TOF PET.

TABLE V
TIME RESOLUTION MEASURED WITH THE LSO 4x4x20 COUPLED TO ONE CHANNEL OF THE
H8711 PHOTOMULTIPLIER

PMT	Time resolution at FWHM, Δt [ps]		Nphe/MeV [phe/MeV]	Nphe for 511keV, N [phe]	$\Delta t\sqrt{N}/\sqrt{ENF}$ [ps \sqrt{phe}] $\times 10^3$
	Measured	Corrected ^{a)}			
H8711	285 ± 9	255 ± 10	3900 ± 100	2000 ± 100	10.6 ± 0.5

a) corrected for the contribution of the BaF₂ reference detector of 128 ± 4 ps

B. Position decoding in a continuous crystal

Application of a continuous crystal instead of a pixelated block detector requires new methods of spatial identification of annihilation quanta interaction point inside the scintillator. Finding the optimal and accurate method of position decoding inside a monolithic crystal is a challenging task. Analysis of the best algorithms is out of the scope of this work, however the main difficulties are mentioned below.

One of the main problem is the reflective layer on the scintillator walls. For the time of flight capability the amount of light collected from the crystal has to be maximized. Moreover, directional information cannot be lost in order to allow the gamma interaction position decoding, so the black wrapping is not useable. The Teflon wrapping assure high light output but the photons reflected from this dispersive layer only create a statistical background useless during the decoding. Mirror-like walls (covered for example by VM2000 film from 3M) seems to be the best choice, since only this kind of wrapping gives a chance to keep the directional information.

LSO/LYSO crystals have a very high level of background due to internal radioactivity. This is a consequence of its composition. These materials are lutetium-based scintillators, which contain the radioactive isotope ¹⁷⁶Lu, a naturally occurring beta emitter. During the measurements with the 20x20x20 mm³ LYSO crystal its natural background gives around 2300 c/s, and can dominate the events resulting from 511 keV annihilation quanta. Such high internal radioactivity is a problem even in coincident measurements (such as PET) causing increase of the random events.

Another important aspect of the discussed detector is the fact that the attenuation length for 511 keV in LYSO crystal is equal to 1.2 cm. It means that gamma interactions occur in the entire volume of the crystal. Such a situation leads to inaccuracy in spatial resolution due to poor depth of interaction (DOI) determination. One of the possibilities of improving the DOI information is adding of 4 avalanche photodiodes on the top of the crystal as proposed by Ojala [4].

C. Conclusions

The presented results suggest that metal channel position sensitive PMTs with very high quantum efficiency can provide very good timing capabilities in a TOF PET detector. On the other hand, the multichannel PMT suffers due to poor photoelectron collection efficiency. The timing performance obtained with the small 10x10x5 mm³ LSO crystal is as good as that of

a fast linear focused photomultipliers. The time resolution of 272 ps measured for a single detector with a monolithic LYSO scintillator corresponds to 385 ps for the same two detectors in coincidence. This value is approximately 200 ps better than the time resolution of commercially available TOF PET scanners.

The continuous crystal detector with improved photocathode uniformity is characterized by a much better homogeneity of the timing response comparing to detectors based on linear focused PMTs and pixelated block detectors. However, the analysis of the experimental data and the requirements of spatial resolution in PET suggests that a pixelated block detector placed on a position sensitive PMT could be a more practical solution.

5. References

- [1] S. Surti, A. Kuhn, M. Werner, A. Perkins, J. Kolthammer, and J. Karp, "Performance of Philips Gemini TF PET/CT scanner with special consideration for its time-of-flight imaging capabilities," *J. Nucl. Med.*, vol. 48, no. 3, p. 471, 2007.
- [2] W. Moses and S. Derenzo, "Prospects for time-of-flight PET using LSO scintillator," *IEEE Trans. Nucl. Sci.*, vol. 46, no. 3, pp. 474–478, 1999.
- [3] A. Kuhn, S. Surti, J. Karp, G. Muehlehner, F. Newcomer, and R. VanBerg, "Performance assessment of pixelated LaBr₃ detector modules for time-of-flight PET," *IEEE Trans. Nucl. Sci.*, vol. 53, no. 3, pp. 1090–1095, 2006.
- [4] P. Ojala, A. Boussselham, L. Eriksson, A. Brahme, and C. Bohm, "Influence of sensor arrangements and scintillator crystal properties on the 3D precision of monolithic scintillation detectors in PET," in *Nuclear Science Symposium Conference Record, 2005 IEEE*, vol. 5. IEEE, 2005, pp. 3018–3021.
- [5] T. Szczesniak, M. Moszynski, L. Swiderski, A. Nassalski, P. Lavoute, and M. Kapusta, "Fast photomultipliers for TOF PET," *IEEE Trans. Nucl. Sci.*, vol. 56, no. 1, pp. 173–181, Feb. 2009.
- [6] T. Szczesniak, M. Moszynski, A. Synfeld-Kazuch, L. Swiderski, M. A. Spurrier-Koschan, and C. L. Melcher, "Timing resolution and decay time of LSO crystals co-doped with calcium," *IEEE Trans. Nucl. Sci.*, vol. 57, no. 3, pp. 1329–1334, Jun. 2010.
- [7] M. Moszynski, M. Kapusta, A. Nassalski, T. Szczesniak, D. Wolski, L. Eriksson, and C. Melcher, "New prospects for time-of-flight PET with LSO scintillators," *IEEE Trans. Nucl. Sci.*, vol. 53, no. 5, pp. 2484–2488, 2006.
- [8] M. Moszynski, M. Kapusta, D. Wolski, M. Balcerzyk, S. Flyckt, P. Lavoute, C. Marmonier, and H. Mach, "New fast photomultipliers with a screening grid at the anode," *IEEE Trans. Nucl. Sci.*, vol. 51, no. 4, pp. 1701–1706, 2004.

11. Timing Resolution and Decay Time of LSO Crystals Co-doped with Calcium

1. Introduction

A. Motivation

Incorporation of information about the time of flight of annihilation quanta in positron emission tomography needs a scintillator optimized for high efficiency of 511 keV gamma detection and characterized by the best possible timing properties. Very good time resolution, below 200 ps for a single detector measured with LSO crystals was presented in previous chapters proving that an LSO scintillator is, at present, the best choice for a TOF PET.

The time resolution of a scintillating crystal depends mainly on the decay time constant of a light pulse and is proportional to the inverse square root of the number of photoelectrons collected in a photodetector (see chapter 9). Recently a new, improved LSO, co-doped with Ca, was reported [1]. The modified scintillators exhibit a faster decay time, reduced to approximately 30 ns, and about 30 % higher light output.

B. Aim of the study

The goal of this chapter is to present a comparative study of LSO samples with different co-doping percentages, ranging from 0 to 0.4 atomic % of Ca added to the starting raw material. Characterization of these co-doped crystals includes measurements of the time resolution with annihilation quanta from ^{22}Na gamma source, number of photoelectrons, and decay time constant.

2. Detector details

A. Scintillators

The studies were carried out on five samples of unpolished $5\times 5\times 5\text{ mm}^3$ LSO crystals doped with 0.1 atomic % Ce (with respect to Lu); each was co-doped with a different amount of Ca. The co-dopant concentrations were equal to 0.0, 0.1, 0.2, 0.3 and 0.4 atomic percent Ca with respect to Lu in the melt from which the crystals were grown. The actual concentrations of the dopant in the crystals themselves have not been measured and will differ from these values due to solid-liquid segregation and the fraction of melt solidified, as discussed in [1] and [2]. In general, the dopant concentrations in the crystals should be around 20% of the melt values, with the precise concentration depending to some degree on the location of the sample in the boule. All of the samples were grown at the University of Tennessee in the same growth station via the Czochralski technique, in an atmosphere composed of nitrogen mixed with a small amount of oxygen. The Lu_2O_3 , SiO_2 , CeO_2 , and CaO starting materials were at least 99.99% pure. More details can be found in [1].

Results obtained with the tested samples were compared with a pre-existing LSO crystal

(LSO2003) that was not co-doped. This sample has dimensions of $10 \times 10 \times 5 \text{ mm}^3$, is polished on all sides and was used during the measurements presented in Chapters 8-10. This crystal was specifically selected from a larger pool of crystals as having one of the highest light outputs, and was put at our disposal by Chuck Melcher in 2003 for use in a fast timing experiments. It is characterized by very good time resolution [3] and light output much above the mean value for standard LSO:Ce.

In all experiments the crystals were wrapped with several layers of white Teflon tape and coupled to a photomultiplier using silicone grease.

B. Photomultiplier

During the study a Photonis XP20D0, SN2026 photomultiplier, equipped with a screening grid at the anode [4] was used as a photodetector. Its blue sensitivity is equal to $13.7 \mu\text{A}/\text{lmF}$ which corresponds to a quantum efficiency of about 34%. This PMT was tested earlier in experiments described in chapters 8-10. A tapered voltage divider was used to assure good linearity of the anode pulse.

C. Experimental methods

The number of photoelectrons per unit energy (phe/MeV) was measured for all the crystals using the Bertolaccini method and ^{137}Cs gamma source.

The time resolution study was performed in coincidence experiments with 511 keV annihilation quanta from a ^{22}Na gamma source. In a reference detector, a BaF_2 crystal in the shape of a truncated cone (20 mm and 25 mm in diameter and 15 mm high) was coupled to the XP20Y0Q/DA PMT. Its time resolution for a 511 keV full energy peak was equal to $143 \pm 4 \text{ ps}$.

Decay time constant measurements were made by the Bollinger-Thomas single photon method [5], [6] using a ^{137}Cs gamma source.

3. Results

A. Number of photoelectrons

Sample spectra of ^{137}Cs gamma source collected with all the tested crystals are presented in Fig. 1. The shape of the single photoelectron spectrum is also shown. The calculated values of photoelectrons per MeV are presented in Table I together with the result obtained for $10 \times 10 \times 5 \text{ mm}^3$ LSO2003, tested in previous chapters.

The lowest photoelectron number was observed for the standard LSO, without co-doping. This crystal gave only 5700 phe/MeV. Co-doping of 0.1% of calcium significantly improved the light output to 7800 phe/MeV. Unfortunately, high co-doping levels gave systematically lower values of the photoelectron numbers and finally led to the result below 6000 phe/MeV for co-doping equal to 0.3% of Ca. The dependency of the photoelectron number versus the Ca co-doping is presented in Fig. 2. These results are in very good agreement with the measurements done in [1].

Taking into account the photoelectron numbers presented here, co-doping with a low amount of calcium seems to be optimal with respect to the light yield; however the LSO2003, without co-dopant, shows comparable performance. This is due to the fact that the LSO2003

crystal was hand-picked from a larger pool of crystals due to its high light yield, while the standard and codoped LSO crystals in this study are representative of the mean value for each composition. In general, the mean light output of calcium co-doped crystals is significantly higher than that of standard LSO.

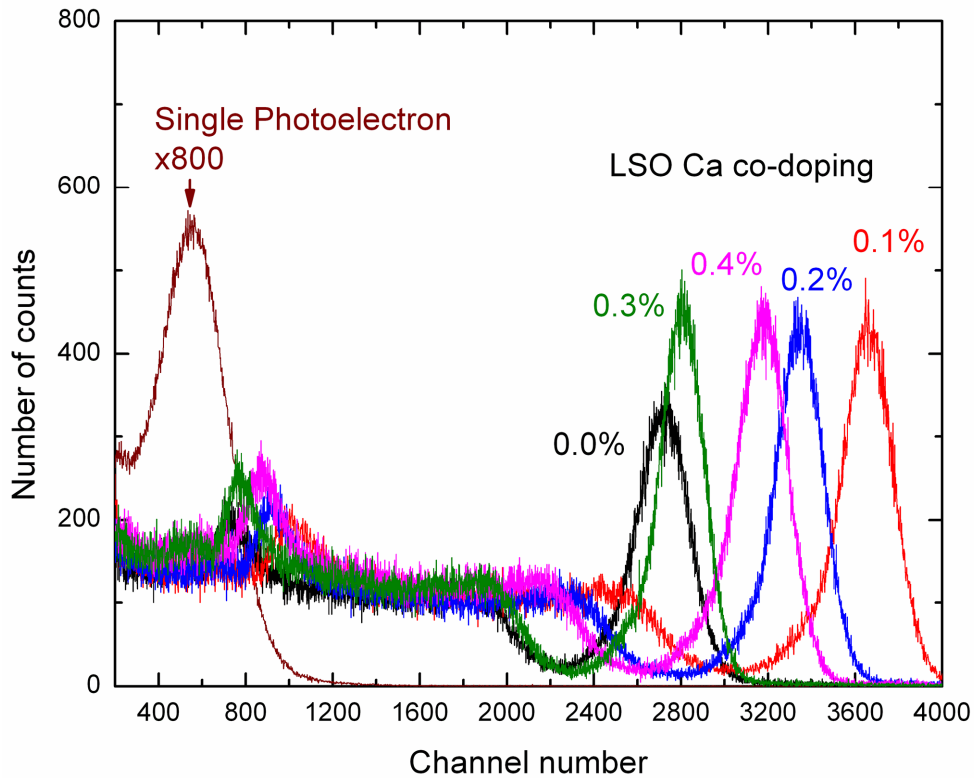


Fig. 1. Sample spectra of the tested LSO crystals with various Ca co-doping collected with ^{137}Cs gamma source.

TABLE I

THE NUMBER OF PHOTOELECTRONS COLLECTED WITH THE TESTED LSO SAMPLES AND SELECTED 10x10x5 LSO2003

Crystal	Nphe/MeV [phe/MeV]
LSO2003 0.0% Ca	8100 ± 200
LSO 0.0% Ca	5700 ± 200
LSO 0.1% Ca	7800 ± 200
LSO 0.2% Ca	6900 ± 200
LSO 0.3% Ca	5900 ± 200
LSO 0.4% Ca	6700 ± 200

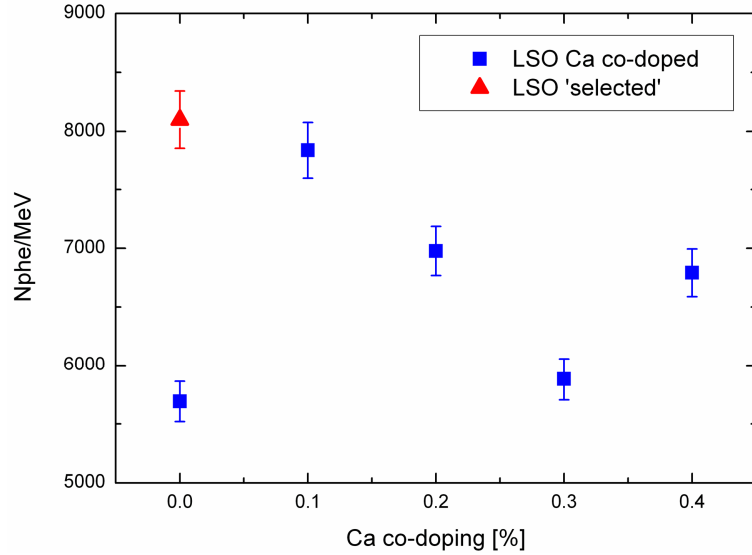


Fig. 2. Dependence of the photoelectron number on the Ca co-doping, measured with the tested samples and selected LSO2003.

B. Time resolution

Examples of the timing spectra obtained with the standard LSO, without co-doping and with the one co-doped with 0.4 % of Ca are presented in Fig. 3.

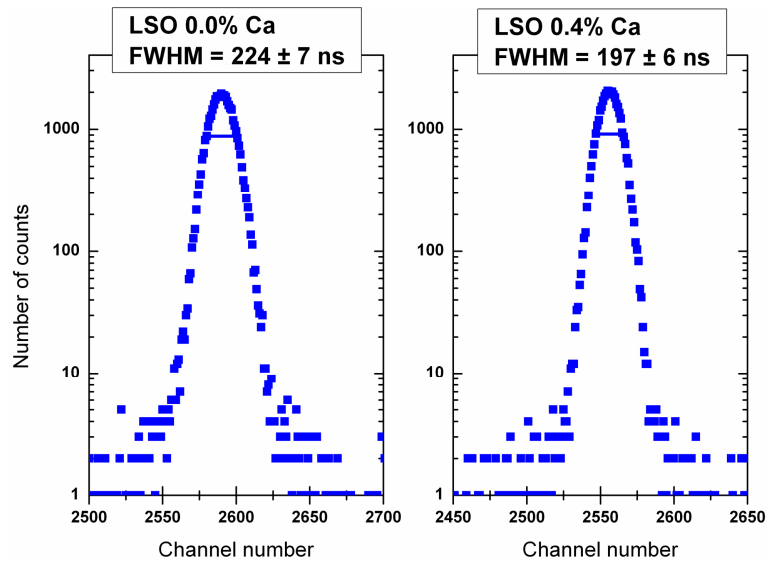


Fig. 3. Sample timing spectra of the tested LSO crystals with 0.0% and 0.4% Ca co-doping collected in coincidence experiments with ^{22}Na gamma source.

In the case of the standard LSO (left spectrum) the measured time resolution was equal to 224 ps, or 173 ps after subtracting the reference BaF_2 detector. This is the worst timing resolution measured during the study. On the other hand, the best time resolution was obtained with the highest Ca co-doping of 0.4%. The collected spectrum is presented on the right in Fig. 3 and shows the coincidence time resolution below 200 ps, which corresponds to 136 ps for a single detector.

All of the timing results together with data for the $10 \times 10 \times 5 \text{ mm}^3$ LSO2003 are presented in

Table II. In the second column of the Table, the measured values for two detectors in coincidence are presented. In the third column the values for a single crystal are given after subtracting the contribution of a reference detector.

TABLE II
TIME RESOLUTION OF THE TESTED LSO SAMPLES AND SELECTED 10X10X5 LSO2003

Crystal	Time resolution at FWHM, Δt [ps]		Nphe for 511keV, N [phe]	$\Delta t\sqrt{N}/\sqrt{ENF}$ [ps $\sqrt{\text{phe}}$] $\times 10^3$
	Measured	Corrected ^{a)}		
LSO 0.0% 'selected'^{b)}	210 \pm 6	166 \pm 9	4100 \pm 100	10.2 \pm 0.5
LSO 0.0% Ca	224 \pm 7	173 \pm 9	2900 \pm 100	8.9 \pm 0.5
LSO 0.1% Ca	201 \pm 6	142 \pm 9	4000 \pm 100	8.5 \pm 0.6
LSO 0.2% Ca	204 \pm 6	145 \pm 9	3500 \pm 100	8.2 \pm 0.5
LSO 0.3% Ca	202 \pm 6	143 \pm 9	3000 \pm 100	7.5 \pm 0.5
LSO 0.4% Ca	197 \pm 6	136 \pm 9	3400 \pm 100	7.6 \pm 0.5

a) corrected for the contribution of the BaF₂ reference detector of 143 \pm 4 ps
b) following chapter 8

It can be easily seen that in all the cases of co-doped crystals the time resolution is improved. However, the difference between 0.1% and 0.4% of calcium is small and within the error range. A plot of a single detector time resolution versus Ca co-doping is presented in Fig. 4. In general, the crystals co-doped with Ca had timing resolution at the level of about 140 ps. Despite the highest photoelectron number, the time resolution of 166 ps for the 10x10x5 mm³ LSO2003 was inferior to the Ca co-doped samples tested in this current study.

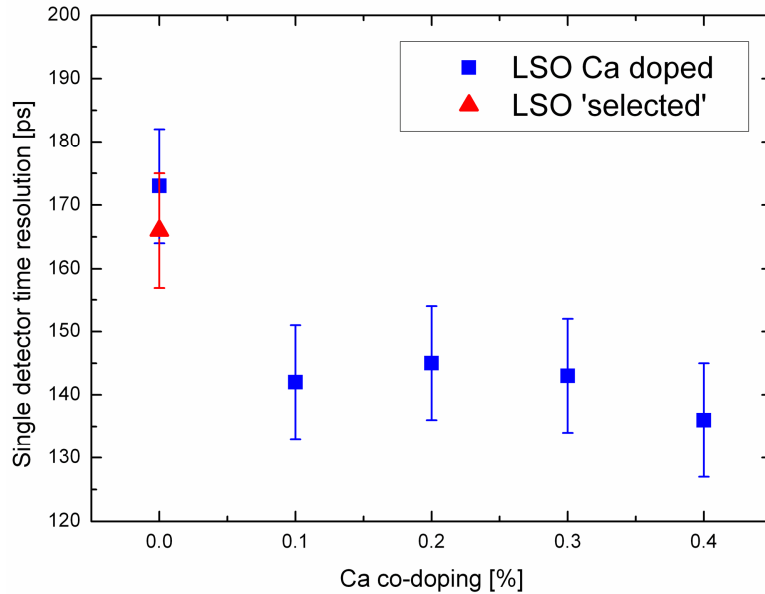


Fig. 4. Dependence of the single detector time resolution versus Ca co-doping measured with the tested samples and the LSO2003.

In the last column of Table II the measured time resolution for a single detector is normalized to the number of photoelectrons for 511 keV, presented in the 4th column, and to

the excess noise factor ($ENF = 1.1$) calculated using FWHM of the single photoelectron spectrum. Improvement of the calculated, normalized time resolution can be observed for successive co-doping. Such behavior suggests differences in the decay time constants of the tested samples, as reported in [1].

C. Decay time constants

The decay time constants were measured using a Bollinger-Thomas single photon method. Examples of the spectra collected for 0.0 % and 0.3 % of Ca co-doping together with fits of a single exponential decay are presented in Fig. 5 and 6. All the results are presented in Table III. The measured quantities agree well with those given in [1].

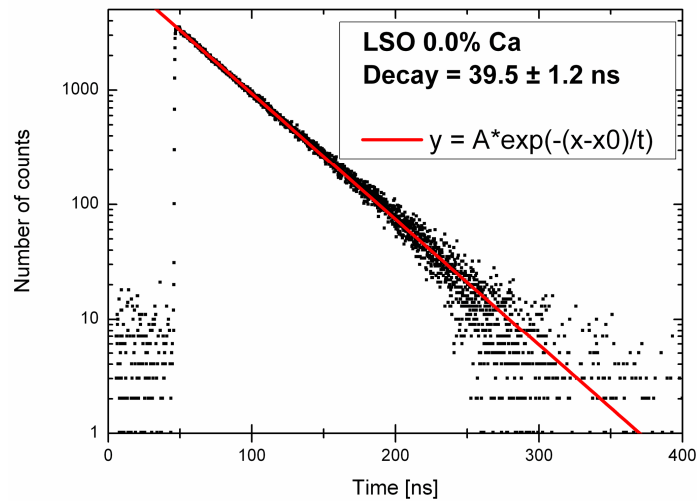


Fig. 5. Time spectra of single photon distribution induced by ^{137}Cs gamma source in the LSO sample with 0.0 % calcium.

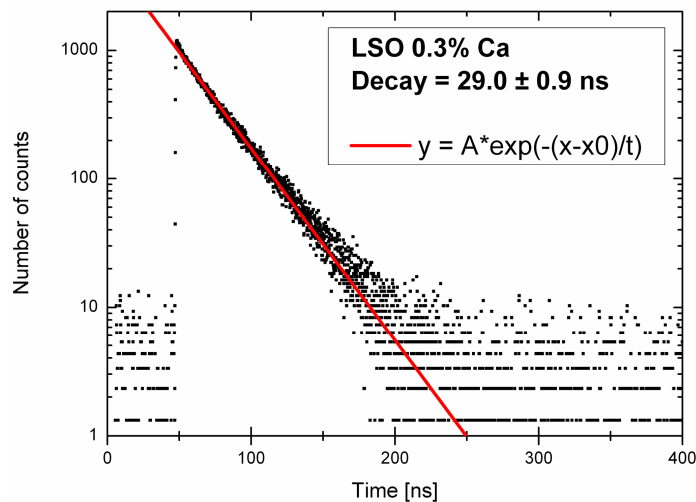


Fig. 6. Time spectra of single photon distribution induced by ^{137}Cs gamma source in the LSO sample with 0.3 % calcium.

Both crystals without Ca co-doping demonstrate the longest decay times, up to 42.4 ns for the LSO2003 and 39.5 ns for the standard LSO sample. The samples with the highest co-

doping of 0.3 % and 0.4 % showed the shortest decay times of around 30 ns. Dependence of the decay time versus Ca co-doping is presented in Fig. 7. Successive co-doping of the LSO led to about 25 % improvement of the decay time constant in comparison to the standard LSO, characterized by a value of approximately 40 ns. However, the question whether it is the limit of the improvement remains open.

TABLE III
DECAY TIME CONSTANTS OF THE TESTED LSO SAMPLES AND SELECTED 10x10x5 LSO2003

Crystal	Decay time constant [ns]	$\Delta t \sqrt{N} / \sqrt{ENF} / \sqrt{\text{Decay}}$
LSO2003 0.0% Ca	42.4 ± 1.3	1.56
LSO 0.0% Ca	39.5 ± 1.2	1.41
LSO 0.1% Ca	36.7 ± 1.1	1.41
LSO 0.2% Ca	34.1 ± 1.0	1.40
LSO 0.3% Ca	29.0 ± 0.9	1.39
LSO 0.4% Ca	30.3 ± 0.9	1.37

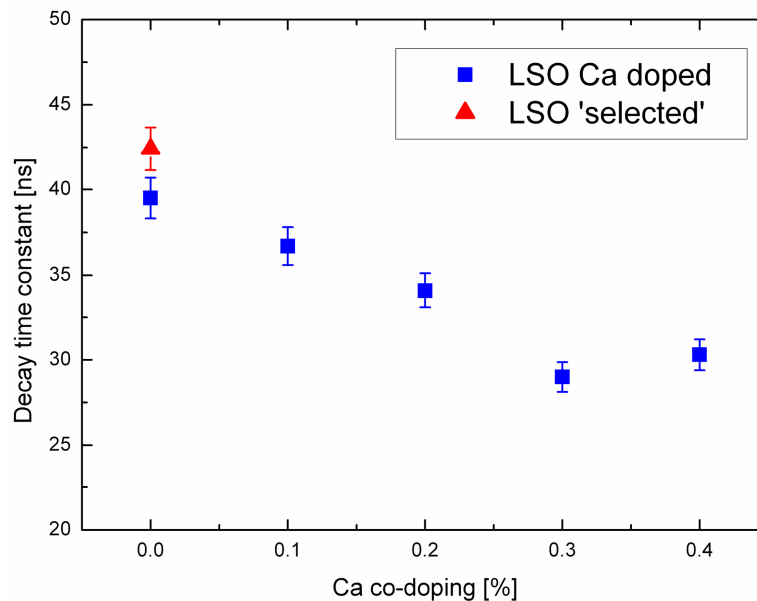


Fig. 7. Dependence of the decay time constants versus Ca co-doping measured with the tested samples and selected LSO2003.

In chapter 9.3.D, dependence of time resolution on a decay time was shown for a wide set of scintillators. A similar plot of the normalized time resolution (from Table II) versus the square root of the decay time is presented in Fig. 8. Linear fit with a slope of 1.4 is also shown. In the last column of Table III the normalized time resolution from Table II (last column) was divided by the square root of the measured decay time constants. The value obtained for all of the tested samples is equal to 1.4 and reflects an influence of the decay time constant on the final timing performance of the detector.

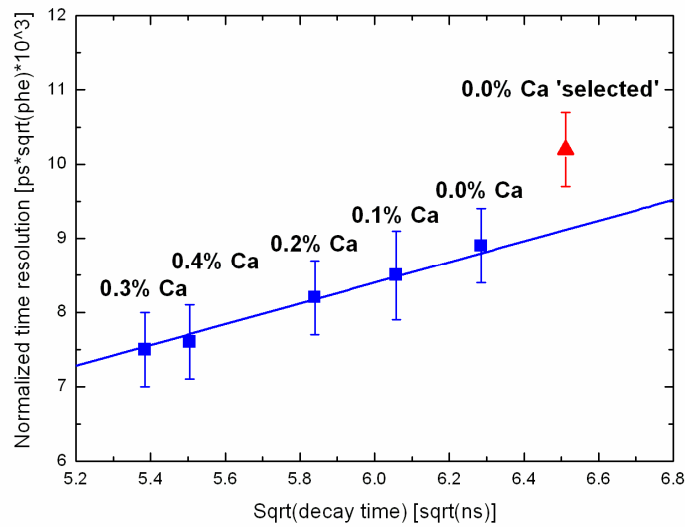


Fig. 8. Dependence of the time resolution normalized to the number of photoelectrons versus a square root of the measured decay time constant.

The value for the LSO2003 is higher and inconsistent with the data obtained for Ca co-doped samples. It is hard to explain such behavior; one thing to consider is that the LSO2003 sample was highly polished, whereas the co-doped crystals were all unpolished, what may have had some influence on the results. In addition, LSO2003 was a different shape than the others, possibly slightly affecting the time distribution of photons reaching the photocathode and therefore the light pulse and light yield.

D. Energy resolution

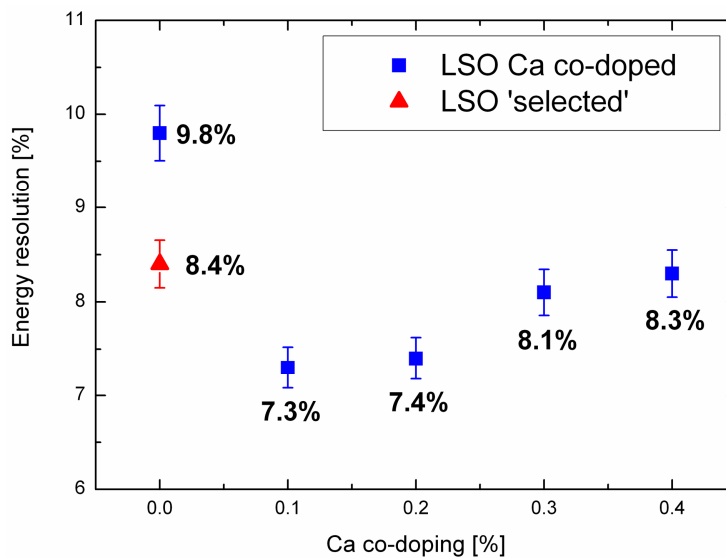


Fig. 9. Dependence of the energy resolution for 662 keV from ¹³⁷Cs gamma source versus Ca co-doping measured with the tested samples and the selected LSO2003.

This chapter is focused on the timing properties of LSO co-doped with calcium, however, since energy spectra with ¹³⁷Cs gamma source were collected during the study (see Fig. 1), the

values of energy resolution will be also presented.

Fig. 9 shows a plot of energy resolution for 662 keV from ^{137}Cs gamma source versus Ca co-doping. The observed trend is similar to the one presented in Fig. 2 in the case of a photoelectron number. For small amount of co-doping an improvement is observed from 9.8% to 7.3%, but further co-doping leads to deterioration of the energy resolution up to 8.3%. It follows the results presented in [7] where detailed study of non-proportionality, energy resolution and afterglow of the crystals tested here can be found.

4. Conclusions

The results presented in this study showed that calcium co-doping in LSO crystals has a significant influence on the properties of these scintillators. The light output is improved with a small amount of Ca co-dopant, although above 0.1% it starts to drop to values similar to the standard LSO. However, all the tested samples were less bright than, or comparable to the specifically selected, not co-doped LSO produced in 2003. The time resolution is improved with Ca co-doping to around 140 ps for a single detector. The best timing value was obtained for 0.4% Ca, however other co-dopings led to similar values. The decay time constant is improved to around 30 ns for co-doping of 0.3% and 0.4% of Ca and no additional components are observed.

The presented study was performed only on one set of samples and it is obvious that more tests have to be done to fully confirm all the properties reported here.

5. References

- [1] M. Spurrier, P. Szupryczynski, K. Yang, A. Carey, and C. Melcher, "Effects of Ca²⁺ Co-Doping on the Scintillation Properties of LSO:Ce," *IEEE Trans. Nucl. Sci.*, vol. 55, no. 3, pp. 1178–1182, 2008.
- [2] C. Brandle, *Crystal Growth*, B. Pamplin, Ed. Pergamon, Oxford, 1980.
- [3] M. Moszynski, M. Gierlik, M. Kapusta, A. Nassalski, T. Szczesniak, C. Fontaine, and P. Lavoute, "New Photonis XP20D0 photomultiplier for fast timing in nuclear medicine," *Nucl. Instr. Meth. A*, vol. 567, no. 1, pp. 31–35, 2006.
- [4] M. Moszynski, M. Kapusta, D. Wolski, M. Balcerzyk, S. Flyckt, P. Lavoute, C. Marmonier, and H. Mach, "New fast photomultipliers with a screening grid at the anode," *IEEE Trans. Nucl. Sci.*, vol. 51, no. 4, pp. 1701–1706, 2004.
- [5] L. Bollinger and G. Thomas, "Measurement of the time dependence of scintillation intensity by a delayed-coincidence method," *Rev. Sci. Instr.*, vol. 32, no. 9, pp. 1044–1050, 1961.
- [6] M. Moszynski and B. Bengtson, "Light pulse shapes from plastic scintillators," *Nucl. Instr. Meth.*, vol. 142, no. 3, pp. 417–434, 1977.
- [7] A. Syntfeld-Kazuch, M. Moszynski, L. Swiderski, T. Szczesniak, A. Nassalski, C. Melcher, M. Spurrier, B. Goliszek, P. Kaminski, and M. Nowaczyk, "Energy resolution of calcium co-doped LSO:Ce scintillators," *IEEE Trans. Nucl. Sci.*, vol. 56, no. 5, pp. 2972–2978, 2009.

12. Time Resolution of Scintillation Detectors Based on SiPMs in Comparison with Photomultipliers

1. Introduction

A. Motivation

First commercially available photomultipliers (PMTs) appeared about 75 years ago. Presently, they belong to the most widely used photodetectors, especially in nuclear medicine. However, photomultipliers have some disadvantages such as sensitivity to magnetic field, high power consumption, fragility or high price due to complicated mechanical structure.

Recently, silicon photomultipliers (SiPMs) become the candidates for PMTs successor in many applications. A SiPM, trade marked by Hamamatsu as a Multi Pixel Photon Counter (MPPC) [1], is a matrix of micro avalanche photodiodes (APDs) working in a Geiger mode. Each micro cell generates a signal after detection of a single photon and a sum of the signals from all the pixels gives the SiPM output pulse, proportional to the number of detected photons. SiPMs while keeping important PMTs advantages, like a single photon detection capability and a high gain in addition are also compact, possess higher quantum efficiency, operate with a low bias voltage and are insensitive to magnetic fields.

Timing properties of silicon photomultipliers are reported to be extremely good although the literature data are very inconsistent. Single photon time jitter of 200 ps at FWHM is quoted by Hamamatsu in the general MPPC technical note [1]. The Hamamatsu datasheet in the case of MPPC S10362-33-050C (used in this study) contains the time jitter values between 500 ps and 600 ps [2]. In the work done by Buzhan, et al. the value of 120 ps at FWHM is shown [3], what is better than the best results achieved with photomultipliers [4] (see chapter 9). In contrast, Ronzhin, et al. presented time resolution for a single photoelectron at the level of 700 ps [5]. Moreover, the reported timing results are below expectations in the case of full detectors with scintillators coupled to SiPMs.

B. Aim of the study

The aim of this work is to present detailed study of the time resolution of the MPPC with scintillators and compare them to the PMTs' data presented in previous chapters of this thesis. The studies are based on experiments with $3 \times 3 \text{ mm}^2$ device produced by Hamamatsu, with micro-pixel size of $50 \text{ }\mu\text{m}$ (S10362-33-050C). This MPPC was chosen due to its very pronounced peaks in single photoelectron spectra for various bias voltages. It allowed quantitative analysis of the obtained data. In the case of $3 \times 3 \text{ mm}^2$ SiPMs from other manufacturers only qualitative discussion might be included due to their poor single photoelectron spectra and hence inaccurate calculation of the photoelectron number.

In this chapter the timing characteristic of the SiPM based detector will be made by analysis of the most important factors of scintillation detectors in timing performance, such as number of photoelectrons, time jitter, excess noise factor and also output pulse properties. The timing results obtained with SiPMs will be compared with the data gathered for PMTs, presented in

previous chapters.

C. The fundamental properties of SiPMs in comparison to PMTs

The time resolution capabilities of a photodetector are described mainly by 3 factors: number of photoelectrons, transit time jitter and excess noise factor (ENF) [6] (see chapter 5 for details).

For photomultipliers, a number of photoelectrons collected on the first dynode is a function of the photocathode sensitivity and photoelectron collection efficiency. For SiPMs a number of fired pixels, equivalent to the photoelectron number is defined by the Photon Detection Efficiency (*PDE*) expressed as:

$$PDE = QE \cdot FF \cdot THR \quad (1)$$

where *QE* is quantum efficiency of silicon, *FF* is a geometrical fill-factor (the ratio of the active pixels area to the total area of the device), and *THR* is a combined probability of electrons and holes to initiate a Geiger breakdown. Because *FF* and *QE* are constant for a given SiPM, *PDE* depends only on the *THR* that is a function of applied bias voltage (HV) [7].

Single photon transit time spread (time jitter) in the case of photomultipliers is associated with different path lengths and initial velocities of electrons traveling from the photocathode to the first dynode. In the case of silicon photomultipliers the transit time spread is a consequence of differences in speed of an avalanche process between single micro-pixels for various bias voltages.

An excess noise factor of PMTs is a result of gain spread in electron multiplication processes. It affects pulse height resolution and timing resolution. The gain variations of the photomultipliers are mostly connected with the multiplication coefficient of the first dynode, which affects the single photoelectron peak resolution. ENF of SiPMs is caused by two effects: crosstalks and afterpulses. Both of them create additional electron-hole pairs, over-proportional to the number of initial photons.

In the case of a full scintillation detector, it means a crystal coupled to a photodetector, also a pulse shape at its output plays important role. In fast timing, except photon statistics during the scintillation decay time also the fast rise time of the light pulse is important, which should not be deteriorated by a photodetector.

2. Experimental details

A. Photodetectors and scintillators

The studies were carried out with Hamamatsu MPPC S10362-33-050C, SN22 of an area of 3x3 mm² and micro-pixel size of 50 μm, delivered to Świerk in 2008. The main properties of the device, following the Hamamatsu data sheet [2] are presented in Table I. The breakdown voltage of this MPPC is equal to 66.9 V and was calculated on the basis of the single photoelectron peak positions measured at various bias voltages.

The time resolution measurements were performed with ²²Na gamma source and 3x3x3 mm³ LSO and LFS-3 (Lutetium Fine Silicate) [8] crystals. The scintillators were polished on all sides, wrapped with Teflon tape and coupled to the MPPC by means of silicone grease.

The reference detector was a truncated cone, 20 mm and 25 mm in diameter and 15 mm high BaF₂ crystal coupled to a XP20Y0Q/DA PMT. Its time resolution of 145 ± 13 ps for the 511 keV full energy peak, was determined on the basis of measurements with two other detectors consisting of similar PMTs and BaF₂ and $10 \times 10 \times 5$ mm³ LaBr₃ scintillators. Timing resolution data of these 3 detectors, measured in coincidence with each other, led to a 3x3 matrix and allowed calculation of the reference detector time resolution without the need of possessing the two identical detector configurations.

TABLE I
MAIN PROPERTIES OF THE TESTED MPPC

Type	S10362-33-050C
Serial No.	22
Active area	3×3 mm ²
Number of pixels	3600
Pixel size	50x50 μm
Fill factor	61.5 %
Gain / bias voltage	7.51×10^5 / 68.66 V
Spectral resp. range	270 -900 nm
Q.E.	70% at 400 nm
Dark count	2.38 Mcts/s
Capacitance	320 pF

B. MPPC preamplifier

To reduce an influence of the MPPC 33-050C capacitance of 320 pF and preserve parameters of a scintillation signal, a current preamplifier with low input resistance of few ohms was build following [9]. The preamplifier posses two outputs: slow – accepted by spectroscopy amplifiers and fast – reflecting the direct SiPM output and used for timing.

3. Results

A. Time resolution

First, an optimization of the electronics was done, in particular a threshold settings of a LE discriminator and a CFD shaping delay. In Fig. 1, the time resolution of a single detector consisting of the MPPC and $3 \times 3 \times 3$ mm³ LFS-3 crystal, as a function of the CFD shaping delay, is presented. An optimum was achieved for a very short shaping time delay equal to only 2 ns. In Fig. 2, the time resolution dependence on the discriminator threshold is presented. The data were recorded for two different shaping time delays of the CFD, the optimal 2 ns and for 1 ns. The 1 ns shaping time delay in the case of Ortec 935 CFD means the work regime of a leading edge discriminator. The best measured timing resolution values were identical in both cases, however, the characteristics of the plotted timing data as a function of the triggered fraction are significantly different. As expected the constant fraction working regime was weakly depended on the triggering fraction, however above the 12% fraction the significant timing resolution deterioration was observed. In the case of the

leading edge settings the time resolution was improving linearly with the fraction decrease.

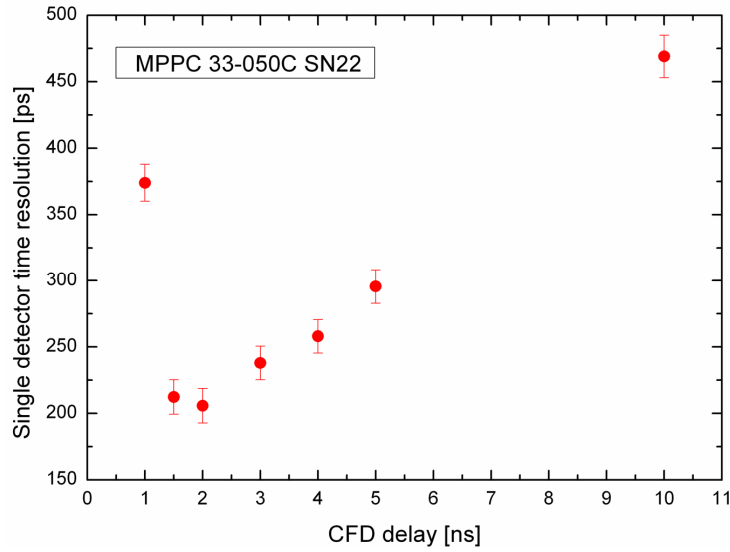


Fig. 1. Single detector time resolution dependence on CFD shaping delay. The data were recorded with $3 \times 3 \times 3 \text{ mm}^3$ LFS-3 crystal coupled to $3 \times 3 \text{ mm}^2$ MPPC (S10362-33-050C, SN22).

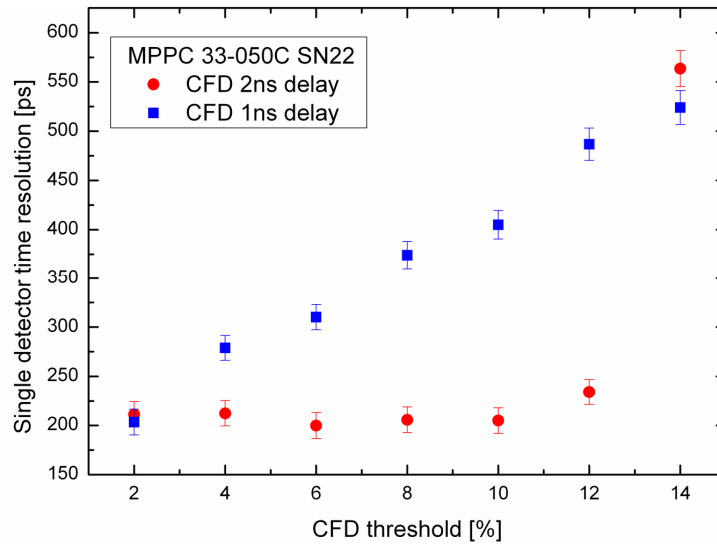


Fig. 2. Single detector time resolution dependence on CFD threshold for the two shaping delays of 2 ns and 1 ns (LE discrimination). The data were recorded with $3 \times 3 \times 3 \text{ mm}^3$ LFS-3 crystal coupled to $3 \times 3 \text{ mm}^2$ MPPC (S10362-33-050C, SN22).

As it was mentioned in section I.C, for a given SiPM, the PDE is a function of the bias voltage. In consequence, timing resolution is expected to vary with HV since it is proportional to the inversed square root of the number of photoelectrons. The plot of the MPPC timing resolution versus applied voltage is presented in Fig. 3. As expected, the best timing resolution was achieved for the highest bias voltage of 69.2 V. Large improvement (45%) of the time resolution was observed for the measurements done in the range of 68 V to 69.2 V of the MPPC bias.

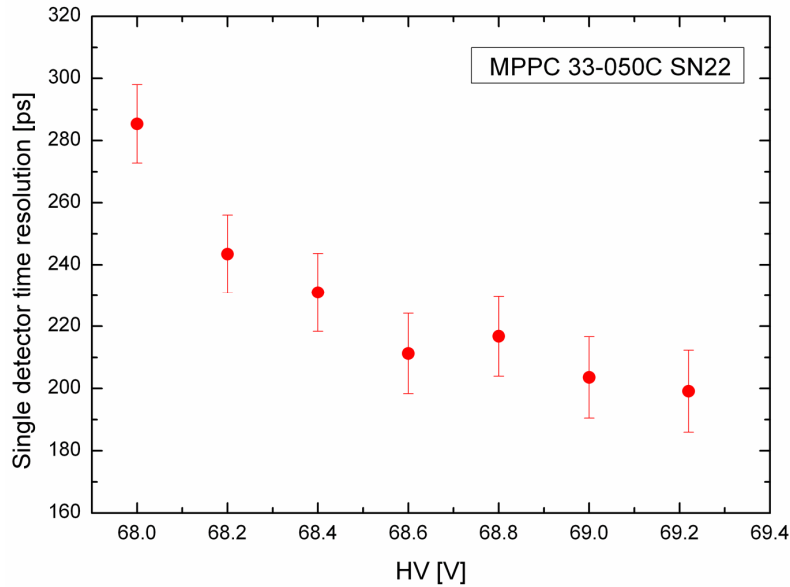


Fig. 3. Single detector time resolution dependence on bias voltage. The data were recorded with $3 \times 3 \times 3 \text{ mm}^3$ LFS-3 crystal coupled to $3 \times 3 \text{ mm}^2$ MPPC (S10362-33-050C, SN22).

Fig. 4 presents an example of the timing spectrum recorded with the optimized experimental setup, it means $HV = 69.2 \text{ V}$, CFD shaping delay of 2 ns and threshold set at the level of about 8% of the signal amplitude. The time resolution of the single MPPC + LFS-3 detector, calculated on the basis of the results shown in Fig. 4, is equal to $199 \pm 13 \text{ ps}$. This value is slightly worse than the best results, presented in previous chapters. Values below 170 ps were obtained with fast photomultipliers like Photonis XP20D0 and LFS-3 or LSO crystals [4], [8], [10]. Similar results at the level of 250 ps in coincidence for two MPPC based LYSO detectors were shown in [11].

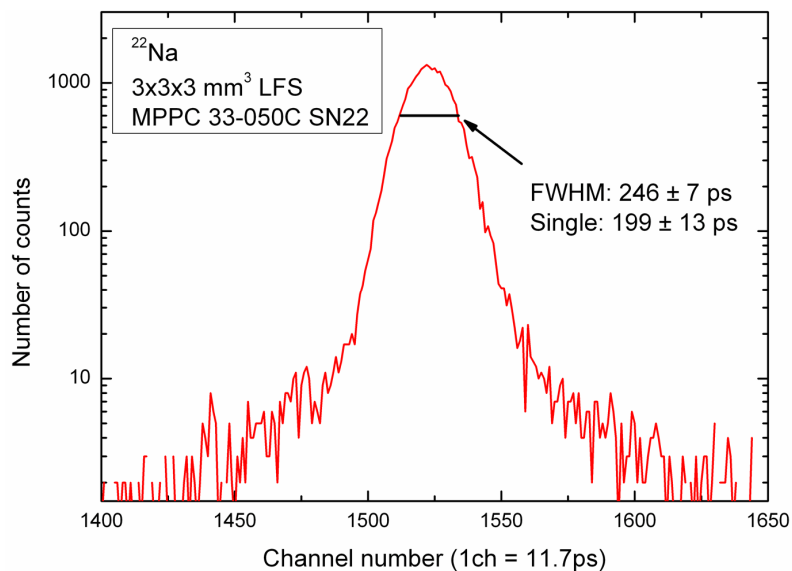


Fig. 4. Example of the timing spectrum recorded with the $3 \times 3 \times 3 \text{ mm}^3$ LFS-3 crystal coupled to the $3 \times 3 \text{ mm}^2$ MPPC (S10362-33-050C, SN22).

B. Light pulse shape

Poor rise time of the MPPC output pulse could be one of the reason of the time resolution deterioration. Each cell in the SiPM matrix contains capacitance and the total capacitance of the detector together with the input resistance of the readout electronics creates a large time constant that destroys the rise time of the output signal. Hence, the timing resolution of the MPPC with scintillators is worse than that measured with PMTs. An example of the output pulse recorded with the tested MPPC SN22 and $3 \times 3 \times 3 \text{ mm}^3$ LSO in comparison to the PMT anode pulse is presented in Fig. 5. An influence of the large terminal capacitance of 320 pF in $3 \times 3 \text{ mm}^2$ MPPC is reflected in the 15 ns rise time of the MPPC output signal.

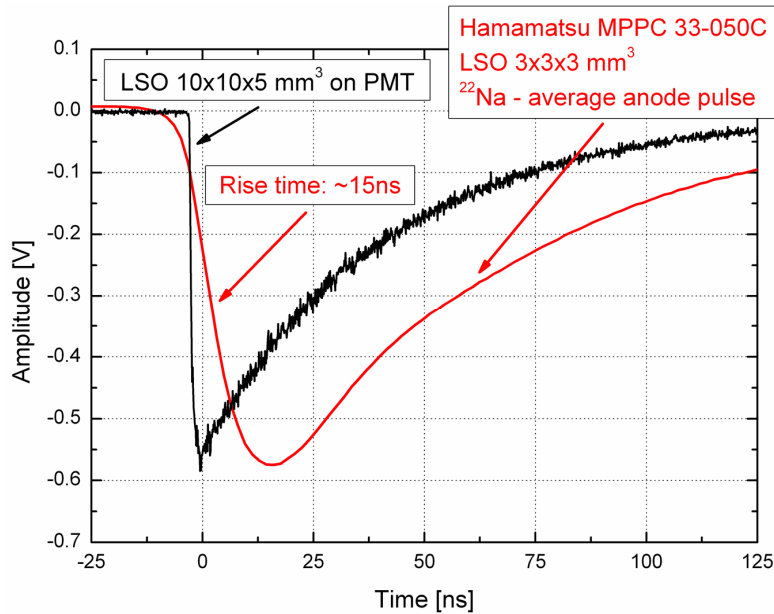


Fig. 5. Photomultiplier light pulse shape in comparison to the averaged MPPC pulse after fast output of the preamplifier used during the studies. The data were recorded with $3 \times 3 \times 3 \text{ mm}^3$ LSO crystal coupled to $3 \times 3 \text{ mm}^2$ MPPC (S10362-33-050C, SN22).

Taking into account the results presented in Fig. 1, it is worth to underline the optimal CFD shaping delay of 2 ns presented in previous section. It is much shorter than the MPPC signal rise time of 15 ns and not consistent with the common conviction about CFD delay that should be set at the level of the rise time. It means, it corrects only the initial rise at the beginning of the MPPC pulse. Influence of the slow rise time on timing resolution can be seen in successive deterioration of the results in the measurements done in the leading edge mode of the discriminator (see Fig. 2).

C. Photon detection efficiency

Fig. 3 in section 3.A showed, that timing resolution for different bias voltages is changing significantly. Such behavior suggest that the PDE, and hence also a number of photoelectrons are improved with the increasing voltage. The number of photoelectrons (fired pixels) per energy unit (phe/MeV) was measured directly (NpheDir) using Bertolaccini method [12], [13]. The measurements were done with three gamma sources: ^{57}Co (122 keV), ^{241}Am (59.5 keV) and ^{109}Cd (22 keV) in order to verify linearity of the MPPC's response in a whole range of applied voltage. The results for all the three sources are presented in Fig. 6. In each

case the experimental value of the N_{pheDir} was corrected for the non-proportionality of the LFS-3 following [8]. The data recorded with LEDs will be discussed in the next section.

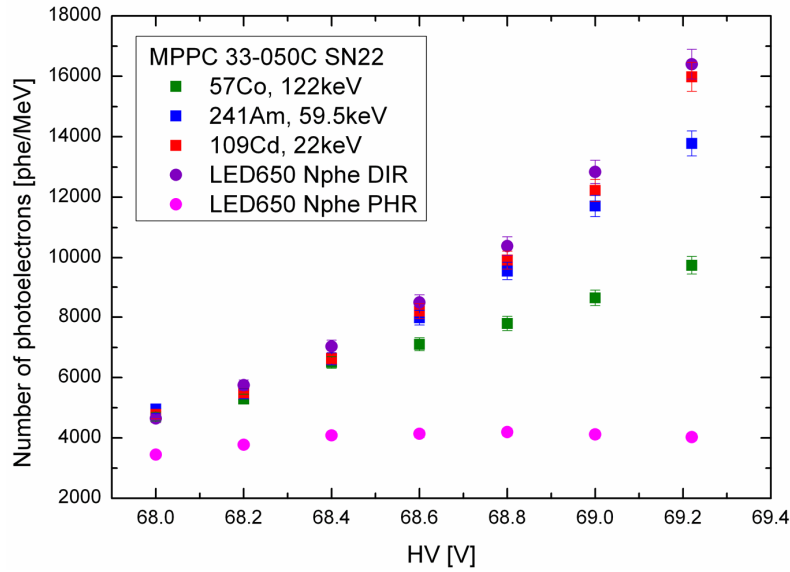


Fig. 6. Number of photoelectrons per MeV recorded with gamma sources and $3 \times 3 \times 3 \text{ mm}^3$ LFS crystal coupled to the $3 \times 3 \text{ mm}^2$ MPPC (S10362-33-050C, SN22). The data obtained with light emitting diodes, without the scintillator are also presented.

The plot shows strong dependence of the photoelectron number on the applied bias voltage and also a high inclination of the MPPC 33-050C to nonlinearity even for low number of photons. In the case of 122 keV gamma peak the nonlinearity appeared at 68.5 V, at the level of only 800 photoelectrons. Linearity was highly improved for lower gamma energy of 59.5 keV and hence, lower number of incident photons. In the case of ^{241}Am gamma source, the nonlinear behavior started to be seen at higher voltage of 68.9 V what corresponds to about 550 photoelectrons. Linear MPPC response in a whole voltage range was achieved only for 22 keV gammas from ^{109}Cd source.

Voltage of 69.2 V was used during the timing measurements with the tested MPPC SN22, what corresponds to about 16000 phe/MeV calculated using the direct, Bertolaccini method. However, this value is certainly overestimated due to a high contribution from crosstalks and afterpulses.

D. Excess noise factor

The processes leading to crosstalks and afterpulses, responsible for an excess noise factor in silicon photomultipliers should have different influence on a pulse amplitude and energy resolution. Both processes create additional photoelectrons, not proportional to the initial number of photons. In consequence, the spectrum in a multichannel analyzer (MCA) may be shifted towards a higher channel number, leading to the overestimated number of photoelectrons. These additional photoelectrons do not carry any statistical information and hence should not improve the pulse height resolution. However, the peak width in the MCA is broadened due to a spread of the MPPC signal amplitude, affected by the crosstalks and afterpulses.

As an alternative to the direct method (NpheDir), the statistics of photoelectrons in the peak originating from the LED light source can be taken into account in calculations of the number of photoelectrons (NphePhr). The statistical contribution δ_{st} to the pulse height resolution (PHR) for SIPMs can be described, as [14]:

$$\delta_{st} = 2.355 \cdot \sqrt{\frac{ENF}{PHE}} \quad (2)$$

where: PHE is the number of photoelectrons (NphePhr) and ENF is the excess noise factor.

According to equation (2), the determined PHE number is proportional to the ENF. In the case of the LED peak, the lowest possible number of photoelectrons, estimated on the basis of PHR, corresponds to the peak width described only by the pure PHE statistics and $ENF = 1$.

The results of the measurements with the LED light source are presented in Fig. 6. The data were obtained with a 650 nm LED light pulser. The number of the emitted photons was adjusted varying the amplitude of the pulse triggering the diode. The number of photoelectrons was set to correspond to that of the ^{109}Cd gamma peak. The LED data represented by circle points in Fig. 6 made possible a comparison of the number of photoelectrons measured by the direct method with that determined from the pulse height resolution of the light pulser peak. A large difference can be observed in Fig. 6 between the photoelectron numbers measured using these two methods. The flat dependence corresponding to the PHR method denotes the lower limit of PHE and $ENF = 1$, whereas the DIR points represent the upper limits of both values. The shape of the PHR dependence is related to saturation of the THR parameter introduced in equation (1), it means to probability close to 1 for generation of an electron-hole pair after the photon detection [7]. Following [7], the crosstalks and afterpulses probability is increasing with overvoltage. It leads to higher amplitude of the MPPC output pulse and increased excess of the photoelectron number which can be seen on the NpheDir plot in Fig. 6.

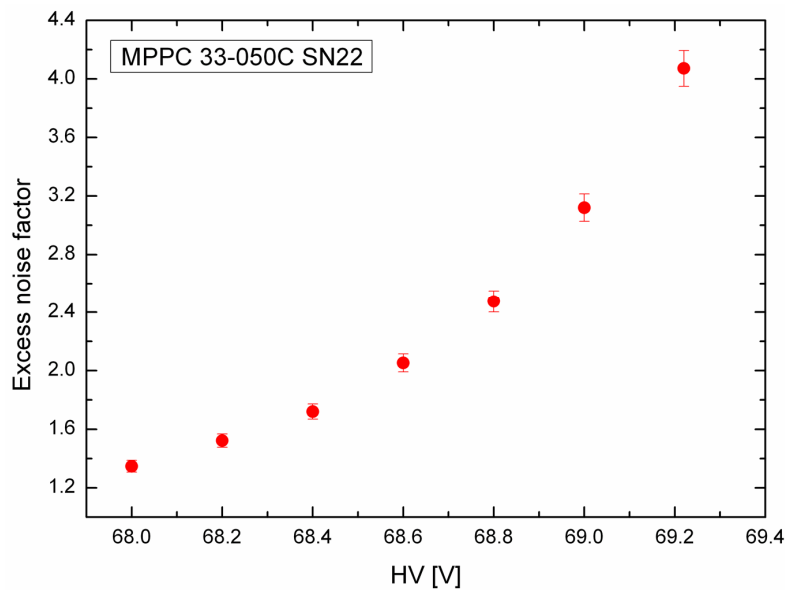


Fig. 7. The upper limit of the excess noise factor of the MPPC 33-050C SN22 for various bias voltages.

The ratio between the NpheDir and NphePhr values is presented in Fig. 7 and reflects the

upper limit of the excess noise factor for a given voltage. The real ENF lays somewhere between the two plots discussed above and presented in Fig. 6.

The values of the excess noise factor for the tested MPPC are much larger comparing to other photodetectors. ENF in case of PMTs is equal to 1.1 – 1.2, for photodiodes with no gain is equal to 1 and for high quality APDs is equal to 2.

E. Time jitter and crosstalks

Time jitter of the tested MPPC was measured using PicoQuant Diode Laser LDH-P-C-405 with 49 ps pulse width (FWHM) and wavelength of 403 nm. The laser driver was triggered by an external pulse generator at frequency of 10 000 Hz. The laser intensity was set in the way that assured detection of only single photons. It was reflected in about 300 cps recorded in the time jitter peak (3% of the emitted light).

Silicon photomultipliers are known to have excellent photon counting capabilities. Its single (or few) photoelectron spectrum is characterized by well separated peaks corresponding to a consecutive number of detected photons. Example of such spectrum, recorded with the tested MPPC is presented in Fig. 8.

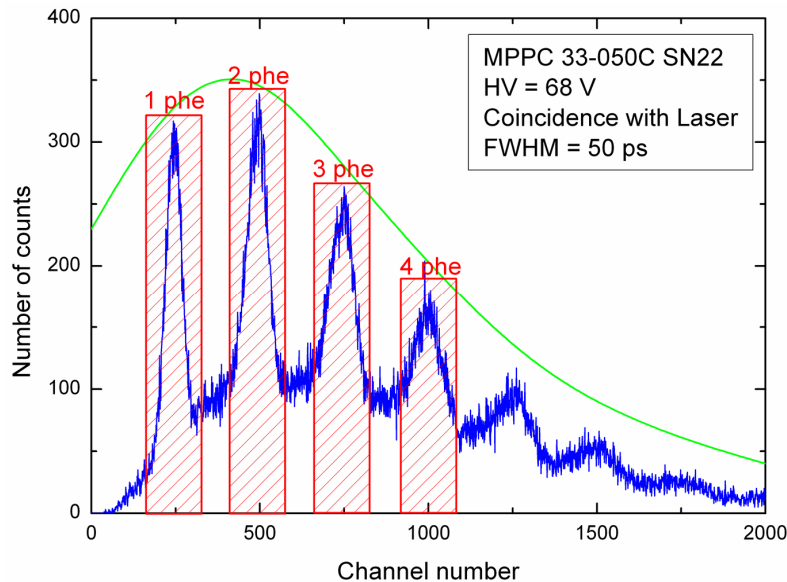


Fig. 8. Example of a single photoelectron spectrum measured in coincidence with the picosecond laser. The rectangle areas indicates the gates set at consecutive photoelectron numbers during the time jitter measurements. The solid line schematically shows the mean number of photoelectrons for a given laser light intensity.

As it was described in chapter 7, measurements of the time spread of the MPPC response to the one photon generated by the laser (time jitter) can be made when the SCA gate (rectangle areas in Fig. 8) is set on the first peak in the spectrum. Timing obtained with the gate set at the second, third or higher photoelectron peak should follow the photoelectron statistics and be inversely proportional to the square root of its number. However, the experiments with such SCA settings and constant laser intensity led to results, which are similar despite the different SCA windows, corresponding to a different number of photoelectrons. The data presented in Fig. 9 show that in the case of the time jitter measurements, the number of pixels triggered in MPPC by the incident laser light cannot be chosen by a simple peak selection in a single

channel analyzer.

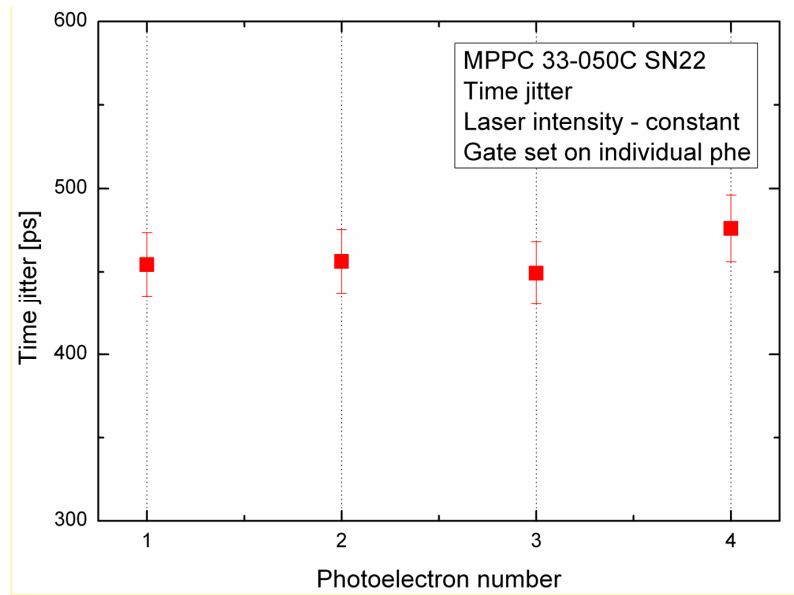


Fig. 9. Time jitter measured with the tested MPPC and SCA gates set at peaks corresponding to a successive number of photoelectrons (see Fig. 8).

The above results suggest that for MPPC the time jitter is determined by the mean number of detected photoelectrons, which can be schematically expressed as an envelope of peaks presented in Fig. 8 (solid curve). This mean photoelectron number can be changed by varying the light source intensity. During the time jitter measurements the adjustment of the laser intensities, corresponding to the first up to the fifth photoelectron, were made using a digital oscilloscope Tektronix TDS 5104B. It was done by monitoring the MPPC output pulse, containing traces of consecutive photoelectron pulses. Laser light intensity was then set in the way that led to an average pulse, which amplitude reflected the desired number of photoelectrons. The average from 10 000 pulses was recorded using a double trigger. The first trigger was set at the laser pulse and the second at the MPPC output pulse. Such configuration prevented the deterioration of the mean pulse by the dark counts. An example of screenshots taken during the measurements performed with the mean amplitude of 1 and 3 photoelectrons is presented in Fig. 10. Timing results obtained for various laser light intensities, corresponding to a different number of photoelectrons, are presented in Fig. 11.

Comparison of the top two screens in Fig. 10 shows that minimal observed mean photoelectron number (top-right screen) is slightly higher than the amplitude of the first photoelectron trace (top-left screen). The lower limit of the mean photoelectron number is equal to about 1.2. Such effect could be a consequence of crosstalks which appear with probability of about 20% at the applied voltage of 69.2 V [7].

In order to estimate the crosstalk influence on the MPPC output pulse the same experimental set-up was used as in the case of the time jitter measurements. Again, the laser intensity was set in the way that assured interactions of only single photons but this time the number of counts per second (cps) in the time jitter peak, in coincidence with the laser light was measured at different CFD thresholds. The counts in background were subtracted from the recorded spectra and then the number of counts under the time jitter curve, was divided by

the measurement live time. Such experimental set-up allowed the measurements in a narrow coincidence window of only 5 ns. This procedure was repeated several times increasing the CFD threshold. The sample spectra and an idea of the cps calculation are presented in Fig. 12.

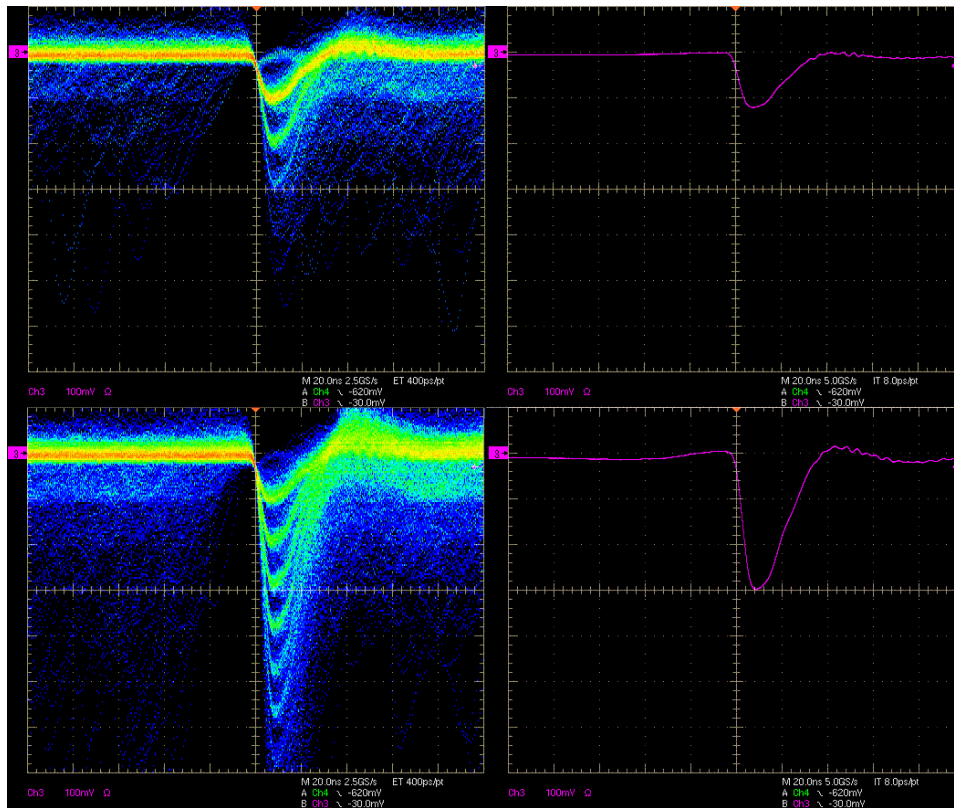


Fig. 10. Screenshots of the MPPC output pulses. On the left, the direct pulses triggered by the laser are presented. On the right, the same pulses but averaged from 10 000 events are shown. Their average amplitudes correspond to 1 (top) and 3 (bottom) photoelectrons.

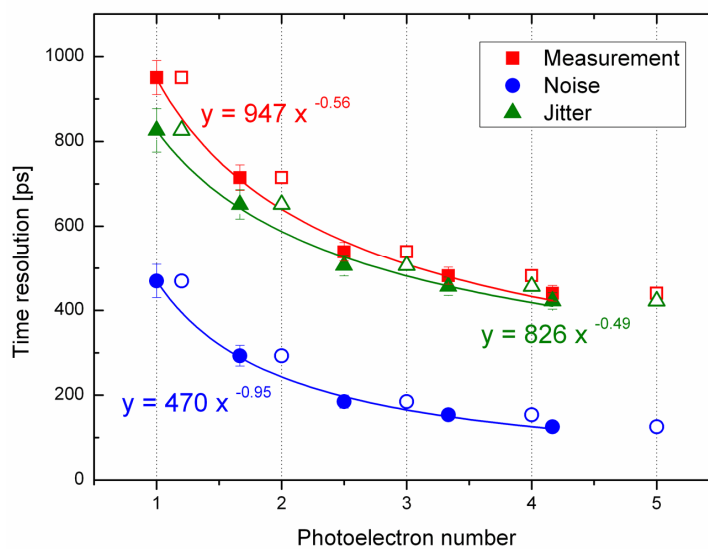


Fig. 11. Time resolution and noise contribution measured for various number of photoelectrons detected in the $3 \times 3 \text{ mm}^2$ MPPC (S10362-33-050C, SN22). The open points represent the experimental data, while the solid points are normalized to the number of incident photons.

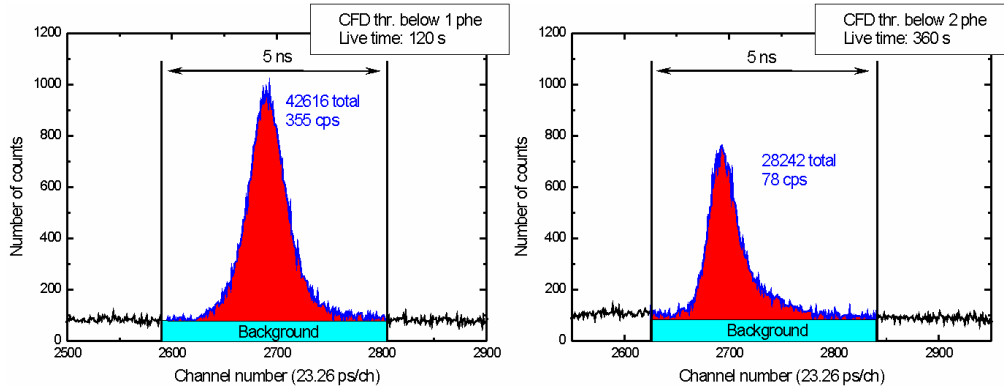


Fig. 12. An example of the time jitter spectra recorded with the 3x3 mm² MPPC (S10362-33-050C SN22) at two different thresholds set in the CFD.

The dependence of the cps value on the discriminator threshold is presented in Fig. 13. The dashed line at the top represents the mean number of counts per second while the threshold was set below the first photoelectron. A sudden drop of events can be observed at about 80 mV threshold which is close to the amplitude of the single photoelectron pulse. The data above 100 mV correspond to multi-photoelectron events, it means the events that produced two photoelectrons (or more) in response to the one laser photon. The dashed line at the bottom marks the mean number of double-photoelectron events induced by a single laser photon and crosstalk. The ratio of cps measured with the threshold set below and above the single photoelectron amplitude gives the number of crosstalk events for a given bias voltage. The observed crosstalk level, which appear with probability of about 20% at the applied voltage of 69.2 V is in good agreement with the data presented in [7]. Moreover, the value of 20% explains the 0.2 excess of the mean single photoelectron amplitude observed in Fig. 10.

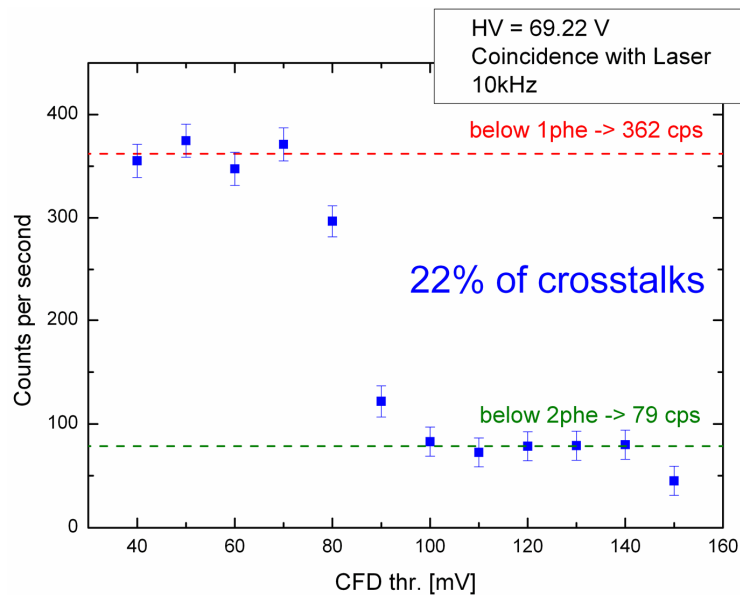


Fig. 13. Number of counts per second versus the CFD threshold. The ratio between the mean values of cps indicated as dashed lines allowed calculation of the crosstalk probability.

Taking into account the crosstalk influence on the mean MPPC output pulse the values of the mean amplitudes read from the oscilloscope (open points in Fig. 11) have to be corrected. Since the amplitude of 1.2 corresponds to one photon striking the MPPC all the data in Fig. 11 have to be rescaled to photons and hence divided by 1.2. (solid points). Such operation assure consistence with the definition of the time jitter measurement based on the single photon events.

In the case of silicon photomultipliers and measurements with a very low light level also the noise component has to be taken into account. The noise was estimated on the basis of timing spectra obtained with a signal from a Pulse Generator fed into the preamplifier. The measurements were made in coincidence with the laser trigger output and the generator signal was set as similar as possible to the MPPC output pulse.

The noise free time jitter values were calculated by subtracting the noise component from the measured spectra. The results in Fig. 11 show that the time jitter is proportional to the inversed square root of the number of photoelectrons. The calculated single photoelectron time jitter of the tested MPPC is equal to 826 ± 54 ps. This value is much worse comparing with fast photomultipliers which are characterized by the time jitter of 500 ps or less (see chapter 9). The obtained resolution is in big disagreement with the data presented in [1] or in [3]. On the other hand the results and functions presented in Fig. 11 follow almost perfectly the predicted dependence on the photoelectron number. Similar results (about 700 ps) and dependencies for the Hamamatsu MPPCs were shown in [5].

The same timing measurement technique, with the average MPPC output pulse set by means of a digital oscilloscope was used for measurements of the time jitter dependence on the MPPC's applied bias voltage. The bias voltage was varied in the range of 68 V to 69.2 V in 0.2 V steps. The results, showing strong dependence of the time jitter on the HV are presented in Fig. 14.

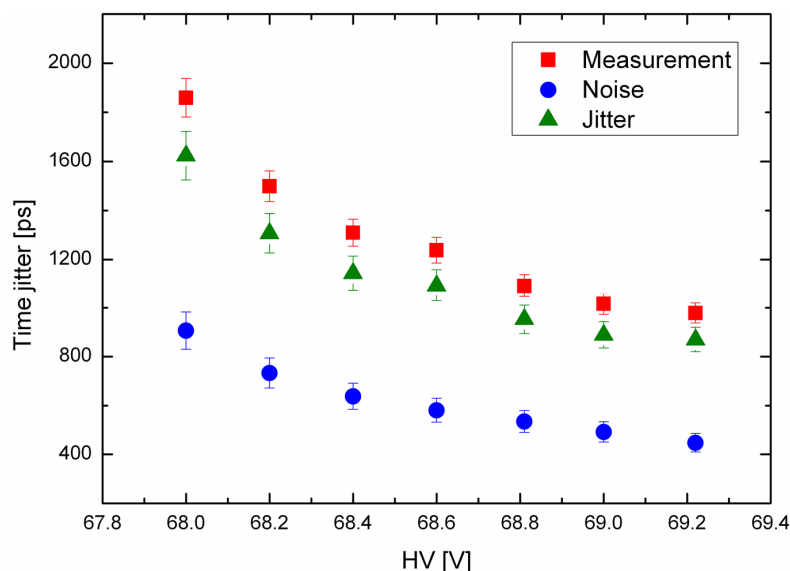


Fig. 14. Time jitter and noise dependence on applied MPPC bias voltage. The data were recorded with the 3×3 mm² MPPC (S10362-33-050C, SN22).

F. Comparison with photomultipliers

In chapter 9 the plot of the normalized time resolution versus the time jitter obtained for a $10 \times 10 \times 5 \text{ mm}^3$ LSO crystal was established for various types of photomultipliers. Similar plot is presented in Fig. 15 with addition of the data gathered for a detector consisting of $3 \times 3 \text{ mm}^2$ MPPC 33-050C, SN22 and $3 \times 3 \times 3 \text{ mm}^3$ LFS-3 scintillator at various bias voltages.

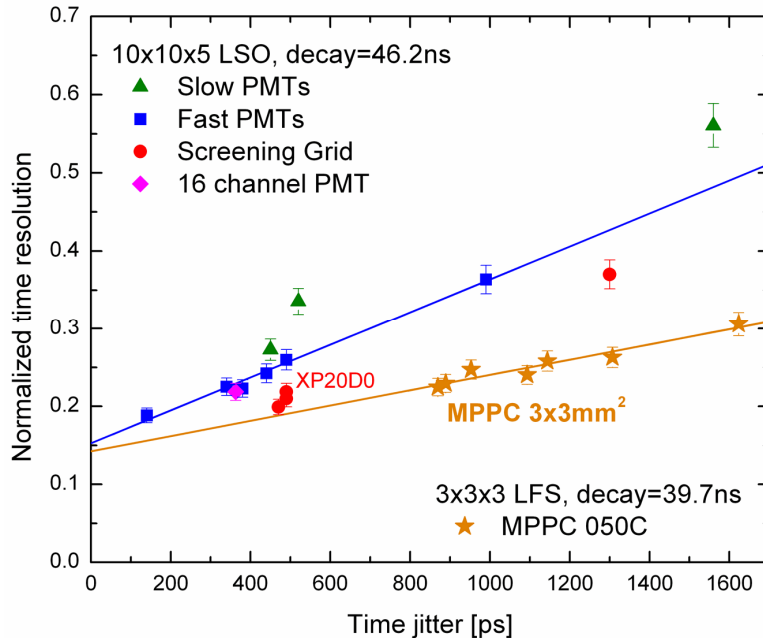


Fig. 15. Normalized time resolution versus a time jitter for various photomultipliers and MPPC 33-050C, SN22. Measurements were performed for the $10 \times 10 \times 5 \text{ mm}^3$ LSO crystal (PMTs) and $3 \times 3 \times 3 \text{ mm}^3$ LFS-3 crystal (MPPC).

Here, the single detector time resolution is normalized to the number of photoelectrons, excess noise factor and decay time of the scintillator used. It means that the values presented in Fig. 3 were multiplied by the square root of the photoelectron numbers for 511 keV, divided by the square root of the ENF and also divided by the decay time of the LFS-3 crystal equal to 39.7 ns [8]. Such normalization follows Hyman's theory of timing with photomultiplier systems [15] (see chapter 6 for details).

It is worth to add that since the timing results are normalized to the number of photoelectrons and excess noise factor at the same time and both these quantities are mutually dependent their values do not have to be known separately. In fact, only the ratio between them is important and hence overestimated N_{pHeDir} value does not change the plot in Fig. 15.

The calculated normalized time resolution, presented on Y-axis in Fig. 15, shows similar timing capabilities of the tested MPPC in comparison to the fast photomultipliers. In the case of fast PMTs the time jitter is always lower than 500 ps, however high potential of silicon photomultipliers in timing applications is clearly visible even despite its poor time jitter. A large difference in the rise time of the slow MPPC pulse comparing to the fast photomultipliers together with a high dark counts rate has a significant influence on the MPPC timing performance and leads to its deterioration. High quantum efficiency of SiPMs which gives very high photoelectron numbers is its biggest advantage. The photoelectron statistics compensates drawbacks of the MPPC like a large time jitter, a high excess noise

factor and poor rise time of the output pulse.

4. Conclusions

The timing resolution of a single detector consisting of MPPC type S10362-33-050C and $3 \times 3 \times 3 \text{ mm}^2$ LFS-3 scintillator is 10% worse comparing to the best detectors where fast photomultipliers are used. The high potential of the MPPC in the timing applications is due to their high quantum efficiency. The other MPPC properties such as time jitter, excess noise factor and signal rise time differ significantly from PMTs characteristics. These factors need to be addressed in the proper construction and optimization of the electronics to achieve the timing resolution of 200 ps.

High QE of the MPPC leads to a high photoelectron number, which is further increased for a higher bias voltage due to a higher probability of a Geiger breakdown. However, this working regime leads to the overestimated number of photoelectrons due to a high excess noise factor.

ENF is a result of crosstalks and afterpulses. Since a probability of these two effects rises with bias voltage also ENF strongly depends on HV and can be higher than 2 in the case of conditions optimized for timing measurements.

The time jitter of a $3 \times 3 \text{ mm}^2$ MPPC at bias voltage of 69.2 V is 2 times larger comparing to modern fast PMTs. The time jitter is also dependent on HV and deteriorated at lower bias voltage. The value of 826 ps was measured for HV at the level of 2.3 V over breakdown.

It is important to note that the MPPC mode of operation optimal for timing correspond to high overvoltage, what in consequence leads to large nonlinearity of the MPPC response.

5. References

- [1] Hamamatsu, MPPC Multi-Pixel Photon Counter Technical Information, 2009.
- [2] ———, *MPPC S10362-33 Series Datasheet*.
- [3] P. Buzhan, B. Dolgoshein, L. Filatov, A. Ilyin, V. Kantzerov, V. Kaplin, A. Karakash, F. Kayumov, S. Klemin, E. Popova *et al.*, “Silicon photomultiplier and its possible applications,” *Nucl. Instr. Meth. A*, vol. 504, no. 1-3, pp. 48–52, 2003.
- [4] T. Szczesniak, M. Moszynski, L. Swiderski, A. Nassalski, P. Lavoute, and M. Kapusta, “Fast photomultipliers for TOF PET,” *IEEE Trans. Nucl. Sci.*, vol. 56, no. 1, pp. 173–181, Feb. 2009.
- [5] A. Ronzhin, M. Albrow, K. Byrum, M. Demarteau, S. Los, E. May, E. Ramberg, J. Va’Vra, and A. Zatserklyaniy, “Tests of timing properties of silicon photomultipliers,” *Nucl. Instr. Meth. A*, vol. 616, no. 1, pp. 38–44, 2010.
- [6] M. Moszynski and B. Bengtson, “Status of timing with plastic scintillation detectors,” *Nucl. Instr. Meth.*, vol. 158, pp. 1–31, 1979.
- [7] P. Eckert, H. Schultz-Coulon, W. Shen, R. Stamen, and A. Tadday, “Characterisation studies of silicon photomultipliers,” *Nucl. Instr. Meth. A*, vol. 620, no. 2-3, pp. 217–226, 2010.
- [8] M. Grodzicka, M. Moszynski, T. Szczesniak, A. Syntfeld-Kazuch *et al.*, “Characterization of LFS-3 scintillator in comparison with LSO,” *Nucl. Instr. Meth. A*, vol. 652, no. 1, pp. 226–230, Oct. 2011.

- [9] S. Seifert, D. Schaart, H. van Dam, J. Huizenga, R. Vinke, P. Dendooven, H. Lohner, and F. Beekman, “A high bandwidth preamplifier for SiPM-based TOF PET scintillation detectors,” in *Nuclear Science Symposium Conference Record, 2008. NSS’08. IEEE*. IEEE, 2008, pp. 1616–1619.
- [10] M. Moszynski, M. Kapusta, A. Nassalski, T. Szczesniak, D. Wolski, L. Eriksson, and C. Melcher, “New prospects for time-of-flight PET with LSO scintillators,” *IEEE Trans. Nucl. Sci.*, vol. 53, no. 5, pp. 2484–2488, 2006.
- [11] C. Kim, G. Wang, and S. Dolinsky, “Multi-pixel photon counters for TOF PET detector and its challenges,” *IEEE Trans. Nucl. Sci.*, vol. 56, no. 5, pp. 2580–2585, 2009.
- [12] M. Bertolaccini, S. Cova, and C. Bussolatti, “A technique for absolute measurement of the effective photoelectron per keV yield in scintillation counters,” in *Proc. Nuclear Electronics Symp., Société Française des Electroniciens et des Radioélectriciens*, 1968.
- [13] M. Moszynski, T. Szczesniak, M. Kapusta, M. Szawlowski, J. Iwanowska, M. Gierlik, A. Syntfeld-Kazuch, L. Swiderski, C. Melcher, L. Eriksson *et al.*, “Characterization of scintillators by modern photomultipliers—a new source of errors,” *IEEE Trans. Nucl. Sci.*, vol. 57, no. 5, pp. 2886–2896, 2010.
- [14] M. Moszynski, “Non-proportionality and energy resolution of scintillation detectors,” *Radiation Detectors for Medical Applications (NATO Security Through Science Series)*, pp. 293–315, 2006.
- [15] L. Hyman, “Time resolution of photomultiplier systems,” *Rev. Sci. Instr.*, vol. 36, no. 2, pp. 193–196, 1965.

13. Summary

Positron Emission Tomography is one of the most widely used technique in cancer diagnosis and treatment. The present state of art of the commercial PET systems, produced by leading medical companies, assure high quality images with spatial resolution close to the physical limits. However, the signal to noise ratio and hence the image contrast is still a problem, especially in the case of heavy patients. Incorporation of the Time-of-Flight information into image reconstruction algorithms makes possible an improvement of the image contrast. In consequence, by using the next generation TOF-PET scanners, even small tumors can be early diagnosed and properly treated, increasing the chance for a patient to be fully recovered.

The need of a fast scintillation block detector that could be applied in the TOF-PET device became a motivation for the time resolution studies in many laboratories in the World, an also for the experiments presented in this thesis. Because laboratory in Świerk do not have access to a full PET system the reported investigations were focused on optimization of a detector design and settings of timing electronics. Close cooperation with Photonis, a producer of photomultipliers, and with LSO makers at University of Tennessee allowed deep studies of the present limits of achievable time resolution with scintillation detectors intended for use in PET.

The time resolution of 170 ps obtained with an LSO crystal coupled to a XP20D0 PMT, demonstrated that a TOF-PET detector based on an LSO scintillator and a fast photomultiplier is a realistic proposition. As is presented in this thesis, the timing results, as well as steps of optimization of electronics, i.e. discriminator settings, are in perfect agreement with the limits predicted by the Hyman theory of timing. It suggest that the values presented in the thesis are the current limit of possible time resolution using LSO and classic, fast photomultipliers.

The dominating role of the number of photoelectrons in timing performance of a scintillation detector was confirmed in measurements with $4 \times 4 \times 20 \text{ mm}^3$ LSO crystal placed in various positions at the photocathode, and also in the case of a common light readout using two photomultipliers.

The studies of a wide set of various types of photomultipliers, including prototypes supplied by Photonis, allowed to show the key factors affecting the time resolution in detectors consisting of a fast photomultiplier and an LSO crystal. It was presented that in the case of scintillators like LSO, characterized by slow decay time of about 40 ns, the dependence of the time resolution on the number of photoelectrons is stronger than the one connected with the time jitter. The performed experiments also highlighted the influence of the initial rise time of the anode pulse on the final time resolution and confirmed validity of the PMT construction with a screening grid placed at the anode.

The introduced plot of the normalized time resolution dependence on the time jitter

provides the general method for comparison of various scintillation detectors. Moreover, the plot allows to predict the limit of the time resolution possible to achieve with a given photomultiplier and LSO crystal. As is also shown, this dependency is valid not only for classic photomultipliers but also in the case when light readout is made by means of silicon photomultipliers.

A part of the reported experiments was focused on a PET detector design where one continuous crystal was used instead of many smaller pixels in a block detector. The idea of such configuration was triggered by improved light collection during the measurements utilizing light readout by means of two PMTs. In the case of a continuous crystal a one, 16-channel PMT was used instead of few PMTs, however the time resolution experiments showed that all benefits due to improved light collection are lost because of the poor photoelectron collection efficiency in the metal channel PMT. The overall timing capabilities of the continuous crystal detector appeared to be similar to the results obtained with linear focused PMTs, although quantum efficiency of the tested 16-channel PMT was about 25% higher comparing to the other photomultipliers used in the experiments. The biggest advantage of the continuous crystal detector is its time resolution homogeneity over the whole surface of the photocathode. Nevertheless, due to a challenging task of reconstruction of the gamma interaction point inside a monolithic crystal and also because of lack of improvement in time resolution, this type of a block detector did not proved to be advantageous over the presently used designs incorporating pixelated crystals and linear focused tubes.

The presented characterization of the new LSO crystals, co-doped with calcium showed that commonly used LSO scintillators in commercially available scanners can be further improved. The results confirms that calcium co-doping in LSO scintillators leads to shorter decay time and higher light output, which directly influence the time resolution. The performed measurements showed that the decay time at the level of 30 ns can be achieved with co-doping of 0.3% or 0.4% of Ca (in the melt from which the crystals were grown) and that no additional components are observed. Moreover, the time resolution at this level of co-dopings can be improved up to 140 ps.

It is worth to underline that the reported tests of the LSO:Ce,Ca samples were one of the first done outside the University of Tennessee, where these crystals were invented.

As a final part of the thesis a study of a silicon photomultipliers in timing applications was made. These devices are presently the most intensively studied type of a photodetector for application in positron emission tomography. The timing characterization of SiPMs was performed in the same way as previous tests of photomultipliers, pointing out such parameters as number of photoelectrons, time jitter, excess noise factor and output pulse characteristics. The obtained time resolution for a 3x3 mm² SiPM is 10% worse comparing to the previous results achieved with timing photomultipliers. Such deterioration is a consequence of slow rise time of the SiPM output pulse, high time jitter and high excess noise factor. The results suggest, that at present classic photomultipliers are still a better solution for a TOF-PET photodetector.

It is worth to underline the performed measurements of the time jitter of SiPMs. The data in

the literature about the transit time spread of these devices are not consistent and differ significantly, even in the range of 100%. As is shown in chapter 12, the experimental method that is correct in the case of photomultipliers, may lead to underestimated values of the time jitter when is applied to SiPMs. The experimental technique proposed by the author assures the correct identification of the photoelectron number that triggers the electronics and therefore accurate calculation of the SiPM time jitter.

Acknowledgments

First of all I would like to thank prof. Marek Moszyński for great scientific and personal support given me from the first day I spent in Świerk. He guided me all these years sharing his knowledge and experience, and helping me to be a better scientist. This thesis, as well as other common activities would not be possible without his assistance, trust and patience. I am glad that I have opportunity to work with the one of the world experts in the field of scintillation detectors, and I am happy to say that he is not only my supervisor but also my friend.

I would like to thank all of my colleagues from P3 Department (presently TJ3 and TJ4). They create unique atmosphere in which work is a pleasure and mutual support is a natural behavior. I am especially thankful for help given me in the field of electronics by Darek Wolski, who always know which resistor or capacitor had to be changed in order to force any device to work properly. I am very indebted to Marek Szawłowski for sharing his knowledge about all kinds of photodiodes and especially about silicon photomultipliers. Special thanks goes to Martyna Grodzicka for continuous support and all that beautiful single photoelectron spectra measured with silicon photomultipliers which I could record thanks to her help. I would like to thank Łukasz Świdorski, Maciek Kapusta and all my friends here in Świerk for many valuable discussions, common measurements and fruitful cooperation. I am also extremely grateful to Andrzej Dziedzic and Krzysztof Leśniewski. Without their magic hands and technical support I would not be able to arrange any experimental set-up.

A big part of this thesis would not exist without cooperation with Photonis. I am deeply indebted to Pascal Lavoute, [EssoFlyckt](#) and all the fantastic people, which I met there. They gave me possibility to dismantle a photomultiplier like a child's toy, so I could understand piece by piece how this device works and how it is built. Common discussions with these PMTs specialists as well as common studies and measurements of various constructions were priceless for me.

I also want to thank [prof. Jan Nassalski](#), Nicole d'Hose, Jacque Marroncle and all my friends from the Compass Experiment. It was a pleasure for me to work with them in laboratories in Cern and CEA Saclay. Participation in this project gave me an opportunity to see how "my" detectors from the laboratory are used in large, high energy physics experiments.

The idea presented in chapter 10 of this thesis was born thanks to discussions with Peter Ojala. I would like to thank him and also Christian Bohm for all valuable conversations and informations they provide me about continuous crystal detector and digital techniques of timing resolution measurements.

I would like to thank prof. Zygmunt Szepliński, who showed me how billiard-balls will move after collision or how UFO is flying, but what is more important, he was the first to teach me what is nuclear medicine and in particular, how positron emission tomography works.

My greatest thanks belongs to my parents and I would like to dedicate this thesis to him. They always positively supported me in any decision. I am very grateful for their patience, help and trust.

Największe podziękowania należą się moim rodzicom i to im chciałbym zadedykować tę pracę. To oni zawsze pozytywnie wspierali mnie w każdej decyzji. Jestem im bardzo wdzięczny za ich cierpliwość, pomoc i zaufanie.

This work was supported in part by the FP6 Commission "Biocare" (Molecular Imaging for Biologically Optimized Cancer Therapy) under the contract number 505785 and by SPUB 621/E-78/SPB/6 PR UE/DIE 458/2004-2007 of Polish Committee for Scientific Research.

This work was supported in part by the EU Structural Funds Project no POIG.01.01.02-14-012/08-00.

